HELLENIC REPUBLIC
UNIVERSITY OF IOANNINA
SCHOOL OF ENGINEERING
DEPARTMENT OF MATERIALS SCIENCE AND ENGINEERING

Computational Modeling of Long Bones during the Fracture Healing Process

Vassiliki T. Potsika

PhD Thesis

IOANNINA 2017

ΕΛΛΗΝΙΚΗ ΔΗΜΟΚΡΑΤΙΑ
ΠΑΝΕΠΙΣΤΗΜΙΟ ΙΩΑΝΝΙΝΩΝ
ΠΟΛΥΤΕΧΝΙΚΗ ΣΧΟΛΗ
ΤΜΗΜΑ ΜΗΧΑΝΙΚΩΝ ΕΠΙΣΤΗΜΗΣ ΥΛΙΚΩΝ

Υπολογιστική Μοντελοποίηση Μακρών Οστών κατά την Πώρωση Καταγμάτων

Βασιλική Θ. Ποτσίκα

ΔΙΔΑΚΤΟΡΙΚΗ ΔΙΑΤΡΙΒΗ

ΙΩΑΝΝΙΝΑ 2017

HELLENIC REPUBLIC
UNIVERSITY OF IOANNINA
SCHOOL OF ENGINEERING
DEPARTMENT OF MATERIALS SCIENCE AND ENGINEERING

Computational Modeling of Long Bones during the Fracture Healing Process

Vassiliki T. Potsika

PhD Thesis

IOANNINA 2017

Η έγκριση της διδακτορικής διατριβής από το Τμήμα Μηχανικών Επιστήμης Υλικών της Πολυτεχνικής Σχολής του Πανεπιστημίου Ιωαννίνων δεν υποδηλώνει αποδοχή των γνωμών του συγγραφέα Ν. 5343/32, άρθρο 202, παράγραφος 2».

Date of application of Mrs. Potsika: 15th June 2010

Date of appointment of PhD Advisory Committee: 16th June 2010

Members of the 3 member Advisory Committee:

Thesis Advisor

Prof. Dimitrios I. Fotiadis, Dept. of Materials Science and Engineering, Polytechnic School, University of Ioannina.

Members

Prof. Demosthenes Polyzos, Dept. of Mechanical Engineering and Aeronautics, Polytechnic School, University of Patras.

Prof. Antonios Charalambopoulos, Dept. of Mathematics, School of Applied Mathematics and Physics, National Technical University of Athens.

Date of Thesis subject definition: 16th June 2010

Title: Computational Modeling of Long Bones during the Fracture Healing Process

Date of appointment of the 7 member Examination Committee: 23rd March 2017

Members of the 7 member Advisory Examination Committee:

1. **Prof. Dimitrios I. Fotiadis,** Dept. of Materials Science and Engineering, Polytechnic School, University of Ioannina, **Thesis Advisor**.
2. **Prof. Demosthenes Polyzos,** Dept. of Mechanical Engineering and Aeronautics, Polytechnic School, University of Patras, **member of the 3 member Advisory Committee**.
3. **Prof. Antonios Charalambopoulos,** School of Applied Mathematics and Physics, National Technical University of Athens, **member of the 3 member Advisory Committee**.
4. **Prof. Dimitrios Koutsouris,** Dept. of Electrical and Computer Engineering, National Technical University of Athens.
5. **Prof. George Babis,** Medical School, National and Kapodistrian University of Athens.
6. **Assoc. Prof. Georgios Matsopoulos,** Dept. of Electrical and Computer Engineering, National Technical University of Athens.
7. **Assist. Prof. Leonidas Gergidis,** Dept. of Materials Science and Engineering, Polytechnic School, University of Ioannina.

The PhD thesis is approved, with **"Excellent"** on **October 18th, 2017.**

The Chairman of the Department	**The secretary of the Department**
Prof. Michail Karakasidis	**Xanthi Toutountzoglou**

Ημερομηνία αίτησης της κα. Ποτσίκα: 15 Ιουνίου 2010

Ημερομηνία ορισμού Τριμελούς Συμβουλευτικής Επιτροπής: 16 Ιουνίου 2010

Μέλη Τριμελούς Συμβουλευτικής Επιτροπής:
Επιβλέπων
Καθ. Δημήτριος Ι. Φωτιάδης, Τμήμα Μηχανικών Επιστήμης Υλικών, Πολυτεχνική Σχολή, Πανεπιστήμιο Ιωαννίνων.
Μέλη
Καθ. Δημοσθένης Πολύζος, Τμήμα Μηχανολόγων και Αεροναυπηγών Μηχανικών, Πολυτεχνική Σχολή, Πανεπιστήμιο Πατρών.
Καθ. Αντώνιος Χαραλαμπόπουλος, Σχολή Ε.Μ.Φ.Ε., Εθνικό Μετσόβιο Πολυτεχνείο.

Ημερομηνία Ορισμού Θέματος: 16 Ιουνίου 2010
Τίτλος: Υπολογιστική Μοντελοποίηση Μακρών Οστών κατά την Πώρωση Καταγμάτων

Ημερομηνία ορισμού Επταμελούς Εξεταστικής Επιτροπής: 23 Μαρτίου 2017
Μέλη Επταμελούς Εξεταστικής Επιτροπής:

1. **Καθ. Δημήτριος Ι. Φωτιάδης,** Τμήμα Μηχανικών Επιστήμης Υλικών, Πολυτεχνική Σχολή, Πανεπιστήμιο Ιωαννίνων **(Επιβλέπων)**.
2. **Καθ. Δημοσθένης Πολύζος,** Τμήμα Μηχανολόγων και Αεροναυπηγών Μηχανικών, Πολυτεχνική Σχολή, Πανεπιστήμιο Πατρών **(μέλος Τριμελούς Συμβουλευτικής Επιτροπής)**.
3. **Καθ. Αντώνιος Χαραλαμπόπουλος,** Σχολή Ε.Μ.Φ.Ε., Εθνικό Μετσόβιο Πολυτεχνείο **(μέλος Τριμελούς Συμβουλευτικής Επιτροπής)**.
4. **Καθ. Δημήτριος Κουτσούρης,** Σχολή Ηλεκτρολόγων Μηχανικών και Μηχανικών Υπολογιστών, Εθνικό Μετσόβιο Πολυτεχνείο.
5. **Καθ. Γεώργιος Μπάμπης,** Τμήμα Ιατρικής της Σχολής Επιστημών Υγείας, Εθνικό και Καποδιστριακό Πανεπιστήμιο Αθηνών.
6. **Αναπλ. Καθ. Γεώργιος Ματσόπουλος,** Σχολή Ηλεκτρολόγων Μηχανικών και Μηχανικών Υπολογιστών, Εθνικό Μετσόβιο Πολυτεχνείο.
7. **Επικ. Καθ. Λεωνίδας Γεργίδης,** Τμήμα Μηχανικών Επιστήμης Υλικών, Πολυτεχνική Σχολή, Πανεπιστήμιο Ιωαννίνων.

Έγκριση Διδακτορικής Διατριβής με βαθμό «**ΑΡΙΣΤΑ**» στις **18 Οκτωβρίου 2017.**

Ο Πρόεδρος του Τμήματος

Καρακασίδης Μιχαήλ
Καθηγητής

Η Γραμματέας του Τμήματος

Ξανθή Τουτουνζόγλου

Dedication

To my Parents

Acknowledgements

First of all, I would like to thank my family, who all these years support my dreams and my effort. My parents deserve special thanks for their unlimited support and encouraging.

I would like to cordially thank my supervisor Prof. Dimitrios I. Fotiadis, Dept. of Materials Science and Engineering, University of Ioannina for his support and great assistance in order to complete this thesis. I would like to emphasize my sincere appreciation for the financial support I had all these years and the contribution of Prof. Fotiadis. I would also like to thank the members of my advisory committee, Prof. Demosthenes Polyzos, Dept. of Mechanical Engineering & Aeronautics, University of Patras and Prof. Antonios Charalampopoulos, School of Applied Mathematics and Physics, National Technical University of Athens, for the inspiration, guidance and continuous support.

I would also like to sincerely thank Dr. Vasilios Protopappas, Dr. Konstantinos Grivas and Dr. Theodoros Gortsas for their collaboration and support all these years, as well as Dr. Maria Vavva for her guidance in the first steps of my research work. I would like to warmly thank all my colleagues and friends from the Unit of Medical Technology and Intelligent Information Systems for the excellent cooperation, friendship and support in demanding working conditions.

Furthermore, I would like to thank Prof. Kay Raum, Berlin-Brandenburg School for Regenerative Therapies, Charité-Universitätsmedizin Berlin, with whom I had an excellent collaboration all these years and provided me with data and knowledge to accomplish this work. Through this cooperation I had the opportunity to participate in an international student exchange program and meet most of the researchers with a high scientific reputation in this research area.

In addition, I would like to refer to the support of the State Scholarships Foundation (IKY) and the German academic exchange service (DAAD) for the fellowship I received and the opportunity to participate in student exchanges between the University of Ioannina, the University of Patras and the Charité-Universitätsmedizin Berlin. Through my participation in this program, I broadened the perspectives and knowledge on my thesis, interacted with young researchers working in similar research fields and exchanged innovative ideas.

Last but not least, I would like to cordially thank Prof. Christos V. Massalas, Professor Emeritus at the Dept. of Materials, Science and Engineering, University of Ioannina for his confidence, support and the opportunity to collaborate with him in writing the first Greek book in the domain of biomechanics.

Table of Contents

List of Figures

List of Tables

List of abbreviations

SAM	Scanning acoustic microscopy
FAS	First arriving signal
IEMA	Iterative effective medium approximation
BEM	Boundary element method
BMU	Basic multicellular unit
μ-CT	Micro-computed tomography
CT	Computed Tomogaphy
HR-pQCT	High resolution peripheral quantitative computed tomography
DEXA	Dual-energy x-ray absorptiometry
BMD	Bone mineral density
vBMD	Apparent bone mineral density
3D	Three dimensional
2D	Two dimensional
MRI	Magnetic Resonance Imaging
HR-MRI	High-resolution Magnetic Resonance Imaging
μ-MRI	Micro-Magnetic Resonance Imaging
TE	Time echo
VEGF	Vascular endothelial growth factor
TMD	Tissue mineral density
BV/TV	Bone volume fraction
Tb.Th	Trabecular thickness
Tb.Sp	Trabecular separation
Tb.N	Trabecular number
QCT	Quantitative Computed Tomography

FTIR	Fourier transform infrared imaging
qBEI	Quantitative backscattered electron imaging
EDX	Energy-dispersive X-ray spectroscopy
NMR	Nuclear magnetic resonance
BW	Bone water
SD	Standard deviation
QUS	Quantitative ultrasound
RL	Resorption lacunae
TOF	Time-of-flight
AIB	Apparent integrated backscatter
(t-f)	Time-frequency
VEGF	Endothelial growth factor
IEMA	Iterative effective medium approximation
RSPWV	Reassigned Smoothed-Pseudo Wigner-Ville
FSAB	Frequency slope of apparent backscatter
ANOVA	Analysis of variance
FEM	Finite Element Method
FDM	Finite Differences Method
FFT	Fast Fourier Transform
FDTD	Finite-difference time-domain
BUA	Broadband ultrasonic attenuation
(f-c_g)	Frequency-group velocity
BUB	Broadband ultrasonic backscatter
PML	Perfectly matched layers
EDTA	Ethylenediamine tetraacetic acid

List of symbols

R	Rigidity, Reflection Coefficient
F	Load
F_{ult}	Ultimate load
σ	Stress
ε	Strain
E	Young's modulus or modulus of elasticity
σ_y	Yield stress
σ_{ult}	Ultimate stress
W	Strain energy density
S_{ij}	Compliance constants
μ	Lamé coefficient, Attenuation coefficient
σ_{ii}	Normal stresses
σ_{ij}	Shearing stresses
G	Shear modulus
K	Bulk modulus
ν	Poisson's ratio
λ	Lamé coefficient, Wavelength
c_l	Longitudinal velocity
c_s	Shear velocity
Z	Acoustic impedance
p	Acoustic pressure, Longitudinal plane mean wave
f	Frequency
T	Time period
c_p	Phase velocity
k	Wavenumber

c_g	Group velocity
r	Amplitude reflection coefficient
t	Amplitude transmission coefficient
T	Transmission coefficient, Traction
θ_c	Critical angle
μ_α	Absorption coefficient
μ_s	Scattering coefficient
I	Acoustic intensity
ω	Angular frequency
c	Phase velocity of Lamb wave, wave propagation velocity
S0, S1, S2	Symmetric Lamb modes
A0, A1, A2	Anti-symmetric Lamb modes
c_R	Rayleigh velocity
d	Thickness,bSpace dimension
n_1	Volume concentration of particles
n_2	Volume concentration of matrix
$g^{(1)}$, $g^{(2)}$	Forward scattering amplitudes of the fluctuating waves
K^{eff}	Bulk moduli of an isotropic material
μ^{eff}	Shear moduli of an isotropic material
ρ^{eff}	Effective density
U	Displacement
q	Pressure flux
x	Space variable
ρ	Density
t	Time variable

Abstract

This thesis deals with the numerical modeling of healing and osteoporotic long bones based on scanning acoustic microscopy images (SAM) and the potential of ultrasound to diagnose and monitor bone pathologies. The outermost aim is the investigation of the complex wave scattering phenomena induced by the composite nature of osseous and callus tissues. In this direction, theoretical and numerical methodologies are applied to identify changes in the scattering amplitude, the propagation of guided waves and the first arriving signal velocity (FAS) at successive healing stages, as well as in computational models of cortical bones with different porosities. Numerical simulations of ultrasound propagation in healthy, healing and osteoporotic bones are conducted using the traditional axial transmission technique, while the backscattering method is also used as a relative new method. Emphasis is given on the investigation of the porous nature of callus and cortical bone, which is incorporated in the numerical models using the SAM data, and alterations which occur due to bone pathologies.

In the first chapter, the biological and mechanical background is given. To fully evaluate bone's mechanical properties, the mechanical properties of its component phases and the structural relationship are presented between the various levels of hierarchical structural organization. The fundamental principles of the theory of elasticity are also analyzed to provide a theoretical background for the characterization of the material and structural properties of bone. Then, the mechanisms of the fracture healing process and osteoporosis are described. More specifically, the evolution of the biological processes and the mechanical and structural properties are analyzed.

The second chapter presents the fundamental principles of ultrasound propagation in the bone. Complex wave propagation phenomena are explained which occur due to the composite nature of bone, as well as due to the presence of soft tissues in the ultrasonic propagation path such as reflection, refraction, attenuation and scattering. The two main parameters for ultrasonic bone assessment are discussed which are the FAS velocity and the propagation of guided waves.

In the third chapter, the state of the art in the field of ultrasonic characterization of bone is presented. The experimental and computational studies in this field are included. It also describes the ultrasonic techniques which have been applied in the literature and more specifically the axial transmission, the through transmission and the backscattering methods for bone evaluation. At the end of the chapter, the objective and the contribution of this thesis are discussed.

In the fourth chapter, ultrasound wave propagation in healing long bones is simulated using an iterative effective medium approximation (IEMA) and SAM images from an animal study. The effectiveness of IEMA in bone characterization is examined: (a) by comparing the theoretical phase velocities with experimental measurements in cancellous bone mimicking phantoms, and (b) by simulating axial wave propagation in complex healing bone geometries. The original material properties and porosity are derived using SAM data in order to apply more realistic conditions. The Boundary Element Method (BEM) is used for the numerical solution of the wave propagation problem. Guided wave analysis is performed for different healing stages.

In the fifth chapter, the backscattering method is used to evaluate healing long bones at successive healing stages. The parameters of interest are the scattering amplitude and the variation of the acoustic pressure in the backward direction. SAM images are used to establish more realistic geometries of healing long bones and incorporate the nonhomogeneous and porous nature of the callus and the cortical tissues. The BEM is used for the numerical solution of the wave propagation problem. The impact of the excitation frequency is also considered.

The sixth chapter presents a parametric and systematic numerical study on ultrasound propagation in cortical bone models to investigate the effect of changes in cortical porosity and the occurrence of large basic multicellular units (BMUs) on the FAS velocity. Two-dimensional geometries of cortical bone are established for various microstructural models mimicking normal and pathological tissue states. Emphasis is given on the detection of large BMUs formation which may provoke the thinning of the cortical cortex and the increase of porosity at a later stage of the disease. The role of the excitation frequency is also discussed.

In the final chapter, the conclusions of this thesis are highlighted based on the results and limitations as they result from the previous chapters. Directions and trends for future research in the field are also discussed.

The main contributions of this thesis can be summarized as: (i) the development of realistic numerical models of healing long bones which account for callus and cortical porosity based on SAM images, (ii) the development of numerical models of healthy and osteoporotic bones which incorporate the occurrence of large BMUs aiming not only to monitor cortical porosity alterations but also to detect regions being at high risk of fracture, (iii) the investigation of the complex scattering phenomena at successive stages of fracture healing, (iv) the application of different ultrasonic methods in order to propose new quantitative parameters for bone assessment and v) the study of the impact of the excitation frequency.

Περίληψη

Η παρούσα διδακτορική διατριβή ασχολείται με την αριθμητική μοντελοποίηση των κατεαγότων και οστεοπορωτικών μακρών οστών με βάση εικόνες ακουστικής μικροσκοπίας σάρωσης και τη δυνατότητα του υπερήχου να χρησιμοποιηθεί για τη διάγνωση και την παρακολούθηση των παθολογιών των οστών. Ο βασικός στόχος είναι η διερεύνηση των πολύπλοκων φαινομένων κυματικής σκέδασης που προκαλούνται από τη σύνθετη φύση του οστικού ιστού και του πώρου. Σε αυτή την κατεύθυνση, εφαρμόζονται θεωρητικές και αριθμητικές μεθοδολογίες για τον εντοπισμό μεταβολών στο πλάτος σκέδασης, την διάδοση των κυματοδηγούμενων ρυθμών και την ταχύτητα του πρώτου αφιχθέντος σήματος σε διαδοχικά στάδια επούλωσης, καθώς και σε αριθμητικά μοντέλα του φλοιώδους οστού με διαφορετικά ποσοστά πορώδους. Η αριθμητική προσομοίωση της διάδοσης υπερήχου σε υγιή, κατεαγότα και οστεοπορωτικά οστά πραγματοποιήθηκε αρχικά με την ευρέως χρησιμοποιούμενη τεχνική αξονικής μετάδοσης, ενώ η μέθοδος οπισθοσκέδασης αξιολογήθηκε επίσης ως σχετικά νέα μέθοδος. Έμφαση δίνεται στη διερεύνηση της πορώδους φύσης του πώρου και του φλοιώδους οστού, η οποία ενσωματώθηκε στα αριθμητικά μοντέλα με τη χρήση των δεδομένων ακουστικής μικροσκοπίας σάρωσης, και σε μεταβολές που συμβαίνουν λόγω των παθολογιών των οστών.

Στο πρώτο κεφάλαιο παρουσιάζεται το βιολογικό και μηχανικό υπόβαθρο της μελέτης. Αρχικά, προκειμένου να αξιολογηθούν πλήρως οι μηχανικές ιδιότητες του οστού, παρουσιάζονται οι μηχανικές ιδιότητες των επιμέρους συστατικών του και τα διαφορετικά επίπεδα ιεραρχικής δομικής οργάνωσης. Οι θεμελιώδεις αρχές της θεωρίας της ελαστικότητας αναλύονται επίσης παρέχοντας ένα θεωρητικό υπόβαθρο για τον χαρακτηρισμό των υλικών και δομικών ιδιοτήτων του οστού. Στη συνέχεια περιγράφονται οι μηχανισμοί της διαδικασίας επούλωσης κατάγματος και οστεοπόρωσης και αναλύονται η εξέλιξη των βιολογικών διαδικασιών και οι μηχανικές και δομικές ιδιότητες.

Το δεύτερο κεφάλαιο παρουσιάζει τις θεμελιώδεις αρχές της θεωρίας της διάδοσης υπερήχων στα οστά. Εξηγείται η εξέλιξη των φαινομένων που παρατηρούνται λόγω της σύνθετης φύσης του οστού καθώς και λόγω της παρουσίας μαλακών ιστών στη διαδρομή της διάδοσης υπερήχων όπως η ανάκλαση, η διάθλαση, η απόσβεση και η σκέδαση. Επίσης, περιγράφονται οι δύο κύριες παραμέτροι για την αξιολόγηση των

οστών, οι οποίες είναι η ταχύτητα του πρώτου αφιχθέντος σήματος και η ανάλυση της διάδοσης των κυματοδηγούμενων ρυθμών.

Στο τρίτο κεφάλαιο, παρουσιάζεται η ανασκόπηση της βιβλιογραφίας στον τομέα του χαρακτηρισμού των οστών με τεχνικές υπερήχου. Περιλαμβάνονται οι πειραματικές και υπολογιστικές μελέτες στον συγκεκριμένο τομέα. Περιγράφονται επίσης οι τεχνικές υπερήχων που έχουν εφαρμοσθεί στη βιβλιογραφία για την αξιολόγηση του οστού και πιο συγκεκριμένα η μέθοδος αξονικής διάδοσης, η μέθοδος εγκάρσιας διάδοσης και η μέθοδος οπισθοσκέδασης. Τέλος, συζητείται ο στόχος και η συμβολή της παρούσας διατριβής.

Στο τέταρτο κεφάλαιο, προσομοιώνεται η διάδοση των υπερηχητικών κυμάτων σε κατεαγότα μακρά οστά χρησιμοποιώντας μια επαναληπτική αυτοσυνεπή μεθοδολογία υπολογισμού της φασικής ταχύτητας και απόσβεσης ενός κύματος και εικόνες ακουστικής μικροσκοπίας σάρωσης από προηγούμενη μελέτη σε ζώα. Πρώτον, εξετάζεται η αποτελεσματικότητα της μεθοδολογίας για το χαρακτηρισμό των οστών: (α) συγκρίνοντας τις θεωρητικές ταχύτητες φάσης με πειραματικές μετρήσεις σε οστικά φαντασμικά συστήματα, και (β) με προσομοίωση της αξονικής διάδοσης κύματος σε σύνθετες γεωμετρίες κατεαγότων οστών. Οι αρχικές ιδιότητες του υλικού και το πορώδες προέρχονται από δεδομένα ακουστικής μικροσκοπίας σάρωσης προκειμένου να εφαρμοστούν πιο ρεαλιστικές συνθήκες. Η μέθοδος συνοριακών στοιχείων χρησιμοποιείται για την αριθμητική επίλυση του προβλήματος κυματικής διάδοσης. Πραγματοποιείται μελέτη της διάδοσης των κυματοδηγούμενων ρυθμών για διαφορετικά στάδια επούλωσης.

Στο πέμπτο κεφάλαιο, η μέθοδος οπισθοσκέδασης χρησιμοποιείται για την αξιολόγηση κατεαγότων μακρών οστών σε διαδοχικά στάδια επούλωσης. Οι παράμετροι που μελετώνται είναι το πλάτος σκέδασης και η μεταβολή της ακουστικής πίεσης στην οπίσθια διεύθυνση. Εικόνες ακουστικής μικροσκοπίας σάρωσης χρησιμοποιούνται για τη δημιουργία ρεαλιστικών γεωμετρικών κατεαγότων μακρών οστών που ενσωματώνουν την ανομοιογένεια και το πορώδες των ιστών του πώρου και του φλοιώδους οστού. Η μέθοδος των συνοριακών στοιχείων χρησιμοποιείται για την αριθμητική λύση του προβλήματος κυματικής διάδοσης. Η επίδραση της συχνότητας διέγερσης επίσης λαμβάνεται υπόψη.

Το έκτο κεφάλαιο παρουσιάζει μια παραμετρική και συστηματική αριθμητική μελέτη της διάδοσης υπερήχων σε μοντέλα φλοιώδους οστού για τη διερεύνηση της επίδρασης των αλλαγών στο πορώδες του συμπαγούς οστού και στην εμφάνιση μεγάλων πολυκύτταρων μονάδων στην ταχύτητα του πρώτου αφιχθέντος σήματος. Διδιάστατες γεωμετρίες του φλοιώδους οστού παρουσιάζονται για διαφορετικά αριθμητικά μοντέλα που ενσωματώνουν την μικροδομή των ιστών ώστε να μιμούνται φυσιολογικές και παθολογικές καταστάσεις. Έμφαση δίνεται στον εντοπισμό του σχηματισμού μεγάλων πολυκύτταρων μονάδων που μπορεί να προκαλέσει την λέπτυνση του φλοιού και την αύξηση του πορώδους σε μεταγενέστερο στάδιο της νόσου. Ο ρόλος της συχνότητας διέγερσης επίσης εξετάζεται.

Στο τελευταίο κεφάλαιο επισημαίνονται τα συμπεράσματα αυτής της διδακτορικής διατριβής με βάση τα αποτελέσματα και τους αναγκαίους περιορισμούς της ερευνητικής εργασίας όπως προκύπτουν από τα προηγούμενα κεφάλαια. Επίσης, συζητούνται κατευθύνσεις και τάσεις για μελλοντική έρευνα στο συγκεκριμένο πεδίο.

Η συμβολή της παρούσας διδακτορικής διατριβής συνοψίζεται στους παρακάτω παράγοντες: (i) την ανάπτυξη ρεαλιστικών αριθμητικών μοντέλων κατεαγότων μακρών οστών που λαμβάνουν υπόψη την πορώδη φύση του πώρου και του φλοιώδους οστού με βάση εικόνες ακουστικής μικροσκοπίας σάρωσης, (ii) την ανάπτυξη αριθμητικών μοντέλων υγιών και οστεοπορωτικών οστών που ενσωματώνουν την ύπαρξη μεγάλων πολυκύτταρων μονάδων στοχεύοντας τόσο στην αποτελεσματική παρακολούθηση της οστεοπόρωσης όσο και στην έγκαιρη πρόβλεψη της νόσου σε αρχικό στάδιο, (iii) τη διερεύνηση των σύνθετων φαινομένων σκέδασης σε διαδοχικά στάδια της πώρωσης καταγμάτων, (iv) την εφαρμογή διαφορετικών τεχνικών διάδοσης υπερήχων ώστε να μελετηθούν νέες ποσοτικές παράμετροι για την αξιολόγηση των οστών, v) τη μελέτη του ρόλου της συχνότητας διέγερσης.

Chapter 1: Introduction to Bone Hierarchical Structure and Mechanical Properties

1.1 Bone Composition and Hierarchical Structure

1.1.1 Bone functions

The skeletal system consists of individual bones and the connective tissue which surrounds them and plays a significant biomechanical and metabolical role. Bone is the main constituent of the skeletal system and forms a protective and supportive framework for the body. More specifically, the skeletal system enables body movement by acting as a lever and point of attachment for muscles, protects vital organs and provides the means for a metabolic activity.

1.1.2 Wolff's law

Bone is a living material as it evolves during life having an effect on bone physiology and biology. It constantly remodels and changes its shape and its internal structure to adapt to mechanical loading. This was conceptualized by Wolff's law in 1892 stating that mechanical stress was responsible for determining the architecture of bone (Wolff, 1982). The remodeling of bone in response to loading is achieved via mechanotransduction, a process of converting forces into biochemical signals and integrating these signals into the cellular response. Wolff's Law explains the

significance of exercise in the treatment of bone pathologies such as osteoporosis and fracture healing. Specifically, weight-bearing and strength exercises are usually recommended by clinicians as a non-medicinal treatment for osteoporosis, while a range of motions and stresses can improve the overall strength of a bone having sustained a fracture.

1.1.3 Bone composition

Bone is a composite material consisting of an inorganic and an organic phase. Approximately 60% of the tissue is inorganic matter, 8-10% is water and the remainder is organic matter (Marcus *et al.,* 2011).

The mineral phase is an impure form of hydroxyapatite, $Ca_{10}(PO_4)_6(OH)_2$, containing constituents such as carbonate, citrate, magnesium, fluoride, and strontium incorporated into the crystal lattice or absorbed onto the crystal surface. Foreign substances such as tetracyclines, polyphosphates, bisphosphonates, and bone-seeking radionuclides can also be incorporated with high affinity (Cowin, 2001).

The organic phase is composed of collagen (90%) and a variety of noncollagenous proteins, and cells (10%). The organic phase of bone plays a key role influencing the structure and the mechanical and biochemical properties of the osseous tissues (Marcus *et al.,* 2011; Cowin, 2001). The role of noncollagenous proteins is unclear. The most abundant ones are osteocalcin, osteonectin, osteopontin, and bone sialoprotein.

1.1.4 Organization of long bones

The skeleton is consisted of two parts: the axial skeleton, which is composed by the bones of the head and trunk and the appendicular skeleton, which includes the bones of the limbs and pelvic girdle. This study deals with the numerical modeling of long bones such as the tibia, femur and humerus which have three main regions: the epiphysis, the metaphysis and the diaphysis as shown in Fig.1.1. The central portion of the long bone is called diaphysis. The epiphysis covers the end of the bone and develops from a center of ossification that is distinct from the rest of the long bone shaft. The metaphysis is the region of transition from the wider epiphysis to the more slender diaphysis (Marcus *et al.,* 2011).

In (Barkaoui *et al.,* 2014; Rho *et al.*, 1998; Katz *et al,.* 1980), five levels of hierarchical organization have been distinguished, shown in Figure 1.2, which have been widely accepted in the scientific community: the macrostructural level, the microstructure, the sub-microstructure, the nanostructure and the sub-nanostructure level.

From a macrostructural point of view, bone consists of the periosteum, bone tissue, bone marrow, blood vessels and nerves. Bone tissue is composed of the cortical or compact bone and the cancellous or trabecular bone (Fig.1.1). In cross-section, the end of a long bone such as the femur has a dense cortical shell with a porous, cancellous interior. The main differentiation between these two types of osseous tissues refers to their degree of porosity and density. In Fig.1.2, the hierarchical structure of bone is presented from the macrostructure to the microstructure level.

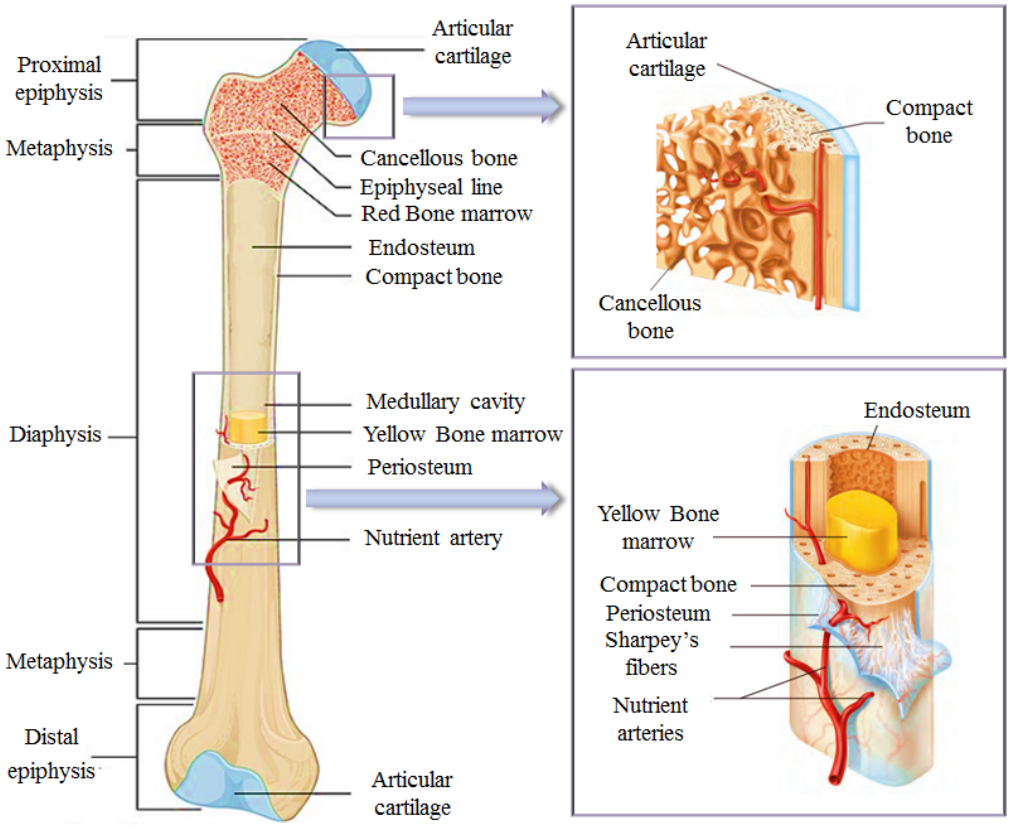

Figure 1.1: The structure of a long bone (Marieb and Hoehn, 2014).

Cancellous bone is found in the inner part of bones and has a significantly porous structure. It is also known as spongy bone due to its high porosity. The porosity in cancellous bone ranges from 50–90%, usually found in cuboidal bones, flat bones and

at the ends of long bones (Wang *et al.,* 2016). In the microstructure level, it is consisted of three-dimensional cylindrical structures, called trabeculae, with a thickness of about 100 μm and a variable arrangement form (Potsika *et al.,* 2014b). The microstructure of cancellous bone is composed of irregular, sinuous convolutions of lamellae (Rho *et al*., 1998). This porous network of cancellous bone includes pores filled with marrow which produces the basic blood cells and consists of blood vessels, nerves and various types of cells. Cancellous bone material properties are important for the characterization of several bone pathologies, and the assessment of various joint implants as cancellous bone is affected by disease sooner than cortical bone.

Cortical bone composes of the external surface of all bones and has a porosity of about 5−10%. Mineralized collagen fibers form into planar arrangements called lamellae (3–7 mm wide). The lamellae wrap in concentric layers (3–8 lamellae) around a central canal to form what is known as an osteon or a Haversian system. The osteon looks like a cylinder with diameter 200–250 μm running roughly parallel to the long axis of the bone. Other forms of cortical bone in which the mineralized collagen fibers are less well organized showing no specific pattern are called woven bone of lamellae (Rho *et al*., 1998).

At the nanoscale, the most significant type of porosity, known as vascular porosity, is formed by the Haversian canals (aligned with the long axis of the bone) and the Volkmanns canals, which are transverse canals connecting Haversian canals, with capillaries and nerves. The lamellae have a twisted plywood arrangement, where neighboring lamellae have different fibril orientations. Here, osteocyte cells reside in lacunae (15–25 μm diameter) that interconnect through canaliculi (100–400 nm in diameter) (Zimmermann *et al.,* 2015). The boundary between the osteon and the surrounding bone is called the cement line.

The basic components in this level are collagen and hydroxyapatite which are made of collagen molecules organized in fibrils. The fibrils are surrounded by polycrystalline extrafibrillar mineral platelets. In addition to mineral, the extrafibrillar and the intrafibrillar matrix contain molecular components, such as non-collageneous proteins or cross-links, promoting the formation of sacrificial bonds. Within the fibrils, type I collagen molecules (1.5 nm diameter, 300 nm length) and hydroxyapatite nanocrystals

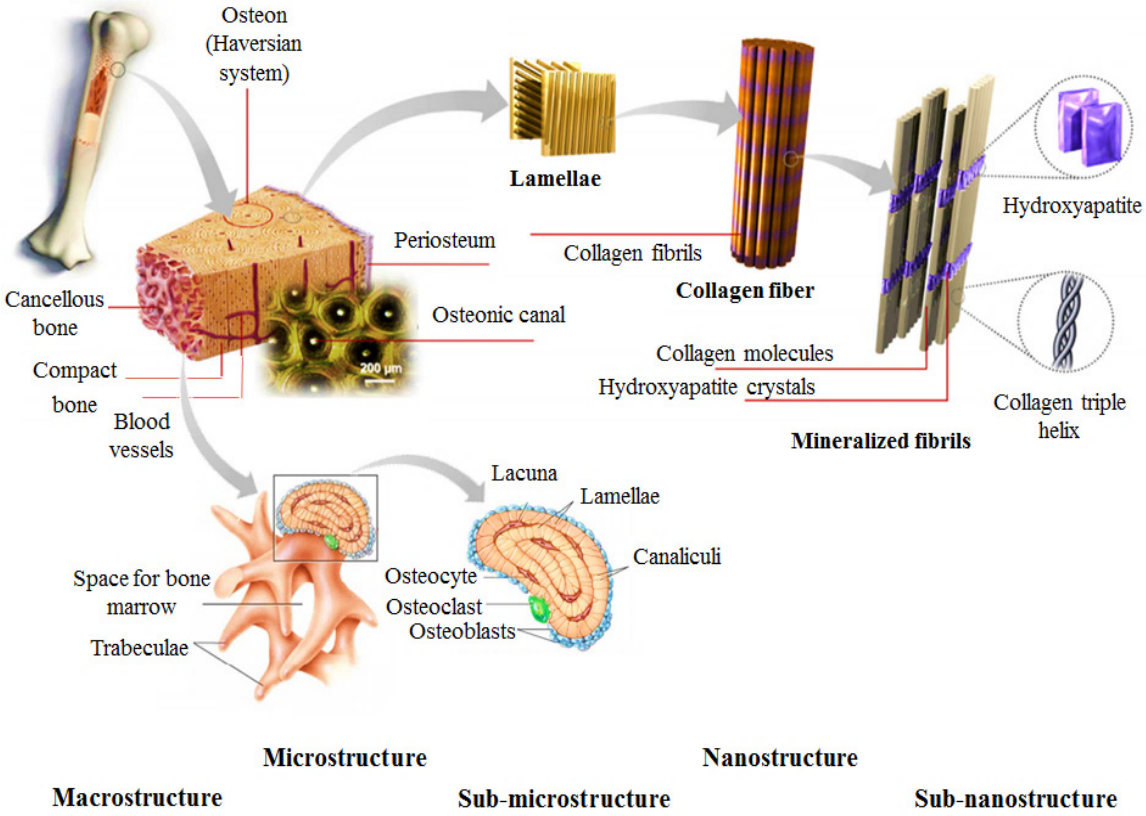

Figure 1.2: The hierarchical structure of a typical long bone at various length scales (Wang *et al.,* 2016; Sadat-Shojai *et al.,* 2013).

(50 nm width, 25 nm height, 1.5–4 nm thickness) form a composite structure, where arrays of collagen molecules staggered at 67 nm are embedded with nano-platelets of hydroxyapatite mineral (Zimmermann *et al*., 2015; Sadat-Shojai *et al.,* 2013; Bienz and Saad, 2013).

Inorganic components (hydroxyapatite crystals) are mainly responsible for the compression strength and stiffness, while organic components (collagen fibers, proteoglycans, osteocalcin) are responsible for tension properties. The hydroxyapatite crystals are located in the interfibrillar spaces. Mineralized fibers are aligned to form bone lamellae of typical thickness of a few micrometers. The orientation of the fibers depends on the lamellae and may change within lamellar sublayers (Potsika *et al*., 2014b).

1.2 Elasticity

Bones are physical objects that obey the laws of mechanics. The primary laws of mechanics that concern deformable objects like bone are the three laws of motion by Sir Isaac Newton in 1687 and the law of elasticity of solid materials described by Robert Hooke in 1678 (Cowin, 2001).

The theory of elasticity deals with the systematic study of the stress, strain and displacement fields in an elastic body under the influence of external forces. The response of a solid body to external forces is influenced by the geometric configuration of the body, as well as by the mechanical properties of the material. The strain and stress fields in a medium are related by laws called constitutive or material laws, characterizing the mechanical behavior of the medium. These are derived from experimental procedures and allow us to have the best description of the experimental results. Although living tissues are not elastic in nature, in limited ranges of stress, strain and temperature they may follow an elastic behavior. Bone mechanics deals with elastic materials, i.e. materials in which the deformation and stress disappear with the removal of the external forces. A deeper understanding of the tissue elastic properties can provide invaluable information about the normal function of various organs, predict changes due to pathophysiological alterations and help to propose methods of surgical treatment and artificial intervention (Fotiadis *et al.*, 2006).

In daily life, the skeletal system is subject to a variety of loads that alternate within the bone according to the type of movement and joint. Biomechanical experiments can be performed using compression, tension, shear, torsion or bending loading to evaluate the rigidity and ultimate load of a long bone (Bankoff, 2012). A compressive strength causes shortening and extension, a tensile strength causes narrowing and elongation, torsional strength creates an angular distortion and the bending strength includes all changes seen in compression, tension and shear. Shear load is characterized by two forces acting parallel to each other but in opposite directions so that one part of the object is moved or displaced relative to another part.

Considering the upper extremity of the femur loaded in a single stance phase configuration, the monopodal loading is mimicked (Laugier and Haïat, 2011). This loading condition can be reproduced *ex vivo* on a testing machine. From this specific experiment, the load applied to simulate a single stance phase configuration and the

corresponding displacement can be measured. In Fig.3, the load-displacement curve is depicted. The rigidity (R) can be assessed from the linear part of the curve from the following equation:

$$R = \frac{F}{\Delta l}, \tag{1.1}$$

where F is the load (in N) and Δl the displacement (in m).

The rigidity reflects the capability of the bone to withstand a load. This parameter evaluates the elasticity of a complex shape (such as bone or a portion of bone, i.e. the proximal femur). The ultimate response of the structure is defined by the ultimate load (failure load) which corresponds to the maximum of the load-displacement curve. These parameters depend on the geometry of the bone. More specifically, with increasing size of the bone, the rigidity and the failure load are higher. Fig. 1.3 presents the load-displacement curve, ultimate load (F_{ult}) and rigidity (R).

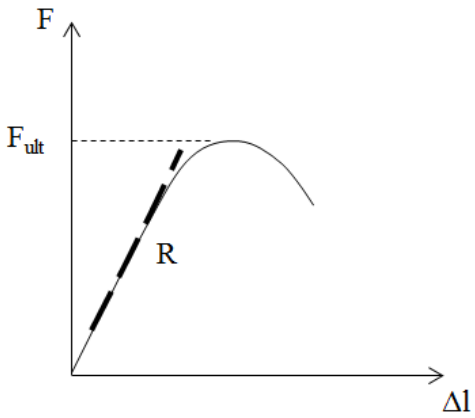

Figure 1.3: Load-displacement curve, ultimate load and rigidity.

The stress is the central physical concept of continuum mechanics and elasticity theory and corresponds to the transmission of force through a continuum medium. The stress (σ) is determined from the measurement of the load (F) applied to a given area (A) as described by the following equation:

$$\sigma = \frac{F}{A}. \tag{1.2}$$

The strain (ε) can be computed from the ratio of the measured displacement (ΔL) and the initial specimen length (L) (Fig. 1.4):

$$\varepsilon = \frac{\Delta L}{L} . \tag{1.3}$$

Figure 1.4 presents the stress-strain curve for mild steel. If the material after loading returns to the initial position, the material presents an elastic behavior. The yield point corresponds to the end of the elastic domain and is defined by the yield stress (σ_y). The most elementary description of material behavior is the well-known Hooke's law which refers to a one-dimensional extensional test:

$$E = \frac{\sigma}{\varepsilon} , \tag{1.4}$$

in which E denotes the Young's modulus or modulus of elasticity.

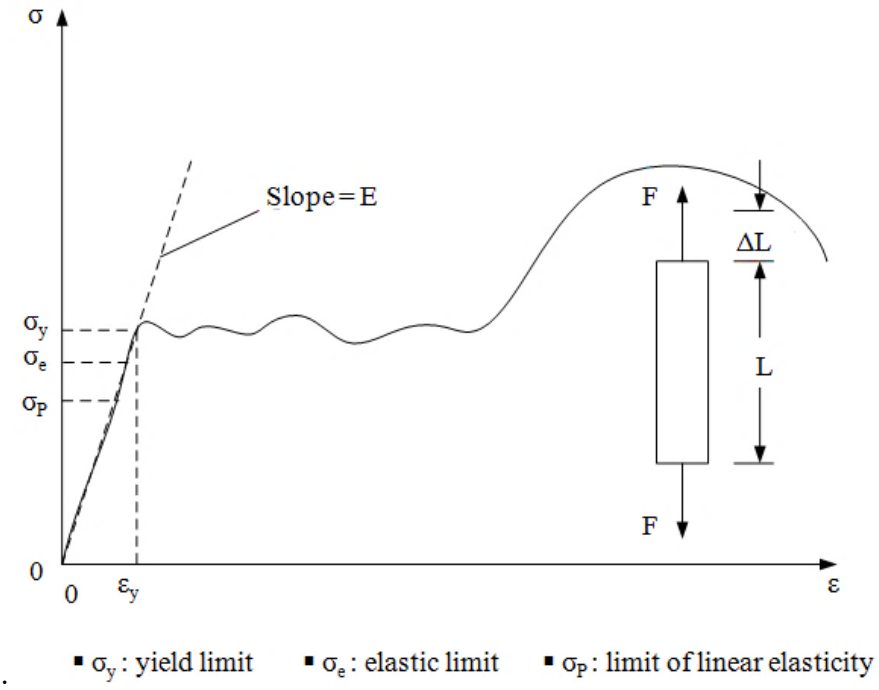

Figure 1.4 Stress-strain curve for mild steel (Fotiadis *et al.*, 2006).

The material elasticity is defined by the Young's modulus which can be assessed as the slope of the linear part of the stress-strain curve. The material that is loaded only to a level below the yield strain and unloads along the same path is called elastic.

If the path is linear as well, the material is said to be linearly elastic. In order to postulate a linear relationship between each component of stress and strain, it is necessary to establish the existence of a strain energy density W that is homogeneous quadratic function of strain components, $W(\varepsilon_{ij})$. For a body which is slightly strained

by gradual application of the loading, while the temperature remains constant, this will produce stress components derivable as follows:

$$\sigma_{ij}=\frac{\partial W}{\partial \varepsilon_{ij}} \ . \tag{1.5}$$

It should be noted that the function should have coefficients such that $W \geq 0$ in order to insure the stability of the material, with $W(0)=0$ corresponding to a natural or zero energy state.

The generalized Hooke's law is expressed by the equation:

$$\sigma_{ij}=C_{ijkl}\varepsilon_{kl} \ , \tag{1.6}$$

where C_{ijkl} is a fourth-order tensor (3^4= 81 components).

The coefficients σ_{11}, σ_{12}, … , σ_{33} are the components of stress. The entire array consists the stress tensor based on the transformation rule, $\sigma_{kl} = \lambda_{ki}\lambda_{lj}\sigma_{ij}$, i,j,k,l=1,2,3, where λ_{ki} are the direction cosines.

Since W is continuous, the order of differentiation in Eq. (1.5) is immaterial and C_{ijkl} is symmetric. Thus, the number of independent components (elastic constants) can be reduced to 21.

The corresponding strain energy function is:

$$\begin{aligned} 2W = \ & C_{11}\varepsilon_{11}^2+2C_{12}\varepsilon_{11}\varepsilon_{22}+2C_{13}\varepsilon_{11}\varepsilon_{33}+2C_{14}\varepsilon_{11}\varepsilon_{12}+2C_{15}\varepsilon_{11}\varepsilon_{23} \\ & +2C_{16}\varepsilon_{11}\varepsilon_{31}+C_{22}\varepsilon_{22}^2+2C_{23}\varepsilon_{22}\varepsilon_{33}+2C_{24}\varepsilon_{22}\varepsilon_{12}+2C_{25}\varepsilon_{22}\varepsilon_{23} \\ & +2C_{26}\varepsilon_{22}\varepsilon_{31}+C_{33}\varepsilon_{33}^2+2C_{34}\varepsilon_{33}\varepsilon_{12}+2C_{35}\varepsilon_{33}\varepsilon_{23}+2C_{36}\varepsilon_{33}\varepsilon_{31} \\ & +C_{44}\varepsilon_{12}^2+2C_{45}\varepsilon_{12}\varepsilon_{23}+2C_{46}\varepsilon_{12}\varepsilon_{31} \\ & +C_{55}\varepsilon_{23}^2+2C_{56}\varepsilon_{23}\varepsilon_{31} \\ & C_{66}\varepsilon_{31}^2 \ . \end{aligned} \tag{1.7}$$

The generalized Hooke's law in matrix form is:

$$\begin{bmatrix} \sigma_{11} \\ \sigma_{22} \\ \sigma_{33} \\ \sigma_{12} \\ \sigma_{23} \\ \sigma_{31} \end{bmatrix} = \begin{bmatrix} C_{11} & C_{12} & C_{13} & C_{14} & C_{15} & C_{16} \\ C_{21} & C_{22} & C_{23} & C_{24} & C_{25} & C_{26} \\ C_{13} & C_{23} & C_{33} & C_{34} & C_{35} & C_{36} \\ C_{41} & C_{42} & C_{43} & C_{44} & C_{45} & C_{46} \\ C_{51} & C_{52} & C_{53} & C_{54} & C_{55} & C_{56} \\ C_{61} & C_{62} & C_{63} & C_{64} & C_{65} & C_{66} \end{bmatrix} \begin{bmatrix} \varepsilon_{11} \\ \varepsilon_{22} \\ \varepsilon_{33} \\ \varepsilon_{12} \\ \varepsilon_{23} \\ \varepsilon_{31} \end{bmatrix}, \tag{1.8}$$

where $C_{ij}=C_{ji}$.

Eq. (1.6) can be written in the inverse form as follows:

$$\varepsilon_{ij}=S_{ijkl}\sigma_{kl}\ , \tag{1.9}$$

or in the analogous to (1.8) form as:

$$\mathbf{S}=\mathbf{C}^{-1}. \tag{1.10}$$

The coefficients $S_{ij}=S_{ji}$ are called the compliance constants.

The transformation of (1.6) and (1.9) follows the rules of the Cartesian tensors.

The preceding characterization of a medium is the most general and refers to an anisotropic material. More specifically, a material is anisotropic when its mechanical properties vary according to the direction of analysis. Several factors contribute to the mechanical anisotropy of bone. These include the orientation of the Haversian porous network, the orientation of the lamellae and the alignment of collagen fibers and hydroxyapatite crystals. In hierarchical structures like bone, the anisotropy depends on the observational level. Most of the engineering materials possess properties of symmetry about one or more of the planes or axes, which allows the number of independent constants to be reduced. This reduction is a function of the symmetry exhibited by the material under consideration.

An orthotropic material has three planes of symmetry which are mutually orthogonal. The existence of the two orthogonal symmetry planes implies the existence of the third. Therefore $\mathbf{C}$ is derived by adding a symmetry plane orthogonal to the preceding one of the monoclinic material. The invariance of $\mathbf{C}$ under a change of reference system carried out by symmetry about the second plane leads to:

$$\begin{bmatrix} C_{11} & C_{12} & C_{13} & 0 & 0 & 0 \\ C_{12} & C_{22} & C_{23} & 0 & 0 & 0 \\ C_{13} & C_{23} & C_{33} & 0 & 0 & 0 \\ 0 & 0 & 0 & C_{44} & 0 & 0 \\ 0 & 0 & 0 & 0 & C_{55} & 0 \\ 0 & 0 & 0 & 0 & 0 & C_{66} \end{bmatrix}. \tag{1.11}$$

Thus, the number of independent elastic constants C_{ij} is reduced to nine.

In first approximation, cortical and cancellous bones can be considered orthotropic, which means that the properties differ according to orthogonal directions. A composite medium such as bone can be considered as being consisted of a fiber embedded in a cylinder of matrix. The material behaves as an orthotropic material having in addition one axis of revolution. The material is then called a transverse isotropic material. A change of reference system produced by an arbitrary rotation about this axis must leave $\mathbf{C}$ unchanged. Considering this property the following equations are satisfied:

$$\begin{gathered} C_{13}=C_{12}, \quad C_{33}=C_{22}, \quad C_{55}=C_{66} \\ C_{44}=\frac{1}{2}\left(C_{22}-C_{23}\right). \end{gathered} \tag{1.12}$$

Thus, the properties of a transverse isotropic material can be determined by five independent elastic constants.

A material is isotropic if its properties are independent of the choice of its reference axes. The usual materials, with the exception of wood, usually satisfy this model at a macroscopic level. In this case $\mathbf{C}$ must be invariant under any change of the orthonormal basis. The application of this property to a unidirectional material leads to:

$$C_{22}=C_{11}, \quad C_{23}=C_{12}, \quad C_{66}=\frac{1}{2}\left(C_{11}-C_{12}\right). \tag{1.13}$$

Thus, the number of independent constants is reduced to two.

Introducing the Lamé coefficients λ and μ the following equations are derived:

$$C_{12}=\lambda, \quad \mu=\frac{1}{2}\left(C_{11}-C_{12}\right), \tag{1.14}$$

and:

$$C_{11}=\lambda+2\mu\,. \tag{1.15}$$

After (1.14) and (1.15) the Hooke's law (1.8) can be written as:

$$\sigma_{ij}=\lambda\delta_{ij}\varepsilon_{kk}+2\mu\varepsilon_{ij}\,, \tag{1.16}$$

where $\varepsilon_{kk}=\varepsilon_{11}+\varepsilon_{22}+\varepsilon_{33}$ is the dilatation of the material and δ_{ij} is the Kronecker's delta.

The normal stresses (i=j) are written as:

$$\sigma_{ii}=\lambda\delta_{kk}+2\mu\varepsilon_{ii} \tag{1.17}$$

and the shearing stresses ($i\neq j$) as:

$$\sigma_{ij}=2\mu\varepsilon_{ij}\,. \tag{1.18}$$

The deformations as functions of stresses are easily obtained as:

$$\varepsilon_{ij}=-\frac{\lambda}{2\mu\left(3\lambda+2\mu\right)}\delta_{ij}\sigma_{kk}+\frac{1}{2\mu}\sigma_{ij}\,. \tag{1.19}$$

In the case of uniaxial tension or compression the only non-vanishing stress is $\sigma_{11}\neq 0$.

It follows from this that $\sigma_{ij}=0$ for $i\neq j$. The normal deformation in the test direction is, by (1.19):

$$\varepsilon_{11}=-\frac{\lambda}{2\mu\left(3\lambda+2\mu\right)}\sigma_{11}+\frac{1}{2\mu}\sigma_{11} \tag{1.20}$$

and

$$\sigma_{11}=E\varepsilon_{11}\,, \tag{1.21}$$

where:

$$E=\frac{\mu\left(3\lambda+2\mu\right)}{\lambda+\mu}\,, \tag{1.22}$$

is the Young's modulus.

The transverse strains are:

$$\varepsilon_{22}=\varepsilon_{33}=-\frac{\lambda}{2\mu(3\lambda+2\mu)}\sigma_{11}=-\frac{\lambda}{2(\lambda+\mu)}\varepsilon_{11}, \tag{1.23}$$

or

$$\varepsilon_{22}=\varepsilon_{33}=-\frac{\nu}{E}\sigma_{11}=-\nu\varepsilon_{11}, \tag{1.24}$$

where

$$\nu=\frac{\lambda}{2(\lambda+\mu)}, \tag{1.25}$$

is called the Poisson's ratio.

In a simple shear test the only non-vanishing stress is $\sigma_{12}=\tau\neq 0$.

The stress-strain relations are then reduced to:

$$\sigma_{12}=2\mu\varepsilon_{12}=\mu\gamma_{12}, \tag{1.26}$$

where γ_{12} denotes the shear strains between the two orthogonal directions x_1, x_2. The coefficient μ=G is called the shear modulus.

The shear modulus is related to the Young's modulus and the Poisson's ratio as:

$$G=\frac{E}{2(1+\nu)}. \tag{1.27}$$

The bulk modulus (K) of an isotropic material measures its resistance to uniform compression (i.e., uniform load applied in all directions). It is linked to the Young's modulus (E) and the Poisson's ratio (ν) by the following relationship:

$$K=\frac{E}{3(1-2\nu)}. \tag{1.28}$$

Only two constants are independent since G=μ and E, v are defined in terms of λ and μ. The Lamé coefficients in terms of E and v are given as:

$$\mu=\frac{\mathrm{E}}{2(1+v)} \quad \text{and} \quad \lambda=\frac{v\mathrm{E}}{(1+v)(1-2v)}. \tag{1.29}$$

In order for λ to remain finite, the Poisson's ratio should be in the range:

$$-1 < v < 0.5\,. \tag{1.30}$$

It is difficult to derive $v < 0$ as this implies that an elongational strain in the direction $\mathbf{e}_1$ would result in an expansion in the direction $\mathbf{e}_3$ as well. For $v = 0.5$ the material is said to be incompressible.

The elasticity equations are usually written as functions of the engineering constants. For an isotropic material these constants are: i) Young's modulus, ii) Poisson's ratio, and iii) shear modulus. These engineering constants are measured employing simple mechanical tests.

Table 1.1 presents the mechanical properties of selected biological and engineering materials. Indicative values of the Young's modulus, ultimate strength and Poisson's ratio of cortical and cancellous bones are also included (Fotiadis *et al.*, 2006).

1.3 Methods for Assessing Bone Quality at different Hierarchical Levels

Nowadays, dual energy X-ray absorptiometry (DEXA) is the most popular method for the assessment of bone quality through measurements of the bone mineral density (BMD) at the spine and hip. It plays an important role in the evaluation of individuals at risk of osteoporosis, and in helping clinicians advise patients about the appropriate use of treatment (Blake *et al.,* 2007).

Nevertheless, the material and structural properties of bone differ according to the examined hierarchical level. The development of realistic numerical models requires the consideration of bone's microstructural effects, as well as the determination of porosity and anisotropy properties. This section presents an overview of the most significant methods for mechanical, geometrical/microarchitectural, and

compositional bone evaluation according to the different length scale of analysis as illustrated in Fig. 1.5.

Table 1.1 Mechanical properties of selected biological and engineering materials (Fotiadis *et al*., 2006).

Material	**Young's Modulus (MPa)**	**Ultimate Strength (MPa)**	**Poisson's ratio**
Actin		2.2	
Elastin	0.3-0.6		
Collagen fibers	$0.1 - 1 \times 10^3$		
Skin	0.1-4		>0.4
Fat	20×10^{-3}		
Smooth Muscle	$10\text{-}100 \times 10^{-3}$		
Blood Vessels Walls	0.2 -0.9		>0.4
Tendon, Ligament	$1\text{-}2 \times 10^3$	50-100	
Cartilage	0.5-1		> 0.45
Cortical Bone	$10\text{-}20 \times 10^3$	100-150	0.37
Cancellous Bone	1×10^3	8-50	0.33
Rubber	10		0.5
Stainless Steel	2.2×10^5	850	0.3
Aluminum Alloy	70×10^3	450	0.35
Titanium	1.1×10^5	900	0.32
Bone Cement	2×10^3	20	0.33

1.3.1 Assessing mechanical properties

Methods for assessing the mechanical properties of bone include whole-bone, bulk tissue, microbeam, and micro and nanoindentation testing techniques. These methods measure the structural strength and material modulus of the bone. Their most important advantage is the direct assessment of bone strength, while specimen destruction during testing is their main disadvantage (Donnelly *et al.,* 2011).

More specifically, from a macroscale point of view, the structural behavior of bones is evaluated using whole-bone mechanical testing. A whole bone is usually loaded to failure in compression, bending, or torsion (Donnelly *et al.,* 2011) to measure the structural stiffness, the failure load, and the energy absorbed to failure. The structural stiffness reflects the bone's resistance to elastic or reversible deformation. The failure

load characterizes the strength of the bone. The energy absorbed to failure is a measure of structural toughness and represents the amount of energy which can be absorbed by the bone before it breaks. However, experimental assessment of bone strength requires destructive whole-bone testing, and a main limitation of testing to failure is that the specimen might be broken during testing.

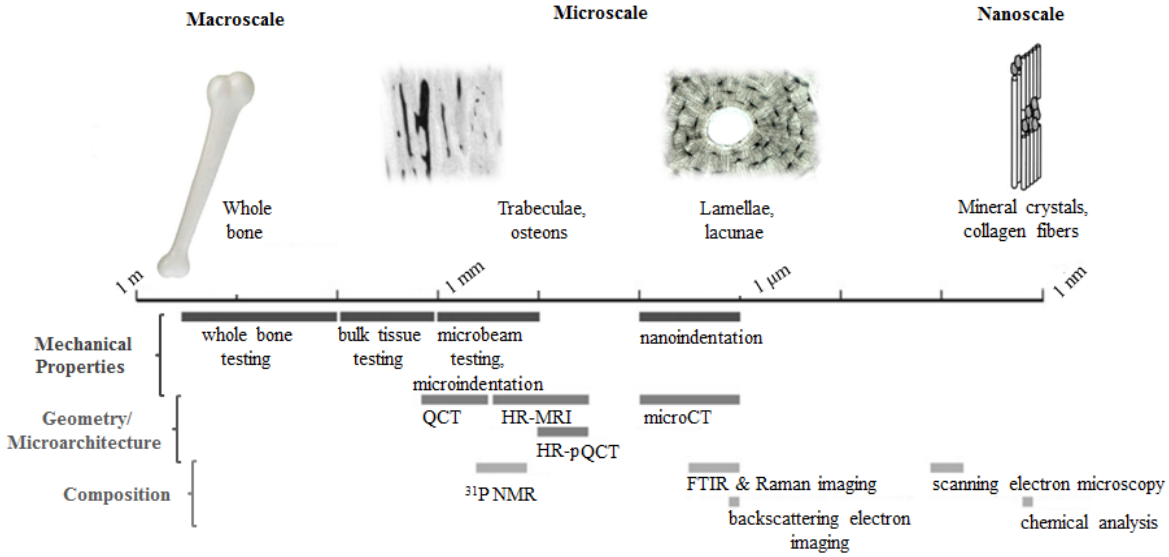

Figure 1.5: The hierarchical structure of bone is depicted schematically on a logarithmic scale. Techniques for mechanical (dark gray bars), geometric/microarchitectural (medium gray bars), and compositional testing (light gray bars) are presented according to the approximate length scale of analysis (Donnelly *et al.,* 2011).

Bulk tissue mechanical testing is applied to assess the mechanical properties of cortical and cancellous bone at the tissue level. The effect of parameters such as the anatomic site, porosity, apparent density, and tissue mineral content on the mechanical properties of osseous tissues is evaluated. In particular, regularly shaped specimens (typically cylinders or cubes with diameters or edge lengths of 5–10 mm) are derived from cortical or cancellous tissue and tested to failure in tension, compression, bending, or torsion to determine the effective elastic modulus and ultimate stress. The effective material properties obtained from these tests are independent of the macroscopic bone geometry but include the effects of porosity and geometric anisotropy arising from osteon or trabeculae orientation (Donnelly *et al.,* 2011).

In microbeam mechanical testing, bending or tensile loads are applied to microbeams (approximately 200 x 200 x 2000 μm) of cancellous or cortical bone to measure the elastic modulus and ultimate stress (Donnelly *et al.,* 2011). The elastic modulus reflects the material's intrinsic resistance to elastic deformation, while the yield stress characterizes the material's intrinsic resistance to plastic deformation. In a recent study (Jimenez-Palomar *et al*., 2015), microbeam testing revealed a decrease of bone elastic modulus properties with osteoporosis.

In microindentation testing, a rigid indenter is pressed with a known force into a flat specimen, and the area of the resulting impression is estimated optically. Microindentation is used routinely to evaluate the elastic properties of bone structural units in both cancellous and cortical sites allowing the characterization of the mechanical properties of individual trabeculae or osteons. This technique has been used *in vitro* to evaluate variations among different anatomical sites, the effect of pathologies on the mechanical properties of bone structural units, the bone matrix quality and the effect of tissue condition (hydrated, dried or embedded) during the test (Dall'Ara *et al.,* 2012). With the possibility to assess elastic and plastic deformation at the tissue level, microindentation is an attractive technique to evaluate to which extent microdamage is associated with tissue mechanical properties. It is a relative easy testing procedure and measurements can be performed in multiple locations within the tissue. However, the main disadvantage is that only the tissue hardness can be assessed.

Nanoindentation can provide information at the microscale level for the mechanical properties of segments of osseous tissue as small as individual lamellae. An indentation test is performed with a depth-sensing indenter tip, often combined with a scanning probe microscope for spatially resolved measurements. The force-displacement data are analyzed to determine the indentation modulus and hardness. Nanoindentation with relatively shallow indentation depths of approximately 100 nm yields spatial resolutions of approximately 1 μm in osseous tissue. Its application in fracture healing provides information on the evolution of material properties of the woven bone during regeneration process (Mora-Macias *et al.,* 2017). This method can measure the material properties of microstructural features such as lamellae and detect localized changes in bone material properties induced by disease or drug treatment. Despite improvements in the instrument accuracy, nanoindentation has limited

capabilities for accurate mapping of the spatial variation in bone heterogeneous mechanical properties. First, measurements are constrained to discrete levels, thus jeopardizing a thorough evaluation of the non-uniform microstructure of bone. Secondly, nanoindentation is inherently destructive leading to a permanent plastic deformation provoked by the indenter tip.

Scanning acoustic microscopy (SAM) is an attractive noncontact imaging modality able to map, over a large surface, the spatial distribution of micro-elastic properties (Rupin *et al.,* 2009). A transmitter generates a radio frequency signal which excites a piezoelectric transducer. The piezoelectric transducer converts the radio frequency signal into an acoustic wave that is made to converge by the lens and propagate onto the sample through a liquid couplant. When the acoustic signal approaches the interface between couplant and sample, a fraction of it is reflected back to the lens. Then, the lens is acting as a receiver transforming the acoustic signal into a voltage proportional to the signal. To obtain an acoustic image of the desired area, the lens is rastered over the sample and the process is repeated pixel by pixel. SAM can be used for imaging the acoustic impedance of nohomogeneous materials like bone with a resolution in the micrometer range. This method could become an interesting tool in basic bone research providing mechanical, as well as histomorphometrical data of calcified bone tissue (Regauer *et al.*, 2006).

1.3.2 Assessment of bone geometry and microarchitecture

Imaging modalities can be used for the assessment of bone geometry and microarchitecture such as quantitative computed tomography (QCT), high-resolution peripheral quantitative computed tomography (HR-pQCT), high-resolution magnetic resonance imaging (MRI), and micro-computed tomography (μ-CT). Based on these techniques, the bone geometry, trabecular morphology, and tissue mineral density can be assessed non-invasively, while the bone strength cannot be measured directly.

The availability of HR-pQCT has made it possible to measure three-dimensional (3D) bone microarchitecture and volumetric bone mineral density *in vivo*, with accuracy previously unachievable and with relatively low-dose radiation (Cheung *et al.,* 2013). More specifically, the advent of HR-pQCT scanners with isotropic resolution of approximately 80 μm has enabled *in vivo* imaging of 3D trabecular morphology at peripheral sites such as the distal radius. HR-pQCT provides unprecedented ability to

measure human bone microarchitecture at the wrist and ankle in clinical practice and these data can provide new insight into changes in bone quality across the lifespan as well as the impact of anti-osteoporosis therapies on bone quality. Using this technique, cancellous bone geometry can be evaluated and morphological parameters such as bone volume fraction (BV/TV), trabecular thickness (Tb.Th), trabecular separation (Tb.Sp), and trabecular number (Tb.N) can be determined. Inclusion of calibration phantoms allows also the calculation of apparent bone mineral density (vBMD). Compared to two-dimensional (2D) measurements based on DEXA, it provides assessment of not only BMD, but also of bone structure and strength (Cheung *et al.,* 2013). Recent studies using this novel imaging tool have increased understanding of age-related changes and sex differences in bone microarchitecture, as well as the effect of different pharmacological therapies. In cross-sectional analyses of population-based cohorts, HR-pQCT has identified substantial age-related differences in vBMD, trabecular structure and cortical thickness in premenopausal and postmenopausal women (Geusens *et al.,* 2014). One advantage of this novel tool is the use of finite element analysis modeling to noninvasively estimate bone strength and predict fractures using reconstructed three-dimensional images. Although these measurements are largely restricted to peripheral sites, they have the concomitant benefit of reduced radiation doses relative to those from whole-body QCT scans (Donnelly *et al.,* 2011).

High-resolution MRI (HR-MRI) allows nonionizing 3D imaging of the cancellous network at peripheral sites. During scanning, a strong magnetic field and a series of radiofrequency (RF) pulses are applied to the specimen to generate 3D images of the hydrogen in the water within skeletal tissues. Bone tissue generates no signal in images as a result of the low water content of the tissue and the chemical environment of the protons within the bone matrix. When the marrow is illustrated, the trabeculae appear as the dark space within the bright marrow. Resolutions as small as approximately 50 x 50 x 200 μm have been achieved *ex vivo*, and resolutions of 156 x 156 x 300 μm are typical *in vivo*. Consequently, MRI-based trabecular morphologic parameters are also affected by partial volume effects. The MRI-based trabecular measures are correlated with their counterparts measured by μ-CT, and MRI can detect age- and disease-induced changes in trabecular morphology. A critical advantage of this technique is its ability to generate 3D images of bone geometry and

microarchitecture without ionizing radiation, while the main disadvantage is the long scan time required to acquire high resolution images of cancellous bone. Cortical bone appears as a signal void with all conventional clinical MRI sequences, because of the rapid decay of the magnetic resonance signal (Shang-Lian *et al.,* 2013; Bae *et al.,* 2012). More recently, ultrashort time echo (TE) sequences with nominal TE of less than 100 μs have created increasing interest and significant information for cortical porosity can be derived.

At the microscale, μ-CT provides *ex vivo* assessment of the microarchitecture of cancellous bone with resolution from 1–6 μm. In μ-CT scanners, the specimen is rotated in angular increments between the X-ray source and detector, and the attenuation data at each position are reconstructed into a 3D array of X-ray attenuation, which can be converted to mineral density values with inclusion of appropriate calibration phantoms. The measured parameters are the BV/TV, Tb.Th, Tb.Sp, Tb.N, trabecular connectivity, and true tissue mineral density (TMD) which is defined as the ratio of the mass mineral to the volume bone tissue. Limitations include a maximum specimen size of approximately 14-mm diameter x 36-mm length in older scanners and 100-mm diameter x 140-mm length in the new generation scanners. Nevertheless, μ-CT is the most popular technique for *ex vivo* quantification of trabecular morphology. The development of desktop *in vivo* μ-CT scanners has enabled characterization of the macroscopic geometry and microarchitecture of the bone. Although high resolutions require relatively long scan times and large radiation doses, these scanners have enabled the examination of skeletal development, adaptation and response to treatment with a resolution up to approximately 10 μm. μ-CT *in vivo* or *ex vivo* with a synchrotron source maximizes resolution of microarchitectural features and local spatial gradients in tissue mineral content. The tightly collimated, monochromatic X-ray source provides a spatial resolution of approximately 1 μm and eliminates the beam hardening artifacts arising from differential attenuation of the polychromatic sources in conventional desktop μ-CT systems. Synchrotron μ-CT is the current gold standard for assessment of local gradients in TMD and is capable of resolving resorption spaces and microcracks. However, the relative inaccessibility of synchrotron facilities limits the widespread use of this technique.

1.3.3 Assessment of tissue composition

Both the inorganic and the organic components of osseous tissues contribute to the structural integrity of bones. Microscopic, spectroscopic, physical, and chemical techniques are available for the assessment of the mineral and the collagenous components of bone tissue.

Nuclear magnetic resonance (NMR) imaging provides information about water content and the structure of the mineral within the tissue. For analyses of water and mineral in bone, the primary isotopes of interest are ^{1}H and ^{31}P, respectively. As in MRI, when placed in a strong magnetic field, the NMR activates ^{1}H and ^{31}P nuclei in the bone mineral resonate at slightly different frequencies depending on their local chemical environment. Thus, NMR spectra are generated by varying the frequency of the applied RF field monitoring the absorption of the specimen. Water in bone tissue, while not detected with typical clinical MRI techniques, can be imaged with appropriate pulse sequences. The percent of bone water in volume can be quantified from the ^{1}H images and can serve as a surrogate measure of cortical porosity. It is inversely correlated with effective ultimate stress estimated from three-point bending tests of cadaveric bones.

Solid-state ^{31}P NMR imaging can be used to characterize the chemical structure of the bone mineral phase, allowing detection of temporal changes in the mineral chemistry. Furthermore, this technique can be used quantitatively to determine the mass of bone mineral in the tissue, enabling detection of hypomineralization in the osteomalacic rabbit tissue at an isotropic spatial resolution of approximately 280 μm. Quantitative NMR analyses of bone mineral chemistry have also been performed *in vivo*, but such studies typically require long acquisition times in specialized scanners and are currently limited to the fingers, the wrist, and the hand. Recent advances in instrumentation have enabled *in vivo* solid state imaging of bone mineral in a clinical scanner.

NMR techniques allow non-invasive, non-ionizing *in vivo* characterization of changes in the composition of bone tissue. Strengths of NMR include the ability to detect subtle changes in the chemical bonding environments of the bone mineral, but this technique cannot provide information about the collagenous component of the matrix.

The low signal-to-noise ratio and the limited spatial resolution remain key challenges for the ^{31}P solid state methods.

More recently, in (Schrof *et al.*, 2016) the structural, chemical, and mechanical properties of osteonal and interstitial domains of human cortical lamellar bone were analyzed by means of synchrotron X-ray phase contrast nano tomography, Raman spectroscopy and SAM. Knowing that the degree of mineralization and the fibril orientation appear as key determinants of the local elastic properties, various independent parameters were analyzed reflecting not only the fibril orientation, the degree of mineralization, and the local elastic properties, but also on the state of mineral maturation in regions of varying tissue age. The parameters derived from these measurements were correlated with two levels of bone structural hierarchy, namely single lamellae and entire tissue domains (i.e. osteonal and interstitial bone structural units) with the aim of getting further insight into the interplay of structural, chemical and mechanical tissue characteristics. Mutual correlation analysis strongly suggested that the characteristic elastic modulations of bone lamellae within single units are the result of the twisting fibrillar orientation, rather than compositional variations, modulations of the mineral particle maturity, or mass density deviations. Furthermore, it was found that predominant fibril orientations in entire tissue units can be rapidly assessed employing Raman parameter maps. This approach could be applied in future studies for non-destructive investigation of small pathologic samples from bone biopsies and a broad range of biological materials and tissues.

1.4 Bone Pathologies

1.4.1 Osteoporosis

Osteoporosis is a metabolic skeletal disorder characterized by low bone mass and microarchitectural deterioration of bone tissue leading to the weakness of the skeleton and increased risk of fracture, particularly of the spine, wrist, hip, pelvis and arm. Osteoporosis causes more than 8.9 million fractures annually worldwide and over one-third of all osteoporotic fractures occur in Europe (Sadat-Shojai *et al.,* 2013). By 2020, almost 14 million individuals older than 50 years are expected to have osteoporosis, and another 47 million will likely have low bone mass (Shuler *et al.,* 2012).

The main cause of osteoporosis is hormonal deficiency, and thus the most frequent disease is post-menopausal osteoporosis. At least 40% of post-menopausal women over the age of 50 and 15–30% of men will sustain one or more fragility fractures (Potsika *et al.,* 2014b). Fracture prevention is a critical component of managing osteoporosis. In elderly people, a fracture at the proximal femur has a negative impact on the quality of life and can even lead to death, with a mortality rate of up to 36% depending on age (Rohde *et al.,* 2014). Sex hormones, particularly estrogen, help to maintain the health and normal density of the skeleton by restraining osteoclast activity and by promoting deposit of new bone. After menopause, however, estrogen secretion wanes, and estrogen deficiency is strongly implicated in osteoporosis in older women.

Other factors that contribute to osteoporosis include: (a) the body size (e.g. small, thin women face a higher risk), (b) insufficient exercise, (c) immobility, (d) a diet poor in calcium and protein, (e) abnormal vitamin D receptors, (f) smoking (which reduces estrogen levels), (g) and hormone-related conditions such as hyperthyroidism, low blood levels of thyroid-stimulating hormone, and diabetes mellitus, (h) family history, (i) ethnicity (e.g. white and Asian women are at highest risk, while black and Hispanic women have a lower risk), (j) use of medication as some medicines increase the risk of osteoporosis. In addition, recent research indicates that a particular gene, dubbed LRP5, may play a role in the occurrence of osteoporosis. This gene inhibits the release of serotonin by cells of the gut. Because serotonin inhibits osteoblast growth, reducing its synthesis increases bone density (Marieb and Hoehn, 2014).

Bone mass is the main measured parameter in clinical practice, and forms the cornerstone for the overall management of the disease including risk prediction, diagnosis, and monitoring of patients. The decline in bone mass is associated with reduced bone strength, resulting in osteoporosis. BMD is defined as the amount of bone mass per unit volume (volumetric density, g/cm^3), or per unit area (areal density, g/cm^2), and both can be measured *in vivo* by densitometric techniques (Sadat-Shojai *et al.,* 2013). It is most often described as a T-score or Z-score, both of which are units of standard deviation (SD). The Z-score describes the number of SDs by which the BMD of an individual differs from the mean value expected for age and sex. The T-score describes the number of SDs by which the BMD of an individual differs from the mean value expected in young healthy individuals. According to the World Health

Organization (WHO), the definition of osteoporosis is based on the T-score for BMD measured from white postmenopausal women and it is defined as a value for BMD equal to or lower than the young female adult mean (Sadat-*Shojai et al.,* 2013, Chen *et al.,* 2013). The three categories for diagnosis include: (a) normal bone (T-score 1.0 and above), (b) low bone mass referred to as osteopenia (T-score between –1.0 and –2.5), (c) osteoporotic bone (T-score –2.5 and below). This threshold was originally developed for measurements of BMD at the spine, hip, or forearm.

Different techniques have been used to measure BMD. Densitometric techniques have evolved over the last century from the use of dental radiographs of mandible by dentists to quantitative morphometry using plain radiographs, ultrasonography-based methods, dual energy absorptiometry, and CT scan-based modalities like peripheral QCT and HR-pQCT (Chen *et al.,* 2013). DEXA is today's established standard for measuring BMD. It is based on an enhanced form of X-ray technology which is used to measure bone loss. This technique is relative simple, quick, noninvasive, portable and less expensive. Although it can be used for screening and as a risk assessment tool, it is not appropriate for diagnosis, treatment, and follow-up.

In addition to BMD measurement, clinical risk factors assessment is significant to determine patients with the highest risk of fracture who should receive the highest priority for treatment. To this end, after rigorous scientific study and debate, a revised description of osteopenia and assessment of osteoporosis was developed by the WHO in 2008 to provide a prediction tool for assessing an individual's risk of fracture in order to enhance clinical decision for patients' treatment. A fracture risk score, called Fracture Risk Assessment Tool (FRAX) is a web-based algorithm designed to calculate the 10-year probability of major osteoporosis-related fracture (clinical vertebral, hip, forearm, or humerus) and hip fractures in men and women based on easily obtained clinical risk factors and BMD of the femoral neck. FRAX accounts for factors such as age, sex, weight, height and clinical risk factors which include previous fragility fractures, premature menopause, parental history of hip fracture, current tobacco smoking, long-term use of glucocorticoids, rheumatoid arthritis, and other causes of osteoporosis (Laugier and Haïat, 2011). The model uses data derived from 9 population-based cohorts from around the world, including centers from North America, Europe, Asia, and Australia, and has been validated in 11 independent cohorts with similar geographic distribution.

Despite the fact that low bone mass in osteoporosis is a major indicator of the risk of fracture, alterations in bone microstructure contribute significantly to skeletal fragility. However, DEXA is not able to directly assess changes in the bone microarchitecture due to osteoporosis such as the increase in cortical porosity which is considered as a good indicator of bone fragility. Also, DEXA is not suitable for mass screenings as it requires specialists, and involves weak exposure to X-ray radiation (Hata *et al.,* 2016). With the development of non-invasive imaging techniques such as computed tomography (CT), μ-CT, and HR-pQCT, imaging of the bone architecture provides important information about age-related changes in bone microstructure and estimates of bone strength. More specifically, the bone resorption starts from the endosteal (inner) surface, leading to the thinning of the cortex and trabecularisation of the inner cortical layer. Fig. 1.6 depicts the contrasting architecture of normal versus osteoporotic bone in scanning electron micrographs. The most common sites of the osteoporotic fractures include the vertebra, femoral neck and distal radius, in which the investigation of the microstructural effects is a key factor to fully understand the disease and improve the prediction of fracture risk. Vertebral strength is mostly preserved by cancellous bone, which is inhomogeneous, with lower bone volume in the central. Increased fragility of osteoporotic femoral neck is attributed to low trabecular bone volume and high compact porosity. Distal radius shows significant variations in cortical porosity (Chen and Kubo*,* 2014).

Bone structural integrity is maintained by the removal of old bone by osteoclasts and synthesis of new bone in its place by osteoblasts. This process, called bone remodeling, is not performed individually by each cell, but by groups of cells functioning as organized units. More specifically, bone remodeling is accomplished by the assembly of osteoclasts and osteoblasts into discrete temporary anatomic structures called large basic multicellular units (BMUs) (Jilka, 2003).

Osteoblasts form bone as they produce the organic matrix of collagen protein, called osteoid, and also secrete hormones and enzymes which later affect the mineralization process. They are entrapped in the matrix of the bone and become mature bone cells, known as osteocytes (Kilappa, 2014). Osteoclasts are large, multinuclear cells derived from macrophages, which secrete enzymes which destroy bone, forming resorption pits (Howship's lacuna or resorption lacuna).

In young populations, this process forms new bone, as the activity of osteoblast is higher, while in adulthood, the resorption and formation processes are ideally balanced, sustaining the mass and shape of the skeleton (Kilappa, 2014). More specifically, approximately 10% of the skeleton is regenerated each year in mature humans (Manolagas, 2000). However, in the elderly, and especially in older females, estrogen deficiency after menopause disrupts the balance of this turnover process, increasing the resorption rate leading to a gradual deterioration of bone mass.

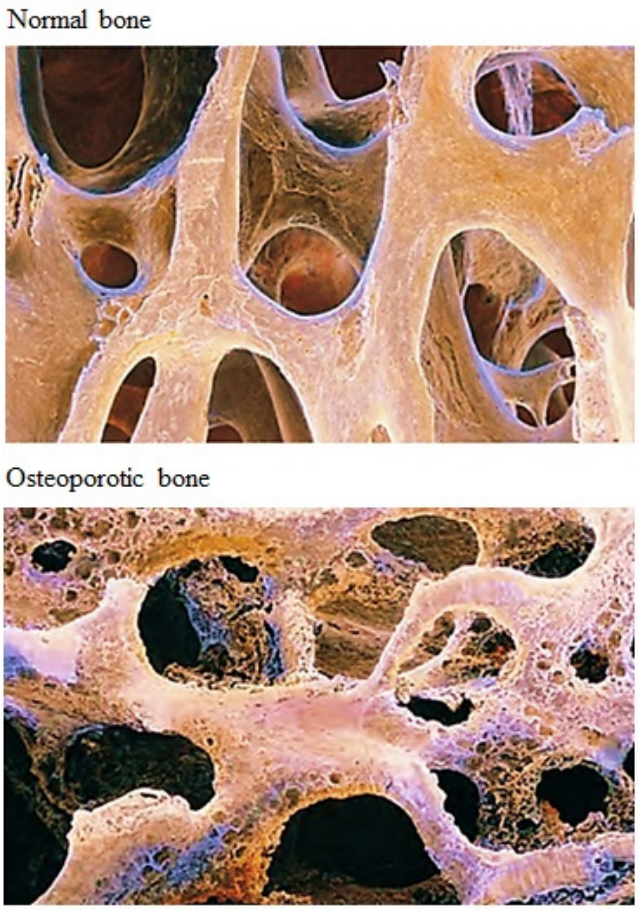

Figure 1.6: The contrasting architecture of normal versus osteoporotic bone in scanning electron micrographs (Marieb and Hoehn, 2014).

The occurrence of BMUs in cortical bone is considered as an early sign of osteoporosis, which leads to cortical thinning and reduced bone strength at a later stage of the disease progression (Bourgnon *et al.,* 2014). In chapter 6 of this thesis, numerical simulations of wave propagation in cortical bone are presented to investigate the interaction of ultrasound with changes in cortical porosity and more

specifically the ability of ultrasound to identify the occurrence of BMUs, simply called non-refilled resorption lacunae (RL).

1.4.2 Fracture healing

Despite their remarkable strength, bones are susceptible to fractures or breaks as a result of a trauma or osteoporosis. Fracture healing is a natural process that can reconstitute injured tissue and recover the original function and shape of the bone. It is a very complex process that involves the coordinated participation of immigration, differentiation and proliferation of inflammatory cells, angioblasts, fibroblasts, chondroblasts and osteoblasts which synthesize and release bioactive substances of extracellular matrix components (e.g., different types of collagen and growth factors) (Doblaré *et al*., 2004).

Young population usually experiences fractures due to a trauma that twists or smashes the bones due to violent physical activity in occasions such as sports injuries, automobile accidents or falls. In the elderly, most fractures occur due to low bone mass and microstructural deterioration of osseous tissue leading to the weakness of the skeleton in osteoporosis. Osteoporotic fractures are usually observed in the spine, hip, wrist, humerus and rib. Hip and spine fractures are the two most serious fracture types, associated with pain, disability, and even death. While bone fractures in healthy individuals occur in high energy traumatic events, osteoporotic bone fractures are associated with fragility fractures occurring with minimal trauma events (Marieb and Hoehn, 2014).

Fractures can be classified based on:

a. The position of the bone ends after fracture. In nondisplaced fractures the bone ends keep their normal position, while in displaced fractures the bone ends are out of normal alignment.

b. The completeness of the break. If the bone is broken through, the fracture is a complete fracture. Otherwise, it is an incomplete fracture.

c. The orientation of the break relative to the long axis of the bone. If the break is parallel to the bone's long axis, the fracture is linear, while if the break is perpendicular to the long axis, it is called transverse.

d. Whether the bone ends penetrate the skin. In this case the fracture is an open (compound) fracture, while a closed (simple) fracture is observed in a different occasion.

Unlike soft tissue healing, which leads to scar formation, in bone healing the anatomy of the osseous tissues is regenerated. Although fracture repair usually restores the damaged skeletal tissue to its pre-injury cellular composition, structure and biomechanical function, about 10% of fractures will not heal normally (Einhorn and Gerstenfeld, 2015). For a simple fracture the healing time is six to eight weeks for small or medium-sized bones in young adults, but it is much longer for large, weight-bearing bones and in the elderly. Delayed union occurs when a bone fails to unite within an average anticipated time. For a given fracture, healing time varies with location and configuration, as well as the specific bone and age group. If this condition persists for 3 consecutive months with no evidence of progression toward healing, it is characterized as a nonunion (Freeland *et al.,* 1986). Pseudarthrosis is the end stage of a nonunion when a false joint, lined with pseudosynovial cells and containing fluid, occurs. A pseudarthrosis generally forms if the bone ends are not united within 2 years (Freeland *et al.,* 1986).

For normal bone healing, two different types of healing are observed, known as primary and secondary fracture healing. Primary healing occurs in cases of extreme stability and negligible gap size, involving a direct attempt of the bone to form its structural and material properties directly. Secondary healing occurs when there is not enough stabilization and the gap size is moderate. In this case, responses within the periosteum and external soft tissues are activated that form an external callus, which reduces the initial movement by increasing stiffness. In most cases secondary healing occurs, which does a more thorough job of replacing old and damaged osseous tissue (Doblaré *et al.,* 2004).

1.4.2.1 Secondary bone healing

Secondary fracture healing is characterized by spontaneous bone reconstruction in the absence of rigid fixation of the fracture site. It is the most common method of bone healing. It involves the following four major stages, which are illustrated in Fig. 1.7 (Geris *et al.,* 2009; Marieb and Hoehn, 2014; Einhorn and Gerstenfeld, 2015):

Inflammatory stage: An injury that interrupts the continuity of bone damages not only the cells, blood vessels, and bone matrix, but also the surrounding soft tissues, including muscles and nerves. A hematoma, a mass of clotted blood, forms at the fracture site. In this clot, activated and degranulating platelets provide a source of growth factors, playing an important role in the healing cascade. Osteocytes at the trauma site become deprived of their nutrition and necrose, as do the damaged tissues in that area. This necrotic process triggers an immediate inflammatory response, bringing inflammatory cells, leucocytes and macrophages to the region. These are followed by the invasion of fibroblasts, mesenchymal stem cells and endothelial cells. Growth factors and cytokines, important regulators of the healing process, are produced by the cells in the regeneration area, as well as released into this area from the surrounding tissues (damaged bone ends, muscles, periosteum and marrow) (Geris *et al.,* 2009). The inflammatory phase peaks in 48 h and disappears almost completely by 1 week post-fracture.

Soft Callus Stage: Within a few days, several events lead to the formation of soft granulation tissue, also called the soft callus. Capillaries grow into the hematoma and phagocytic cells invade the area and begin cleaning up the debris. In the meanwhile, fibroblasts and osteoblasts occupy the fracture site from the nearby periosteum and endosteum and begin reconstructing the bone. Mesenchymal stem cells differentiate into chondrocytes (cartilage-forming cells) in the central fracture area, where the soft callus will gradually take on the appearance of cartilage, mechanically stabilizing the fracture zone. As chondrocyte differentiation progresses, the cartilage extracellular matrix undergoes mineralization and this phase of fracture repair terminates with chondrocyte apoptosis. This entire mass of repair tissue, now called the fibrocartilaginous callus, connects the broken bone.

Hard callus stage: In this phase blood vessels invade the calcified cartilage, bringing along osteoblasts. These osteoblasts will produce a hard callus tissue consisting of mineralized woven bone matrix in a process called endochondral ossification receiving enough oxygen and subjected to the proper mechanical stimuli. When the fracture ends are connected by a bony callus, clinical union is reached. This stage continues until a firm union is formed about two months later.

Bone remodeling: The final remodeling phase begins with osteoclastic resorption of unnecessary or poorly placed parts of the regenerated bone and the formation of lamellar bone. In particular, the first mineralized matrix produced during primary bone formation is resorbed by osteoclasts, and then the secondary bone laid down during the period of cartilage resorption is also resorbed. As the bony callus tissue continues to be resorbed, this prolonged period is characterized by coupled cycles of osteoblast and osteoclast activity in which the callus tissue is remodeled to the bone's original cortical structure. The excess material on the diaphysis exterior and within the medullary cavity is removed, and compact bone is laid down to reconstruct the shaft walls. The remodeling phase takes place for a prolonged period of time, gradually reverting the blood supply to a normal state and restoring the bone at the regeneration site to its original shape and strength.

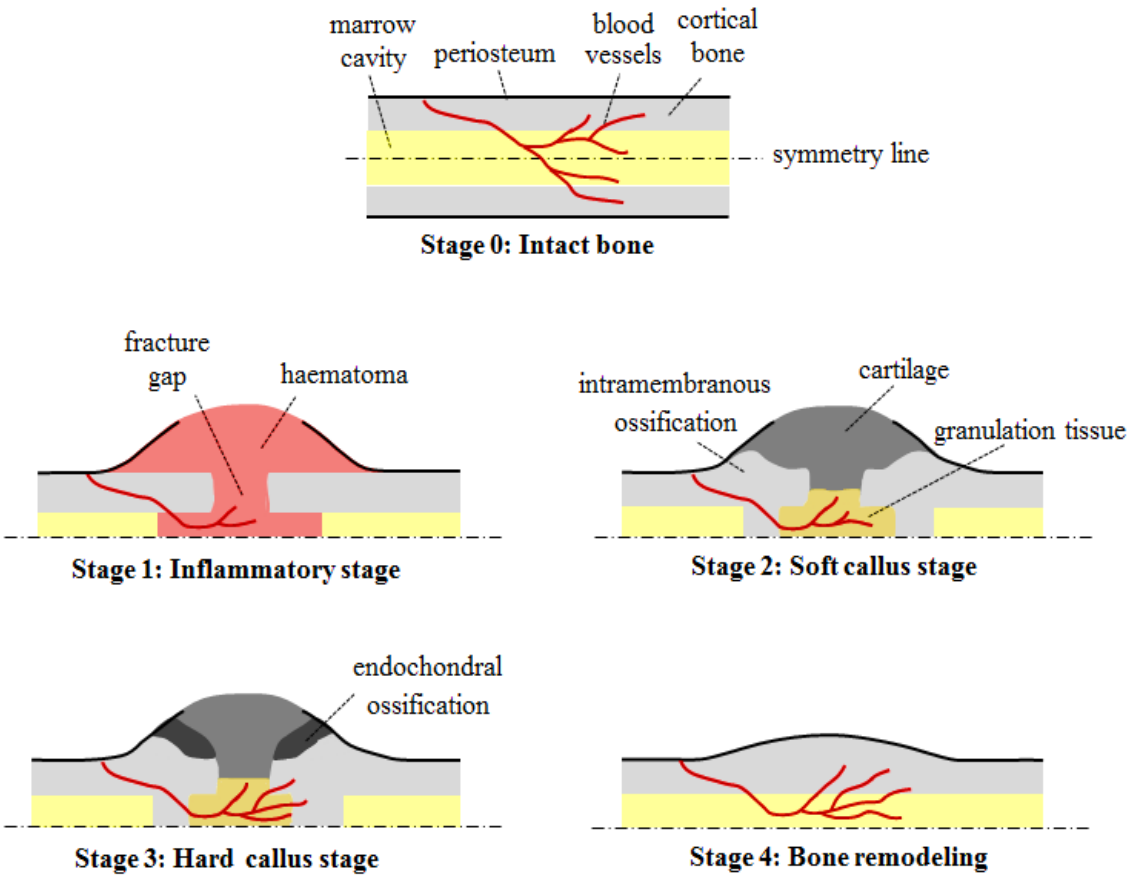

Figure 1.7: Schematic representation of the different stages of fracture healing.

1.4.2.2 Primary bone healing

Primary bone healing requires rigid stabilization with or without compression of the bone ends. Unlike secondary bone healing, this rigid stabilization suppresses the formation of a callus in either cancellous or cortical bone. Because most fractures occurring worldwide either are untreated or are treated in a way that results in some degree of motion (sling or cast immobilization, external or intramedullary fixation), primary healing is rare (Sfeir *et al.,* 2005). However, this type of healing is often the primary goal to achieve after open reduction and internal fixation surgery. When these requirements are achieved, direct bone healing can occur by direct remodeling of lamellar bone, the Haversian canals and blood vessels. Depending on the species, it usually takes from a few months to a few years, before complete healing is achieved (Marsell and Einhorn, 2011). Primary healing of fractures can either occur through contact healing or gap healing. Both processes involve an attempt to directly re-establish an anatomically correct and biomechanically competent lamellar bone structure. If the gap between bone ends is less than 0.01 mm and interfragmentary strain is less than 2%, contact healing occurs. Under these conditions, cutting cones are formed at the ends of the osteons closest to the fracture site. The tips of the cutting cones consist of osteoclasts which cross the fracture line, generating longitudinal cavities at a rate of 50–100 μm/day. These cavities are later filled by bone produced by osteoblasts residing at the rear of the cutting cone. In this way, the simultaneous generation of a bony union and the restoration of Haversian systems formed in an axial direction are achieved. Gap healing differs from contact healing as bony union and Haversian remodeling do not evolve simultaneously. It occurs if stable conditions and an anatomical reduction are achieved, although the gap must be less than 800 μm to 1 mm (Marsell and Einhorn, 2011). In this process the fracture site is primarily filled by lamellar bone oriented perpendicularly to the long axis, requiring a secondary osteonal reconstruction unlike the process of contact healing.

1.4.2.3 Assessment of fracture callus structure and material properties

Assessment of the hard callus microstructure: The calculation of morphometric indices is a standard method for describing trabecular bone microarchitecture. Indices such as Tb.N, Tb.Th, Tb.Sp, degree of anisotropy, connectivity density, standard deviation of the trabecular thickness and trabecular separation have been shown to be

potential predictors of the resistance to fracture of bone (Casanova *et al*., 2014; Bouxsein *et al.,* 2010). Recently, these trabecular measures were used by (Mehta *et al.,* 2013) to evaluate the mineralized struts of the callus in the late reparative phase, which were correlated with the resistance to re-fracture. It was observed that a combination of the morphometric measures mentioned beforehand predicted the resistance to fracture as good as basic bone quantity parameters such as BV/TV. The results suggest that in the analysis of the mechanical behavior of the callus, morphometric descriptors of the microstructure may enhance the capacity to predict callus strength.

Morphometric indices of trabecular structures can be assessed together with bone callus quantity parameters using μ-CT. In rodent models, the whole callus has to be scanned with a resolution below 10 mm to reliably depict the small size of trabeculae (Bart *et al.,* 2013, Donelly *et al.,* 2011). To achieve this resolution, HR μ-CT is needed. HR μ-CT could also be used to assess whether complete bridging of mineralization across the callus or defect has occurred. This is an important issue that is usually overlooked in the analyses of the callus, where bone mass is used as an indicator of the healing progress. Algorithms for HR μ-CT that take into account the location and the extent of struts bridging across the callus will enable a better estimation of the resistance to re-fracture (Casanova *et al.,* 2014).

Assessment of the soft callus microstructure: A tool which is able to identify and quantify cartilage in the soft callus would provide benefits in the assessment of fracture repair. A promising imaging approach is the micro-magnetic resonance imaging (μ-MRI) as it provides good contrast for soft tissues which are abundant in the young fracture callus. However, the resolution of μ-MRI measurements is in the order of 100 mm (in the longitudinal direction), which is rather low compared with desktop μ-CT in the micrometer regime (Kim *et al.,* 2012). In addition, strong magnetic fields have been suspected of interfering with bone healing processes (Nakahira *et al.,* 2003). Consequently, the application of μ-MRI for the assessment of bone repair is still limited in preclinical studies. μ-CT could be possibly used in the future for the evaluation of the soft tissues in the callus. Recently, (Hayward *et al.,* 2012) developed a contrast-enhanced protocol for μ-CT imaging of the soft callus in an *ex vivo setting.*

Assessment of the callus material properties: Raman spectroscopy, Fourier transform infrared imaging (FTIR), quantitative backscattered electron imaging (qBEI) and energy-dispersive X-ray spectroscopy (EDX) are potential methods to characterize the callus material properties (Pezzuti *et al.,* 1998; Ouyang *et al.,* 2004). Both Raman spectroscopy and FTIR measure partially overlapping subsets of the specimen's vibrational spectrum (Casanova *et al.,* 2014; Carden and Morris, 2000) and they give access to important bone quality factors by describing the quality of the newly formed bone tissue of the callus, such as the mineral-to-matrix ratio, the carbonate to phosphate ratio and collagen cross-linking (Morris *et al.,* 2010). The mineral to matrix ratio could be used to determine the changes in mineralization in specific regions of the callus, and the carbonate to phosphate ratio could provide important insights into callus quality as it varies depending on the architecture of the collagen tissue, its age and its mineral crystallinity (Ouyang *et al.,* 2004; Mendelsohn *et al.,* 2000). Collagen can be considered to be the backbone of the bone's mineral structure, and it is therefore an important factor for assessing bone strength. For the fracture callus, it means that non-completely mineralized areas present during the first stages of the reparative phase could be evaluated based on their collagen structure, which will show different levels of maturity. Recently, (Meganck *et al.,* 2013) applied Raman spectroscopy to callus to analyze the effect of bisphosphonates on bone material properties for two different mouse models. This study showed that there was no significant change in the mineral to matrix ratio, but there were significant changes in crystallinity between the two mouse strains. A high intragroup and intrasample variation was also observed in the callus in the mineral to matrix ratio, crystallinity and carbonate to phosphate ratio. Nonetheless, Raman spectroscopy has been shown to be a powerful tool to detect changes in material properties in murine bones interacting with bisphosphonates (Juillard *et al.,* 2010). Therefore, spectroscopic techniques have a potential application to assess the quality of healing bone tissue, which can help understanding how treatments influence its recovery (Brennan *et al.,* 2009).

Backscattered microscopy or qBEI is a form of scanning electron microscopy where backscattering of incident electrons colliding with atoms of the sample is recorded to estimate the local bone mineralization level (Casanova *et al.,* 2014). This technique

was successfully used to investigate the mineralization degree in the callus tissue (Manjubala *et al.,* 2009).

EDX is a technique applied to study the atomic composition of a sample by analyzing the emission of characteristic X-rays through an energy-dispersive spectrometer. EDX can be particularly helpful to detect specific elements in the callus, which cannot be distinguished by Raman spectroscopy or by FTIR. For example, (Bruel *et al.,* 2011) used EDX to investigate the presence of strontium ranelate in the callus after specific treatment with this drug. As EDX can detect the presence of specific atoms, it is appropriate for studies including treatments, which involve exogenous atoms.

Assessment of the callus mechanical properties: The most common techniques for measuring local biomechanical properties of bone tissue are nanoindentation and SAM (Oyen, 2010; Eckardt and Hein, 2001). For nanoindentation tests, a diamond tip penetrates the specimen up to a certain depth and the exerted forces are recorded to extrapolate the mechanical properties (Oyen, 2010). In (Leong and Morga, 2008) the local mechanical properties of rodent callus were investigated via nanoindentation, demonstrating the usefulness of this technique in characterizing the heterogeneous mixture of tissues present in the callus. In contrast, SAM uses measurements of a sample's reflection of acoustic waves to derive its stiffness (Hube *et al.,* 2006). SAM was already successfully adopted to investigate the relationship between resistance to fracture and local mechanical properties in ovine callus (Preininger *et al.,* 2011). A strong correlation between the two parameters was found. Both techniques provide the stiffness of the region under investigation at high spatial resolution. Compared with SAM, nanoindentation has the advantage to concomitantly extrapolate the elastic modulus and the hardness of the investigated tissue which is not possible with SAM.

Chapter 2: Ultrasound Propagation in Bone

2.1 Fundamentals of Ultrasound

According to Chapter 1, elasticity is a solid's most important property for restoring its shape and volume after the termination of the action of external forces, while for liquids and gases, only the volume is restored. Elastic vibrations are vibrations of a mechanical system (an elastic medium or its part) which arise under mechanical disturbances. Elastic or acoustic waves are mechanical disturbances reproduced in an elastic medium (Nazarchuk *et al.,* 2017).

Ultrasound is a mechanical wave propagating at frequencies above the audible range (20 kHz). For medical applications frequencies typically above 1 MHz are used. The wave propagates through a medium as a disturbance of the individual particles supporting the wave. These disturbances induce a displacement of the particles and are transmitted gradually to other parts of the medium.

Ultrasound propagates as a longitudinal or compressional wave (Fig. 2.1), when the molecules oscillate sinusoidally within the medium, moving forward and backward along the direction of propagation. Alternatively, the particles may oscillate transversely, perpendicularly to the direction of propagation. Such a wave is called a transverse or shear wave. Shear waves and compressional waves are the two main

modes of propagation of acoustic energy in biological hard tissues such as bone. The compressional wave speed is related to the bulk elasticity modulus of the medium while the shear wave speed is related to the shear elasticity modulus. However, typically, in soft tissues, liquids and gas ultrasound bulk shear waves are usually of little relevance and are neglected as they are highly attenuated at ultrasonic frequencies. Fig. 2.1 shows that within the wave, regular pressure variations occur with alternating areas of compression, which correspond to areas of high pressure and high amplitude, and with areas of rarefaction or low pressure zones where expansion of particles occurs.

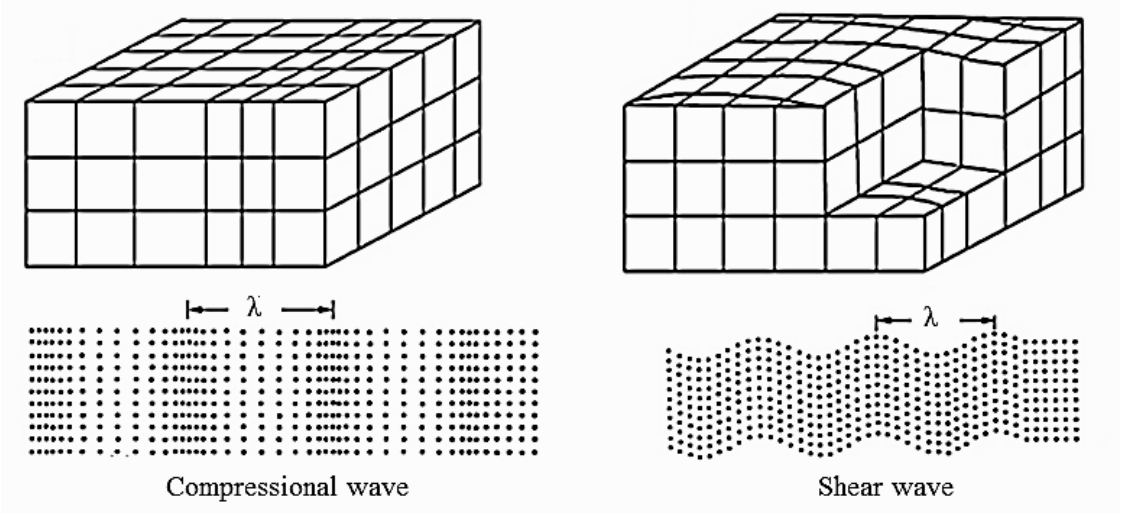

Figure 2.1: Distribution of wave vibrations for: (a) a compressional, and (b) a shear wave (Z. Nazarchuk *et al.,* 2017).

In an infinite isotropic homogeneous solid body, in which the propagating wave does not interact with the boundary of the medium, the longitudinal (c_l) and shear (c_s) propagation velocity are given by:

$$c_l = \sqrt{\frac{c_{11}}{\rho}} = \sqrt{\frac{\lambda + 2\mu}{\rho}} \,, \tag{2.1}$$

and

$$c_s = \sqrt{\frac{c_{11} - c_{12}}{2\rho}} = \sqrt{\frac{\mu}{\rho}} \,, \tag{2.2}$$

in which c_{11}, c_{12} are the two stiffness coefficients, λ (bulk modulus) and μ (shear modulus) are the Lamé coefficients and ρ is the density of the medium of propagation.

Except for the longitudinal and shear velocity, the acoustic impedance is another parameter that characterizes the medium of wave propagation. The acoustic impedance (Z) is defined as the ratio of the acoustic pressure (p) at a point in the medium to the particle speed (u) at the same point:

$$Z=\frac{p}{u}. \tag{2.3}$$

Considering the propagation of plane waves in a non-attenuating medium, the acoustic impedance is defined by the product of the mass density and the speed of sound c (also known as the wave propagation velocity or sound velocity):

$$Z=\rho\cdot c\cdot \tag{2.4}$$

Table 2.1 presents typical values of sound velocity and acoustic impedance in different biological tissues (Laugier and Hait, 2011). It should be mentioned that these values are indicative of the order of magnitude, due to the significant biological variability.

The frequency f and period T of a longitudinal wave are related to the speed of sound and its wavelength, λ, by the equation:

$$c=\lambda f=\frac{\lambda}{T}\cdot \tag{2.5}$$

Table 2.1 Typical values for ultrasound propagation velocity and characteristic acoustic impedance, in different biological tissues for temperatures in the range between 20°C and 37°C.

Tissue	**Ultrasound Propagation velocity (m/s)**	**Characteristic Acoustic impedance ($kg\cdot s^{-1}\cdot m^{-2}$)**
Water (20 °C)	1480	$1.48\cdot10^{6}$
Cancellous Bone	1450 −1800	$1.54\cdot10^{6}-2.2\cdot10^{6}$
Cortical Bone	3000 − 4000	$4\cdot10^{6}-8\cdot10^{6}$
Fat	1450	$1.38\cdot10^{6}$
Muscle	1550 − 1630	$1.65\cdot10^{6}-1.74\cdot10^{6}$
Skin	1600	$1.7\cdot10^{6}$

Typical diagnostic ultrasound devices use frequencies in the range of 2–15 MHz. In cortical bone a typical sound velocity approximates the value 4000 m/s

calculated for a wavelength of 16 mm and frequency 250 kHz or for 4 mm at 1.0 MHz. In cancellous bone of the human calcaneus, a typical sound velocity approximates the value 1500 m/s when the wavelength is 3.1 mm and the frequency 500 kHz (Laugier and Haiat, 2011). A typical sound velocity for soft tissue is 1540 m/sec (Aldrich, 2007).

2.1.1. Phase velocity-Group velocity

Two fundamentally different sound velocities can be distinguished. Phase velocity (c_p) corresponds to the propagation velocity of a given phase that is of a single frequency component of a periodic wave. The phase velocity is calculated as:

$$c_p = \frac{\omega}{k}\,, \tag{2.6}$$

in which ω denotes the angular frequency and k is the wavenumber. The wavenumber is inversely proportional to the wavelength λ according to the equation:

$$k = \frac{2\pi}{\lambda}\,. \tag{2.7}$$

A propagating medium is called dispersive if the phase velocity is a function of frequency or wavelength, which is the case for example in all attenuating media. This means that the different frequencies contained in the signal do not propagate at a constant velocity.

The group velocity refers to the velocity of propagation of a wavepacket. A wavepacket is a short "burst" or "envelope" of localized wave action that travels as a unit (Fig. 2.2). Each wave of the wavepacket propagates with the phase velocity c_p, but the wavepacket propagates with the group velocity. The group velocity (c_g) is defined as:

$$c_g = \frac{d\omega}{dk} = c_p + k\frac{dc_p}{dk}\,. \tag{2.8}$$

The group velocity corresponds physically to the velocity at which energy or information is conveyed along the direction of propagation. In the case of a dispersive medium, the group velocity may differ from the phase velocity. It is

important to account for velocity dispersion because it potentially affects the accuracy of sound velocity measurements.

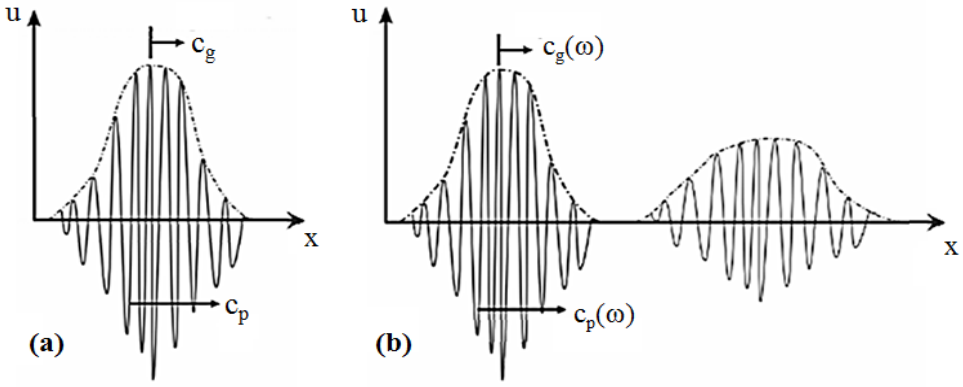

Figure 2.2: (a) A wavepacket propagating at the x direction with the group velocity c_g. Every wave of the wavepacket propagates with the phase velocity c_p, (b) a wavepacket propagating in a dispersive medium. The group and phase velocities are frequency dependent and therefore the signal envelop changes its form (Protopappas, 2006b).

2.2 Reflection and Refraction

As ultrasound energy propagates in a composite medium such as bone, interactions that occur include reflection, refraction, scattering, and absorption. Reflection and refraction occur at the boundary between two media with different characteristic acoustic impedances or different wave propagation velocities. Even if the incident wave is purely longitudinal or purely transverse, the refracted and reflected waves will be in general superpositions of longitudinal and transverse waves propagating in different directions (Lautrup, 2011). In composite media such as bone, wave reflection and refraction occur when the size of the heterogeneity d (size of pores with marrow in osseous tissues) is much larger than the wavelength (Manolis *et al.,* 2017).

If the surface is smooth, specular reflections occur whereas for rough surfaces, reflections are diffuse. Specular reflection forms the basis of pulse-echo ultrasonic imaging (echography) and contributes to image formation displaying organ boundaries. Figure 2.3 shows reflection and refraction between two fluid media, and between a fluid and a solid medium. These phenomena represent realistically the ultrasound interaction in the boundary of soft tissue and cortical bone. However, the interaction between ultrasound and cancellous bone is more complicated as the contribution of scattering phenomena is also significant.

The wave propagation phenomena of Fig. 2.3a, at the boundary between two fluid media can be described by the Snell's law. More specifically, the reflection angle θ_1 is equal to the angle of the incident wave and the transmitted wave is refracted away from the direction of the incident wave θ_1 at a refraction angle θ_2 given by:

$$\frac{\sin\theta_2}{c_2} = \frac{\sin\theta_1}{c_1}, \tag{2.9}$$

where c_1 and c_2 are the sound velocities of the first and second medium.

The ratio of the reflected to the incident acoustic pressure amplitude is called amplitude reflection coefficient r. The ratio of the transmitted to the incident acoustic amplitude is called amplitude transmission coefficient t. Coefficients t and r are given by:

$$r = \frac{Z_1 - Z_2}{Z_1 + Z_2} \tag{2.10}$$

and

$$t = \frac{2Z_2}{Z_1 + Z_2} \cdot \tag{2.11}$$

Similarly intensity reflection (R) and transmission coefficients (T) are defined by the ratio of the reflected to the incident acoustic intensity and the ratio of the transmitted to the incident acoustic amplitude, respectively:

$$R = \left(\frac{Z_1 - Z_2}{Z_1 + Z_2} \right)^2 \tag{2.12}$$

and

$$T = \frac{4Z_1Z_2}{(Z_1 + Z_2)^2}, \tag{2.13}$$

where Z_1 and Z_2 are the characteristic acoustic impedances of the first and second medium for longitudinal waves, respectively. One can verify that T + R = 1, which corresponds to the conservation of energy equation. The

amount of energy in the reflected wave depends on the impedance discontinuity of the two media. The larger the difference, the larger is the reflected energy.

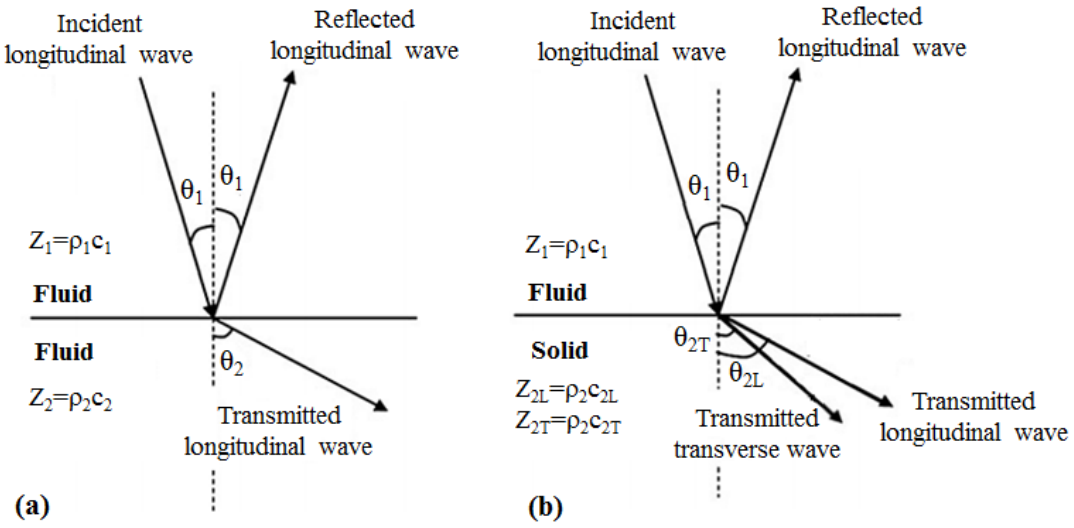

Figure 2.3: Reflection and refraction at the boundary: (a) between two fluid media, (b) between a fluid and a solid medium.

At the boundary between a fluid and a solid medium (Fig. 2.3b), the Snell's law obtains the following form:

$$\frac{\sin\theta_1}{c_1}=\frac{\sin\theta_{2L}}{c_{2L}}=\frac{\sin\theta_{2T}}{c_{2T}}, \tag{2.14}$$

in which the subscripts "2L" and "2T" correspond to the refracted longitudinal and shear waves in the solid medium (e.g., cortical bone).

As longitudinal waves in solids propagate with a higher speed of sound than in fluids, the refraction angle θ_{2L} is larger than the angle of incidence θ_1. When θ_1 is higher than a certain value θ_c, total internal reflection occurs and the longitudinal wave is no longer transmitted into the solid. The refracted wave is termed evanescent as it travels parallel to the interface and decays exponentially from the boundary. The corresponding incident angle θ_c is termed the first critical angle and is given by:

$$\sin\theta_c=\frac{c_1}{c_{2L}}\ . \tag{2.15}$$

According to the range of longitudinal wave velocity values in cortical bone (Table 2.1), the typical values of θ_c are between 20° and 25°.

2.3 Attenuation

When an ultrasonic wave propagates through osseous tissues, the effects of scattering and absorption lead to the reduction of acoustic pressure amplitude and are the two mechanisms that contribute to ultrasound attenuation. The loss of incident acoustic energy is characterized by the attenuation coefficient which can be defined as the sum of the absorption coefficient μ_α and the scattering coefficient μ_s:

$$\mu=\mu_\alpha+\mu_s \,. \tag{2.16}$$

Ultrasound attenuation is characterized by the following exponential decrease of the pressure amplitude p and of the amplitude of the acoustic intensity I with the traveling distance z:

$$p=p_0 e^{-\alpha z} \,, \tag{2.17}$$

and

$$I=I_0 e^{-2\alpha z} \,, \tag{2.18}$$

where, p_0 and I_0 are the pressure and intensity at z = 0, respectively. The quantity α (expressed in cm^{-1}) is the pressure frequency-dependent attenuation coefficient. The factor 2 in the exponential term of the intensity equation results from the transformation of pressure into intensity, as intensity is proportional to the square of pressure.

Different mechanisms are responsible for absorption phenomena such as thermal conductance, chemical and viscous effects. So far, the phenomena responsible for ultrasound absorption in biological tissues have not been completely understood. The role of scattering is described in subsection 2.3.1.

Attenuation differs substantially between fluid-like soft tissues and porous media such as bone, in which (i) viscous friction effects due to the relative motion of marrow and solid frame, (ii) scattering of the ultrasonic wave by bone heterogeneity and (iii) longitudinal to shear mode conversion contribute significantly. Acoustic attenuation in cancellous bone is almost one order of magnitude higher than in cortical bone. This is likely due to the large bone surface-to-volume ratio, which reinforces scattering, mode conversion and viscous friction. Recent studies suggest that loss mechanisms

such as mode conversion may be a significant contributor to the overall attenuation in bone in the diagnostic frequency range. Further important factors that contribute to the total wave intensity attenuation in a complex medium composed of layers of different media (surrounding soft tissues, bone, marrow) are diffraction, reflection and refraction. Due to diffraction phenomena, the acoustic beam emitted from a planar (unfocused) transducer will increase its diameter as the wave propagates and the intensity will decrease with increasing distance from the source. Reflection and refraction losses at tissue interfaces depend on the impedance mismatch at the interfaces.

Finally, normal bone demonstrates higher attenuation and is associated with higher velocity values compared to osteoporotic bone (Laugier *et al.,* 2002).

2.3.1 Scattering

When a plane wave travels through a suspension of particles like particulate composites (solid particles in solids), liquid suspensions (solid particles in fluid), and emulsions (fluid inclusions in fluid), multiple scattering occurs and part of the incident energy is transferred to the scattered fields. Parameters such as the frequency of the incident wave, the relative position among the particles, the geometry of the particles and the material properties of both matrix and inclusions affect the amount of this energy (Aggelis *et al.,* 2004).

Scattering phenomena result from the interaction between a primary ultrasonic wave and the boundaries of particles if their physical properties such as density or elasticity are different from those of the surrounding medium. In this case, the oscillatory movement of the scatterer is different from that of the surrounding medium, which leads to the emission of a secondary wave denoted scattered wave. The scattering regime of a single particle depends on the ratio between its dimension and the wavelength (λ). If λ is much smaller than the size of the heterogeneity, specular reflection occurs obeying the usual laws of reflection. In contrast, a scattered wave is created if the dimensions of the heterogeneities are comparable to or lower than the wavelength.

The scattering problem of light and sound by small scatterers was first solved by Lord Rayleigh (Rayleigh and Lindsay, 1878) and is therefore called Rayleigh scattering.

For scatterers much smaller than the wavelength, the intensity of the scattered waves is proportional to the fourth power of the frequency of the incident wave and to the sixth power of the size of the scatterers (Morse and Ingard, 1986). The case of scatterers with larger sizes or sizes comparable to the wavelength involves more complicated calculations. The scattered intensity from soft tissues is generally considerably smaller than the specularly reflected intensity from organ boundaries. However, similarly to specular reflection, such scattering events are of primary importance for image formation and for assessing micro-structural properties of the medium such as scatterer's size and scatterers' number. In ultrasound images of soft tissues, scattering causes the grainy aspect, also denoted as speckle.

2.4 First Arriving Signal Velocity

Fig. 2.4a shows the propagation of a broadband spherical wave emitted by a source S located in the water interface separating water and bone. Considering that the longitudinal bulk velocity of bone ($c_l \approx 4000$ m/s) is larger than that of the water ($c_w \approx 1490$ m/s), this configuration leads to the propagation of the so-called lateral wave (Bossy *et al.,* 2002). The lateral wave in the fluid/solid case connects the longitudinal refracted wave front to the reflected wave front, and propagates along the surface with the longitudinal bulk velocity c_l Eq. (2.1). Fig. 2.5 shows the propagation of the wave fronts of the lateral, reflected and refracted waves in non-absorbing media when the direct wave is spherical. The orientation of this lateral wave front depends on the ratio of the shear velocity to the longitudinal velocity.

The time-of-flight (TOF) is the main estimated parameter in ultrasound propagation measurements in order to calculate the FAS velocity. Fig. 2.6 shows a source and a receiver at a distance d from the water-bone interface, separated by a distance r. The lateral wave exists at the receiver only if $r>2d \tan(\theta_c)$, so that the path BC exists. Supposing that r always verifies this condition for the lateral wave, the theory predicts that the TOF corresponds to the geometrical path ABCD, traveling with velocity c_w on part AB and CD and with velocity c_l on part BC. Using the axial transmission method, the time of arrival of the lateral, direct and reflected waves can be calculated as:

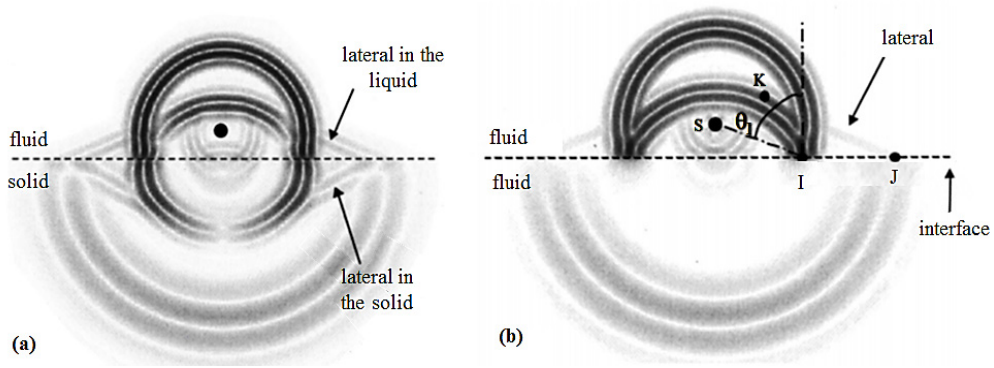

Figure 2.4: Snapshot of the wave propagation, in (a) the fluid/solid case, after the longitudinal refracted wave front has disconnected from the incident wave front, (b) for comparison purposes the fluid/fluid case is also depicted (Bossy *et al.,* 2002).

$$t_{lateral} = \frac{2d\cos\theta_c}{c_w} + \frac{r}{c_1}, \tag{2.19}$$

$$t_{direct} = \frac{r}{c_w}, \tag{2.20}$$

$$t_{reflected} = \frac{\sqrt{r^2+(2d)^2}}{c_w}. \tag{2.21}$$

It can be seen from these expressions that r must be large enough, so that the lateral wave, propagating along the surface at $c_1 > c_w$ arrives first. The corresponding condition $t_{direct} - t_{lateral} > 0$ therefore yields a value r_{min}, so that for $r > r_{min}$, the TOF of the lateral wave is less than that of the direct wave.

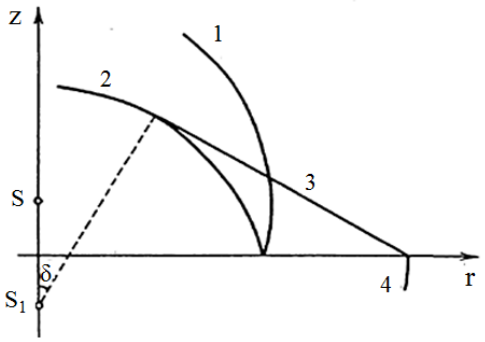

Figure 2.5: Wave fronts in non-absorbing media when the direct wave is spherical: curve 1-direct wave, curve 2-specular reflected wave, curve 3-lateral wave, curve 4-refracted wave (Brekhovskikh and Godin, 1999).

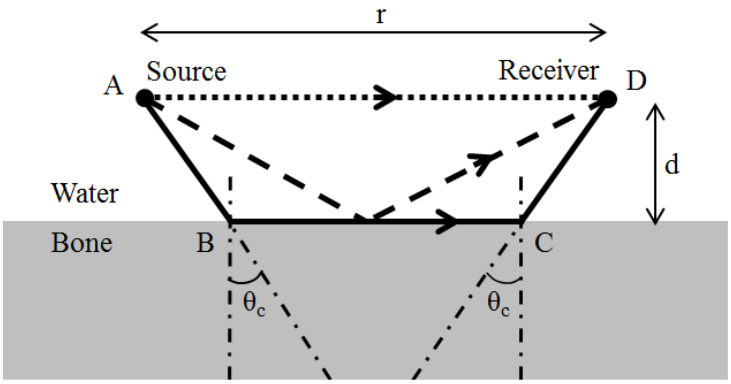

Figure 2.6: Propagation paths for the direct (...), reflected (- - -) and lateral wave (---).

Then, the FAS velocity can be calculated if the TOF and the propagation path have been determined. Several time criteria, have been used to identify the TOF at the receiver, including extrema, zero crossings or threshold-based time criteria as illustrated in Fig 2.7.

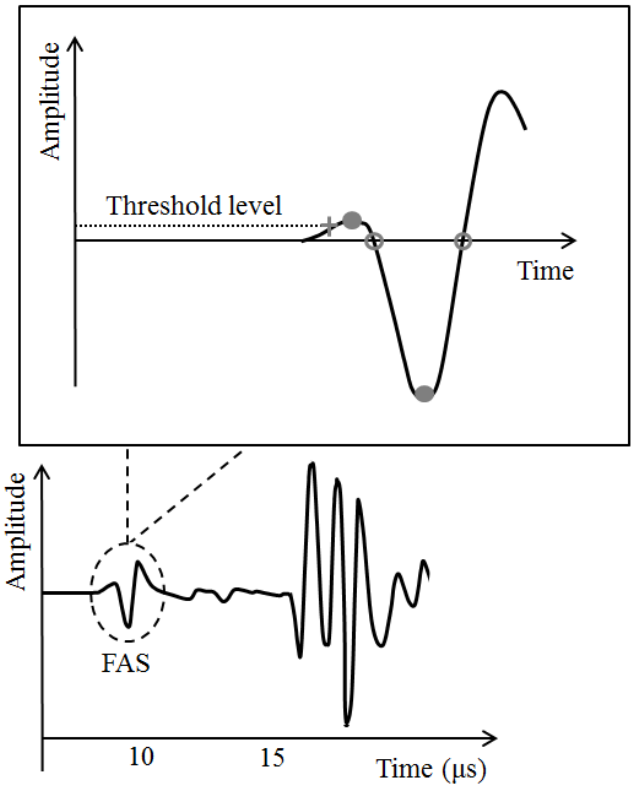

Figure 2.7: Illustration of different time detection criteria such as threshold-time, zero-crossings, extrema.

In intact long bones, the FAS velocity measured in cortical bone is known to be strongly correlated with the bone macrostructure and microstructure properties, i.e. matrix stiffness, porosity and thickness (Grondin *et al.,* 2010; Rohde *et al.,* 2014;

Grimal *et al.,* 2013). Therefore, FAS velocity measurements can provide significant quantitative information concerning bone deterioration in cases of bone pathologies such as osteoporosis and fracture healing.

2.5 Guided waves

Wave propagation through bounded media results in multiple reflections of the waves at the boundaries, and mode conversion occurs between longitudinal and shear waves. When the propagation medium is thin compared to the wavelength, superpositions cause the formation of wave packets, which are commonly referred to as guided wave modes (Protopappas *et al.,* 2006a). The wave guide character of the sound propagation has been evidenced for cortical bone in the 0.25–2 MHz frequency range (Laugier and Haiat, 2011). In this case, cortical bone can be modeled as a plate-like (2D representation) or a tube-like (3D representation) layered medium.

In the case of a homogeneous isotropic elastic plate with traction-free upper and lower surfaces (free plate), the guided waves are plane strain waves called plate waves or Lamb waves. Lamb waves are dispersive implying that the velocity at which a wave propagates within a plate is a function of the frequency and the plate thickness. The dispersion of Lamb waves is described by the following equation known as the Rayleigh-Lamb frequency relation:

$$\frac{\tan\beta d/2}{\tan\alpha d/2}=\left\{-\frac{4\alpha\beta k^2}{\left(k^2-\beta^2\right)^2}\right\}^{\pm 1}, \tag{2.22}$$

where d is the plate thickness, k=ω/c is the component of the wavenumber parallel to the interface, ω is the angular frequency, c is the phase velocity of the Lamb wave and α, β are given by:

$$\alpha=\frac{\omega^2}{c_l^2}-k^2, \tag{2.23}$$

and

$$\beta=\frac{\omega^2}{c_s^2}-k^2, \tag{2.24}$$

where c_l is the bulk longitudinal and c_s is the shear velocity of the medium.

In Eq. (2.22), the exponent of the right-hand term is +1 for symmetric modes and −1 for anti-symmetric modes. Symmetric modes, denoted as S0, S1, S2, etc., are waves with motion symmetric with respect to the midplane of the plate, whereas in anti-symmetric modes, denoted as A0, A1, A2, *etc.* the motion is anti-symmetric (Fig. 2.8).

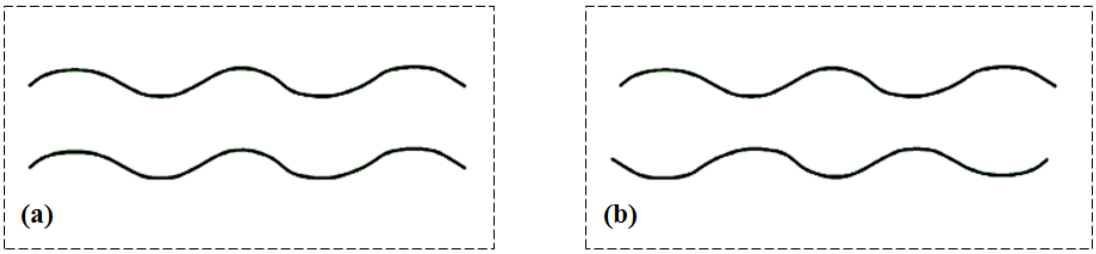

Figure 2.8: Propagation of: (a) symmetric, and (b) anti-symmetric modes.

Numerical evaluation of Eq. (2.22) yields Lamb wave dispersion curves which define the variation in phase velocity as a function of the frequency–thickness product F × d (Fig 2.9). Also, from Eq. (2.8), the group velocity dispersion curves can be calculated.

Each continuous curve in Fig. 2.9 represents a guided wave mode. From these dispersion curves it can be seen that all but the two fundamental modes, S0 and A0, have a cut-off frequency–thickness product. Thus, for very low frequencies, or for very thin plates, only the fundamental S0 and A0 modes can be excited. In these conditions, the phase velocity of the S0 wave can be calculated by the following equation (Nicholson *et. al,* 2002):

$$c_p = \sqrt{\frac{E}{(1-\nu^2)\rho}}\,, \tag{2.25}$$

where E is Young's modulus, ν is the Poisson ratio, and ρ is the density.

With increasing F × d, the velocities of all Lamb modes asymptotically approach the Rayleigh velocity. The Rayleigh velocity c_R is that of a pure non-dispersive surface wave, given by (Graff, 1991) as:

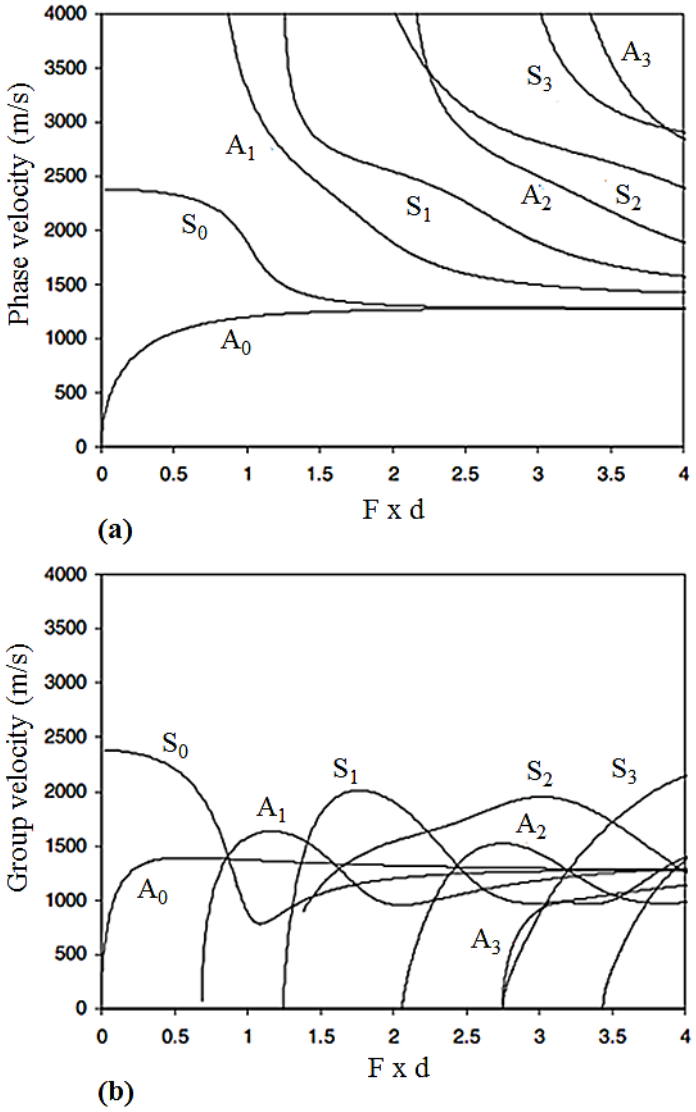

Figure 2.9: Theoretical Lamb wave dispersion curves for the first four symmetrical (S0–S3) and anti-symmetrical (A0–A3) guided modes in acrylic plates: (a) phase velocity, (b) group velocity.

$$c_R \approx \frac{c_s(0.87+1.12\nu)}{(1+\nu)} \quad . \tag{2.26}$$

If a wave is guided by the bone cortex with a phase velocity greater than that of the compression wave of the surrounding soft tissues, the energy propagating in the bone cortex can leak into the soft tissue. The boundary conditions are modified by the presence of a surrounding medium and the characteristics of Lamb waves in a fluid-immersed plate are different from those of Lamb waves in a free plate. For example, if the phase velocity of the fluid is close to the phase velocity of a Lamb mode, the mode continuously radiates into the fluid and, therefore, its attenuation is high

(Nicholson *et. al,* 2002). However, the theoretical background is not described herein as the analysis in Chapter 4 has been based on the free plate problem.

2.5.1 FAS velocity and guided waves

In the receiving element, the FAS can be defined as the first component of the signal which emerges from noise. The velocity of the FAS is measured in the time domain. FAS velocity can be easily calculated by means of numerical simulations using numerical tools such as the finite difference time domain (FDTD) method (Bossy *et al.,* 2004; Nicholson *et al.,* 2002). According to such FDTD simulation studies based on homogeneous bone models with uniform geometries, the nature of FAS, and subsequently the FAS velocity, changes with the thickness to wavelength (λ_L) ratio. Specifically, λ_L refers to the compression bulk wave inside bone, in the direction of bone axis. For thickness larger than λ_L, FAS is the so called lateral wave which is the trace on the surface of the compression bulk wave in the material (Camus *et al.,* 2000). If cortical thickness is much larger than the wavelength (3–4 mm at frequencies close to 1 MHz) no impact on FAS of thickness variability can be expected (Prevrhal *et al.,* 2001) according to numerical predictions (Bossy *et al.,* 2004). Therefore, in this case FAS velocity does not depend on the thickness and is close to c_1. For thickness in the range $\lambda_L/2-\lambda_L$, the reflection of compression bulk waves on the inner surface impacts the FAS velocity. For lower thickness, FAS velocity decreases with thickness and approaches the low frequency limit of the phase velocity of the guided wave S0 on plates. In this thickness range, thickness related variations of FAS velocity qualitatively agree with the dispersion of the S0 wave. The FAS velocity is expected to increase nonlinearly with thickness and to reach a plateau for the thickest samples.

In agreement with guided wave analysis, the precursor of the signal is related to the wave component which has the highest group velocity and width. For instance, when the frequency bandwidth of the excitation signal contains low enough frequency components, the FAS is expected to originate in the S0 wave. In this frequency domain, the S0 wave is slightly dispersive, i.e. its waveform is expected to be only slightly distorted with propagation distance. However, its amplitude is small due to the fact that it induces a longitudinal displacement field across the whole thickness.

In agreement with numerical predictions, several studies on plastic samples (acrylic, PVC, perspex) with varying thickness showed that FAS velocity varies with thickness when it is smaller than the wavelength λ_L (Moilanen *et al.,* 2004; Njeh *et al.,* 1999). The largest variations of FAS velocity were obtained for the smallest nominal frequency (200 kHz).

2.6 Ultrasonic Transducers

Ultrasonic probes are sensors which can generate acoustic signals and detect returned signals. A sound wave is typically produced by a piezoelectric transducer encased in a probe. Piezoelectric crystals change size and shape when a voltage is applied. For specific applications, proper piezoelectric materials are chosen according to a number of factors such as their piezoelectric performance, dielectric properties, elastic properties and stability (Zhou *et al.,* 2014).

The beam pattern of a transducer can be determined by the active transducer area and shape, the ultrasound wavelength, and the sound velocity of the propagation medium. The sound is focused either by the shape of the transducer using a lens in front of the transducer, or by a complex set of control pulses from the ultrasound scanner machine. In this way, an arc-shaped sound wave is generated. The wave travels into the body and is focused at a desired depth. Almost all piezoelectric transducers are made of crystals (quartz) or ceramic materials such as Lead Zirconate Titanate, Lithium Niobate and Lead Metaniobate. The transducer may be in contact with the body surface, or inserted into the body.

Since the piezoelectric material exhibits a higher acoustic impedance (≈30 MRayl) than that of biological tissue or water (≈1.5 MRayl), a substantial part of the acoustic energy would be lost at the rear interface and not directed into the forward direction, resulting in poor resolution and sensitivity, if not properly matched acoustically.

Fig. 2.10 presents a diagram of a typical transducer construction. The backing material is located behind the piezoelectric element to prevent excessive vibration. Reducing excessive vibration will cause the element to generate ultrasonic waves with a shorter pulse length, improving resolution in images. Ultrasonic waves transmitted from the piezoelectric element are reflected by a target because there is a big difference in acoustic impedance between the piezoelectric element and the object. To

avoid this phenomenon, an intermediate material is inserted to ensure that ultrasonic waves can efficiently enter the object. This is the role of the acoustic matching layer. The acoustic lens is attached to the tip of the probe. Ultrasonic waves transmitted from the probe would spread and travel like light. The acoustic lens prevents the ultrasonic waves from spreading and focuses them on a specific target.

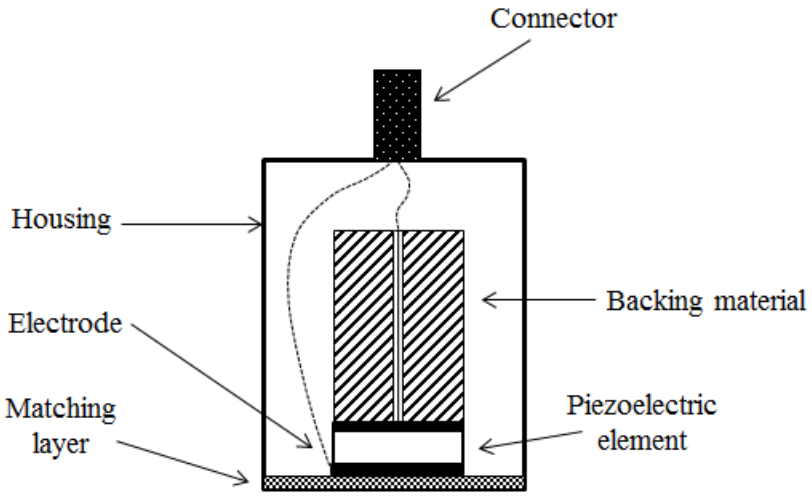

Figure 2.10: Diagram of a typical transducer construction.

In bone applications two are the most popular ultrasonic configurations known as the axial and through transmission techniques. A schematic view of the two techniques is presented in Fig. 2.11. When the axial transmission method is applied, the transducers are aligned along the bone axis to measure the FAS velocity and guided waves in the cortical layer of long bones. As bone is a highly attenuating medium, most studies use relatively low frequencies from 100 kHz to 2.0 MHz which are substantially lower than the frequencies used in conventional ultrasonography of soft tissues.

Axial transmission FAS velocity reflects both structural and intrinsic material properties of cortical bone. Experimental studies on excised human radii demonstrated the sensitivity of the velocity of the FAS to porosity and degree of mineralization (Bossy *et al.,* 2004b) and also to intrinsic elastic properties (Raum *et al.,* 2005).

The transverse transmission technique uses two piezoelectric transducers, a transmitter and a receiver, placed on opposite sides of the skeletal site. The transverse transmission technique provides estimates of the FAS velocity and frequency-

dependent attenuation known as broadband ultrasonic attenuation. While the calcaneus (heel bone) is the preferred skeletal site, this method has been applied at the finger phalanxes. More recently, devices have been presented to measure the ultradistal radius at the forearm (Mano *et al.,* 2006; Otani *et al.,* 2009) or the proximal femur at the hip (Barkmann *et al.,* 2010; Barkmann *et al.,* 2008).

The application of these techniques for the assessment of healthy and pathologic bones is discussed in detail in chapter 3 which describes the state-of-the art analysis in this research field and presents the cornerstone studies in the literature.

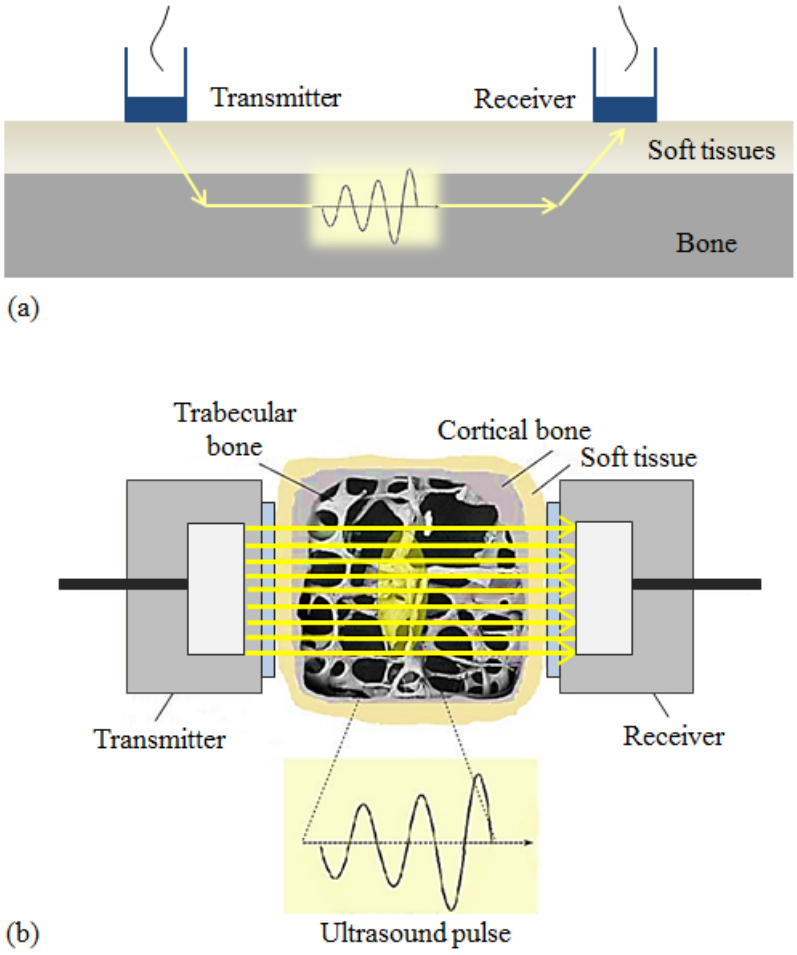

Figure 2.11: Schematic view of the: (a) axial transmission, and (b) through transmission methods.

Concerning medical imaging, four different modes of ultrasound are used (Carovac *et al.,* 2011). These are:

- A-mode: A-mode is the simplest type of ultrasound. A single transducer scans a line through the body with the echoes plotted on a screen as a function of depth.
- B-mode: In B-mode, a linear array of transducers simultaneously scans a plane through the body which can be viewed as a two-dimensional image.
- M-mode: M stands for motion. In M-mode a rapid sequence of B-mode scans enables doctors to see and measure the range of motion, as the organ boundaries that produce reflections move relative to the probe.
- Doppler mode: The Doppler effect is used to measure and visualize blood flow. Doppler sonography plays an important role in medicine. Sonography can be enhanced with Doppler measurements, which employ the Doppler effect to assess if a medium (e.g. blood) is moving towards or away from the probe, and the relative velocity. By calculating the frequency shift of a particular sample volume, for example a jet of blood flow over a heart valve, its speed and direction can be determined and visualized. This is particularly useful in cardiovascular studies and essential in many areas such as determining reverse blood flow in the liver vasculature in portal hypertension.

Chapter 3: Literature Overview

3.1 Introduction

Quantitative ultrasound (QUS) has received considerable interest during the last few decades for its potential to assess bone structural and material properties which reflect the risk of bone fragility. In the quite rich literature, several experimental and computational studies have been presented aiming to correlate QUS propagation parameters with bone microstructural alterations in pathological cases (Casciaro *et al.*, 2015; Barbieri *et al.,* 2011, Cheung *et al.,* 2011; Krieg *et al.,* 2008; Kaufman *et al.,* 2007; Protopappas *et al.,* 2006a).

The axial transmission technique is considered as the "gold standard" method for ultrasonic bone evaluation using a single or multiple emitters and receivers aligned along the long axis of the bone in contact with the skin or directly with the bone (Hata *et al.,* 2016; Foiret *et al.,* 2014; Talmant, 2009). The FAS velocity and attenuation have been used as the main quantitative parameters for bone characterization (Hata *et al.,* 2016; Baron *et al.,* 2007; Potsika *et al.,* 2016a; Barbieri *et al.,* 2011). However,

when the wavelength is comparable to or smaller than the thickness of the cortex, the FAS propagates as a lateral wave reflecting only material and geometrical changes in the cortical surface. The signals obtained at the receiver(s) are the combination of all waves propagating axially along the long axis of the bone. A few studies indicate that cortical bones support the propagation of guided waves, despite absorption phenomena due to the heterogeneity of osseous tissues (Bochud *et al.,* 2017; Minonzio *et al.,* 2011; Minonzio *et al.,* 2010; Vavva *et al.,* 2009). Therefore, the study of the propagation of guided waves has attracted the interest of several research groups in order to investigate microstructural changes occurring at deeper bone layers in healthy and pathological bones (Foiret *et al.,* 2014; Kilappa *et al.,* 2014; Vavva *et al.,* 2009). Ultrasonic axial transmission is widely applied along the axis of long bones such as the radius or tibia, while the through transmission and the backscattering methods have been used to a more limited extent and for different application sites (Potsika *et al.,* 2016b).

The through-transmission method has been also widely used to perform ultrasonic measurements in bone (Grimal *et al.,* 2013; Rohrbach *et al.,* 2013; Kaufman *et al.,* 2007; Barbieri *et al.,* 2011; Glinkowski and Gorecki, 2006). In this ultrasonic configuration, two transducers are placed in opposite directions and are mainly applied to the heel bone and at the distal radius. The FAS velocity or attenuation and the propagation of guided waves are the main examined parameters reflecting changes in healthy and pathological bones. The through-transmission and the axial transmission methods have been used in the literature for the evaluation of both osteoporotic and healing bones.

The backscattering method has been applied in skeletal sites such as the hip and spine where through-transmission measurements are difficult to be performed (Casciaro *et al.,* 2015). In backscattering measurements a single transducer is used and the main parameters of interest are the integrated reflection coefficient, the broadband ultrasound backscatter and apparent integrated backscatter (AIB), the time slope of apparent backscatter and the frequency slope of apparent backscatter. The backscattering method has been widely used for the ultrasonic evaluation of cancellous bone (Hoffmeister *et al.,* 2016; Liu *et al.,* 2015; Hoffmeister *et al.,* 2012; Karjalainen *et al.,* 2012), while it has been applied to a lesser extent for the evaluation

of cortical bone (Eneh *et al.,* 2017; Iori *et al.,* 2015). Backscatter difference measurements may be used to detect changes in bone caused by osteoporosis.

This chapter presents a thorough survey on ultrasonic characterization methods for the evaluation of fracture healing to highlight the significant monitoring role of QUS and its positive impact on the acceleration of the bone healing process. Emphasis is given on computational methods. At the end of this chapter, the aim and contribution of this thesis is presented compared to the current state-of-the art.

3.2 Animal studies for the evaluation of bone healing using ultrasonic methods

Animal studies on fracture healing can be divided into two main categories. The first one examines the bone status at a specific healing stage, while the studies of the second category monitor the complete healing process.

More specifically, in (Floriani *et al.,* 1967), an animal study on 40 guinea pigs with a femoral fracture was presented. The animals were sacrificed at the 6^{th} postoperative month and the bones were classified as completely healed, partly healed, and non-unions. Ultrasonic waves at 100 kHz were applied and the velocity of propagation was measured. It was shown that for completely healed bones the velocity approximated the ratio 94% of the control value, while for partly healed bones and non-unions the corresponding ratio was 81% and 67% of the control value, respectively. In (Abendschein and Hyatt, 1972), a midfemoral graft model on 96 guinea pigs was used to examine the relation of ultrasound velocity with the modulus of elasticity of the healing bone. The animals were sacrificed 6 months postoperatively and the ultrasonic velocity was measured at 100 kHz by positioning the transducers at the proximal and distal ends of the femoral shaft. Then, a three-point bending test was performed. It was found that the modulus of elasticity determined biomechanically was in linear relation with that determined by ultrasound. Another study on 36 rabbit tibiae fractures was presented by (Gill *et al.,* 1989) examining the correlation coefficient of the ultrasonic velocity with the load at failure, stiffness, and modulus of elasticity derived from the three-point bending test. Ultrasonic measurements were performed at 0.5 and 1 MHz and higher correlation coefficients were found at 1 MHz. In (Yang *et al.,* 1996), the exposure of 79 rat femur

fracture models to low-intensity ultrasound showed that ultrasound stimulation increased the mechanical properties of the healing fracture callus by stimulating earlier synthesis of extracellular matrix proteins in cartilage, possibly altering chondrocyte maturation and endochondral bone formation. More recently, in (Ferreira *et al.,* 2010), the ability of ultrasound backscatter parameters in differentiating normal bones from bones with pseudarthorsis was investigated. A diaphyseal osteotomy of the femur was conducted for twelve young adult rats. A radiological study on the left forward limbs of all subjects was performed after a period of 120 days followed by euthanasia. An *in vitro* ultrasonic analysis of four bone samples with pseudarthrosis was realized with a 5-MHz circular transducer and the AIB was measured. Higher AIB values were found for pseudarthrosis comparing to normal bone.

In (Maylia *et al.,* 1999; Saha *et al.,* 1982), ultrasound measurements were performed on ulnar fractures in rabbits to monitor the successive phases of the healing process. The amplitude of the FAS was calculated and a healing index was proposed as the ratio of the amplitude from the healing limb to that from the contralateral. The healing index was found to increase linearly with the healing time. Additional *in vitro* experiments revealed that the proposed healing index was positively correlated with the bending strength of bone. The positive effect of QUS on bone healing was also shown in (Pilla *et al.,* 1990), investigating intervals between 14 and 28 days in rabbits. More specifically, torsional testing revealed that the application of QUS for 20 minutes daily increased the rate of return of mechanical strength of an osteotomized rabbit fibula. Quantitative SAM at 50 MHz was applied in (Preininger *et al.,* 2011) for the assessment of the microstructural and elastic changes of mineralized callus and cortical tissue in sheep tibiae subjected to a transverse osteotomy. The 2^{nd}, 3^{rd}, 6^{th} and 9^{th} postoperative weeks were the examined healing stages and different types of stabilization were considered. The callus stiffness was found to increase while its porosity to decrease during the healing process. Different observations were derived for cortical bone as the cortical porosity increased at later healing stages and its stiffness decreased. In another animal study, (Barbieri *et al.,* 2011), a model of a transverse mid-diaphyseal osteotomy of the tibiae of 21 sheep was used to measure ultrasound propagation velocity and attenuation. The subjects were distributed into three equal groups after 30, 60, and 90 days of healing and were finally sacrificed. Then, the ultrasound velocity and attenuation were measured at the osteotomy site in

the transverse and longitudinal direction. The intact left sheep tibia was used as reference case for comparison purposes. The ultrasound propagation velocity increased, whereas the broadband ultrasound attenuation decreased during the healing process, with significant differences between the examined healing stages. In (Rohrbach *et al.,* 2013), a non-invasive monitoring system for fracture healing in small animals was presented. Specifically, a focused transmission system at 5 MHz was applied in a 2-mm osteotomy of twelve-month-old female rats aiming to discriminate alterations in osseous tissue during the early stages of fracture healing. Different healing stages after 6 weeks of consolidation were realized by different treatments and 2D projection images of TOF, speed of sound and ultrasound attenuation were measured. It was found that the osteotomy gap regions filled with fibrous tissue have similar properties compared to adjacent muscle tissue, while regions containing cartilage and mineralized callus tissue differed significantly (Rohrbach *et al.,* 2013). In (Malizos *et al.,* 2006; Protopappas *et al.,* 2005), a system was proposed for the ultrasonic monitoring of fracture healing which was applied on a sheep tibial osteotomy with an external fixation device. The system consisted of a pair of miniature implantable ultrasound transducers, a wearable device and a centralized unit. The transmitter and receiver were positioned anterolaterally on each side of the osteotomy region with a distance of 25 mm among them and ultrasound measurements were conducted at 1 MHz. After the osteotomy, the assessment of the fracture healing progress proceeded on a 4-day basis until the 100^{th} postoperative day and the ultrasound velocity was the parameter of interest. Measurements were also performed for the case of intact bone. Three different patterns of ultrasound velocity variation were detected corresponding to: (a) secondary healing, (b) primary healing, and (c) delayed union (Protopappas *et al.,* 2005). More specifically, for the case of secondary fracture healing, the velocity initially decreased by an average 17% after the osteotomy and continued to decrease by a further 13% until the 38^{th} day. The results were attributed to the inflammatory response and the increased osteoclastic activity occurring at the early stages of the secondary healing, which broaden further the fracture gap. Then, the velocity gradually increased reflecting the formation and consolidation of the callus. Radiographic examination revealed the evolution of primary bone healing for 3 animals showing a constant increase in velocity after the osteotomy. In this case, the occurrence of direct bony union in the fracture gap was detected without the formation of the callus tissue. Finally, a non-union was identified

in 2 specimens as no systematic velocity variation profile was observed. It was also reported that the velocity of healed bones on the last postoperative day exceeds on average 80% the corresponding value of the intact bone. Therefore, the monitoring role of the ultrasound velocity was highlighted reflecting a dynamic healing process and potential complications such as a non-union or pseudarthrosis during the early stages of fracture healing.

3.3 Computational studies

3.3.1 Fracture healing

Computational modeling has emerged as a powerful new approach to better comprehend the functionality and manipulate biological systems. Several methods have been proposed to model, visualize, and rationally alter systems at various hierarchical bone levels. In the case of ultrasonic bone assessment, numerical approaches have several benefits as: i) they give insight to complicated wave propagation phenomena which cannot be investigated via traditional clinical and experimental procedures, ii) the exposure of patients in experimental procedures is not required, reducing thus human suffering, relative costs as well as time constraints.

Therefore, numerical simulations of ultrasonic propagation in bone have now become a standard tool for assessing osteoporosis and fracture healing. The rapid technological development has provided robust computational tools making efficient use of the computational time, power and available memory. Simultaneously, the evolution of imaging modalities and especially μ-CT and SAM, which provide bone microstructure with an analysis down to the μm range, lead to more realistic 2D and 3D numerical models (Rohde *et al.,* 2014; Potsika *et al.,* 2014a; Moilanen *et al.,* 2007; Baron *et al.,* 2007).

In the first numerical studies, the cortical and callus tissues were simulated as 2D, homogeneous and isotropic media and the axial transmission method was applied to simulate the ultrasonic propagation problem (Dodd *et al.,* 2008; Dodd *et al.,* 2007; Protopappas *et al.,* 2006a). In (Dodd *et al.,* 2007; Dodd *et al.,* 2008), different geometries of bone fractures were established and the propagation of ultrasonic waves was examined at 200 kHz. The presence of the discontinuity of the fracture led to lower FAS velocities and an energy attenuation of the FAS due to wave propagation

interaction phenomena which evolve in the gap. Also, the occurrence of an oblique fracture led to the reduction of the extra time delay of the propagating wave comparing to the transverse case and to the decrease of the signal amplitude. Different oblique fracture angles were also considered and it was found that as the fracture angle decreases relative to the direction of wave propagation, the extra time delay decreases, while the signal loss increases. More recently, in (Machado *et al.,* 2010) four numerical daily-changing healing models were presented to study the compositional factors in fracture healing affecting ultrasound axial transmission at 1 MHz. The callus tissue was consisted of six tissue types with different Young's modulus and Poisson's ratio values to simulate fibrous tissue, immature cartilage, mature cartilage, immature bone, intermediate bone and mature bone, respectively. The FAS velocity and energy attenuation were the parameters of interest. It was concluded that the FAS velocity increases consistently during callus consolidation for all the examined cases showing that ultrasonic measurements can reflect the degree of mineralization of the callus, as well as potential consolidation delays and non-unions. Nevertheless, the FAS velocity was sensitive only to superficial geometrical and material alterations in the propagation path, while the effect of callus composition on energy attenuation was not completely understood.

In (Machado *et al.,* 2011), experimental and numerical means were combined to investigate the effect of cortical bone mineralization on ultrasound axial transmission measurements. A cortical bovine femur sample was used, in which a 3 mm fracture gap was drilled. A 3 mm thick cortical bone slice, extracted from another location in the bone sample, was submitted to a progressive demineralization process with ethylenediamine tetraacetic acid (EDTA) for 12 days. Axial transmission measurements and simulations using a 1 MHz probe were performed with the demineralized slice placed into the fracture gap to mimic different stages of mineralization during the healing process. The calcium loss of the slice due to the EDTA treatment was recorded everyday, and its temporal evolution could be modeled by an exponential law. A 50 MHz SAM was also used to assess the mineralization degree of the bone slice at the end of the intervention. These data were used in the numerical simulations to derive a model of the time evolution of bone slice mechanical properties. From both the experiments and the simulations, a significant and progressive increase in the TOF of the propagating waves was observed during

the beginning of the demineralization process (first 4 days). Although the simulated TOF values were slightly larger than the experimental ones, they both exhibited a similar time-dependence, validating the simulation approach. The results suggested that TOF measured in axial transmission is affected by local changes of speed of sound induced by changes in local mineralization and could contribute to the monitoring of callus maturation.

In (Protopappas *et al.,* 2006a), a 2D model of a bone-mimicking plate was proposed to simulate bone healing as a 7-stage process. The FAS velocity was found to decrease during the first two healing stages and increase at later healing stages. Also, guided wave analysis was conducted based on three time-frequency (t-f) distribution functions: (a) the reassigned Spectrogram, (b) the smoothed-pseudo Wigner-Ville, and (c) the reassigned version of it. For intact bone, the S2, A3 Lamb modes were found to be the dominant waves for a 1 MHz excitation frequency, while the S2, S0 at 0.5 MHz. During bone healing, alterations in the callus tissue mechanical and structural properties affected the theoretical Lamb modes. Therefore, it was concluded that the study of the propagation of guided waves throughout the thickness of the cortical bone and the investigation of their sensitivity to both mechanical and structural changes during fracture healing could provide supplementary qualitative information to velocity measurements and enhance the monitoring capabilities of QUS. A guided wave analysis in fracture healing was also presented in (Vavva *et al.,* 2008a) and emphasis was given on the impact of boundary conditions which were not considered in previous studies. Three different cases of fluid loading boundary conditions were simulated as follows: (a) blood occupied the semi-infinite spaces of the upper and lower surfaces of the 2D cortical cortex, (b) the upper cortical surface was covered with a 2 mm layer of blood and the lower surface consisted of a semi-infinite fluid corresponding to bone marrow, (c) the upper bone surface was loaded by a 2 mm blood layer and the lower cortical surface consisted of a 2 mm bone marrow layer. The callus tissue consisted of different evolving ossification regions to simulate serial fracture healing stages. The FAS velocity was found to decrease in the first stage and to increase gradually in stages 2 and 3 for all the examined boundary conditions. The application of different boundary conditions had a significant effect on the propagation of guided waves compared to numerical models in which the cortical cortex was assumed free. Then, the same numerical model of callus was used

in (Vavva *et al.,* 2008b) proposing a new ultrasound configuration in which the transducers are placed on the pins of an already applied external fixation device instead of being implanted into the cortical bone. This method could offer several advantages *in vivo* compared to the previously described methods and its effectiveness was examined by performing FAS velocity measurements. Initially, intact bone models were examined to derive reference values and then the callus tissue was incorporated into the models. The effect of a possible non-perpendicular pin insertion was also investigated considering five additional cases for different angles. Only apparent velocity values could be derived from the proposed method corresponding to the whole propagation path (i.e. pins, bone and fracture) rather than to the fracture zone justifying the increased velocity values which were observed for all examined cases. Thus, it was reported that the sensitivity of the method is limited and the identification of small alterations in the callus during bone healing is more difficult compared to other QUS transmission methods. The examination of the pin inclination angle revealed that this parameter had a minor impact on the results implying that the proposed method may provide accurate results when applied *in vivo.*

Recently, in (Li *et al.,* 2017), a 2D FDTD simulation study was presented on transverse and oblique long bone fracture evaluation by low order ultrasonic guided waves. More specifically, an axial transmission technique was used to quantify the impact of the gap breakage width and fracture angle on the amplitudes of low order guided wave modes S0 and A0 under a 100 kHz narrowband excitation (Liu *et al.,* 2015; Li *et al.,* 2017). The models of long bones were composed of three layers with a soft tissue overlay and marrow underlay. The simulations of the transversely and obliquely fractured long bones showed that the amplitudes of both S0 and A0 decreased as the gap breakage widens. Fixing the crack width, the increase of the fracture angle perpendicular to the long axis was found to enhance the amplitude of A0, while the amplitude of S0 showed a non-monotonic trend with the decrease of the fracture angle.

The aforementioned numerical studies presented 2D numerical models of healing long bones. In (Protopappas *et al.,* 2007), 3D finite element numerical models of intact and healing bones were presented. More specifically, fracture healing was simulated as a three-stage process and the propagation of guided waves as well as the variation of the FAS velocity were examined for a 1-MHz excitation frequency. It was shown that the

irregularity and anisotropy of the bone, as well as the material and geometrical changes during bone healing have a significant impact on the dispersion of guided waves. The FAS velocity was found to decrease in stage 1, remained the same up to stage 2, and then increased in stage 3. However, when the FAS corresponded to a lateral wave, its propagation velocity was almost unaffected by the elastic symmetry and geometry of the bone and could not characterize the callus tissue throughout its thickness (Protopappas *et al.,* 2007).

3.3.2 Intact bone

Most of the aforementioned numerical studies are based on the classical linear theory of elasticity. However, the classical elasticity cannot adequately describe bone's mechanical behavior since only homogeneous media and local stresses are considered which cannot effectively reflect the mechanical behavior of materials with microstructure in which the stress state has to be defined in a non-local manner (Vavva *et al.,* 2014; Vavva *et al.,* 2009). To this end, in (Vavva *et al.,* 2009) the simplified Mindlin Form-II or dipolar gradient theory of elasticity was used for the determination of symmetric and anti-symmetric modes propagating in a 2D and free of stresses gradient elastic plate. The main advantage of the proposed theory compared to other couple stresses, micropolar, gradient elastic, and non-local elastic theories is its simplicity and the symmetry of all classical and non-classical stress tensors involved. More specifically, two terms were added in the constitutive equations representing the characteristic length in bone: (a) the gradient coefficient g introduced in the strain energy, and (b) the micro-inertia term h, in the kinetic energy. The plate was considered free of stresses. Two different values were examined for the micro-inertia term ($h=10^{-4}$ m and $h=10^{-5}$ m). For each value three different combinations between g and h were assumed: (a) $g>h$, (b) $g<h$, and (c) $g=h$. The selection of these values was in agreement with typical values of the osteon's size. The velocity dispersion curves of guided waves were calculated and compared with the solutions derived from the Lamb wave theory based on the classical elasticity to investigate the microstructural effects on guided modes. It was observed that when g is not equal to h, cortical microstructure affects mode dispersion by inducing both material and geometrical dispersion. Thus, gradient elasticity could provide supplementary information to better understand guided waves in bones.

Nevertheless, for frequencies higher than 0.8 MHz, ultrasound propagates rather as a dispersive surface Rayleigh wave than a dispersive guided wave considering that the wavelengths are smaller than cortical thickness. Since the classical elasticity cannot support dispersion in bulk and Rayleigh waves, in (Papacharalampopoulos *et al.,* 2011) the Mindlin's Form-II gradient elastic theory was applied to examine the dispersion of Rayleigh waves in media with microstructure. The gradient elasticity was used along with the boundary element method (BEM) and the reassigned smoothed pseudo Wigner–Ville transform for the numerical determination of the dispersion curves of Rayleigh and guided waves propagating in a cortical bone model. More specifically, various cases of intrinsic parameters were examined that serve as a means for investigating the dispersive nature of the Rayleigh wave and its relationship with the intrinsic parameters of the Form-II gradient elasticity. Then, BEM simulations were performed for a free of stresses cortical plate with intrinsic parameters according to (Ben-Amoz, 1976). The results demonstrated the efficiency of gradient elasticity to describe Rayleigh wave dispersion along the bone surface.

In (Vavva *et al.,* 2014), the role of microstructural effects was considered by incorporating four intrinsic parameters in the stress analysis, namely l1, l2, h1 and h2. The examined cases correspond to the three different combinations between the gradient coefficient c and the microinertia term h in the dipolar elasticity examined in (Georgiadis *et al.,* 2004). Calculations were performed for the cases: (a) case 1: $l1=l2=h1\neq h2$ ($l1=1.04\text{x}10^{-4}$ m, $l2=1.04\text{x}10^{-4}$ m, $h1=1.04\text{x}10^{-4}$ m, $h2=0.74\text{x}10^{-4}$ m), (b) case 2: $l1=h1$, $l2=h2$ ($l1=1.04\text{x}10^{-4}$ m, $l2=0.74\text{x}10^{-4}$ m, $h1=1.04\text{x}10^{-4}$ m, $h2=0.74\text{x}10^{-4}$ m), (c) case 3: $l1=l2=h2\neq h1$ ($l1=0.74\text{x}10^{-4}$ m, $l2=0.74\text{x}10^{-4}$ m, $h1=1.04\text{x}10^{-4}$ m, $h2=0.74\text{x}10^{-4}$ m), (d) case 4: $l2=h1=h2\neq l1$ ($l1=1.04\text{x}10^{-4}$ m, $l2=0.74\text{x}10^{-4}$ m, $h1=0.74\text{x}10^{-4}$ m, $h2=0.74\text{x}10^{-4}$ m), (e) case 5: $l1=h1=h2\neq l2$ ($l1=0.74\text{x}10^{-4}$ m, $l2=1.04\text{x}10^{-4}$ m, $h1=0.74\text{x}10^{-4}$ m, $h2=0.74\text{x}10^{-4}$ m), and (f) case 6: $l1=l2$, $h1=h2$ ($l1=0.74\text{x}10^{-4}$ m, $l2=0.74\text{x}10^{-4}$ m, $h1=1.04\text{x}10^{-4}$ m, $h2=1.04\text{x}10^{-4}$ m). The group and phase velocity dispersion curves were calculated and compared with existing computational results and semi-analytical curves for a simpler case of Rayleigh waves in dipolar gradient elastic half-spaces. Comparisons were also presented with the velocity of the first-order antisymmetric mode propagating in a dipolar plate in order to investigate the Rayleigh asymptotic behavior (Vavva *et al.,* 2014). For a transmitter-receiver distance 60 mm, the semi-analytical frequency-

group velocity dispersion curves of the Rayleigh wave in both Mindlin's Form II gradient and classical elasticity were converted to (t-f) curves and were superimposed on the (t-f) plane of the corresponding signals obtained from the BEM model in (Papacharalampopoulos *et al.,* 2011). Except for the very low frequency range, the agreement between BEM simulations and theoretical results from gradient elasticity was perfect. Also, it was found that Mindlin's Form II gradient elasticity can effectively describe the dispersive nature of Rayleigh waves.

3.4 Ossification process and angiogenesis predictions in bone healing under the ultrasound effect

From a biological point of view, fracture healing is a complex process involving specific regenerative patterns and a sequence of cellular actions and interactions, regulated by biochemical and mechanical signals. The occurrence of a fracture is followed by the formation of a hematoma in the gap region due to blood vessel disruption. The hematoma consists of cells from both peripheral and intramedullary blood, as well as bone marrow cells (Marsell and Einhorn, 2011). Bone regeneration is achieved when mesenchymal stem cells are recruited, proliferate and differentiate into osteogenic cells (Marsell and Einhorn, 2011). Thus, stem cells approach the fracture region and endothelial cells migrate and proliferate forming new vessels. Angiogenesis plays significant role in bone healing since it re-establishes blood circulation at the fracture region which limits ischaemic necrosis and enhances bone repair. Several growth factors such as the transforming growth factor, the bone morphogenetic protein, the fibroblast growth factor, and the vascular endothelial growth factor (VEGF) regulate the vascularization process having direct or indirect osteogenic and angiogenic influence (Vavva *et al.,* 2015). However, the VEGF pathway is considered to be the key regulator in the neoangiogenesis and revascularization of the fracture region.

According to (Lam and Lui, 2013) elevated VEGF level has been reported with the use of low-intensity pulsed ultrasound in the treatment of fracture. The effect of ultrasound on fracture healing mechanisms has been investigated experimentally in (Reher *et al.,* 1999; Doan *et al.,* 1999). More specifically, these studies examined the impact of ultrasound on human mandibular osteoblasts, gingival fibroblasts and peripheral blood mononuclear cells. Various ultrasound application techniques,

intensities and frequencies were examined. It was observed that in all cases the cytokines that are related with angiogenesis were highly stimulated in osteoblasts, and the VEGF levels were increased. Also, in (Cheung *et al.,* 2011) the effect of ultrasound on osteoporotic fracture rat models led to the increase in the VEGF. According to (Mundi *et al.,* 2009) angiogenesis is enhanced by low-intensity pulsed ultrasound through an increase in mRNA expression and production of VEGF by both human osteoblasts and periosteal cells. Thus, ultrasound plays a key role on the proliferation of osteoblasts via osteocytes and enhances blood vessel formation due to alterations in the transport of VEGF and fibroblast growth factor which are related to angiogenesis.

Computational studies in the field of bone mechanobiology have also been presented aiming to provide insight to the evolution of cell activities and angiogenesis mechanisms during the fracture healing process (Shefelbine *et al.,* 2005; Claes and Heigele, 1999). In a more recent study (Peiffer *et al.,* 2011), sprouting blood vessel growth and branching were simulated. Nevertheless, these models do not account for the effect of ultrasound on the fracture healing mechanisms and angiogenesis. To this end, in (Grivas, 2016; Vavva *et al.,* 2015), a deterministic hybrid model was presented for bone healing and angiogenesis predictions under the impact of ultrasound. The proposed mathematical model was based on the model of (Peiffer *et al.,* 2011) extended by: (a) including an additional equation describing the spatiotemporal evolution of ultrasound acoustic pressure, and (b) modifying the equation that describes the spatiotemporal evolution of VEGF. Processes of the normal fracture healing evolution such as intramembranous and endochondral ossification were considered. Then, numerical simulations were performed for different values of the newly introduced parameters aiming to provide comprehensive knowledge on the cellular mechanisms that accelerate bone healing due to ultrasound. It was observed that the application of ultrasound causes the upregulation in VEGF expression in weeks 3 and 4 after the fracture occurrence which is in agreement with previous experimental findings (Reher *et al.,* 1999; Doan *et al.,* 1999; Cheung *et al.,* 2011). Therefore, ultrasound enhances blood vessel growth and the proposed model could be useful for the ultrasonic characterization of the biological processes involved in bone fracture healing.

3.5 The objectives of this Thesis

The aim of this thesis is threefold: (a) to develop more realistic computational models of healing long bones which incorporate callus porosity using SAM images, (b) to evaluate fracture healing not only using traditional parameters such as guided waves and FAS velocity, but also assess new monitoring indicators such as ultrasonic attenuation and scattering, and (c) to investigate numerically the risk for fracture using ultrasonic methods to identify the occurrence of BMUs in cortical bone.

Initially, SAM images are used from (Preininger *et al.,* 2011) in order to establish numerical models of healing long bones which account for callus porosity alterations during the healing process. More specifically, according to (Preininger *et al.,* 2011) increased stiffness and decreased porosity were observed in the callus tissue over the course of the healing process, while cortical porosity increased and stiffness decreased over time. The composite and porous nature of callus give rise to multiple scattering phenomena, which are evaluated for the first time using both theoretical and numerical means. Through the exploitation of SAM images, the evolution of the microstructure of the osseous and callus tissues can be better understood during bone healing. Therefore, this thesis presents a theoretical analysis to evaluate the frequency dependent attenuation coefficient and group velocity during bone healing which is accompanied by traditional ultrasonic axial transmission simulations to investigate the FAS velocity alterations and the propagation of guided waves in successive healing stages.

Then, this thesis focuses on the evaluation of new quantitative and qualitative criteria for the monitoring of the fracture healing process. More specifically, although the backscattering method has been widely used for the evaluation of cancellous bone, its potential to monitor bone fracture healing has not been addressed so far in the literature. To this end, this thesis presents a numerical study on the monitoring of the fracture healing process using the backscattering method. The potential of the scattering amplitude and the acoustic pressure, calculated in the backward direction, for the assessment of fracture healing is investigated for the first time.

Finally, the axial transmission method is used to perform FAS velocity measurements in small, predefined propagation paths in order to detect alterations in cortical

porosity focusing on the occurrence of large BMUs. The main objective is to identify regions of the cortical cortex which are subjected to a higher risk of fracture due to the formation and concentration of pores with a size larger than the typical diameter of the Haversian canal. In this way, the early signs of an osteoporotic fracture could potentially be detected aiming at the effective prognosis of the disease at the first stages and the prevention of a future fracture.

Fig. 3.1 summarizes the three branches of the objective, the methods and novelty of this thesis.

3.6 Contribution of this Thesis

The evaluation of intact, osteoporotic and healing bones using QUS has been addressed in several experimental, computational and theoretical studies over various levels ranging from macrostructure to nanostructure. This section presents the contribution of this thesis and how the proposed methodologies and results are presented and structured in the following chapters.

Chapter 4-A theoretical and computational study is presented based on an iterative effective medium approximation (IEMA) to investigate the evolution of the complex scattering propagation phenomena during fracture healing (Potsika *et al.,* 2014a). For the first time realistic numerical models of healing long bones are developed incorporating the porous nature of callus with material and structural properties based on SAM images (Preininger *et al.,* 2011). The imaging data represent 3-mm osteotomies in the right tibia of female Merino sheep and correspond to the 3rd, 6th and 9th postoperative week. Guided wave analysis is performed accompanied by wave dispersion and attenuation predictions using both computational and theoretical tools. According to the literature, the evolution of scattering, material dispersion and absorption phenomena during secondary fracture healing has not been addressed in the past. Through the combination of theoretical and numerical means these complex wave propagation phenomena can be better understood by focusing on parameters that cannot be easily examined in experimental studies. For example, using numerical methods the effect of the callus porosity on wave dispersion and attenuation can be investigated separately keeping other parameters constant (e.g. cortical porosity, cortical thickness), which cannot be discriminated using traditional experimental and clinical approaches.

Chapter 5-The backward propagating acoustic field is evaluated in healing long bones aiming to provide insight into the complex scattering mechanisms and better comprehend the processes of bone regeneration (Potsika *et al.,* 2017).

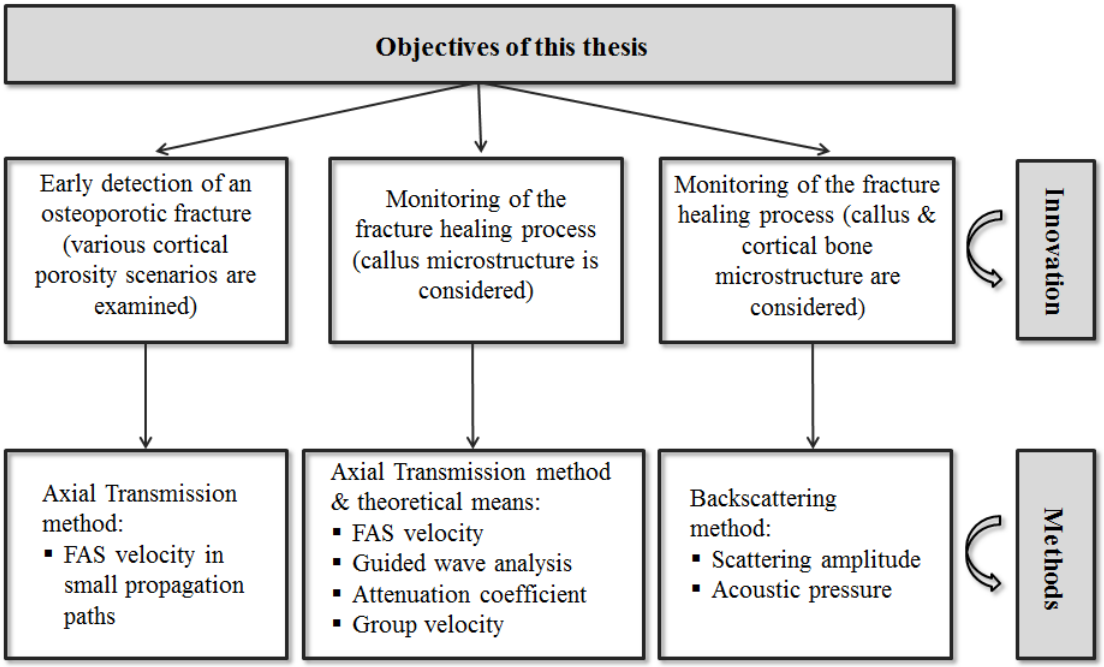

Figure 3.1: The objectives of this thesis.

Numerical models of healing long bones are established based on SAM from successive postoperative weeks considering the effect of the nonhomogeneous callus and cortical structure. More specifically, the scattering amplitude and the acoustic pressure variation are calculated in the backward direction to investigate their potential to serve as new quantitative and qualitative indicators for the monitoring of the bone healing process. The role of the excitation frequency is also examined considering frequencies in the range 0.2–1 MHz. The application of the backscattering method for the evaluation of fracture healing is an open research field as except for the experimental work of (Ferreira *et al.,* 2010), studying bones with pseudarthrosis and healthy bones, no other study has been presented especially for secondary healing. Also, the innovation of this study compared to previous numerical studies is that except for the callus porosity the cortical porosity is also incorporated into the numerical models based on the findings of (Preininger *et al.,* 2011).

Chapter 6-The potential of ultrasound to early detect a region of high risk for an osteoporotic fracture is examined numerically. More specifically, a parametric and systematic numerical study is presented on ultrasound propagation in cortical bone

models to investigate the effect of changes in cortical porosity and the occurrence of large BMUs, simply called non-refilled RL, on the FAS velocity. 2D geometries of cortical bone are established for various microstructural models mimicking normal and pathological tissue states. Emphasis is given on the detection of RL formation which may provoke the thinning of the cortical cortex and the increase of porosity at a later stage of the disease. The central excitation frequencies 0.5 and 1 MHz are examined. The proposed configuration consists of one point source and multiple successive receivers in order to calculate the FAS velocity in small propagation paths (local velocity) and derive a variation profile along the cortical surface. To the best of the author's knowledge, this is the first study to investigate whether the local FAS velocity can capture cortical porosity changes including the occurrence of RL with different number, size and depth of formation considering the impact of the excitation frequency.

Chapter 4: Theoretical and numerical evaluation of the effect of callus porosity on ultrasonic wave propagation

4.1 Introduction

The study of wave propagation in porous media such as cancellous bone and fracture callus is a challenging research field since scattering is predominant giving rise to material dispersion of velocity and attenuation. Wave dispersion due to porosity is difficult to be investigated alone since it is usually accompanied by geometry-induced dispersion.

Many authors aiming at the ultrasonic assessment of cancellous bone have reported phase velocities that decrease with frequency, a phenomenon known as negative dispersion (Bauer *et al.,* 2008; Anderson *et al.,* 2008; Chakraborty *et al.,* 2008; Haiat *et al.,* 2008). Specifically, in (Bauer *et al.,* 2008) this phenomenon was investigated by performing through transmission measurements in a cancellous bone phantom. Negative dispersion was observed at specific spatial locations of the plate at which the attenuation coefficient was increasing linearly with frequency. In (Anderson *et al.,*

2008) the modified Biot–Attenborough model was used to simulate multiple-mode wave propagation in cancellous bone. It was found that negative dispersion can arise when signals consisted of overlapped fast and slow waves are analyzed as a single longitudinal wave. Another study (Chakraborty *et al.,* 2008) presented a nonlocal version of Biot's theory of poroelasticity to investigate the dependence of the phase velocity and attenuation for both porosity and frequency variation. It was shown that the phase velocities exhibit a negative dispersion where the magnitude of dispersion is strongly dependent on porosity. It was also observed that the Lamb modes show negative dispersion when predicted by the nonlocal poroelastic theory. In (Haiat *et al.,* 2008), trabecular bone was assumed to be a composite medium consisting of infinite cylinders immersed in a saturating matrix. The generalized self-consistent method was used to describe the homogeneous effective material by considering two concentric cylinders immersed in the medium. The authors suggested that scattering effects are responsible for the negative dispersion. However, the factors which affect the variability of the phase velocity and lead to the observed abnormal negative dispersion in cancellous bone are not yet fully understood.

Several multiple scattering theories have been proposed aiming at the quantitative determination of wave dispersion and attenuation phenomena induced by a random distribution of inhomogeneities-scatterers in composite media (Kim, 2010; Kanaun and Levin 2008; Layman *et al.,* 2006; Linton and Martin, 2005; Fikioris and Waterman, 1964). The so-called self-consistent theories use self-consistent expressions derived from the solution of the single scattering problem in order to estimate the frequency dependent phase velocity and attenuation coefficient. Recent theoretical studies dealing with the quantitative determination of wave dispersion and attenuation in cancellous bone have been based on multiple scattering theories. Here one can mention the representative works of (Haïat *et al.,* 2011; Haïat *et al*., 2008) and (Molero *et al.,* 2012). In the analytical studies (Haïat *et al.,* 2011; Haïat *et al.,* 2008), multiple and independent scattering theories were presented to derive the frequency dependence of phase velocity. In (Molero *et al.,* 2012) an analytical approximation of the corrected model of (Waterman and Truell, 1961) was presented to conduct phase velocity predictions. In these studies, the theoretical results were found to be in agreement with experimental data in bone mimicking phantom samples

(Wear *et al.,* 2005). However, for increasing scatterers' volume concentrations the theoretical results were found to diverge from the experimental findings.

Another approach based on the self-consistent theories is the iterative effective medium approximation (IEMA) of (Aggelis *et al.,* 2004). Comparisons of the phase velocity and the attenuation coefficient calculated theoretically using IEMA with experimental findings in various nonhomogeneous media have shown the significant efficiency and accuracy of the methodology even in cases of scatterers with volume fractions as high as 50%. It should be mentioned that multiple scattering theories have not been exploited so far to investigate how the porous nature of callus can influence the evolution of scattering effects during bone healing.

This chapter deals with wave scattering phenomena induced by the porous nature of callus. More specifically, ultrasound wave propagation in healing long bones is simulated using IEMA. First IEMA is applied to the cancellous bone mimicking phantoms presented in (Wear *et al.,* 2005), and the results are compared with experimental and theoretical findings (Molero *et al.,* 2012; Haïat *et al.,* 2011; Wear *et al.,* 2005) in order to examine the effectiveness of the methodology. Then, group velocity and attenuation predictions are performed for the callus region of healing bones in the frequency range from 24 – 1200 kHz. The material and geometrical properties of the callus tissue were obtained from a sheep study (Preininger *et al.,* 2011) using SAM images corresponding to different consolidation weeks. Subsequently, 2D healing bone models are presented having the original material properties of callus derived using SAM, and the equivalent homogeneous and isotropic numerical models with the effective material properties derived from IEMA. For comparison purposes FAS velocity measurements and guided wave analysis were performed. Finally, the effective material properties and the attenuation coefficient derived from IEMA are incorporated in BEM computational models of healing long bones representing different healing stages. The propagation of guided waves is investigated in the (t-f) domain.

The novelty of this thesis consists in that (a) multiple scattering theories, although recently incorporated in the ultrasonic evaluation of cancellous bone, have not been used so far in the monitoring of bone healing, (b) this is the first systematic study investigating the evolution of scattering effects in the callus region at different healing stages based on realistic material and geometrical properties derived from SAM

images, and (c) the proposed methodology can contribute to the reduction of the simulation time in complicated geometries through the development of simple, homogeneous and isotropic computational models of healing bones, which however have equivalent geometrical and material properties with the original composite medium.

4.2 Application of an effective medium theory for composite materials and particle suspensions

In this section the IEMA is briefly described which was originally presented in detail in (Aggelis *et al.,* 2004; Verbis *et al.,* 2001). IEMA is used to compare the theoretical wave dispersion and attenuation predictions in cancellous bone mimicking phantoms to those taken either experimentally or theoretically through other multiple scattering theories. According to (Aggelis *et al.,* 2004), IEMA is a single theoretical model that predicts effectively wave dispersion and attenuation in composite materials, suspensions and emulsions through an iterative computational procedure which is simple and easily implemented especially for the case where the material inhomogeneities are considered as spherical inclusions. Moreover, it provides reasonable results for a wide range of particle concentrations and wavenumbers.

The main idea of the method is very simple and it is based on the hypothesis that a plane wave propagating in nonhomogeneous media such as healing bones can be considered as a sum of: a) a mean wave travelling in the medium with the dynamic effective properties of the composite, and b) fluctuating waves derived from the multiple scattering of the mean wave by the material inhomogeneities. Then, at the direction of the propagating plane wave, one can say that the dynamic effective properties of the nonhomogeneous material are those corresponding to a mean wave that propagates without deriving fluctuating waves at the propagation direction. For a composite material with particles embedded in a matrix medium or solid particles suspended in a fluid matrix that idea can be expressed by the self-consistent condition (Kim *et al.,* 1995):

$$n_1 g_{p,s}^{(1)}(\hat{\boldsymbol{k}}) + n_2 g_{p,s}^{(2)}(\hat{\boldsymbol{k}}) = 0\,, \tag{4.1}$$

where n_1, n_2 represent the volume concentration of particles and matrix, respectively, implying that $n_1+n_2=1$, $\hat{\boldsymbol{k}}$ is the direction in which a longitudinal (p) or shear (s) plane

mean wave propagates and $g^{(1)}$, $g^{(2)}$ are the forward scattering amplitudes of the fluctuating waves derived from the solution of the scattering problems 1 and 2, respectively, presented schematically in Fig. 4.1.

Employing the self-consistent condition of Eq. (4.1), the IEMA evaluates the frequency dependent phase velocity and attenuation of a plane wave propagating in the considered composite material or suspension through an iterative procedure described in what follows. First, the composite medium is replaced by an elastic homogeneous and isotropic material with bulk and shear moduli K^{eff} and μ^{eff}, respectively, calculated using the static mixture model of (Christensen 1990) via the equations:

$$K^{eff} = K_2 + \frac{n_1(K_1-K_2)(K_2+\frac{4}{3}\mu_2)}{n_2(K_1-K_2)+(K_2+\frac{4}{3}\mu_2)}, \tag{4.2}$$

$$A(\frac{\mu^{eff}}{\mu_2})^2 + 2B(\frac{\mu^{eff}}{\mu_2}) + C = 0, \tag{4.3}$$

$$\lambda^{eff} = K^{eff} - \frac{2}{3}\mu^{eff}, \tag{4.4}$$

with A, B, C being functions of μ_1, μ_2, n_1 given in (Christensen, 1990), while the indices 1, 2 correspond to the material properties of the inclusion and the matrix, respectively, and λ^{eff}, μ^{eff} stand for the Lamé constants of the composite medium. It should be mentioned here that both λ^{eff}, μ^{eff} are real numbers and remain the same throughout the iterations.

The effective density of the nonhomogeneous medium for the first step of iterations is defined as:

$$(\rho^{eff})_{step1} = n_1\rho_1 + n_2\rho_2 \ . \tag{4.5}$$

Thus, for a longitudinal wave the effective wave number $(k_d^{eff})_{step1}$ is calculated as:

$$(k_p^{eff})_{step1} = \frac{\omega}{C_p^{eff}} = \omega\sqrt{\frac{(\rho^{eff})_{step1}}{\lambda^{eff}+2\mu^{eff}}}, \tag{4.6}$$

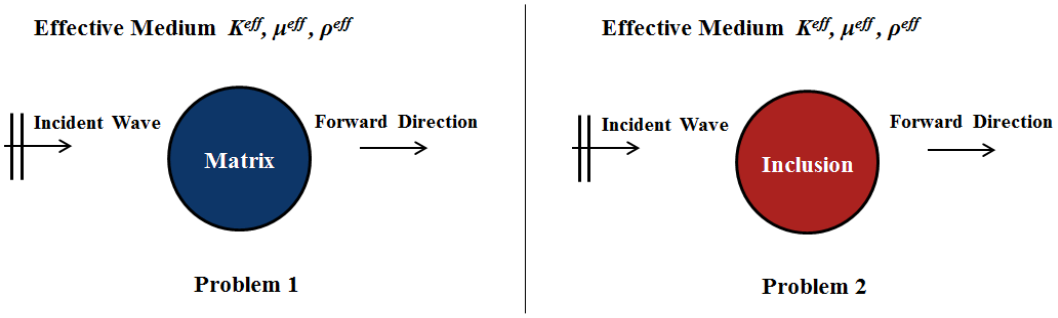

Figure 4.1: A plane mean wave propagating in the effective medium and being scattered by: a) a matrix inclusion (Problem 1), and b) a particle inclusion (Problem 2).

and for a shear wave it is defined as:

$$(k_s^{eff})_{step1} = \frac{\omega}{C_s^{eff}} = \omega\sqrt{\frac{(\rho^{eff})_{step1}}{\mu^{eff}}} \quad . \tag{4.7}$$

Next, utilizing the material properties λ^{eff}, μ^{eff}, $(\rho^{eff})_{step1}$, the forward scattering amplitudes $g^{(1)}, g^{(2)}$ corresponding to the scattering problems 1 and 2 (Fig. 4.1) are evaluated and the validity of the self-consistent relation (4.1) is checked. In case where Eq. (4.1) is not satisfied, the second step should be followed. In that step, the simple dispersion relation is used proposed by (Foldy *et al.,* 1945) so as to define the new effective wavenumber of the mean wave:

$$(k_{p,s}^{eff})_{step2} = (k_{p,s}^{eff})_{step1} + \frac{3n_1 g_{p,s}^{step1}(\hat{\boldsymbol{k}})}{a^3 (k_{p,s}^{eff})_{step1}}, \tag{4.8}$$

where a is the radius of the spherical inclusion and $g_{p,s}^{step1}(\hat{\boldsymbol{k}})$ is defined as:

$$g_{p,s}^{step1}(\hat{\boldsymbol{k}}) = \left[n_1 g_{p,s}^{(1)}(\hat{\boldsymbol{k}}) + n_2 g_{p,s}^{(2)}(\hat{\boldsymbol{k}}) \right]^{step1} . \tag{4.9}$$

Using Eqs. (4.6) or (4.7) and (4.8) the new $(\rho^{eff})_{step2}$ can be calculated which is complex now due to the complex nature of Eq. (4.9). Then, the procedure of the first step is repeated for material properties $\lambda^{eff}, \mu^{eff}, (\rho^{eff})_{step2}$ and the validity of Eq. (4.1) is checked again. Supposing that Eq. (4.1) is satisfied at step *n*, then the phase velocity $C_{p,s}^{eff}(\omega)$ and the attenuation coefficient $\alpha_{p,s}^{eff}(\omega)$ are evaluated through the complex wave number $\left(k_{p,s}^{eff}(\omega)\right)_{stepn}$ with a real part that corresponds to the ratio $\omega / C_{p,s}^{eff}(\omega)$ and an imaginary part that corresponds to the attenuation coefficient:

$$\left(k_{p,s}^{eff}(\omega)\right)_{stepn} = \frac{\omega}{C_{p,s}^{eff}(\omega)} + i\alpha_{p,s}^{eff}(\omega), \tag{4.10}$$

The use of the complex density as the main parameter that controls the iteration procedure was found in (Aggelis *et al.,* 2004) to provide results being in a very good and sometimes in excellent agreement with the available experimental data.

4.2.1 Validation of the IEMA in cancellous bone mimicking phantoms

In (Aggelis *et al.,* 2004; Verbis *et al.,* 2001), multiple scattering problems were studied and the presented methodology was found significantly effective by comparing the theoretical predictions with experimental data in particulate and fiber composites, suspensions of solids in liquids and liquid in liquid emulsion systems. In the present work the results derived from the application of IEMA in cancellous bone phantoms are presented and compared with experimental (Wear *et al.,* 2005) and theoretical findings (Molero *et al.,* 2012; Haïat *et al.,* 2011). Cancellous bone was assumed to be a composite medium in which water was the material of the matrix and nylon the content of the spherical inclusions. The material properties are shown in Table 4.1 (Wear *et al.,* 2005). Two sets of calculations were performed: a) first, the scatterer diameter was set to 254 μm and the volume fraction of nylon to 7.9%. The phase velocity was estimated for frequencies from 0.4 – 0.8 MHz, b) then, applying a constant frequency 500 kHz and a scatterer diameter 254 μm, the scatterers' volume concentration was gradually increased from 1.8 – 11.4% to investigate the phase velocity dependence on the scatterers' volume fraction.

Table 4.1 Material properties of nylon and water.

Cancellous bone composites	**Young's modulus (Gpa)**	**Density (kg/m^3)**	**λ (Gpa)**	**μ (Gpa)**	**Poisson's ratio**
Nylon	4.96	1100	3.72	1.86	0.39
Water	300.50×10^{-9}	1000	2.19	100×10^{-9}	0.50

Figure 4.2 shows the phase velocity estimations derived from IEMA as a function of frequency and inclusions' volume concentration. Experimental findings from (Wear *et al.*, 2005) and theoretical results from (Molero *et al.,* 2012; Haiat *et al.,* 2011) are also depicted for comparison purposes.

In Fig. 4.2a, the phase velocity calculated using IEMA was found to slightly decrease

from 1506 m/s down to 1504 m/s with increasing frequency from 0.4 – 0.8 MHz, exhibiting a negative dispersion. The results are in perfect agreement with experimental findings (the relative errors were found in the range 0.01 – 0.12%). Slight differences exist between the phase velocities derived from IEMA and that of previous theoretical studies. On the other hand, the phase velocity was found to increase from 1485 – 1519 m/s as the inclusions' volume fraction was increasing from 1.8 – 11.4% (Fig. 4.2b). It can be observed that the phase velocities calculated from IEMA are almost identical to the experimental and theoretical ones for low volume concentrations (i.e. up to 3%). For volume concentrations higher than 3% the phase velocity is slightly lower that the experimental observations (the relative errors were found in the range 0.08 – 0.28%).

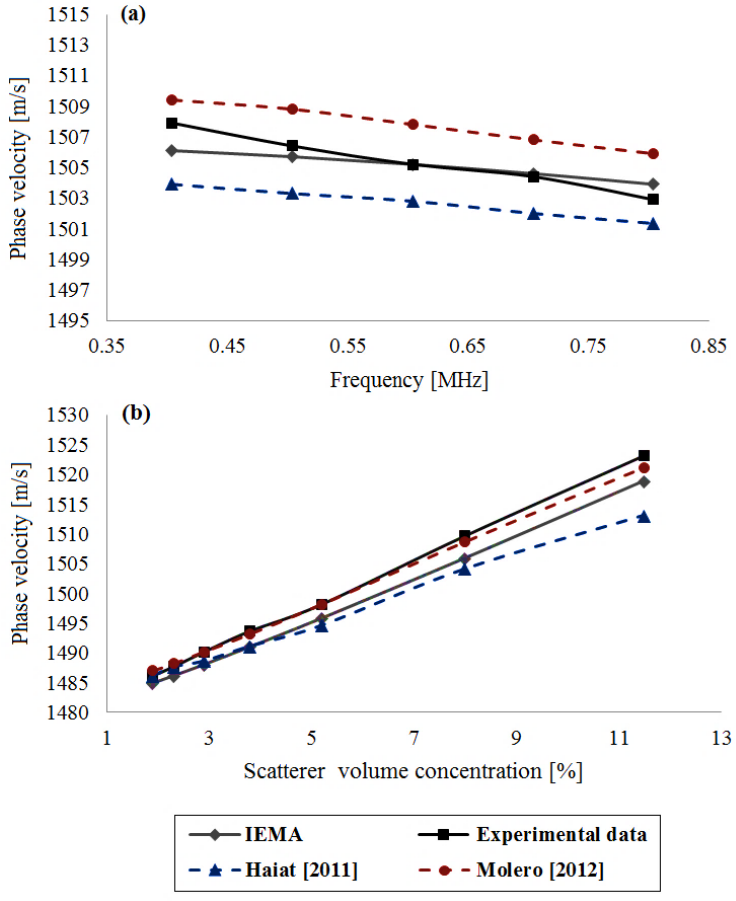

Figure 4.2: Phase velocity dependence on: a) the examined range of frequencies, b) the scatterer volume concentration. Comparison to experimental and theoretical results (Haiat *et al.,* 2011; Molero *et al.,* 2012; Wear *et al.,* 2005).

4.3 Determination of fracture callus wave propagation properties through IEMA

4.3.1 Scanning acoustic microscopy images

The geometry and the material properties of the callus were derived from SAM images representing different healing stages of an animal study. SAM is a micro elastic imaging technique that has been extensively used to investigate the microstructural and elastic alterations of mineralized callus and cortical tissues (Preininger *et al.,* 2011; Raum *et al.,* 2006). The acoustic impedance images of embedded longitudinal sections of 3-mm osteotomies in the right tibia of female Merino sheep were obtained from a previous study (Preininger *et al.,* 2011). All specimens were subjected to SAM measurements, using a spherically focused 50 MHz transducer with spatial resolution 23 μm and scan increment 16 μm. Each SAM image corresponds to a representative healing stage after 3, 6 and 9 weeks of consolidation (Fig. 4.3). The original material properties of the mineralized callus tissue were directly transferred from the SAM images into the IEMA procedure in order to investigate the evolution of the scattering effects during the healing process.

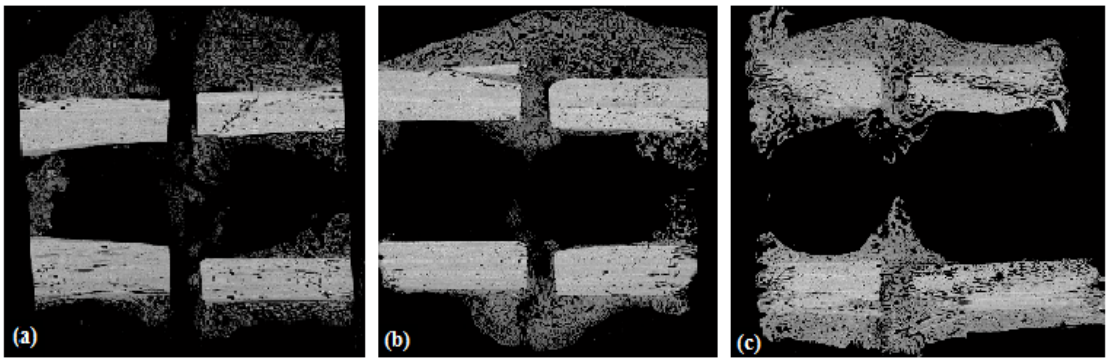

Figure 4.3: Scanning acoustic microscopy images representing the: (a) third, (b) sixth and (c) ninth postoperative week.

4.3.2 Material properties

The material properties of each pixel composing the cortical and callus tissues in Fig. 4.3 were derived using empirical equations. The density ρ was calculated via the equation (Raum *et al.,* 2011):

$$Z=1.02\rho^{2.83}, \tag{4.11}$$

where Z is the acoustic impedance.

Next, the elastic constant in the axial direction c_{33} was determined as (Preininger et al. 2011):

$$c_{33}=2.75\cdot\rho^{3.99}\cdot \tag{4.12}$$

The Young modulus E was finally defined as:

$$E=\frac{(1+\nu)(1-2\nu)}{(1-\nu)}c_{33}\ , \tag{4.13}$$

where ν denotes the Poisson's ratio and was set to 0.3.

4.3.3 Wave dispersion and attenuation coefficient predictions using IEMA

Tables 4.2 – 4.3 present the average material properties of cortical bone and callus derived from Eqs. (4.11), (4.12), (4.13), while Table 4.4 presents the callus effective material properties calculated using IEMA. Callus was assumed to be a composite medium consisting of a matrix with circular inclusions. In week 3, blood was considered as the matrix of the medium and osseous tissue as the material of the spherical scatterers. The opposite assumption was made in weeks 6 and 9 since at later healing stages the presence of osseous tissues is dominant in the callus region. Blood was assumed to have Young's modulus E_{blood} = 3 MPa, density ρ_{blood} = 1055 kg/m^3 and Poisson's ratio ν_{blood} = 0.49979 (Vavva *et al.,* 2008a).

Table 4.2 Average cortical bone material properties calculated using SAM images.

Healing stage	Young's modulus (GPa)	Density (kg/m^3)	λ (GPa)	μ (GPa)
Week 3	29.1	2001	16.8	11.2
Week 6	32.7	2039	18.8	12.6
Week 9	30.3	2016	17.5	11.7

Table 4.3 Average callus material properties calculated using SAM images.

Healing stage	Young's modulus (GPa)	Density (kg/m^3)	λ (GPa)	μ (GPa)
Week 3	13.6	1425	7.9	5.2
Week 6	17.1	1729	9.9	6.6
Week 9	21.1	1881	12.2	8.1

Table 4.4 Callus effective material properties calculated using IEMA.

Healing stage	Young's modulus (GPa)	λ (GPa)	μ (GPa)	Poisson's ratio	Density (kg/m^3) - 300 kHz	Density (kg/m^3) - 500 kHz	Density (kg/m^3) - 1000 kHz
Week 3	$1.9*10^{-6}$	3.8	$645.7*10^{-9}$	0.50	1131.9	1444.4	1201.0
Week 6	7.5	6.2	2.8	0.35	1803.8	1815.5	1867.0
Week 9	13.5	9.0	5.1	0.32	1871.6	1873.3	1880.8

Group velocity and attenuation coefficient estimations were performed in the frequency range 24 – 1200 kHz. The average scatterers' diameter and volume concentration introduced in the iteration procedure were derived from multiple sampling measurements in the callus region of the SAM images as: a) 350 μm and 44.8% in week 3, b) 200 μm and 38.7% in week 6, and c) 120 μm and 22.7% in week 9, respectively.

Figure 4.4 shows the group velocity and the attenuation coefficient predictions derived from IEMA for the callus tissue at different healing stages in the frequency range 24 – 1200 kHz. In Fig. 4.4a, it can be observed that the group velocity decreases: a) from 1826 – 1609 m/s in week 3, b) from 2555 – 2403 m/s in week 6, and c) from 3202 – 3167 m/s in week 9, exhibiting a negative dispersion. In Fig. 4.4b the attenuation coefficient was found to increase exponentially in the examined frequency range: a) from 0.06 – 76.36 m^{-1} in week 3, b) from 0 – 51.86 m^{-1} in week 6, and c) from 0 – 1.91 m^{-1} in week 9.

4.4 Numerical simulations of wave propagation in healing bones using IEMA

In this section numerical simulations of wave propagation in healing long bones are presented. First, 2D healing bone models are developed with original material properties derived from the callus segments of Figs. 4.5b, 4.5c, and then the equivalent homogeneous and isotropic numerical models are constructed with the effective material properties calculated from IEMA. The effectiveness of IEMA as a homogenization method is investigated numerically by conducting FAS velocity measurements and guided wave analysis. Secondly, the effective material properties and the attenuation coefficient derived from IEMA are incorporated in BEM computational models of healing long bones corresponding to the third, sixth and ninth week of consolidation. The dispersion of guided waves is investigated in the

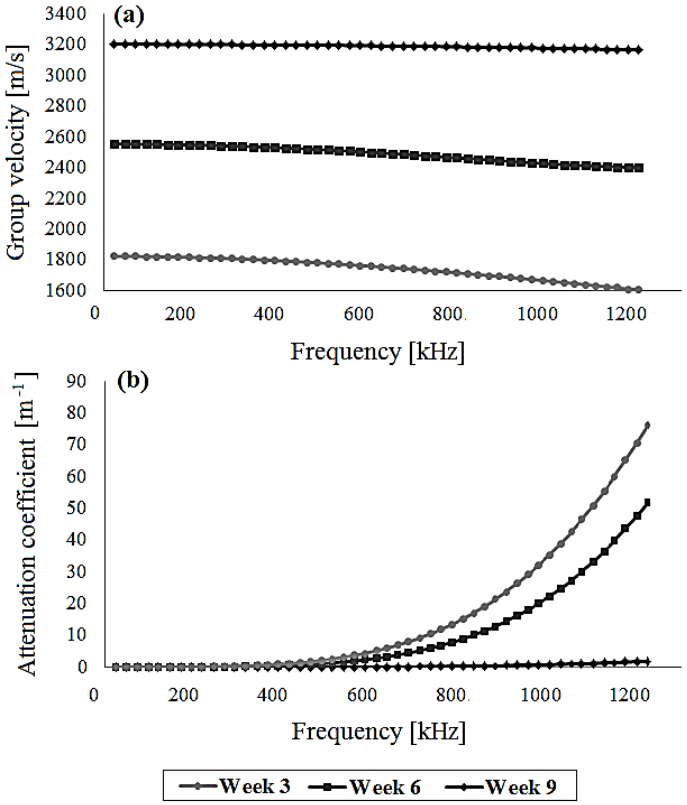

Figure 4.4. IEMA Estimation of the a) group velocity, and b) the attenuation coefficient for each healing week in the frequency range 24 – 1200 kHz.

(t-f) domain.

4.4.1 Ultrasound excitation

The numerical solution of the 2D wave propagation problem was performed by using the BEM based on the software package ISoBEM. A Hanning sine pulse was used as the excitation signal expressed by the equation:

$$p(t)=\begin{cases}\frac{A}{2}[1-\cos(2\pi ft/n)]\cos(2\pi ft), & \forall t\leq {}^{n}\!/_{f}\\ 0, & \forall t> {}^{n}\!/_{f}\end{cases}, \tag{4.14}$$

where A=1 MPa is the amplitude of the excitation pulse, f is the central angular frequency and n is the number of the sinusoidal cycles in the pulse. The examined central angular frequencies were 300 kHz, 500 kHz and 1 MHz, while the excitation signal included four sinusoidal cycles in the pulse. The duration of the simulated signals recording was 40 μs. The accuracy of the solution depends on the relation between the element size and the wavelength. In this respect, at least four three-noded quadratic line elements were used per smallest wavelength.

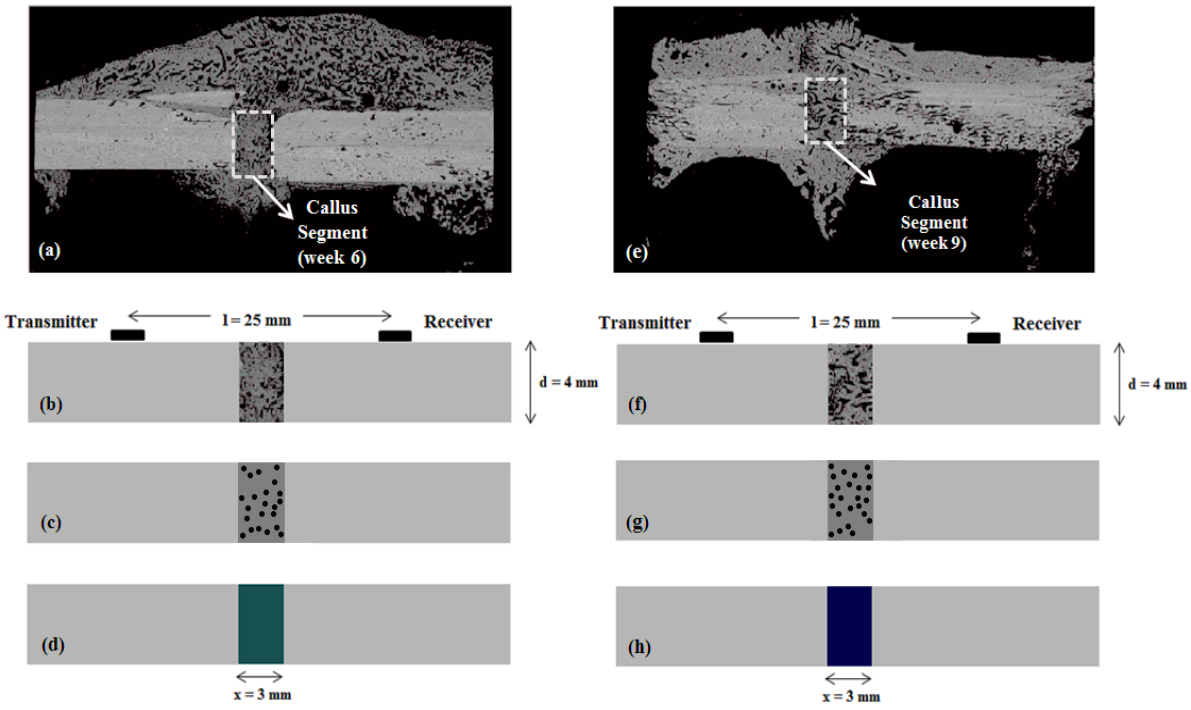

Figure 4.5: a) Segment of the callus derived from the SAM image at week 6, b) simulated geometry corresponding to week 6, c) callus was modeled as a nonhomogeneous medium including a random distribution of circular inclusions, d) callus was modeled as a homogeneous and isotropic medium having the effective material properties calculated using IEMA, and e-h) represent the corresponding cases for week 9.

4.4.2 Representation of Lamb waves in the time-frequency domain

Time-frequency analysis was conducted in order to represent the propagating wave modes. The reassigned smoothed-pseudo Wigner-Ville (RSPWV) distribution function was used as it was found to be effective in representing and isolating guided modes (Protopappas *et al.,* 2006a). Frequency-group velocity (f-c_g) dispersion curves were computed for the plate model based on the Lamb wave theory. Plate thickness was set to 4 mm, which is an average value of multiple, random measurements on the upper and lower cortical bone segments of the SAM images. The (f-c_g) dispersion curves were superimposed to the (t-f) representations in order to investigate guided wave propagation. Compared to other techniques (Moilanen *et al.,* 2003; Nicholson *et al.,* 2002; Bossy *et al.,* 2002) the main advantage the proposed analysis is that a single broadband excitation is needed to represent the dispersion of multiple wave modes. In Fig. 4.6, analytically derived Lamb dispersion curves of symmetric and antisymmetric modes are illustrated.

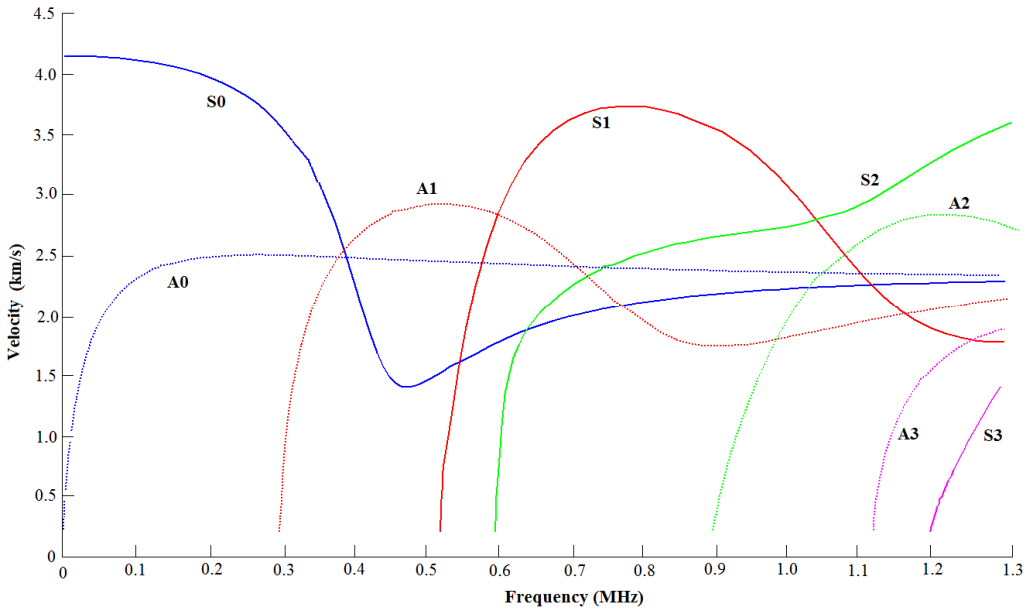

Figure 4.6: Group velocity dispersion curves of the Lamb modes for a free plate. The solid lines correspond to the symmetric modes, while the dashed lines to the anti-symmetric modes. The bulk longitudinal and shear velocity in the plate are 4500 m/s and 2405 m/s, respectively, and the plate thickness is 4 mm.

4.4.3 Estimation of the first arriving signal

Axial-transmission measurements were performed by keeping constant the center-to-center distance between the transducers to 25 mm. The transducers' size was set to 3 mm and they were placed equidistantly from the osteotomy gap directly onto the cortical bone surface. The ultrasound propagation velocity was determined by dividing the transducers' in-between distance to the transition time of the FAS. In order to detect the FAS in the receiving signal a threshold was used, corresponding to 10% of the amplitude of the first signal extremum.

4.4.4 Numerical simulations in cortical bone and callus with effective properties

In this section, two sets of simulations of wave propagation in healing bone models were conducted to investigate whether IEMA could be used as a numerical tool of modeling media with a complicated porous nature and provide supplementary information for the status of bone healing.

The callus segments of Figs. 4.5a, e (length = 3 mm and width = 4 mm) were incorporated in two simple computational cortical bone geometries. In the first case, callus was modeled as a nonhomogeneous medium including circular scatterers (Figs.

4.5c, g) and the original material properties were derived from the SAM images. Osseous tissue was considered as the matrix of the composite and blood as the material of the circular inclusions. Blood volume concentrations were measured 25.78% (corresponding to 22 spheres) and 28.68% (corresponding to 24 spheres) in the callus segments of Figs. 4.5b, c and Figs. 4.5f, g respectively, while the radius of the scatterer was set to 200 μm. In the second case (Figs. 4.5d, h), the complex callus regions were replaced by a homogeneous and isotropic medium having the effective material properties calculated using IEMA. The material properties of cortical bone were derived from Table 4.2 and correspond to the ninth postoperative week. Table 4.5 presents the average material properties of the callus segments in Figs. 4.5a and 4.5d calculated through the Eqs. (4.10), (4.11), (4.12), as well as the effective material properties derived using IEMA for the excitation frequency of 300 kHz.

Axial transmission measurements of the FAS velocity were conducted for the excitation frequency of 300 kHz and thereafter guided wave analysis was performed. Concerning the computational models of Figs. 4.5c, d the FAS velocity was calculated as 3928 m/s, while for the computational models of Figs. 4.5g, h the FAS velocity was 3985 m/s.

Table 4.5 Material properties of the callus segment of Figs. 4.5c, d and Figs. 4.5g, h.

	Original callus properties (Frequency Independent)	Effective callus properties 300 kHz	Original callus properties (Frequency Independent)	Effective callus properties 300kHz
	Week 6		Week 9	
Young's modulus (GPa)	16.5	9.8	21.0	11.7
λ (GPa)	9.5	7.0	12.1	8.2
μ (GPa)	6.3	3.7	8.1	4.4
Poisson's ratio	0.30	0.33	0.30	0.33
Density (kg/m^3)	1770	1557	1882	1630
Attenuation coefficient (m^{-1})	(-)	101	(-)	118

Figure 4.7 shows the (t-f) representations corresponding to the Figs. 4.5c, d and 4.5g, h. The A1 mode was identified in all the examined cases. The (t-f) representations are significantly attenuated (Figs. 4.7b, d) when IEMA is used in comparison to the

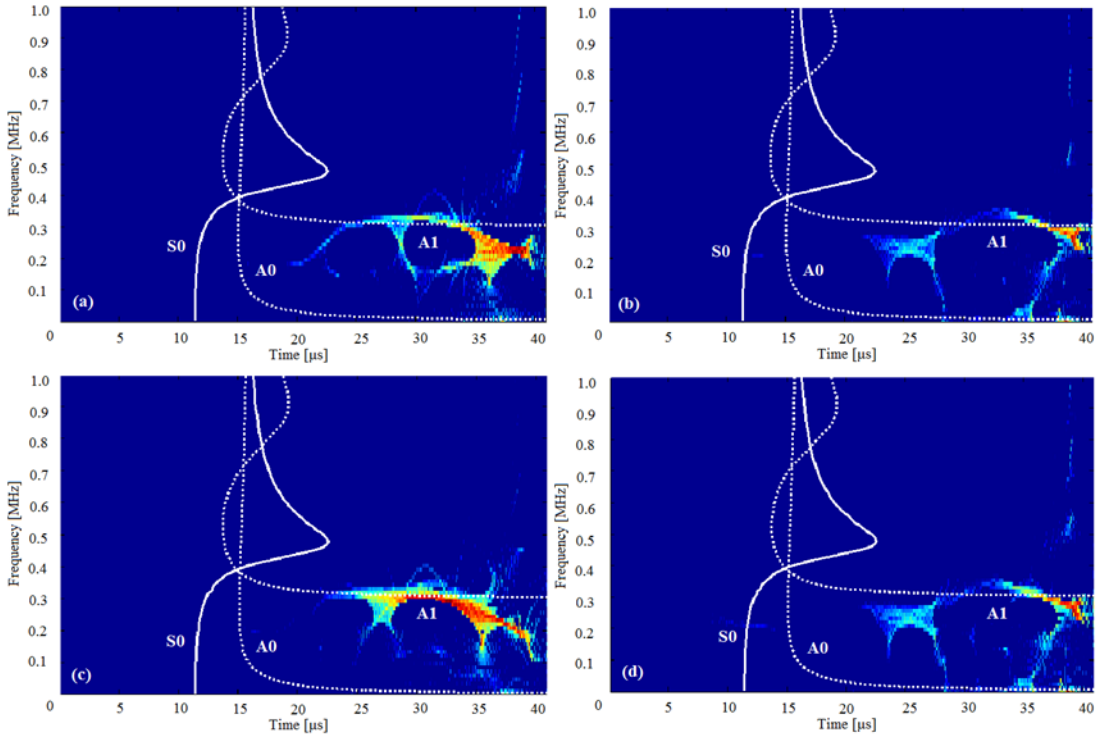

Figure 4.7: The RSPWV distributions for the excitation frequency of 300 kHz of the signals obtained: a, c) when the callus has the original material properties (a: week 6, c: week 9), and b, d) from the equivalent homogeneous medium having the effective material properties derived from IEMA (b: week 6, d: week 9).

original signal (Figs. 4.7a, c). Moreover, the (t-f) diagrams for the two homogenized models of week 6 and week 9 are similar (Figs. 4.7b, d).

4.4.5 Simulations in different healing stages

2D computational models of healing long bones were developed corresponding to the third, sixth and ninth postoperative week (Fig. 4.8). The complex callus region was replaced by a homogeneous and isotropic medium having the effective material properties derived from IEMA (Tables 4.4, 4.6, 4.7). An intact bone model was also developed having the material properties of the cortical bone in week 9 (Table 4.2). The guided mode features derived from the osteotomy numerical models were compared to the intact bone estimations.

The (t-f) representations of the signals obtained from the intact bone model and the osteotomy bone models after three, six and nine weeks of consolidation are illustrated in Figs. 4.9 – 4.11.

Table 4.6 Callus effective density for the examined central frequencies.

Healing stage	Density (kg/m^3)		
	300 kHz	500 kHz	1000 kHz
Week 3	1132	1144	1201
Week 6	1804	1816	1867
Week 9	1872	1873	1881

Table 4.7 Callus attenuation coefficient for the examined central frequencies.

Healing stage	Attenuation coefficient (m^{-1})		
	300 kHz	500 kHz	1000 kHz
Week 3	0.39	2.55	37.73
Week 6	0.17	1.34	23.93
Week 9	0.0073	0.06	0.92

The (t-f) representations are depicted in the form of pseudo-color 2D images, where the color of a point corresponds to the amplitude (in dB) of the energy distribution. At each healing stage the (f-c_g) dispersion curves of Fig. 4.6 were superimposed to the (t-f) representations to investigate the propagation of guided waves during bone healing. Figures 4.9a, 4.10a, 4.11a correspond to the intact bone model, Figs. 4.9b, 4.10b, 4.11b represent week 3, Figs. 4.9c, 4.10c, 4.11c represent week 6, and Figs. 4.9d, 4.10d, 4.11d correspond to week 9.

For the excitation frequency of 300 kHz (Figs. 4.9a – d) the S0 and A0 modes were found to be the dominant modes, while the A1 mode was also identified. In particular, for the intact bone model the S0 and A0 modes were detected in the frequency ranges 0.28 – 0.42 MHz and 0.19 – 0.38 MHz. In week 3 the S0 mode was detected from 0.20 – 0.42 MHz. In weeks 6 and 9 the S0 and A0 were the dominant modes in the frequency ranges 0.28 – 0.38 MHz, 0.21 – 0.38 MHz and 0.31 – 0.38 MHz, 0.21 – 0.38 MHz, respectively. In week 9 the A1 was also identified from 0.30 – 0.38 MHz. The significant restoration of the dominant modes during the final healing stages is shown in Figs. 4.9 c, d approaching the intact bone observations (Fig. 4.9a).

For 500 kHz (Figs. 4.10a – d), the dominant modes were S0 and S1 during the whole healing process, while the mode A1 was also detected in weeks 6 and 9. Specifically, for the intact bone model the S0 and S1 modes were detected for frequencies from

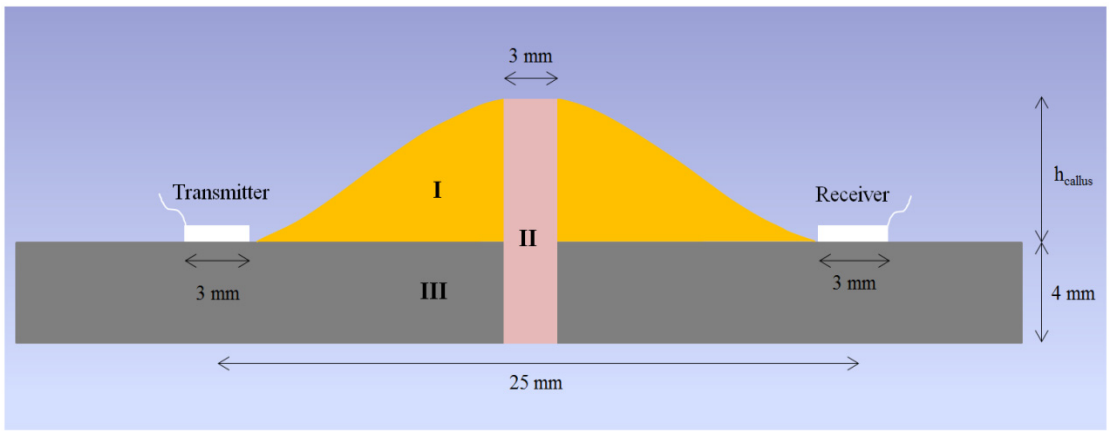

Figure 4.8: A generic model of callus in which regions I-II have the effective material properties derived from IEMA and differ according to the examined healing stage. Regions I, II, III represent callus, blood and cortical bone, respectively. Specifically: a) week 3 includes regions I, II, III and h_{callus} was 6 mm, b) week 6 includes regions I, III and h_{callus} was 5 mm (region II is incorporated in region I) , and c) week 9 includes the same regions with week 6 and h_{callus} was 3 mm.

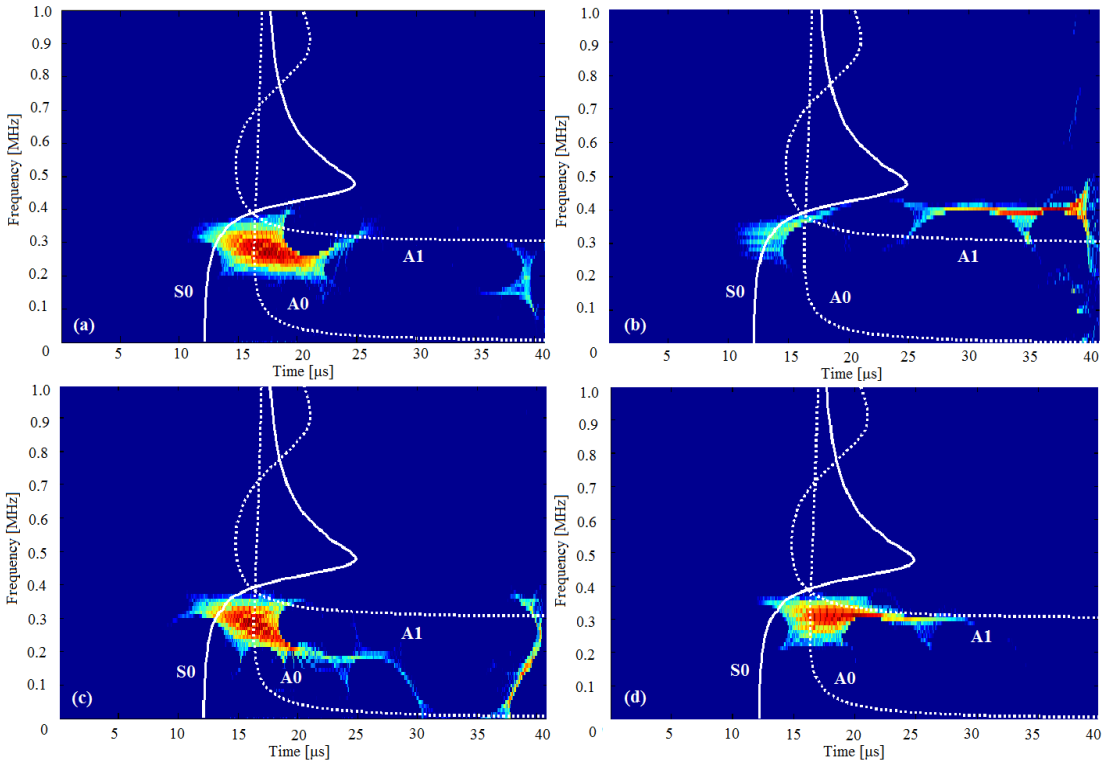

Figure 4.9: The RSPWV distribution for the excitation frequency of 300 kHz of the signals obtained from: a) the intact bone, b) week 3, c) week 6, and d) week 9 after the osteotomy.

0.43 – 0.66 MHz and 0.52 – 0.56 MHz, respectively.

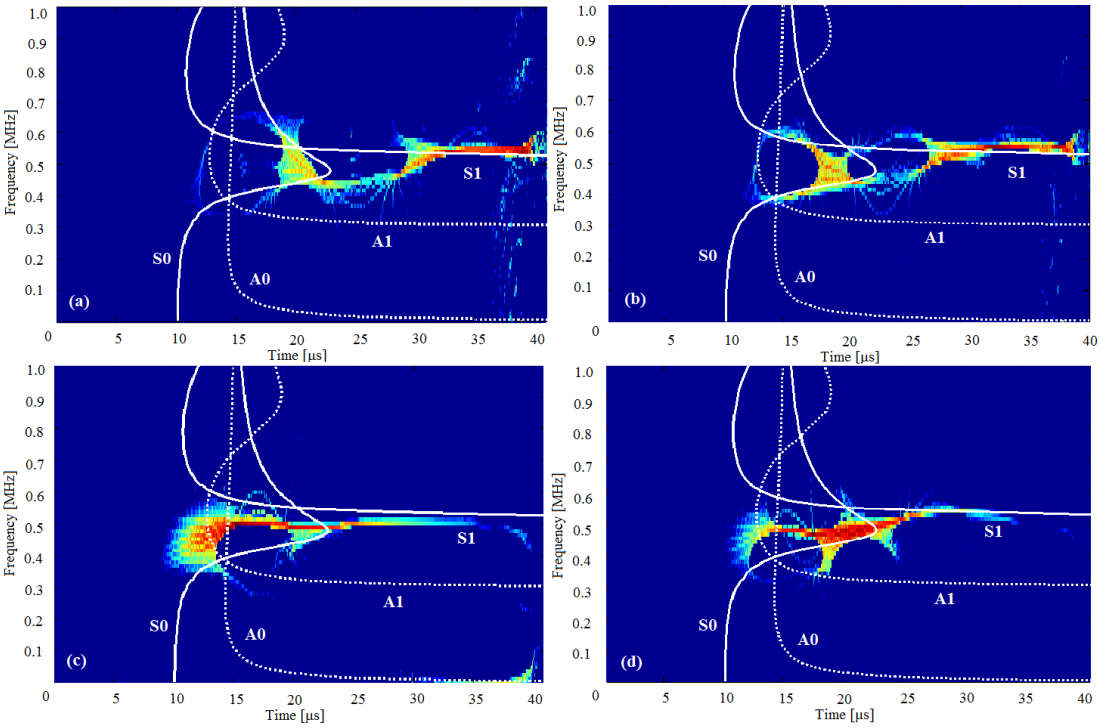

Figure 4.10: The RSPWV distribution for the excitation frequency of 500 kHz of the signals obtained from: a) the intact bone, b) week 3, c) week 6, and d) week 9 after the osteotomy.

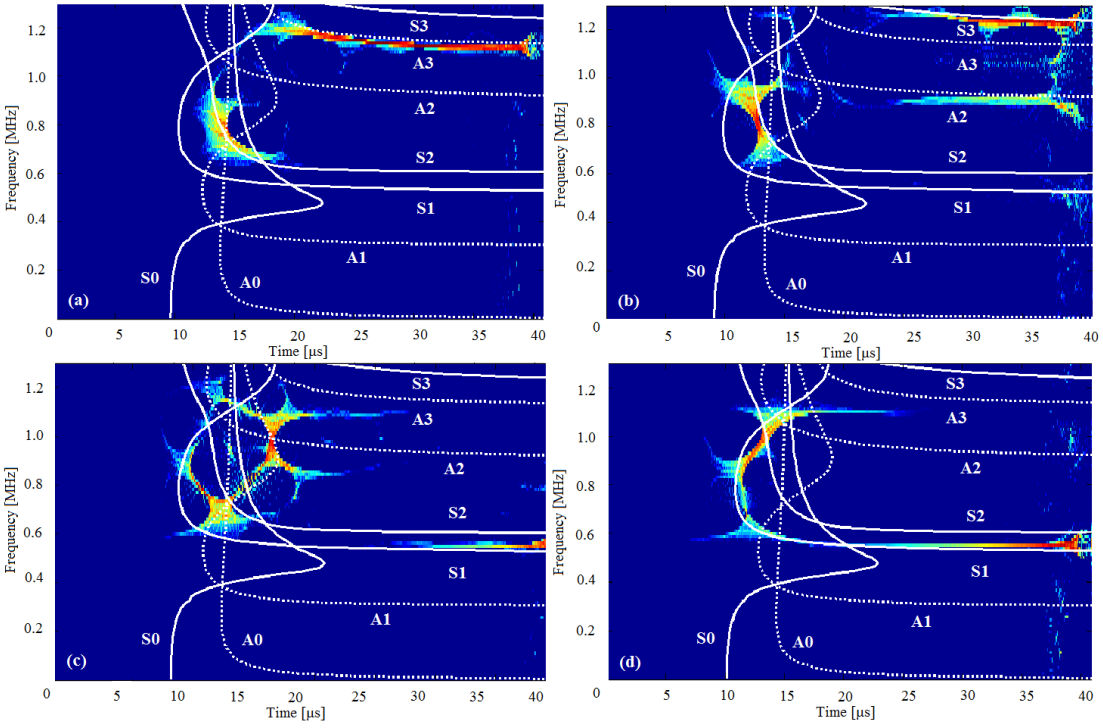

Figure 4.11: The RSPWV distribution for the excitation frequency of 1 MHz of the signals obtained from: a) the intact bone, b) week 3, c) week 6, and d) week 9 after the osteotomy.

In week 3 the S0 and S1 modes were identified in the frequency ranges 0.38 – 0.55 MHz and 0.52 – 0.59 MHz, respectively. In week 6 the S0 modes is identified for frequencies from 0.34 – 0.51 MHz, while in week 9 the modes S0 and S1 were mainly detected in the frequency ranges 0.42 – 0.55 MHz and 0.52 – 0.55 MHz, respectively, showing a significant restoration in comparison to the intact bone model.

Finally, some high-frequency modes were also supported when the central frequency of 1 MHz was applied (Figs. 4.11 a-d). The dominant modes were S1 and S2. Concerning the intact bone model, the modes S1, S2 and A3 were identified in the frequency ranges 1.10 – 1.20 MHz, 0.62 – 1.00 MHz, 0.65 – 0.92 MHz, and 1.10 – 1.20, respectively. In week 3 the modes S2, S3 and A2 were detected for frequencies between 0.68 – 0.97 MHz, 1.20 – 1.30 MHz, and 0.92 – 0.93 MHz, respectively. In week 6, the S1 and A1 were the dominant modes in the frequency ranges 0.53 – 1.14 MHz, 0.60 – 1.13 MHz, respectively, while the S2 mode was also detected from 0.65 – 0.76 MHz. Finally, in week 9 the S1 mode was clearly observed in the frequency range 0.51 – 1.11 MHz, while the S2 mode is also detected between 0.92 – 1.12 MHz.

4.5 Numerical evaluation of the effect of callus porosity and pores' size on the FAS velocity

This section presents computational models of a healing bone corresponding to a late healing stage to investigate the influence of different pores' sizes and concentrations in the callus tissue on ultrasound propagation. Calculations of the FAS velocity are performed for different excitation frequencies and the impact of callus and cortical porosity on the FAS wave is examined.

4.5.1 Model geometry

The geometry and the material properties of the computational models were derived from (Potsika *et al.,* 2014a) and correspond to a healing bone at the ninth week of consolidation. The cortical bone thickness was 4 mm and the callus region 3 mm. Callus was considered as a composite medium consisted of a matrix material including circular blood scatterers. The scatterers were randomly distributed in the callus region. Two series of calculations were performed. In the 1st series (Fig. 4.12a), cortical bone was considered as a compact medium and five cases were examined for different callus porosity distributions : i) callus porosity 0% (Problem I),

ii) callus porosity 22.70%, pores' diameter 120 μm (Problem II), iii) callus porosity 22.70 %, pores' diameter 240 μm (Problem III), iv) callus porosity 11.35%, pores' diameter 120 μm (Problem IV), v) callus porosity 11.35 %, pores' diameter 240 μm (Problem V). In the 2nd series (Fig. 4.12b), the callus region was ignored and the whole region of cortical plate was considered as a composite medium with blood scatterers with: i) porosity 11.35%, pores' diameter 120 μm (Problem VI), ii) porosity 11.35%, pores' diameter 240 μm (Problem VII). This series was included in this study aiming to analyze the influence of pores' size alone on the characteristics of wave propagation. The case of intact homogeneous bone was also considered. Table I summarizes the material properties assigned to cortical bone, callus and blood.

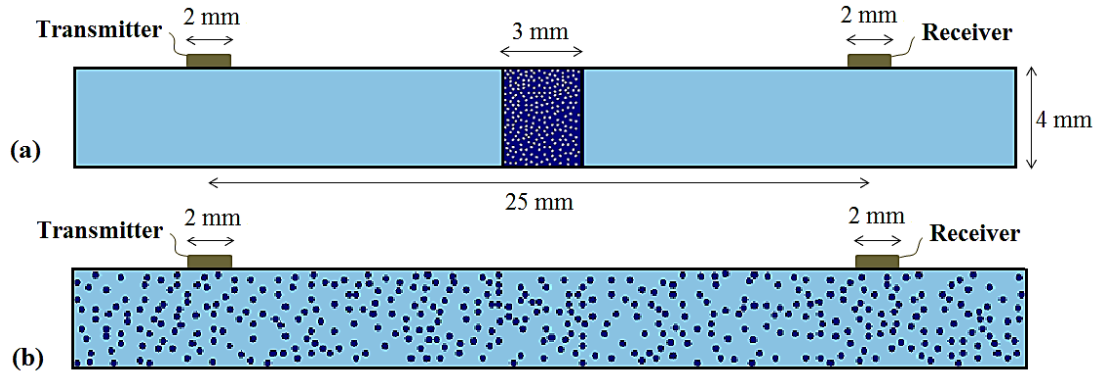

Figure 4.12: Ultrasound configuration for: a) the 1st series of calculations (Problem II), b) the 2nd series of calculations (Problem VII).

Table 4.8 Material properties of bone, callus and blood.

	Bone	Callus	Blood
ρ (kg/m^3)	2016.2	1881.1	1055.0
E (GPa)	30.3	21.1	3x10^{-3}
λ (GPa)	17.5	12.2	2.6
μ (GPa)	11.7	8.1	0

4.5.2 Ultrasound configuration

Concerning Problems I-V, axial-transmission calculations were performed by placing one transmitter and one receiver on each side of the fracture gap directly onto the cortical bone surface. The transducers' size was set to 2 mm, their center-to-center distance was 25 mm and they operated in the longitudinal mode. The same configuration was used for Problems VI-VII. Fig. 4.12 presents the ultrasound configuration for the two series of calculations. Absorption elements were considered

at the ends of cortical bone to simulate an infinitely long plate and neglect reflection from the boundaries.

4.5.3 Numerical simulations and signal analysis in the time domain

The numerical solution of the 2D wave propagation problem was carried out using the Finite Element Method (FEM). In order to describe the propagation of ultrasonic waves in plates, a model of forced vibration was used:

$$[M]\{\ddot{u}\}+[D]\{\dot{u}\}+[K]\{u\}=\{P(t)\}, \quad (4.15)$$

where $[M]$ is the mass matrix, $[D]$ is the damping matrix, $[K]$ is the stiffness matrix, $\{\ddot{u}\}$ is the acceleration vector, $\{\dot{u}\}$ is the velocity vector, $\{u\}$ is the nodal displacement vector of the particles and $\{P(t)\}$ is the vector of the excitation force (Potsika *et al.*, 2014c; Courant *et al.,* 1928).

A triangular element type was selected to achieve a reasonable time and memory cost, and the element size was set to $l < \lambda/10$, in which λ is the wavelength. Also, 512 equal timesteps were applied according to the criterion: $\Delta t \leq 1/(10\times f)$, in which f denotes the central frequency. These restrictions were applied to acquire a stable analysis, conformed to the Courant–Friedrichs–Lewy condition.

A Hanning sine pulse was used as the excitation signal according to Eq. (4.14). The examined central frequencies were 0.3, 0.5 and 1 MHz for the 1st series of calculations and the excitation signal included four sinusoidal cycles in the pulse. The same central frequencies were also examined in the 2nd series of calculations. The duration of the simulated signals recording was 30 μs. In order to detect the FAS a threshold was used, corresponding to the detection of the first signal extremum.

4.5.4 Results

Fig. 4.13 presents the FAS velocity values for the 1st series of calculations. It can be seen that the highest FAS velocity measurements were calculated for Problem I corresponding to the case of a homogeneous callus region. On the other hand, the lowest FAS velocity values were measured for Problems II and III corresponding to the highest porosity concentrations. It is also shown that the velocity values computed for Problems II and III, as well as for problems IV and V approximately coincide.

Concerning the frequency dependence of ultrasound propagation, the lowest FAS velocity values were calculated for the central frequency of 0.3 MHz, while the highest values were observed for 1 MHz. Particularly, the FAS velocities were in the range : i) 2884 – 2944 m/s for 0.3 MHz, ii) 3227 – 3308 m/s for 0.5 MHz, and iii) 3547 – 3634 m/s for 1 MHz. The FAS values associated with numerical models of fractured long bones were lower in comparison to the case of intact bone.

In the 2nd series of calculations, the FAS velocity was: a) 2777 m/s for Problem VI and 2701 m/s for Problem VII for the excitation frequency 0.3 MHz, and b) 3035 m/s for Problem VI and 3004 m/s for Problem VII for excitation frequency 0.5 MHz. These problems revealed an about 10% FAS velocity decrease compared to the corresponding cases of intact bone for the same frequency, whereas the change of the scatterer's radius had an influence less than 2%.

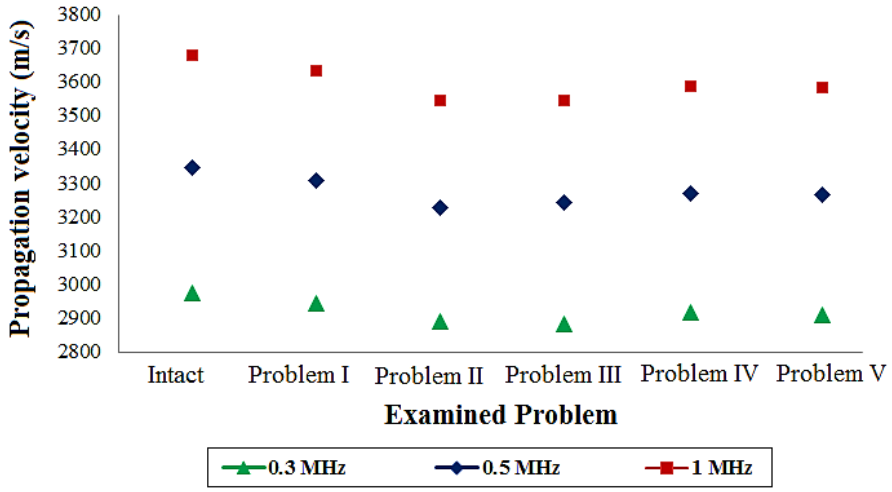

Figure 4.13: FAS velocity calculations for different callus porosity distributions and frequencies.

4.6 Discussion

In this chapter, a theoretical and computational study was presented based on an effective medium theory application for the modeling of ultrasound wave propagation in healing long bones. Numerical models of healing long bones were developed with material and geometrical properties derived from SAM images. For the first time wave dispersion and attenuation predictions were conducted in the callus tissue at different healing stages using IEMA. Moreover, 2D BEM simulations of bone healing were carried out and the porous nature of callus was taken into consideration in the

solution of the wave propagation problem. The proposed methodology is of great importance as the estimation of wave dispersion and attenuation using IEMA could provide valuable information for the callus restoration during the healing process.

The effectiveness of the iterative procedure was examined by comparing the predictions of IEMA with experimental and other theoretical findings in trabecular bone mimicking phantoms. It was shown that the phase velocity decreases when the frequency increases exhibiting, thus, a negative dispersion. However, when the Kramers-Kronig relations are used to estimate the dispersion of a medium with an increasing attenuation coefficient, the expected result is a phase velocity which increases logarithmically with frequency, known as positive dispersion (Anderson *et al,.* 2008; Marutyan *et al.,* 2006; Waters *et al.,* 2005). Nevertheless, a negative dispersion has been also reported in various experimental and numerical studies investigating wave dispersion in cancellous bone (Molero *et al.,* 2012; Bauer *et al.,* 2008; Anderson *et al.*, 2008; Haiat *et al.,* 2008; Wear *et al.,* 2005). According to (Marutyan *et al.,* 2006), the apparent negative dispersion of ultrasonic waves propagating in bone can arise from the interference between fast and slow longitudinal modes, each exhibiting positive dispersion. The results of IEMA were in excellent consistency with the observations of (Molero *et al.,* 2012; Haiat *et al.,* 2008; Wear *et al.,* 2005). Apart from the findings of this thesis for bone assessment, IEMA has been also found effective in various scattering problems presented in (Aggelis *et al.,* 2004). Therefore, this is considered as an accurate methodology which models effectively the actual physics of a composite medium.

Wave dispersion and attenuation predictions were conducted for the first time in the callus region at successive healing stages. A negative dispersion was exhibited in all the examined cases in the frequency range 24 – 1200 kHz. The present method is an analytical low frequency approach for solving scattering problems since the product of the wavenumber and the scatterer's radius was found lower than 1 ($ka<<1$) for all the examined cases, implying that the wavelength is much larger than the heterogeneity size ($\lambda>>2\pi a$). However, the role of the wavelength to the heterogeneity size regarding the relationship with the negative dispersion needs further parametrical research. Also, it was observed that the calculated values of both the attenuation coefficient and the group velocity corresponding to week 9 vary slightly with increasing frequency in comparison to weeks 3 and 6. This could be attributed to the

consolidation of the osseous tissue at the final healing stages, followed by a gradual decrease of the inclusions' volume concentration and diameter. Thus, the role of scattering, material dispersion and absorption phenomena is more significant during the early healing stages enhancing wave dispersion and attenuation estimations.

The effectiveness of the methodology predictions in bone healing was investigated by developing two types of 2D numerical healing bone models: a) with the original material properties of the callus derived from SAM images, b) with the equivalent homogeneous and isotropic callus geometries having the effective material properties derived from IEMA. The same FAS velocity values were calculated for the original and the equivalent effective homogeneous geometries based on IEMA showing the significant accuracy of the methodology. However, the (t-f) analysis indicated that IEMA cannot capture wave dispersion but rather some of the dominant modes in spite of the significant attenuation of the signal. The ability of IEMA to replace composite media with equivalent homogeneous and isotropic media could provide an alternative, simple and effective solution for guided mode characterization in complicated problems.

Further to this benchmark analysis, ultrasound propagation during bone healing was simulated by incorporating the effective material properties and the attenuation coefficient derived from IEMA in 2D boundary element computational models of healing long bones. In comparison to previous computational studies (Machado *et al.,* 2010; Vavva *et al.*, 2008a; Protopappas *et al.*, 2006a), more realistic conditions are applied based on SAM images. In addition, the porous nature of callus was taken into consideration through its numerical modeling by using the effective material properties derived from IEMA. Guided wave propagation was studied, which depends on both the geometrical and material properties of bone. For all the examined frequencies, the restoration of the dominant modes was apparent in weeks 6 and 9 compared to the estimations of intact bone, while in week 3 guided mode features were different especially for the frequencies of 0.3 MHz and 1 MHz. This could be attributed to the gradual restoration of bone material and geometrical properties at the final healing stages approaching the structural integrity of intact bone. For the excitation frequency of 0.3 MHz, the S0 and A0 modes were mainly identifiable. Previous studies using low-frequency transducers (at 0.1 and 0.25 MHz) have also examined the evolution of the S0 and A0 modes (Moilanen *et al.,* 2003; Nicholson *et*

al., 2002; Bossy *et al.,* 2002). For the excitation frequency of 0.5 MHz the dominant modes were S0 and S1, while for the excitation frequency of 1 MHz the modes S1 and S2 were mainly detected. The results derived from the homogenized models using IEMA showed similar trends in guided mode features as in previous research findings in bone healing (Vavva *et al.,* 2008a; Protopappas *et al.,* 2006a). An experimental validation of the model behavior was not performed, although the effectiveness of the present methodology for bone characterization was verified both theoretically and numerically. Nevertheless, experimental validation of the model behavior will be performed in future studies.

In addition to the numerical simulations of section 4.4, a parametric study was presented in section 4.5 to investigate the influence of the callus pores' size and concentration on the propagation of ultrasonic waves in a healing long bone. A simple 2D geometry was developed in which callus was considered as a composite medium consisted of a matrix with circular scatterers. Compared to the approximation followed in section 4.4, the callus region was not replaced by a homogeneous region with effective material properties using IEMA, while the influence of cortical porosity on wave propagation was also investigated. FAS velocity calculations were performed for different frequencies and porosity distributions of cortical bone and callus to give insight to the multiple scattering phenomena and determine quantitatively the interaction of ultrasound with the microstructure of callus and osseous tissues.

It was shown that the FAS velocity increases with increasing frequency, which is in agreement with (Potsika *et al.,* 2012). Moreover, the highest FAS velocity values were measured in the case of Problem I corresponding to a homogeneous callus region. This is attributed to the presence of the circular scatterers which provokes the attenuation of the signal and increases the time of arrival at the receiver. Also, this is reasonable as the propagation velocity in blood is lower in comparison to the callus tissue. Higher FAS velocity values were observed for lower porosity concentrations (Problem IV, V), which however remained lower in comparison to Problem I.

Another significant conclusion was drawn for Problems II and III, as well as Problems IV and V, having the same porosity concentration and different pores' diameters. In these cases, FAS velocity calculations were approximately the same. This reveals that changes in callus porosity concentration have a more significant influence on the

propagation of the FAS velocity in comparison to changes in the diameter of the scatterers. Nevertheless, FAS velocity calculations for Problems VI and VII revealed that the scatterers' diameter plays a key role on FAS velocity when larger porous areas are examined such as the whole surface of cortical bone.

However, several assumptions were made for the development of the computational models. The effect of the fluid loading boundary conditions on the features of guided wave propagation was neglected. The soft tissues provide leakage paths for the ultrasonic energy resulting in the so-called leaky guided waves and in this case the dispersion curves are modified (Vavva *et al.,* 2008a). Moreover, IEMA introduces the assumption that the geometry of the inclusions is spherical which is not realistic as a better representation for the newly formed callus tissue would be a cylindrical shape. The modification of the iteration procedure in order to incorporate cylindrical scatterers constitutes an objective for future research. Another assumption is that the random distributed inclusions all have the same size. This condition is not realistic as different callus sub-regions have significantly different inclusions' diameters derived even from the same healing stage. Also, the size and the volume concentration of the inclusions inside the osteotomy differ in comparison to the callus tissue surrounding the osteotomy gap. Nevertheless, the exploitation of IEMA can simplify the solution of the wave propagation problem and give insight to the changes occurring in the callus microstructural effects and porosity during healing. Therefore, this methodology could be used in order to investigate numerically wave propagation scattering effects in computational models of osteoporotic bones (chapter 6).

Chapter 5: Backscattering simulation of ultrasonic wave propagation in computational models of healing long bones

5.1 Introduction

The investigation of ultrasonic scattering in bone has attracted the interest of several research groups worldwide (Liu *et al.*, 2015; Karjalainen *et al.*, 2012; Hoffmeister *et al.*, 2012; Malo *et al*., 2014; De Marco *et al.*, 2016). The propagation of an ultrasonic wave through a composite medium with strong acoustic impedance differences between the constituent materials like bone may induce multiple scattering. A part of the incident energy is transferred to the pores (Aggelis *et al*., 2004; Verbis *et al*., 2001). The frequency of the incident wave, the distribution and geometry of the scatterers, as well as the physical properties of the pores and the surrounding medium affect the amount and distribution of the scattered intensity (Aggelis *et al.,* 2004). Scattering in healing bones occurs due to the interaction of ultrasound with the complex microstructure of callus and cortical bone. In contrast to the axial transmission technique, the backscatter technique is more versatile, since it can be

easier applied to skeletal sites with thicker soft tissue layers between bone surface and skin, such as the hip and spine (Casciaro *et al.*, 2015).

The ultrasonic scattering characteristics of cancellous bone has been extensively studied in the literature (Liu *et al.*, 2015; Karjalainen *et al.*, 2012; Hoffmeister, 2011; Hoffmeister *et al.*, 2012; De Marco *et al.*, 2016; Wear, 2008; Padilla *et al*., 2006; Wear, 1999). The broadband ultrasonic backscatter (BUB) is the main parameter of interest reflecting the frequency averaged backscatter coefficient. However, the calculation of BUB requires knowledge on the attenuation along the ultrasonic wave propagation path which is not always available. In this case, parameters such as the apparent backscatter coefficient, the AIB and the frequency slope of apparent backscatter (FSAB) are examined (Hoffmeister *et al.*, 2012; Malo *et al*., 2014; De Marco *et al.*, 2016; Casciaro *et al.*, 2015).

Fewer studies have addressed the interaction of ultrasonic backscattering with cortical microstructure (Bourgnon *et al.*, 2014; Gortsas *et al.*, 2015; Iori *et al.*, 2015) focusing on the discrimination of large BMUs from Haversian canals. Numerical models with various porosities and pore sizes have been established and the scattering amplitude, the average spectra of the backscattered signals, the AIB and the FSAB were calculated. It was reported that the backscattering signals convey significant information for the evaluation of cortical porosity and the detection of BMUs.

Concerning bone healing, the assessment of pseudarthrosis with ultrasound backscattered signals in rats was investigated experimentally in (Ferreira *et al.*, 2010). The AIB was calculated for normal bones and bones with pseudarthrosis, showing higher values for the latter. Theoretical and numerical approaches incorporating the effects of porosity determined through SAM were combined in (Potsika *et al*., 2014a) to evaluate the ultrasonic attenuation of the callus at different stages of healing. However, the interaction of backscattering parameters with alterations in the callus and cortical microstructure during bone healing is considered as an open research field.

This chapter investigates the backward propagating acoustic field induced by changes in material properties and structure of the mineralized callus at successive healing stages in an ovine osteotomy healing model. The callus stiffening and the decrease in callus porosity, as well the cortical softening and the increase in cortical porosity are

incorporated in numerical models using SAM images from the second (week 2), third (week 3), sixth (week 6) and ninth (week 9) postoperative weeks (Preininger *et al*., 2011). For the first time the monitoring potential of the backward propagating acoustic field in bone healing and the role of the central excitation frequency are investigated numerically considering the propagation of a plane wave at different frequencies in the range 0.2–1 MHz. The numerical solution of the scattering problem is performed using the BEM. The parameter of interest here is the scattering amplitude in the backward direction, which gives a measure of the energy scattered to this direction when a pressure wave strikes the bone structure, as well as the acoustic pressure variation. Initially, the model geometry, material properties, ultrasound configuration and numerical solution of the scattering problem using BEM are described. Then, the results are presented concerning the scattering amplitudes in the backward direction and near-field acoustic pressure. Finally, a thorough discussion is included based on the findings of this thesis compared to the literature.

5.2 Model geometry

This section presents the 2D numerical models of healing long bones based on SAM imaging data derived from a previous experimental study (Preininger *et al*., 2011). Figs. 5.1(a)–(l) show the SAM images for successive bone healing stages corresponding to weeks 2, 3, 6 and 9 after the osteotomy. Each image represents an acoustic impedance map of embedded longitudinal sections of 3-mm osteotomies in the right tibia of female Merino sheep. All specimens were subjected to SAM measurements, using a spherically focused 50-MHz transducer. For each healing stage, 3 different SAM images were used from different animals and 3 numerical models were established. As it can be seen in Fig. 5.1, a specific abbreviation is assigned to each SAM image to denote the week of healing and the number of the numerical model (e.g. the abbreviation W2-M1 corresponds to week 2 and the 1st numerical model). However, it should be noted that as each SAM image is derived from a different animal, the numerical association of the model number is random (e.g. the results from W2-M1 can be directly compared with each one of the models of the next healing stage W3-M1, W3-M2 or W3-M3 having no specific association with W3-M1).

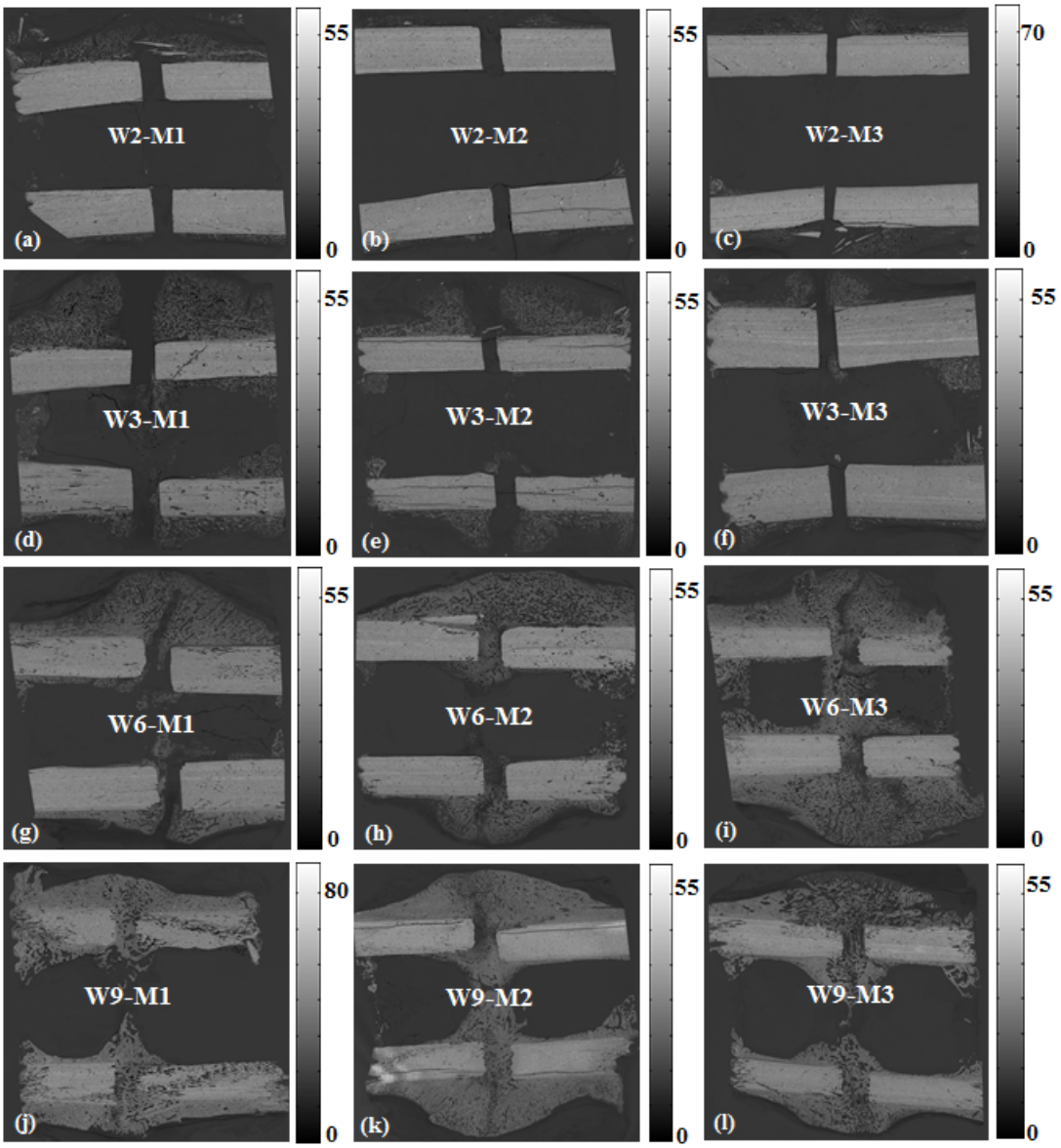

Figure 5.1: Scanning acoustic microscopy images for: (a)-(c) week 2, (d)-(f) week 3, (g)-(i) week 6, and (j)-(l) week 9 after osteotomy. The colorbar reflects the Young's modulus in GPa.

An algorithm in MATLAB (The Mathworks, Inc., MA) was developed to detect the borders of cortical bone and callus considering differences in the greyscale values (Fig. 5.2). The pixel size is 12 μm. Then, the coordinates of the points comprising the pixel borders were calculated and directly transferred into numerical models developed based on the software package ISoBEM (ISoBEM, version v.1.0.11, BEM S&S, Greece). Also, 3 additional models were established to simulate intact cortical bone as reference cases. The numerical models for intact bone were developed based on the material and geometrical properties of cortical bone derived from the SAM

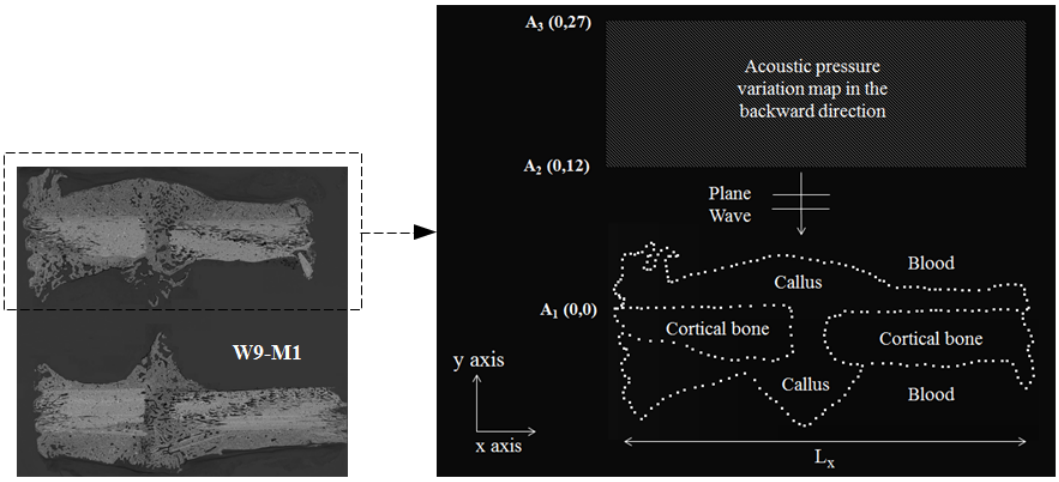

Figure 5.2: The ultrasonic configuration is demonstrated considering the numerical model W9-M1 and the upper cortical fragments.

images of week 2 (Fig. 5.1(a) – (c)) restoring the bone discontinuity by removing the fracture gap. The cortical length (L_x) was different for each SAM image (Fig. 5.2). The 2D models of intact and healing long bones were assumed to be immersed in blood in order to account for the soft tissues surrounding the osseous tissues.

5.3 Material properties

Initially, a segmentation between the mineralized tissue and the embedding material was performed using a threshold for the acoustic impedance ($Z_{threshold}$=3.50 Mrayl) based on the specifications described in (Preininger et al., 2011). The material properties of the surrounding medium were derived from the literature and correspond to blood with bulk modulus K_{blood} = 2.38 GPa, density ρ_{blood} = 1055 kg/m^3 and Poisson's ratio ν_{blood} =0.49979 (Vavva *et al.,* 2008; Potsika *et al*., 2014a).

The calculation of the material properties of the cortical bone and callus tissue was performed in two stages: a) empirical equations were used to derive the medium density and Young's modulus from the acoustic impedance images as previously described in (Preininger *et al*., 2011; Raum, 2011), b) the iterative effective medium approximation (IEMA) of (Aggelis *et al*., 2004) was used to calculate the effective material properties of the cortical and callus tissue as shown in Fig. 5.3.

Initially, the density ρ was derived from the acoustic impedance values Z using the conversion provided in Table 16.5 from (Raum, 2011) as:

$$Z_1=1.02\rho^{2.83}. \quad (5.1)$$

Then, the elastic coefficient c_{11} in the direction normal to the longitudinal section surface was calculated as:

$$c_{11}=0.608Z_1^{1.923}. \quad (5.2)$$

If the Poisson's ratio *v* is set to 0.3 (Preininger *et al*., 2011), the Young modulus E can be defined as:

$$E_1=\frac{(1+\nu)(1-2\nu)}{(1-\nu)}c_{11}\,. \quad (5.3)$$

Concerning the second stage and the application of IEMA, the composite medium (cortical bone or callus) is replaced by an elastic homogeneous and isotropic material with effective material properties respectively (Aggelis *et al*., 2004, Christensen, 1990) as illustrated in Fig. 5.3. IEMA was analytically described in Chapter 4. Tables 5.1 and 5.2 present the osseous and callus tissue effective material properties calculated based on Eqs. (5.1) – (5.3) and the application of IEMA for the excitation frequencies 0.2, 0.4, 0.6 , 0.8 and 1 MHz. These values were determined assuming circular scatterers with the material properties of blood (Fig. 5.3). The medium porosity and particle diameter in cortical bone and callus for each healing stage are also presented in Tables 5.1 and 5.2. The callus porosity was not considered for the numerical models of week 2 as callus porosity, callus area and matrix stiffness could not be assessed reliably at this time point because of the small mineralized callus area (Preininger *et al.,* 2011).

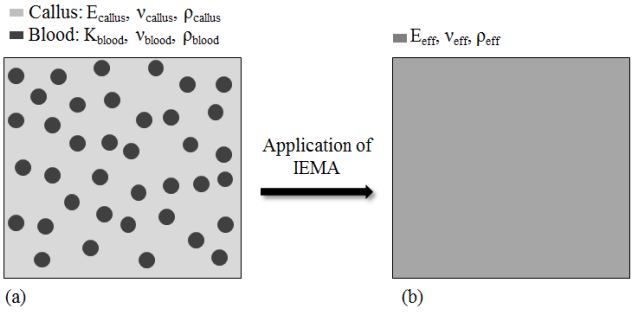

Figure 5.3: The composite medium in (a) is replaced by an elastic homogeneous and isotropic material in (b) with effective material properties (E_{eff}, ν_{eff}, ρ_{eff}) calculated from IEMA.

Table 5.1 Cortical bone effective material properties calculated using IEMA and SAM images.

Numerical model (Week-Model No.)	Young's modulus (GPa)	Poisson's ratio	Density (kg/m^3) – 0.2–1 MHz	Porosity (%)	Pores' diameter (μm)
W2-M1	23.26	0.3000	2048	0.33	50
W2-M2	23.47	0.2998	2050	0.42	50
W2-M3	24.49	0.2998	2066	0.45	50
W3-M1	18.24	0.3022	1957	2.87	50
W3-M2	19.23	0.3011	1975	2.15	50
W3-M3	20.34	0.3009	1999	0.55	50
W6-M1	20.36	0.3008	1996	1.80	50
W6-M2	21.31	0.3018	2014	1.98	50
W6-M3	22.35	0.3008	2032	1.25	50
W9-M1	18.34	0.3049	1970	6.09	50
W9-M2	22.57	0.3011	2036	2.50	50
W9-M3	21.68	0.3011	2020	1.65	50

Table 5.2 Callus effective material properties calculated using IEMA and SAM images.

Numerical model (Week-Model No.)	Young's modulus (GPa)	Poisson 's ratio	Density (kg/m^3) – 0.2 MHz	Density (kg/m^3) – 0.4 MHz	Density (kg/m^3) – 0.6 MHz	Density (kg/m^3) – 0.8 MHz	Density (kg/m^3) – 1 MHz	Porosity (%)/ Pores' diameter (μm)
W3-M1	$1.95\text{x}10^{-6}$	0.499	1173	1181	1194	1213	1239	44.8/350
W3-M2	$2.40\text{x}10^{-6}$	0.499	1176	1184	1198	1218	1245	46.3/350
W3-M3	$3.70\text{x}10^{-6}$	0.499	1183	1192	1206	1227	1255	48.2/350
W6-M1	5.06	0.349	1630	1636	1645	1656	1668	29.4/200
W6-M2	5.70	0.354	1763	1806	1821	1841	1863	38.7/200
W6-M3	5.83	0.345	1694	1670	1709	1721	1735	30.0/200
W9-M1	8.00	0.329	1761	1762	1764	1767	1771	22.7/120
W9-M2	10.03	0.316	1783	1784	1785	1787	1788	12.8/120
W9-M3	6.10	0.343	1709	1711	1714	1719	1725	30.0/120

5.4 Ultrasound configuration

The ultrasound configuration is presented in Fig. 5.2 for the 2D model W9-M1. The established models included both the upper and the lower cortical and callus regions of the SAM images. However, Fig. 5.2 presents only the borders of the upper cortical and callus surface for illustration purposes. The same ultrasound configuration was considered for all the examined numerical models for intact bone, week 2, week 3, week 6 and week 9. Plane waves of frequencies 0.2, 0.4, 0.6, 0.8 and 1 MHz were used as the incident wave propagating in the –y-direction (i.e., 0 degrees). The scattering amplitude was calculated in the backward direction (i.e., 180 degrees). Also, Fig. 5.2 shows that multiple receiving positions were considered in the

backward direction (+y-direction) to calculate the acoustic pressure in a distance from 12 mm (A_2 (0,12)) to 27 mm (A_3 (0,27)) relative to the cortical cortex (A_1 (0,0)) covering an area width of 15 mm. The area length in the +x-direction was different for each SAM image according to the cortical length L_x as it is shown in Fig. 5.2.

5.5 Numerical solution of the scattering problem using the Boundary Element Method

The 2D fluid structure interaction scattering problem solved in the present work concerns the scattering of a pressure wave by an elastic structure immersed in an infinitely extended fluid. Assuming harmonic time dependence, the excited fluid pressure field p(**x**) and the corresponding elastic displacements u(**x**) at any field point **x** of the analyzed domain can be calculated from the following integral representations, respectively (Wrobel, 2002; Aliabadi, 2002; Polyzos *et al.*, 1998):

$$c(\mathbf{x})p(\mathbf{x}) + \int_S \partial_n G(\mathbf{x},\mathbf{y},\omega)p(\mathbf{y})dS_y = \int_S G(\mathbf{x},\mathbf{y},\omega)\partial_n p(\mathbf{y})dS_y + p^i(\mathbf{x}), \qquad (5.4)$$

$$\left[1-c(\mathbf{x})\right]\mathbf{u}(\mathbf{x}) + \int_S \mathbf{T}(\mathbf{x},\mathbf{y},\omega)\mathbf{u}(\mathbf{y})dS_y = \int_S \mathbf{U}(\mathbf{x},\mathbf{y},\omega)\mathbf{t}(\mathbf{y})dS_y, \qquad (5.5)$$

where **y** represents a source point always lying at the surface of the scatterer S, ω is the frequency of the harmonic incident wave, G(**x**,**y**,ω), **U**(**x**,**y**,ω) are the fundamental solutions of the Helmholtz and Navier-Cauchy equations, respectively, **T**(**x**,**y**,ω) and **t**(**x**) are the traction fields corresponding to elastic fundamental solution **U**(**x**,**y**,ω) and displacement **u**(**x**), respectively, $p^i(\mathbf{x})$ is the incident harmonic, plane wave propagating in the fluid region, ∂_n denotes directional derivative with respect to the unit vector being normal to the surface of the scatterer, while the coefficient c(**x**) takes the values 0, 1 and 0.5 when the field point **x** lies inside, outside and at the boundary of the elastic scatterer, respectively. Both the field point **x** and the source point **y** are vectors defined with respect to a Cartesian coordinate system located usually inside to the scatterer.

At the fluid-structure interface the following boundary conditions are satisfied:

$$\left.\begin{aligned} \frac{1}{\omega^2\rho^f}\partial_n p &= -\hat{\mathbf{n}}\cdot\mathbf{u} \\ p &= \hat{\mathbf{n}}\cdot\mathbf{t} \end{aligned}\right\} \mathbf{x}\in S\ , \tag{5.6}$$

with ρ^f being the density of the fluid and $\hat{\mathbf{n}}$ the unit vector normal to the surface S.

Writing the total pressure field p(**x**) as a sum of the incident and scattered wave, i.e. $p(\mathbf{x}) = p^i(\mathbf{x}) + p^s(\mathbf{x})$, far away from the scatterer the following asymptotic expression of the scattered field is valid (Dassios *et al.*, 1987):

$$\frac{\mathbf{x}-\mathbf{y}}{|\mathbf{x}-\mathbf{y}|} = \hat{\mathbf{r}} + O\left(\frac{1}{r}\right),\ p^s = g(\hat{\mathbf{r}},\hat{\mathbf{k}})\frac{e^{ikr}}{\sqrt{kr}},\ r\to\infty, \tag{5.7}$$

where $\hat{\mathbf{r}}$ is unit vector across the radial variable r of the polar coordinate system, O refers to the origin of the polar coordinate system, k is the wavenumber of the incident wave and $g(\hat{\mathbf{r}},\hat{\mathbf{k}})$ is the scattering amplitude representing the energy scattered at $\hat{\mathbf{r}}$ direction when an acoustic wave impinges upon the $\hat{\mathbf{k}}$ direction, having the integral form:

$$g(\hat{\mathbf{r}},\hat{\mathbf{k}}) = \frac{1-i}{4\sqrt{\pi}}\int_S \left[p(\mathbf{y})ik(\hat{\mathbf{r}}\cdot\hat{\mathbf{n}})e^{-ik\hat{\mathbf{r}}\cdot\mathbf{y}} - q(\mathbf{y})e^{-ik\hat{\mathbf{r}}\cdot\mathbf{y}}\right]dS_y,\ \ q = \partial_n p\ . \tag{5.8}$$

According to the BEM, the fluid-structure interface is discretized into quadratic three-noded line elements and both integral equations (5.4) and (5.5) are collocated at the nodes of the discretized surface deriving the following linear systems of algebraic equations, respectively:

$$\left[\mathbf{H}^{acoustic}\right]\cdot\{\mathbf{p}\} = \left[\mathbf{G}^{acoustic}\right]\cdot\{\mathbf{q}\} + \{\mathbf{p}^i\},\ q = \partial_n p, \tag{5.9}$$

$$\left[\mathbf{H}^{elastic}\right]\cdot\{\mathbf{u}\} = \left[\mathbf{G}^{elastic}\right]\cdot\{\mathbf{t}\}, \tag{5.10}$$

where the vectors $\{\mathbf{p}\},\{\mathbf{q}\},\{\mathbf{u}\},\{\mathbf{t}\}$ represent all the nodal values of the pressure, pressure flux, elastic displacement and traction, respectively, $\{\mathbf{p}^i\}$ is a vector containing the contribution of incident wave to the fluid-structure interfacial nodes and $\left[\mathbf{H}^{acoustic}\right],\left[\mathbf{G}^{acoustic}\right],\left[\mathbf{H}^{elastic}\right],\left[\mathbf{G}^{elastic}\right]$ matrices contain integrals with kernels

$\partial_n G(\mathbf{x},\mathbf{y}), G(\mathbf{x},\mathbf{y}), \mathbf{T}(\mathbf{x},\mathbf{y}), \mathbf{U}(\mathbf{x},\mathbf{y})$, respectively, all evaluated via advanced integration techniques explained in (Polyzos *et al.*, 1998).

Satisfying the boundary conditions of (5.6) and rearranging, the system of algebraic equations (5.7) and (5.8) obtains the final form:

$$[\mathbf{A}]\{\mathbf{x}\} = \{\mathbf{p}^i\}, \tag{5.11}$$

with the vector $\{\mathbf{x}\}$ containing all the unknown nodal values of the vectors $\{\mathbf{p}\}, \{\mathbf{q}\}$, $\{\mathbf{u}\}$ and $\{\mathbf{t}\}$.

Solving the system (5.9) through a standard LU decomposition algorithm and evaluating the nodal values $\{\mathbf{p}\}, \{\mathbf{q}\}$, the scattering amplitude $g(\hat{\mathbf{r}}, \hat{\mathbf{k}})$ is easily evaluated via its integral representation (5.8), whilst the scattered pressure field outside to the scatterer is evaluated through the integral representation (5.4).

5.6 Statistical Analysis

A statistical analysis was conducted to evaluate the backward propagating acoustic field in successive healing stages for different excitation frequencies. More specifically, for each healing stage, the scattering amplitude values at 180 degrees have been averaged over the 3 models and the results are presented as mean scattering amplitudes of the three numerical models for each healing stage ±standard error. One-way analysis of variance (one-way ANOVA) is also used to investigate the impact of frequency. The statistical findings are considered significant for p-values lower than 0.05. Additionally, a post hoc analysis is conducted based on the Tukey-Kramer method to compare results from different weeks pairwise.

5.7 Results

Figures 5.4–5.9 present the results derived from the simulations of the backward propagating acoustic field and the excitation frequencies 0.2, 0.4, 0.6, 0.8 and 1 MHz. Specifically, in Fig. 5.4 the variation of the magnitude of scattering amplitude in the backward direction is presented for intact bone, week 2, week 3, week 6 and week 9 after the osteotomy. The scattering amplitude is a quantitative parameter reflecting the scattered energy far away from the examined geometry depending on the size of the scatterer. Then, in Figs. 5.5–5.9 the variation of the acoustic pressure is illustrated

from multiple receiving positions in the backward direction. The acoustic pressure map reflects the amplitude of the vibration induced by the scattered wave.

5.7.1 Scattering amplitudes in the backward direction

Figures 5.4(a)–(e) show the magnitude of the mean scattering amplitude values derived from the three numerical models of each postoperative week for all the excitation frequencies. The standard error bars demonstrate the scattering amplitude variation in each healing stage. All the diagrams include the intact bone value for comparison purposes. Specifically, in Fig. 5.4(a) the mean scattering amplitude decreases from 0.31 in week 2 to 0.09 in week 3 and 0.07 in week 6, respectively. Finally, in week 9 the scattering amplitude increases to 0.12. In Fig. 5.4(b) for the excitation frequency 0.4 MHz, the mean scattering amplitude values for serial healing stages were: (a) 0.13 for week 2, (b) 0.09 for week 3, (d) 0.06 for week 6, and (e) 0.11 for week 9. When the excitation frequencies 0.6 and 0.8 MHz were applied, a decrease of the scattering amplitude was observed showing no restoration in week 9. In particular, in Fig. 5.4(c) for the excitation frequency 0.6 MHz, the mean scattering amplitude values were calculated from 0.39 in week 2 to 0.08 in week 9, while in Fig. 5.4(d) and at 0.8 MHz a decrease from 0.26 in week 2 to 0.09 in week 9 was observed. Finally, in Fig. 5.4(e) the excitation frequency of 1 MHz leads to an increase of the scattering amplitude value in week 9 as observed at 0.2 and 0.4 MHz. The calculated scattering amplitude values were: (a) 0.44 in week 2, (b) 0.14 in week 3, (d) 0.07 in week 6, and (e) 0.11 in week 9. Concerning one-way ANOVA, the p-values were lower than 0.05 for all the examined frequencies and more specifically the calculated values were: (a) 0.004 at 0.2 MHz, (b) 0.02 at 0.4 MHz, (c) 0.02 at 0.6 MHz, (d) 0.04 at 0.8 MHz, and (e) 0.004 at 1 MHz.

Although, a similar scattering amplitude variation was observed among the examined healing weeks at 0.2, 0.4 and 1 MHz, the Tukey-Kramer test did not reveal significant differences between the healing stages week 3-week 6, week 6-week 9 and week3-week9, when pairwise comparisons were performed. More specifically, the Tukey-Kramer test showed significant statistical differences between two means only for the following cases:

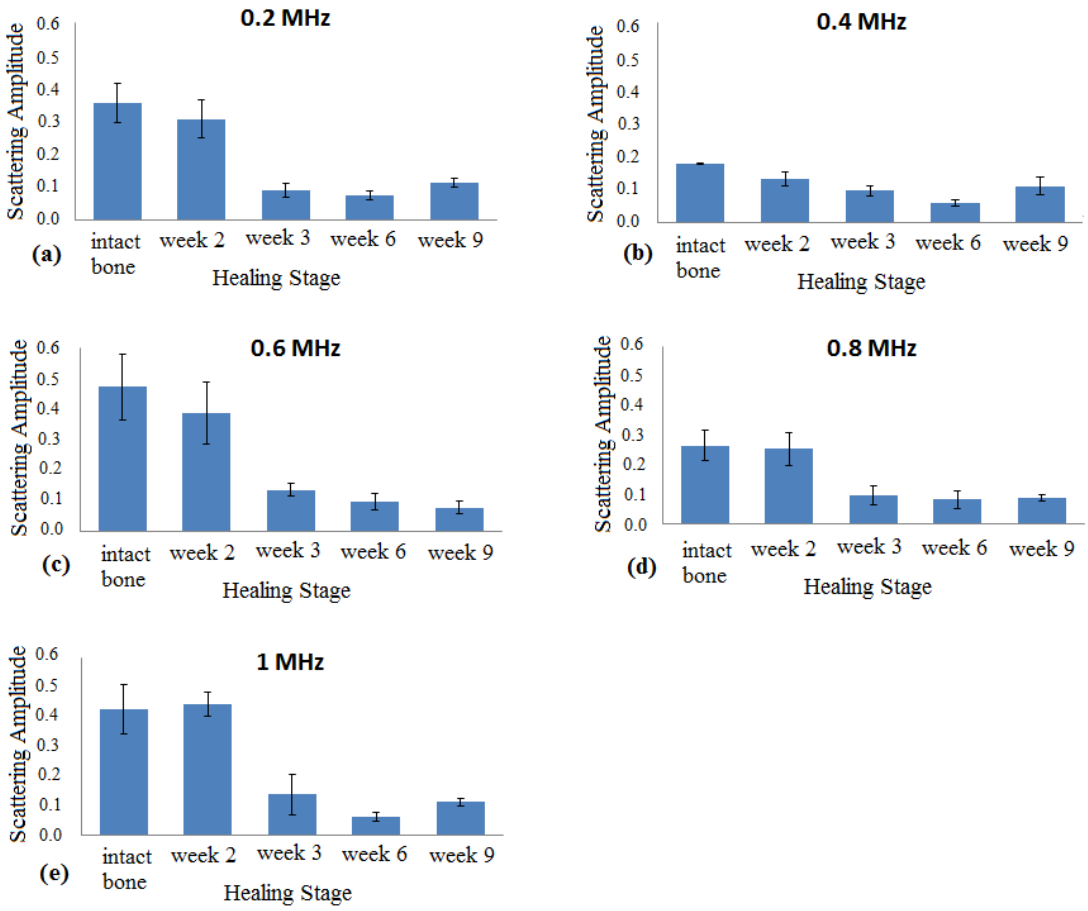

Figure 5.4: The magnitude of the scattering amplitude (in arbitrary units) during the bone healing process for the excitation frequencies: (a) 0.2 MHz, (b) 0.4 MHz, (c) 0.6 MHz, (d) 0.8 MHz, and (e) 1 MHz. The standard error bars demonstrate the scattering amplitude variation in each healing stage.

(a) excitation frequency 0.2 MHz and the examined pairs intact bone-week 3, intact bone-week 6, intact bone-week 9, week2-week 3, week 2-week 6, (b) excitation frequency 0.4 MHz and the case intact bone-week 6, (c) excitation frequency 0.6 MHz and the pairs intact bone-week 6, intact bone-week 9, and (d) excitation frequency 1 MHz and the cases intact bone-week 3, intact bone-week 6, intact bone-week 9, week2-week 3, week 2-week 6, week 2-week 9. Concerning the frequency 0.8 MHz, there are no significant differences in the scattering amplitudes measured at different healing stages.

5.7.2 Acoustic pressure

Figures. 5.5–5.9 present the variation of the acoustic pressure in the backward direction from multiple receiving positions covering the area illustrated in Fig. 5.2.

The value of the incident pressure amplitude is 1 Pa. For all the color maps, which follow, a color bar is also included consisting of a linear scale with 10 subdivisions based on the maximum pressure of the entire field, denoted as P_{max}. The P_{max} values for all the examined cases are presented in Table 5.3. It should be mentioned that each acoustic pressure map corresponds to one of the three numerical models established for each healing week.

Fig. 5.5 presents the acoustic pressure variation map at 0.2 MHz. In Figs. 5.5(a), (b) the scattering energy of the plane wave in the backward direction is illustrated as parallel planes for intact bone and week 2. The pressure amplitude is not evenly distributed in the x-direction probably due to the diffraction effect. In Figs. 5.5(c), (d) the formation of the callus leads to the disruption of the parallel distribution of the scattered energy which shows an arched form following the structure of the callus tissue.

Finally, in Fig. 5.5(e) the parallel distribution of the scattered waves in the backward direction is gradually restored in week 9. As it can be observed from the Pmax values of Table 5.3 and the color maps of Fig. 5.5, higher acoustic pressure values were derived during the first healing weeks, while lower values were calculated for weeks 6 and 9. Also, it is shown that the presence of the callus tissue changes the distribution of the Pmax values showing the direction of the scattered energy field.

Table 5.3 Maximum values of the acoustic pressure field (Pmax) in the backward direction for all the examined excitation frequencies.

Numerical model (Week-Model No.)	Acoustic Pressure P_{max} (Pa)				
	0.2 MHz	0.4 MHz	0.6 MHz	0.8 MHz	1 MHz
Intact-M1	2.32	2.17	1.97	2.47	2.59
Intact-M2	2.18	2.42	1.97	2.19	2.53
Intact-M3	2.02	2.30	2.35	2.34	2.24
W2-M1	1.79	2.40	1.78	2.37	2.34
W2-M2	2.14	2.19	1.94	2.06	2.30
W2-M3	1.87	2.38	2.20	2.16	2.40
W3-M1	2.12	2.12	2.56	2.16	2.18
W3-M2	1.99	1.83	2.08	2.04	2.05
W3-M3	2.05	2.27	2.55	2.60	2.45
W6-M1	1.81	1.43	1.75	1.89	2.05
W6-M2	1.59	1.61	1.90	2.06	2.02
W6-M3	1.88	1.63	2.08	2.17	2.67
W9-M1	1.89	1.71	2.13	2.17	2.47
W9-M2	1.69	1.85	1.57	1.58	1.74
W9-M3	1.85	1.53	1.77	1.80	1.97

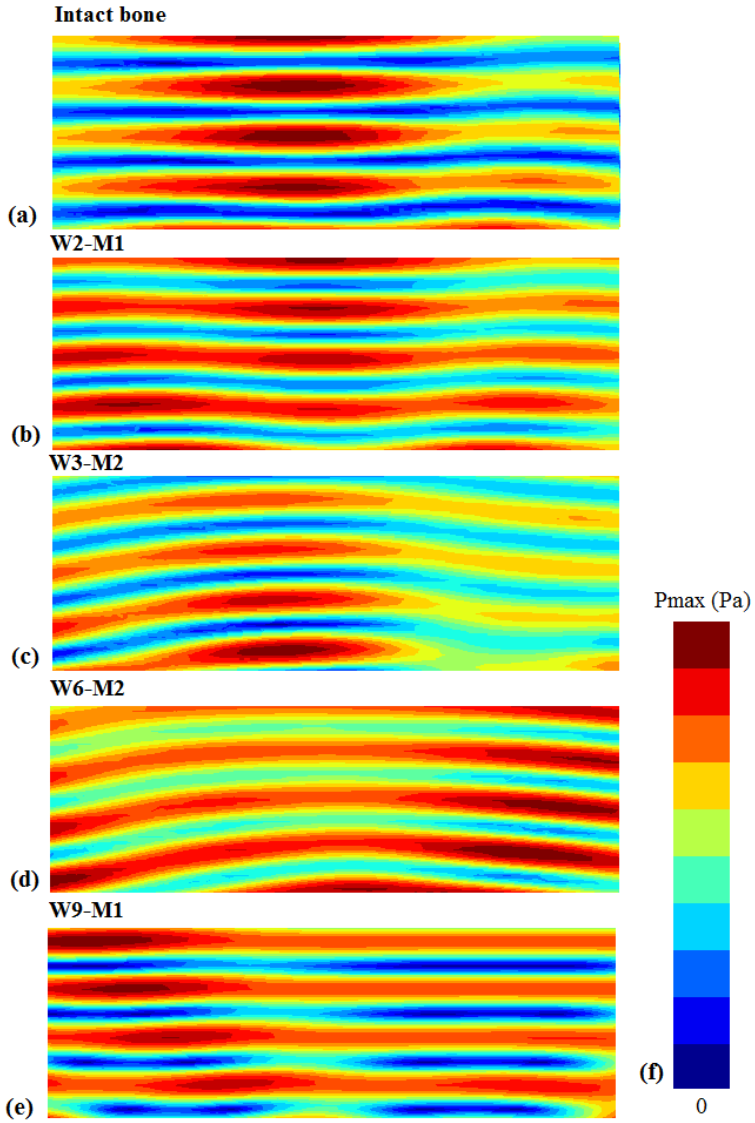

Figure 5.5: Acoustic pressure variation map for 0.2 MHz and the cases of: (a) intact bone, (b) W2-M1, (c) W3-M2, (d) W6-M2, and (e) W9-M1.

Thus, for intact bone and week 2 the Pmax values are calculated above the center of the plate, while in weeks 6 and 9 the Pmax values are depicted near the boundaries of the plate. In Fig. 5.6, the acoustic pressure maps are depicted for the excitation frequency 0.4 MHz. It can be seen that the scattering energy of the plane wave in the backward direction is illustrated as parallel planes for intact bone. Next, the presence of the gap in weeks 2 and 3 interrupts the continuity of the parallel planes around the fracture site. The formation of callus in weeks 6 and 9 which closes the fracture gap leads to an arched form of the backscattered in week 6 and a parallel distribution in week 9.

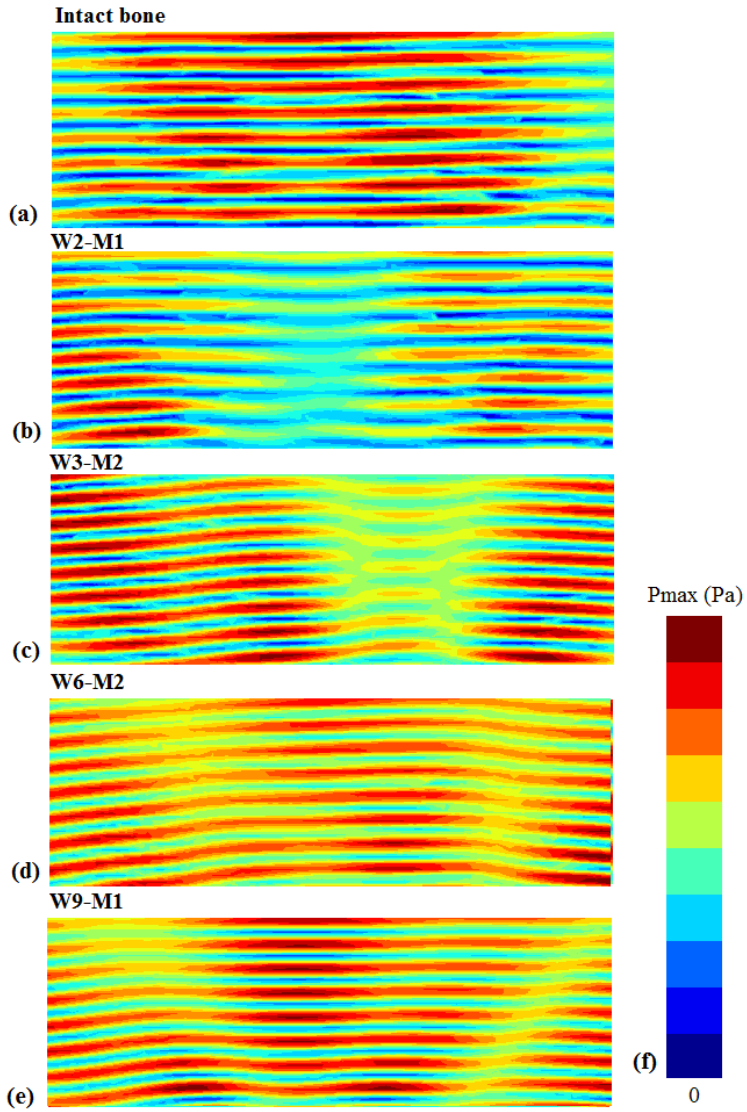

Figure 5.6: Acoustic pressure variation map for 0.4 MHz and the cases of: (a) intact bone, (b) W2-M1, (c) W3-M2, (d) W6-M2, and (e) W9-M1.

Nevertheless, for the excitation frequencies 0.6–1 MHz no specific acoustic pressure pattern can be observed in Figs. 5.7–5.9. Thus, a random distribution of the energy in the backward direction is shown which does not reveal the callus restoration and cannot provide any qualitative information for the fracture healing process. Finally, according to Table 5.3, higher Pmax values were calculated in week 3 and lower values in weeks 6 and 9, respectively.

5.8 Discussion

In this chapter, 2D numerical simulations of wave propagation in healing long bones were performed using the BEM aiming to provide new knowledge on the multiple

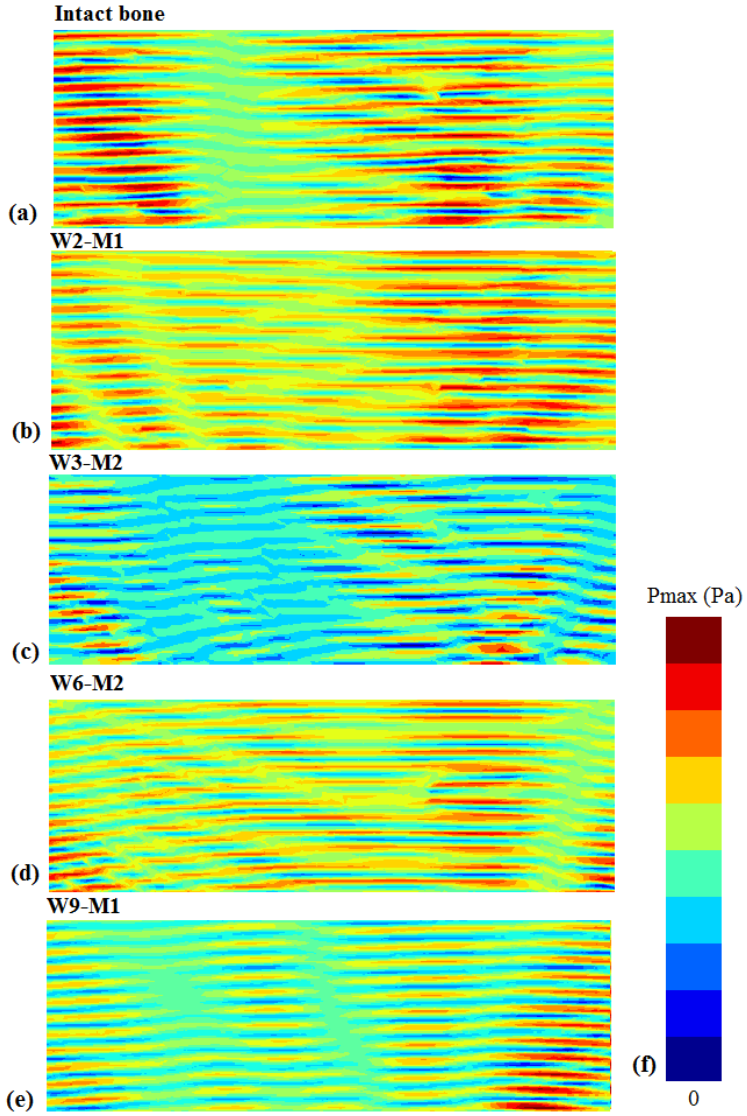

Figure 5.7: Acoustic pressure variation map for 0.6 MHz and the cases of: (a) intact bone, (b) W2-M1, (c) W3-M2, (d) W6-M2, and (e) W9-M1.

scattering phenomena and their contribution to the resulting acoustic field during bone healing (Potsika et al. 2017). The propagation of a plane wave was considered and different propagation frequencies were examined in the range 0.2-1 MHz. The scattering amplitude was calculated as well as the acoustic pressure in the backward direction. To the best of the author's knowledge, this is the first computational study to evaluate the backward propagating acoustic field in healing long bones based on imaging data from scanning acoustic microscopy (Preininger *et al.,* 2011) considering the impact of the excitation frequency. The outer and inner borders of the cortical bone and callus were directly converted to realistic osseous tissue dimensions and introduced to the

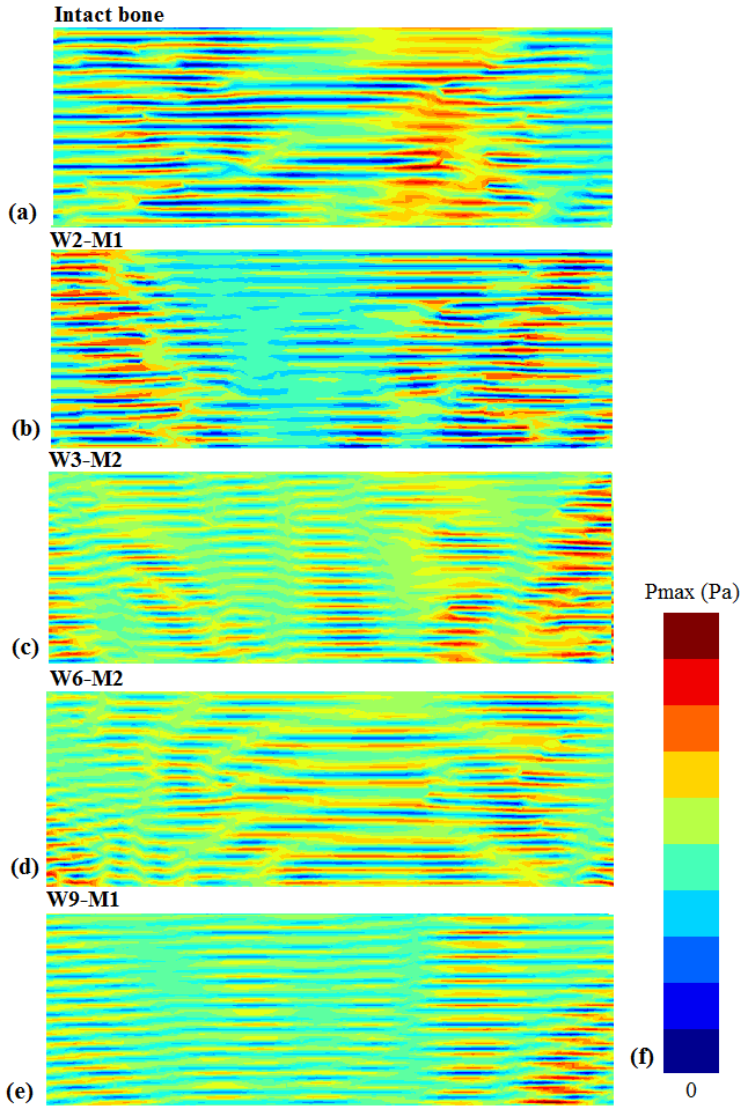

Figure 5.8: Acoustic pressure variation map for 0.8 MHz and the cases of: (a) intact bone, (b) W2-M1, (c) W3-M2, (d) W6-M2, and (e) W9-M1.

boundary element software. The material properties of the cortical and callus tissues and their composite structure were incorporated into the numerical models using the iterative effective medium approximation of (Aggelis *et al*., 2004). Except for the callus stiffening and the decrease in callus porosity, the softening of the osseous tissue and the increase in cortical porosity are also considered during bone healing according to (Preininger *et al.,* 2011).

Concerning the selection of the numerical method, the main advantage of the BEM, as it is compared to the FEM and the FDM, is its requirement for boundary only discretization and not for surface plus volume discretization as FEM and FDM do. Thus, BEM is ideal for solving wave scattering problems where infinite domains are

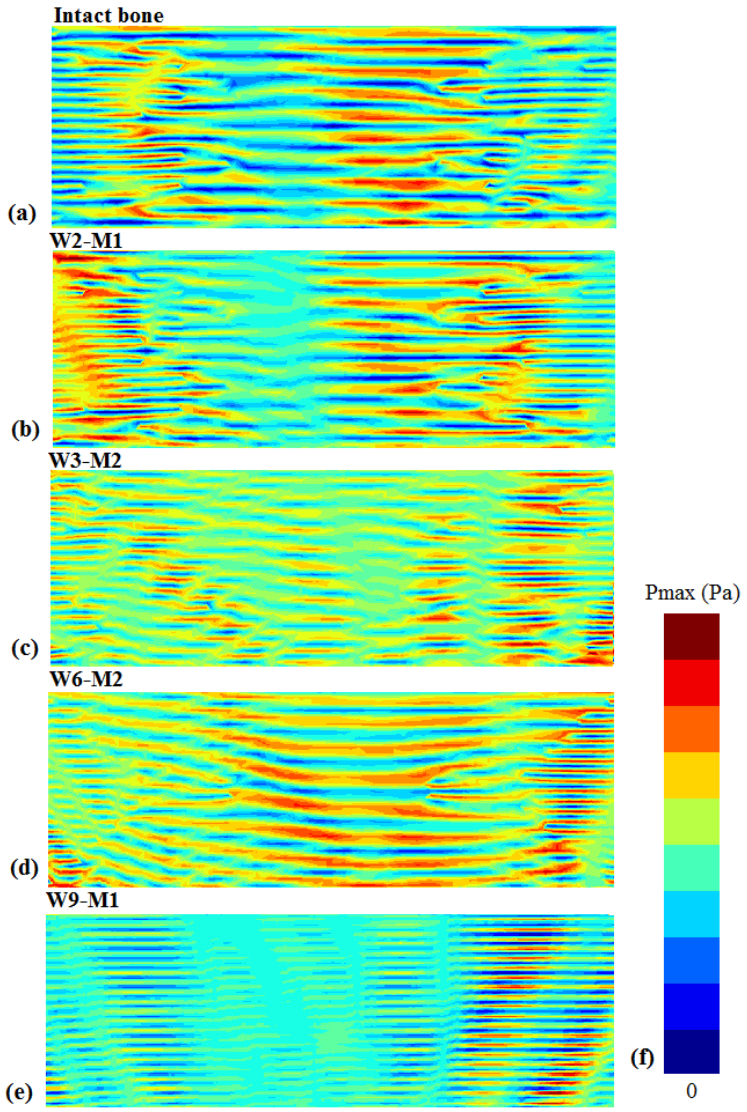

Figure 5.9: Acoustic pressure variation map for 1 MHz and the cases of: (a) intact bone, (b) W2-M1, (c) W3-M2, (d) W6-M2, and (e) W9-M1.

dealt with. This advantage becomes more pronounced in 3D problems. For pulse-echo signals, BEM works perfectly with the aid of Fast Fourier Transform (FFT). BEM uses the frequency domain for the solution of the problem corresponding to FFT spectrum of incident pulse and then by using the inverse FFT the results are converted to time domain. Since the BEM utilizes the integral representation of the solution of the problem, it is more stable and accurate than domain methods like FEM and FDM, which actually solve the partial differential equation of the problem.

In Fig. 5.4, it can be observed that for the excitation frequencies 0.2, 0.4 and 1 MHz the scattering amplitude in the backward direction decreases in weeks 3 and 6 compared to week 2 and increases in week 9 as the callus consolidation progresses.

Nevertheless, the Tukey-Kramer test revealed that not all the changes are statistically significant. More specifically, according to (Laugier and Haïat, 2011) in soft tissue, the density and compressibility of scatterers are close to those of the surrounding medium and the contribution of scattering to the overall attenuation is relatively small. Thus, the lower scattering amplitude values in weeks 3, 6 and 9 can be explained by the presence of soft callus. Subsequently, the higher scattering amplitude values in intact bone and week 2 are attributed to the higher elastic coefficient values of cortical bone in the transverse direction derived from the SAM images (Preininger et al., 2011).

Also, the calculated p-values were lower than 0.05 for all the examined cases indicating that there are statistically significant differences between group means. The lowest p-values were calculated for the frequencies 0.2 and 1 MHz. However, statistical tests performed using the Tukey-Kramer method did not reveal significant differences between the healing stages week 3-week 6, week 6-week 9 and week 3-week 9 when pairwise comparisons were performed for the excitation frequencies 0.2, 0.4 and 1 MHz. Moreover, no statistically significant differences were detected for the frequency 0.8 MHz among all the examined cases, while for the excitation frequency 0.6 MHz only the pairs intact bone-week 6 and intact bone-week 9 revealed significant statistical differences between two means. Therefore, for the most of the examined healing weeks and frequencies, statistically significant decreases in scattering amplitude were detected at later stages of healing compared to the earlier stages of healing. Nonetheless, the results indicate that the use of the scattering amplitude value, as the main quantitative parameter for the evaluation of fracture healing, cannot discriminate effectively successive healing stages and more specifically variations between week 3-week 6, week 3-week 9 and week 6-week 9. Therefore, this study should be further extended considering more numerical models per healing stage as well as a longer monitoring period.

The frequency dependence of wave attenuation and scattering was also investigated theoretically in (Potsika *et al*., 2014a) in which the attenuation coefficient was found to be higher in the first healing stages and increased with increasing the frequency in the range 0–1.2 MHz. It should be mentioned that at low MHz frequencies, attenuation by scattering in soft tissue is typically 10–15% of the total attenuation,

while scattering is likely to be an important attenuation mechanism in the bone (Laugier and Haïat, 2011).

The bone healing process was also evaluated qualitatively from the acoustic pressure maps of Figs. 5.5–5.9. The maximum values of the acoustic pressure field (Pmax) in the backward direction were higher than 1 Pa for all the examined excitation frequencies reflecting the total pressure field which is the sum of the incident and scattered wave. Specifically, at 0.2 and 0.4 MHz and for the cases of intact bone, week 2 and week 9 a regular distribution of the acoustic pressure values was detected in almost parallel planes. Also, the presence of the fracture gap was clearly observed in the acoustic pressure maps at 0.4 MHz for weeks 2 and 3 as the parallel planes were interrupted around the fracture region. This indicates that the acoustic pressure maps derived for the proper excitation frequency could potentially provide information not only for the occurrence of a gap, but also for the size of the fracture. For higher frequencies no specific qualitative information was derived. This could be attributed to the higher attenuation of the propagating wave in higher frequencies. Also, among the numerical models of weeks 3, 6 and 9 which include the formation of callus, higher acoustic pressure values were derived during the early healing stages. This can be attributed to the callus consolidation followed by a gradual decrease of the inclusions' volume concentration and diameter during the healing process as well as by the cortical bone softening according to (Preininger *et al*., 2011).

However, the study of the complex bone scattering phenomena during fracture healing has received limited attention comparing to the evaluation of the FAS velocity, attenuation and the propagation of guided waves (Protopappas *et al*., 2005; Dodd *et al*., 2008, Machado *et al*., 2010; Machado *et al*., 2011; Rohrbach *et al*., 2013; Potsika *et al*., 2014a). The calculation of the sound pressure level using an axial transmission technique has been also proposed as a parameter which reflects the attenuation of the signal energy when it passes through the fracture gap (Machado *et al*., 2010; Dodd *et al*., 2008). It was found that the sound pressure level values initially decrease, while a great variation was observed in later healing stages. This was explained by the varying inner callus structure according to the different examined models, leading to different scattering/diffraction phenomena inside the fracture gap (Machado *et al.,* 2010).

An experimental study has been also presented by (Ferreira *et al.,* 2010) in which the backscattering method was applied for the characterization of pseudarthrosis in rats. An *in vitro* ultrasonic analysis of four bone samples with pseudarthrosis was presented using a 5-MHz circular transducer. The apparent integrated backscatter was measured and the calculated values for pseudarthrosis were always higher compared to normal bone. This was attributed to the complex matrix composition made of fibrous tissue, cartilage and calcified points with different acoustic impedance. Also, it was reported that the smaller attenuation and reflection in pseudarthrosis compared to bone permit a greater penetration of acoustic energy through the water sample interface. However, pseudarthrosis describes the non-consolidation or nonunion of a fracture when the process of bone repairing stops for some reason, while the present study deals with the evaluation of the backward propagating acoustic field in successive healing stages considering a normal process of bone healing.

Nevertheless, the numerical simulations were based on necessary assumptions and limitations. First of all, 2D geometries were established from the 2D SAM imaging data. Also, circular scatterers with a constant diameter for each healing stage were considered to calculate the effective material properties, while the geometry and distribution of the scatterers is random. However, it should be mentioned that the diameter of the pores is not the same even for the cortical fragments of the same SAM image. The effectiveness and accuracy of IEMA has been examined in (Potsika *et al*., 2014a; Aggelis *et al*., 2004) and this methodology has proven to be a useful tool which could simplify complex wave propagation numerical simulations in composite media via their replacement with equivalent homogeneous media with effective material properties. Furthermore, BEM provides accurate and stable frequency and time domain results through FFT. Consequently, for a known microstructure, the accuracy of the obtained results is given. Of course uncertainties related to the assumptions made about bone microstructure always exist. Also, according to (Ojanen *et al.*, 2016) embedding trabecular bone samples can strongly influence the acoustic impedance measured by SAM. It seems possible that material properties of the callus which are estimated from impedance measurements may be affected in a similar way. The application of a continuous incident wave is another limitation, while this study will be extended in the future to apply more realistic experimental conditions. Although the scattering amplitude alterations for the case of intact bone and different

excitation frequencies can be attributed to the application of IEMA, further investigation is required as for most tissues, the attenuation coefficient is a monotonically increasing function of frequency. Finally, despite the fact that 3 different geometries were used for each healing stage, all the SAM images were derived from different animals with varying material and geometrical features of the osseous and callus tissues. Therefore, this study lays the foundations for future experimental research to assess the backscattering method during fracture healing by performing serial measurements *in vivo* for the same specimens.

Chapter 6: The impact of cortical porosity on ultrasound propagation features

6.1 Introduction

Aging is associated with accelerated bone loss and increased bone fragility. For the assessment of osteoporosis, QUS became attractive as it is free of ionizing radiation, less expensive, and has a potential to assess bone material, strength, and structure, providing information relevant to bone strength beyond BMD (Sakata *et al.,* 2004). Best results from QUS measurements have been achieved using the through transmission technique at the calcaneus, a skeletal site consisting predominantly of trabecular bone (Grasel *et al.,* 2017). However, cortical bone also substantially contributes to the breaking strength of bones. In (Sakata *et al.,* 2004), an *in vitro* study on the assessment of human finger phalanges using QUS showed that the FAS velocity is affected by cortical area, cortical bone density, and cortical porosity, whereas attenuation only depends on the geometry of the medulla.

This chapter deals with the potential of QUS to detect changes in cortical microstructure using computational methods. Concerning the first 2D computational studies, the cortical bone was modeled as a linear elastic homogeneous plate and ultrasound simulations were performed for different plate thicknesses to investigate the thinning of the cortical cortex due to osteoporosis (Nicholson *et al.,* 2002; Bossy

et al., 2002). In (Moilanen *et al.,* 2007), X-ray computed tomography reconstructions were derived from the human radius in order to develop more realistic 3D computational models of cortical bone. It was shown that for plate thicknesses larger than the wavelength the FAS corresponds to a lateral wave which propagates at the bulk longitudinal velocity of bone, while for very thin plates the FAS wave propagates as the lowest-order symmetric plate mode. More recent 2D and 3D computational studies (Rohde *et al.,* 2014, Bourgnon *et al.,* 2014; Moilanen *et al,.* 2007; Grimal *et al.,* 2013; Granke *et al.,* 2011; Potsika *et al.,* 2017) take into consideration cortical microstructure, porosity and anisotropy. In (Grimal *et al.,* 2013), SAM images of human femoral neck were used to develop numerical models which account for the sample's overall shape, microstructure, cortical porosity, heterogeneous matrix elasticity and density. It was found that the FAS velocity is not influenced by trabecular bone properties or by the heterogeneities of the cortical bone mineralized matrix. On the other hand, the FAS was sensitive to variations in cortical porosity. In addition, in (Rohde *et al.,* 2014), SAM human femoral neck cross-sections were used to develop multivariate models for the prediction of pore size, porosity, and cortical thickness. It was shown that the FAS velocity decreases with increasing porosity, while an increase of the cortical thickness and pores' diameter leads to an increase in FAS velocity. It was also reported that cortical porosity has the strongest effect on the prediction of the FAS velocity. In addition, a 3D micromechanical model consisting of an anisotropic matrix pervaded by cylindrical pores was developed in (Granke *et al.,* 2011). It was found that, for the elderly population, the elastic properties of the mineralized matrix do not undergo large variations among different samples, while changes in the intracortical porosity account for most of the variations of mesoscopic elasticity.

The following subsections present a 2D computational study of ultrasonic propagation on healthy and osteoporotic models of cortical bone to examine the effect of porosity on the FAS velocity. The established numerical models incorporate the occurrence of BMUs, simply called non-refilled resorption lacunae (RL), as the predominance of resorption causes an increase in Haversian canal size leading to the increase of cortical porosity and fragility (Bourgnon *et al.,* 2014; Thomson, 1980). Initially, various microstructural models are established, mimicking normal and pathological tissue states with porosity of 5%, 10% and 16%. Then, numerical models are

presented to investigate the impact of changes in the number, size, position and depth of the RL on the FAS. The central excitation frequencies 0.5 and 1 MHz are examined. This is the first systematic and parametric numerical study to evaluate the FAS velocity variation along cortical bone derived from small, serial propagation paths for different porosities and frequencies, including the occurrence of pores with different sizes. The microstructural features were derived from SAM images from human tibia cross-sections (Raum *et al.,* 2014). Fig. 6.1a corresponds to a healthy specimen, while Fig. 6.1c to an osteoporotic bone with reduced cortical thickness. In Fig.6.1b increased number of unrefilled RL indicates an early stage of osteoporosis.

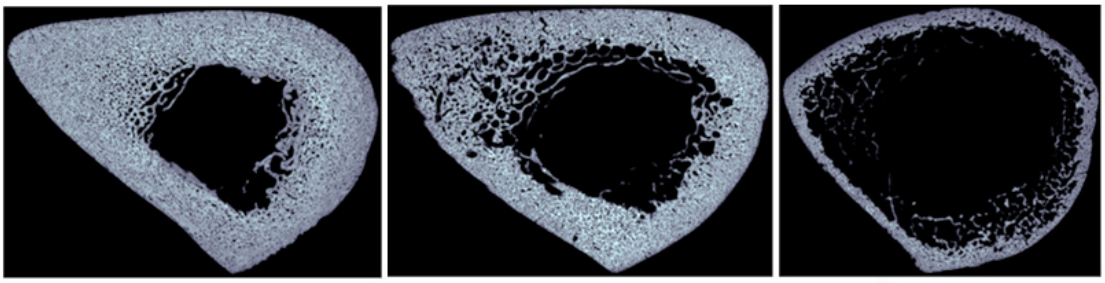

(a) Male, 70 years **(b)** Female, 85 years **(c)** Female, 94 years

Figure 6.1: Differences in the tibia in patients of increasing age depicted by 50-MHz using SAM. The progression of bone deterioration (from left to right) results in an accumulation of large RLs, cortical thinning and changes in the tissue stiffness (Potsika *et al.,* 2014d).

6.2 Validation of the Numerical Method: A Benchmark Problem

The most popular numerical methods for ultrasonic evaluation of cortical bone are the FDM, FEM and BEM. According to (Treeby *et al.,* 2012), for time domain modeling of broadband or high-frequency waves these methods can become cumbersome and slow due to the requirements for many grid points per wavelength and small time-steps to minimize unwanted numerical dispersion. In order to validate the FDTD code that is used in this work based on the software SimSonic, LIP, Paris, France (Bossy *et al.,* 2010; Bossy *et al.,* 2007), a benchmark problem was established. The results of the FDTD method are compared with the MATLAB toolbox k-Wave which combines pseudo-spectral and k-space methods, so the spatial gradients are calculated by using FFT rather than by using a finite difference stencil (Treebe *et al.,* 2012). The computational model of Fig. 6.2a was used corresponding to an intact cortical plate with thickness of 4 mm and length 40 mm surrounded by water. The material properties of bone and water are presented in Table 6.1. The grid size was set to 20

μm and the wave propagation simulation time was 10 μs. A point source and receiver were used to calculate the velocity at a distance of 12.5 mm between the transducers. The transducers were placed directly onto the cortical surface. A 1-MHz Gaussian pulse was used as the excitation signal. According to the results of Fig. 6.3, the two waveforms have the same time of arrival of the FAS, as well as the same qualitative behavior over time enhancing the accuracy of the FDTD method.

Table 6.1 Elastic coefficients and density used for the simulations (Potsika et al., 2016a, Bourgnon et al., 2014).

Propagation medium	**C_{11} (GPa)**	**C_{12} (GPa)**	**C_{66} (GPa)**	**P (g/cm^3)**
Water	2.25	2.25	0	1.00
Bone	28.71	10.67	9.02	1.85

In order to provide quantitative information for the differences of the two waveforms, a convergence study is conducted for the grid sizes of 50, 30 and 20 μm. The methodology of waveform rectification was used followed by numerical integration via the trapezoidal method. A full-wave rectifier converts the examined waveform to a waveform of constant polarity (positive or negative).

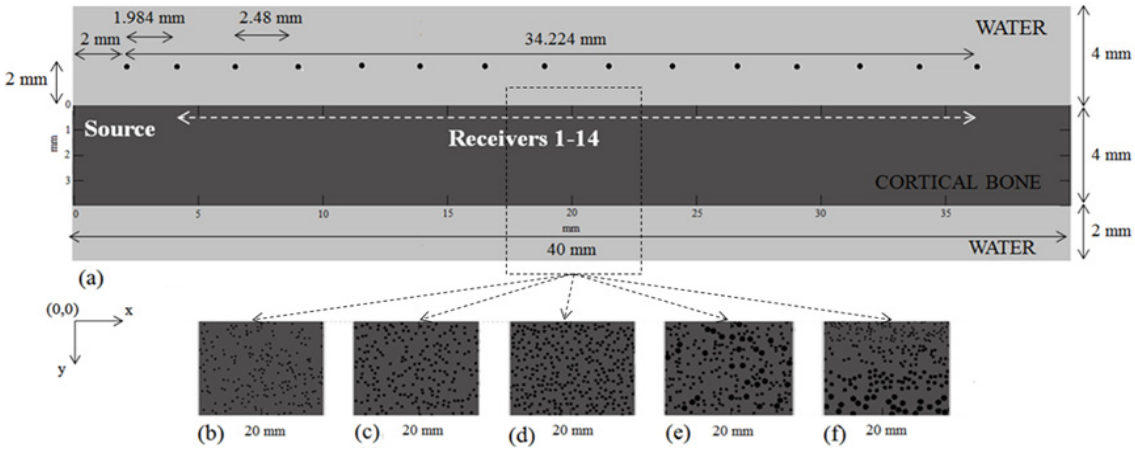

Figure 6.2: Numerical models of cortical bone corresponding to the first set of simulations (Series I_Po0-16) and Table 6.2, namely: (a) B_Hom, (b) B_Po5, (c) B_Po10, (d) B_Po16, (e) B_Po16_RL, (f) B_Po16_Gradual. For each geometry, only one of the three random porosity distributions is depicted in the form of 5 mm cortical segments derived from the original 40mm × 4mm plates. The ultrasound configuration is also presented in (**a**).

Specifically, the excitation signal was rectified, as well as the received waveforms from k-Wave and Simsonic. Numerical integration was applied using the trapezoidal method to derive the emitted and received signal area. Next, the ratio of the emitted signal area to the received waveforms' area is calculated, which is a quantitative indicator reflecting the whole area of interest. E_{sim} denotes this ratio calculated using Simsonic and E_{kw} using k-Wave. More specifically, the corresponding values were: (a) E_{kw} = 1166, E_{sim} = 1084 (difference$_{50\mu m}$ = 82) for 50 μm, (b) E_{kw} = 1935, E_{sim} = 1921 (difference$_{30\mu m}$=14) for 30 μm and (c) E_{kw} = 2924, E_{sim} = 2919 (difference$_{20\mu m}$ = 5) for 20 μm. Therefore, by further decreasing the grid size the value for E_{kw} will coincide with the value of E_{sim} indicating the accuracy of the 2 numerical methods.

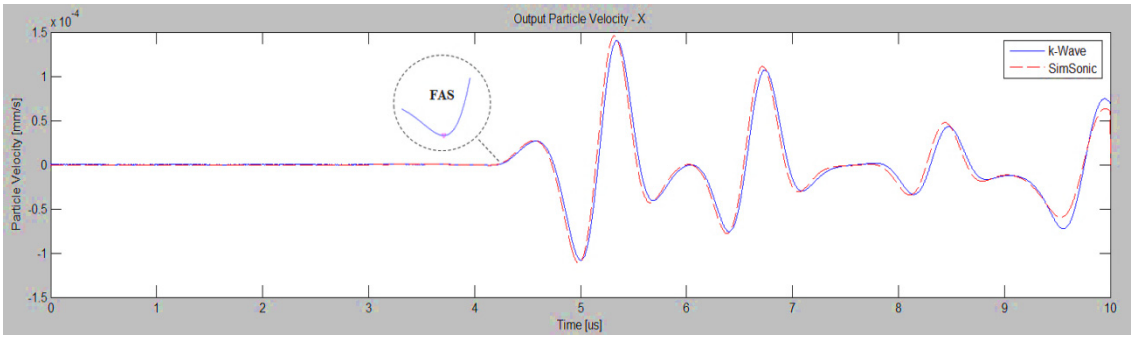

Figure 6.3: Particle velocity waveforms derived from two different numerical tools, Simsonic and k-Wave, for grid size 20 μm. The threshold for the detection of the FAS is also depicted.

6.3 Numerical Evaluation of Cortical Porosity Using Ultrasonic Techniques

6.3.1 Model geometry

In this section, the structural features of the computational models are described representing different cases of cortical porosity and pores' sizes as well as different number and distribution of RLs. The structural and material properties were derived from (Bourgnon *et al.,* 2014; Potsika *et al.,* 2016a), in which the Haversian canals of normal size were differentiated from the RLs to distinguish healthy bones (with no or few RL) from degenerated ones. As can be seen in Fig. 6.2, the cortical bone was modeled as a 2D plate (length 40 mm, width 4 mm) surrounded by water (upper surface 4 mm, lower surface 2 mm).

Two sets of numerical simulations were performed in order to evaluate: (a) porosity changes from 0% to 16% covering the whole region of cortical bone (Series I_Po0-16), (b) the occurrence of a single or a cluster of RLs in small propagation paths (Series II_RL). The selection of the porosities of Series I_Po0-16, and the sizes of the RL were based on previous studies investigating the interaction of ultrasound with cortical porosity (Rohde *et al.,* 2014; Malo *et al.,* 2013; Potsika *et al.,* 2014b; Bourgnon *et al.,* 2014). However, it should be emphasized that the evaluation of cortical porosity depends on several parameters such as age, gender and region of interest (Malo *et al*., 2013). The first set is presented in Fig. 6.2, in which cortical bone was modeled both as a homogeneous and nonhomogeneous medium to account for the cases of: (a) intact bone (Fig. 6.2a), (b) porosity 5% (Fig. 6.2b), (c) porosity 10% (Fig. 6.2c), and (d) porosity 16% (Fig. 6.2d, e, and f). In Table 6.2, the exact structural features are presented concerning the porosity as well as the number and dimensions of the normal and larger pores. For each microstructural scenario of Table 6.2, a total of three numerical models were established and the mean local FAS velocity values were calculated, as well as the standard error.

Circular scatterers were considered in the transverse direction and the selected radii of normal pores and RL are presented in Table 6.2. Given the porosity and the dimensions of the plate and scatterers, the number of the pores can be calculated. An algorithm was developed to generate the osseous and soft tissues as greyscale values and the “porosity maps” with a random distribution of the pores. The scatterers were not in contact and did not merge with each other as well as with the cortical boundaries.

Fig. 6.4 illustrates cortical segments of Series II_RL in which the cortex of a long bone was modeled initially as a 2D homogeneous plate including the presence of 1 RL at different lengths, depths and diameters (Fig. 6.4a–e). Then, Fig.6.4f–h account for cortical microstructure to simulate the case of normal remodeling (Table 6.2: cases B_Po5_RL1, B_Po5_RL3, B_Po5_RL5) including a single or a cluster of RL in the center of the plate.

6.3.2. Material properties

The cortical bone was modeled as an isotropic, linear elastic medium. It was assumed that the soft tissues surrounding the cortical plate, as well as the circular pores are

composed of water. Table 6.1 summarizes the material properties assigned to the cortical bone, scatterers and soft tissues which were derived from (Potsika *et al.,* 2016a, Bourgnon *et al.,* 2014).

Table 6.2 Examined cases in the tangential direction for the second set of the simulations.

	Description	**Porosity (%)**	**No. of pores**	**Pores' radius (μm)**	**No. of RL/RLs**	**Radius of RL/RLs (μm)**
B_Hom	Homogeneous bone	0	0	–	–	–
B_Po5	Porous bone, normal pores	5	1592	40	–	–
B_Po5_RL 1	Porous bone, normal pores and 1 RL	5	1592	40	1	115
B_Po5_RL 3	Porous bone, normal pores and 3 RLs	5	1592	40	3	115
B_Po5_RL 5	Porous bone, normal pores and 5 RLs	5	1592	40	5	115
B_Po10	Porous bone, normal pores	10	1592	60	–	–
B_Po16	Porous bone, normal pores	16	2263	60	–	–
B_Po16_RL	Porous bone, normal pores and RLs	16	1400	60	235	115
B_Po16_ Gradual	Gradual distribution of the pores, normal pores and RLs	16	1775	40, 60, 80	192	115

6.3.3. Ultrasound configuration

Simulations of ultrasound propagation were performed in the tangential direction (Fig. 6.2a). Calculations were conducted by placing one point source and 14 point receivers: (a) at a distance 2 mm from the upper cortical layer (non-contact transducers), (b) directly onto the cortical cortex (implanted transducers). The distance between two successive receivers was 2.48 mm implying that the distance between the emitter and the receivers ranges from 1.984 to 34.224 mm (receiver 1 (R1) – receiver 14 (R14)). The width of each transducer was equal to 11 elements.

The use of a linear array of transducers is in agreement with existing ultrasonic devices for bone characterization such as the bidirectional device in (Muller *et al.,* 2005).

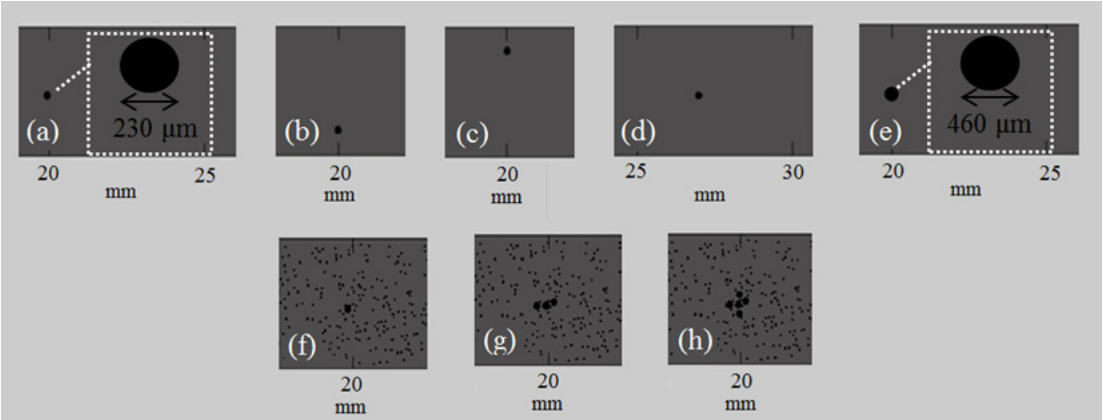

Figure 6.4: Numerical models of cortical bone corresponding to the second set of simulations (Series II_RL) focusing on the regions of the occurrence of RL: (a) homogeneous bone, 1 RL with center coordinates (x, y) = (20, 2), (b) homogeneous bone, 1 RL with center coordinates (x, y) = (20, 3), (c) homogeneous bone, 1 RL with center coordinates (x, y) = (20, 1), (d) homogeneous bone, 1 RL with center coordinates (x, y) = (27, 2) mm, (e) homogeneous bone, 1 RL with center coordinates (x, y) = (20, 2) and double the diameter, (f) B_Po5_RL1, (g) B_Po5_RL3, (h) B_Po5_RL5.

6.3.4. Determination of the ultrasonic wave propagation path and velocity

The "local FAS velocities" correspond to small propagation paths and were calculated as the difference in the FAS arrival time of the signals from successive receivers (distance 2.48 mm). In this way, the structural changes along small regions of cortical bone can be estimated due to porosity variations or to the presence of larger pores. When multiple receivers are considered, the change in the FAS arrival time Δt (μs) can be calculated using $\Delta t(x) = t(x_i) - t(x_{i-1})$, where i is the number of the receiving position, $t(x_i)$ is the arrival time of the signal at receiver i and $t(x_{i-1})$ is the arrival time at the previous receiver (Dodd *et al.,* 2008). For the detection of the FAS a threshold was applied to the receiving waveforms corresponding to the identification of the first signal extremum (Fig. 6.3) (Potsika *et al.,* 2014c).

6.3.5. Boundary conditions

The cortical cortex was surrounded by soft tissues and perfectly matched layers (PML) were used to limit spurious reflections from the boundaries simulating an

infinitely long model. The PML efficiency was set to 80 dB which means that the wave reflected by the PML is expected to be 80 dB below the amplitude of an incident wave, in the case of normal incidence (Bossy *et al.,* 2010; Bossy *et al.,* 2007).

6.3.6. Numerical simulation and signal analysis in the time domain

The numerical solution of the 2D wave propagation problem was carried out by using an FDTD code (Bossy *et al.,* 2010; Bossy *et al.,* 2007). The computations are based on a system of elastodynamic equations corresponding to the propagation of mechanical waves in continuous media which obey Hooke's law and are expressed as:

$$\rho(x)\frac{\partial u_i}{\partial t}(x,t)=\sum_{j=1}^{d}\frac{\partial T_{ij}}{\partial x_j}(x,t)+f_i(x,t)\,, \tag{6.1}$$

$$\frac{\partial T_{ij}}{\partial t}(x,t)=\sum_{k=1}^{d}\sum_{l=1}^{d}c_{ijkl}(x)\frac{\partial u_k}{\partial x_l}(x,t)+\theta_{ij}(x,t)\,, \tag{6.2}$$

where subscripts i={1,…,d} refer to the direction of space and d to the space dimension (*d*=2 for 2D computational models), x and t are the space and time variables, ρ(x) is the mass density and c(x) is the fourth-order rigidity tensor. These parameters entirely define the material properties and geometry of the medium. u_i (x, t) are the vector components of the particle velocity field, T_{ij} (x, t) are the components of the stress tensor, while f_i denote the vector components of force sources and θ_{ij} denote the tensor components of strain rate sources.

A Hanning pulse was used as the excitation signal including four sinusoidal cycles (Potsika *et al.,* 2014a). The examined central angular frequencies were 0.5 and 1 MHz. The duration of the simulations was 25 μs. The accuracy of the solution depends on the relation between the element size and the wavelength. According to the software requirements, the stability condition is defined as:

$$\Delta t \leq \frac{1}{\sqrt{d}}\frac{\Delta x}{c_{max}}\,, \tag{6.3}$$

where Δt and Δx denote the time and spatial steps used to approximate time or spatial derivatives, c_{max} is the largest speed of sound amongst all the simulated materials (c_{max} = c_{bone} = 3939 m/s), and d refers to the space dimension (d=2). The grid size was

set to 8 μm, and a convergence study is presented in the following subsection to demonstrate the accuracy of the findings.

The grid size must be dense enough to ensure an accurate numerical solution and to minimize the computational cost. In addition, it must be small enough in comparison to the diameter of the pores. The convergence study is based on the numerical model B_Po5 which integrates the smallest scatterers among all the geometries of Table 2. Two transducers were considered which were placed directly onto the cortical surface and their distance was set to 20 mm. FDTD simulations were conducted and the FAS velocities were calculated for the central excitation frequency 1 MHz and the grid step sizes 4, 8, and 16 μm. The calculated FAS values were 3499 m/s for 4 μm, 3495 m/s for 8 μm, and 3489 m/s for 16 μm. It can be concluded that the 8-μm grid size is a good compromise for an accurate numerical solution and less time consuming simulations.

6.3.7. Statistical analysis

A statistical analysis was conducted and the results are presented as local mean FAS velocity ± standard error. Linear regression analysis and one-way analysis of variance (one-way ANOVA) were used to evaluate changes in porosity. The statistical findings were considered significant for p-values less than 0.05 (Rohrbach *et al.,* 2012).

6.4 Results

Figs. 6.5–6.13 present the results derived from the two simulation sets of Figures 6.2 and 6.4 and the central excitation frequencies 0.5 and 1 MHz. As multiple receivers were considered and small propagation paths were examined, the horizontal axis represents the distance of each receiving element from the starting point of the plate with coordinates (x, y) = (0, 0). First, in subsection 6.4.1, the results are presented for porosity changes from 0–16%, and then, in subsection 6.4.2, the findings corresponding to the occurrence of a single or a cluster of RLs in small propagation paths at different depths, lengths and sizes.

6.4.1. First set of simulations (Series I_Po0-16)

6.4.1.1. Implanted transducers

Figure 6.5 presents the FAS velocity variation profile from multiple implanted receivers considering cortical bone as a nonhomogeneous medium with porosity from 0 to 16%. The local FAS velocities were calculated as the mean values from the same receiving position of three simulation maps with different random distributions of the pores keeping the same microstructure characteristics. The mean FAS velocities and the standard error bars for the excitation frequency 0.5 MHz are presented in Fig. 6.5a–c and for 1 MHz in Fig. 6.5d–f.

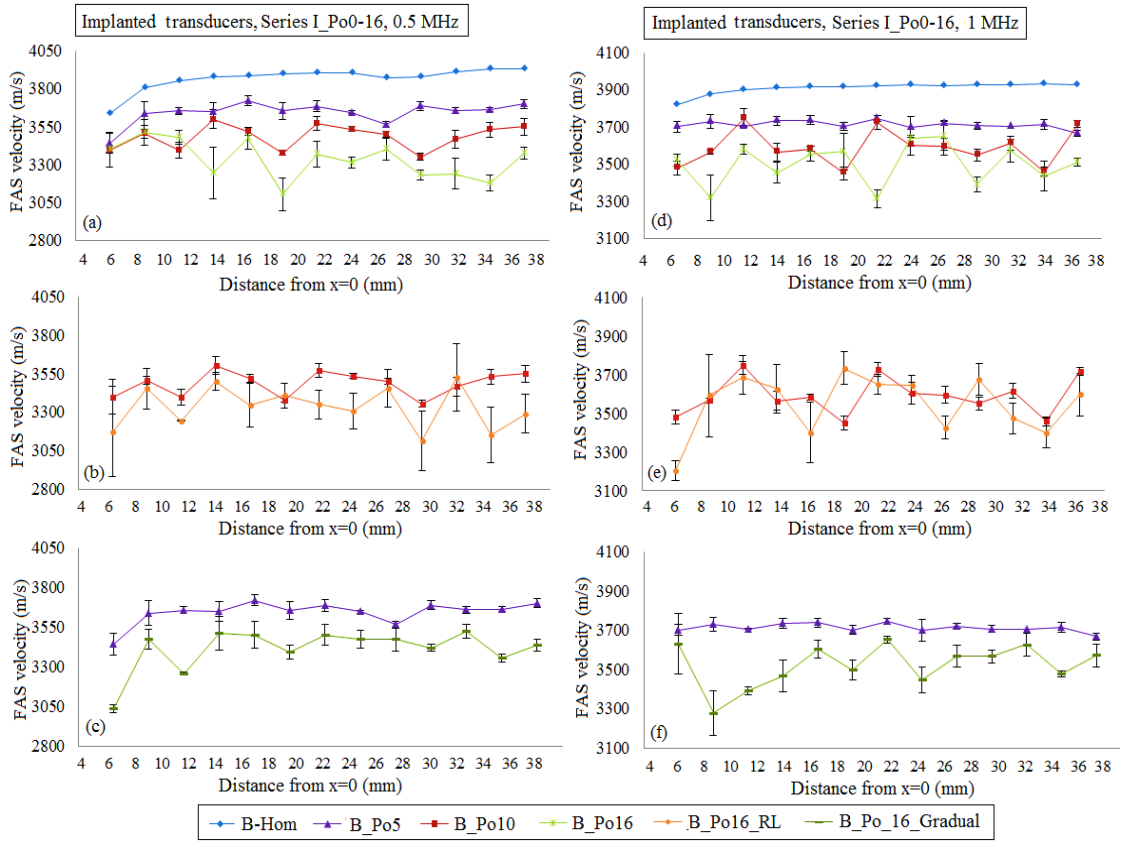

Figure 6.5: The potential of the mean local FAS velocity to detect changes in cortical porosity from 0%–16%. The diagrams correspond to the first set of simulations under the assumption of implanted transducers and the excitation frequencies: (a)–(c) 0.5 MHz and (d)–(f) 1 MHz. The standard error bars demonstrate the FAS velocity variation for the three numerical models established for each porosity scenario.

It can be observed that a porosity increase leads to the decrease of the FAS velocity variation profile, and this is more apparent for the excitation frequency 0.5 MHz.

More specifically, considering the case B_Hom as the reference case, the relative percentage differences in Fig. 6.5a for the cases B_Po5, B_Po10 and B_Po16 were calculated in the range 4.32–7.87%, 6.58–13.53% and 6.41–20.34%, respectively. These findings can be directly compared with Fig. 6.5d. For the excitation frequency 1 MHz, the relative percentage differences for the cases B_Po5, B_Po10 and B_Po16 were from 3.14% to 6.67%, 3.91–12.10% and 7.35–15.56%, respectively. Then, Figures 4b, c, e, and 4f present more realistic scenarios of pathology including both normal pores and RLs for the case B_Po16_RL (Fig. 6.5b for 0.5 MHz and Figure 4e for 1 MHz) and the gradual formation of osteoporosis (Fig. 6.5c for 0.5 MHz and Fig. 6.5f for 1 MHz). In Fig. 6.5b, a porosity increase up to 16% including the occurrence of RLs (B_Po16_RL) leads to a decrease of the local FAS velocities and the relative percentage differences were from 9.23% to 19.71% for the excitation frequency 0.5 MHz. In addition, it was observed that there are few positions (e.g. Fig. 6.5b, x = 30–32 mm) which show a minor increase of the FAS velocity locally despite the porosity increase. Fig. 6.5e presents the FAS velocities for B_Po16_RL and the excitation frequency 1 MHz. It can be seen that as the frequency increases it is more difficult to discriminate a specific FAS velocity behavior among the cases B_Po10 and B_Po16_RL. Finally, Fig. 6.5c and 6.5f show the potential of the local FAS velocity to detect the gradual formation of osteoporosis.

The diagram B_Po5 is depicted in the same diagram with B_Po16_Gradual as when osteoporosis is gradually formed the upper cortical layer has the microstructure of a healthy bone, while the porosity and pores' size increase starts from the endosteal region. The relative percentage differences for the case B_Po16_Gradual keeping B_Hom as the reference case were calculated from 8.70% to 16.63% for the excitation frequency 0.5 MHz (Fig. 6.5c) and from 5.02% to 15.49% for 1 MHz (Fig. 6.5f), respectively.

Then, one-way ANOVA was conducted and the p-value was calculated. It was found to be lower than 0.05 ($p \approx 0$), implying that there are significant differences between group means. Linear regression analysis was also performed, as in some receiving positions of Fig. 6.5 the mean FAS velocity was found to increase locally despite the porosity increase. Fig. 6.6 shows that linear regression analysis is not influenced by local phenomena, and the examined cases can be discriminated. The corresponding equations, coefficients of determination (R^2) and root mean square errors (RMSE) are

included in Tables 6.3, 6.4. All the results are not presented graphically to reduce complexity, as similar findings to Fig. 6.6 were derived.

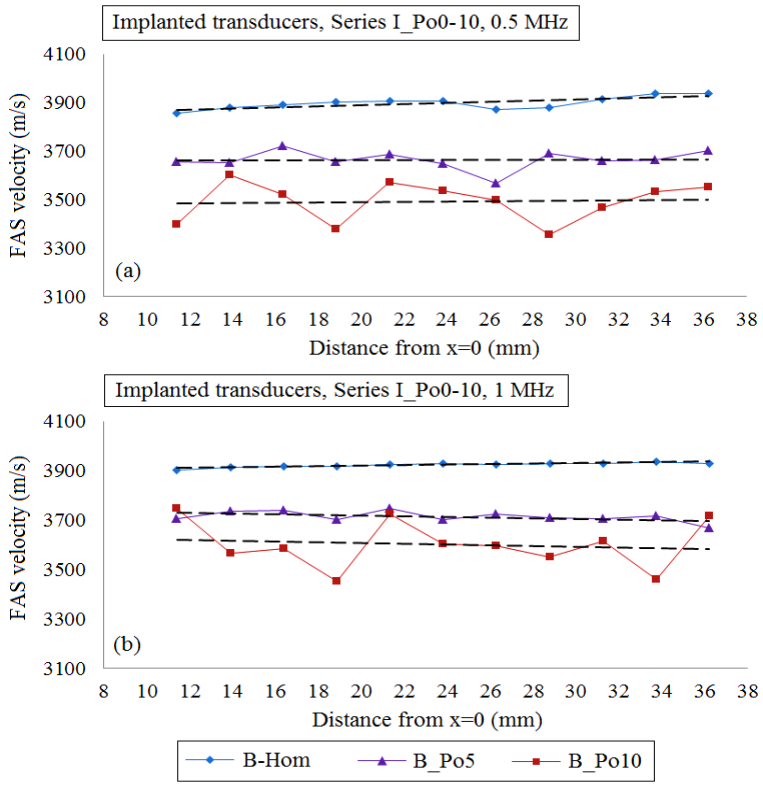

Figure 6.6: Linear fit derived from multiple receiving positions for cortical porosities from 0 to 10%. The diagrams correspond to the first set of simulations under the assumption of implanted transducers and the excitation frequencies: (a) 0.5 MHz, and (b) 1 MHz. The corresponding equations, coefficients of determination and root mean square errors are presented in Tables 6.3, 6.4.

Table 6.3 Linear fit of the mean FAS velocities derived from all the receiving positions and the excitation frequency 0.5 MHz.

	Implanted transducers			**Transducers at a distance of 2 mm from the cortical surface**		
	y = ax + b	**R^2**	**RMSE**	**y = ax + b**	**R^2**	**RMSE**
B_Hom	y = 2.27x + 3844	0.54	16.56	y = 3.00x + 3815	0.52	22.79
B_Po5	y = 0.17x + 3661	0.01	37.94	y = 2.81x + 3577	0.17	48.84
B_Po10	y = 0.72x + 3475	0.01	78.51	y = 0.28x + 3489	0.01	66.92
B_Po16	y = −4.37x + 3417	0.09	110.08	y = −3.64x + 3385	0.53	24.58
B_Po16_RL	y = −4.09x + 3434	0.06	123.45	y = −3.23x + 3410	0.06	92.93
B_Po16_ Gradual	y = 1.38x + 3409	0.02	75.88	y = 1.57x + 3397	0.03	59.72

Table 6.4 Linear fit of the mean FAS velocities derived from all the receiving positions and the excitation frequency 1 MHz.

	Implanted transducers			**Transducers at a distance of 2 mm from the cortical surface**		
	y = ax + b	**R^2**	**RMSE**	**y = ax + b**	**R^2**	**RMSE**
B_Hom	y = 1.08x + 3898	0.80	4.26	y = 1.65x + 3879	0.80	6.37
B_Po5	y = −1.41x + 3748	0.28	17.82	y = −1.81x + 3759	0.19	29.16
B_Po10	y = −1.54x + 3639	0.02	93.23	y = −1.78x + 3628	0.06	57.31
B_Po16	y = −1.36x + 3549	0.01	100.58	y = −0.06x + 3510	0.01	30.84
B_Po16_RL	y = −5.38x + 3702	0.13	111.10	y = −3.21x + 3647	0.28	36.73
B_Po16_ Gradual	y = 3.96x + 3440	0.15	72.96	y = 4.49x + 3406	0.16	73.61

6.4.1.2. Transducers at a distance of two millimeters from the cortical cortex

Figure 6.7 presents snapshots of ultrasound wave propagation for indicative cases considering the excitation frequency 1 MHz and time instant 10 μs. It is shown that, as porosity increases, multiple scattering mechanisms evolve (Figs. 6.7d, e, and f). In addition, it can be observed that the application of PML limits spurious reflections from the boundaries, but the phenomenon is not totally diminished.

Then, in Fig. 6.8 the received waveforms are illustrated derived from receiver R8, which is placed above the region of the cluster of 5 RLs (Fig. 6.5h) for indicative cases and the excitation frequency 1 MHz. It can be seen in Fig. 6.9a that the increase of porosity induces a delay in the propagation of the signal if we compare the zero-crossing times.

An increase in amplitude was also found with increasing the porosity. A comparison of the waveforms of the cases B_Po16 and B_Po16_RL is presented in Fig. 6.8b, showing that the occurrence of the larger pores has an effect on the received waveforms. However, in Fig. 6.8c, the waveforms for the cases B_Po5 and B_Po5_RL5 almost coincide, while no difference can be observed at the corresponding snapshots of Fig. 6.7.

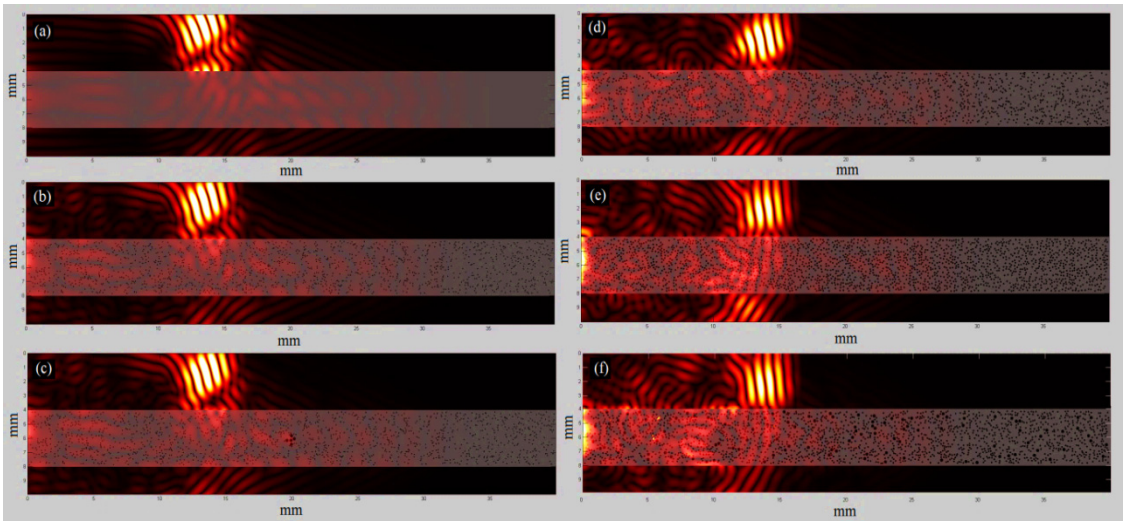

Figure 6.7: Snapshots of wave propagation for the first set of simulations using non-contact transducers for the excitation frequency of 1 MHz and time instant 10 μs for the cases: (a) B_Hom, (b) B_Po5, (c) B_Po5_RL5, (d) B_Po10, (e) B_Po16, and (f) B_Po16_RL.

Fig. 6.9 presents the mean FAS velocities and standard error bars when the transducers are placed at a distance of 2 mm from the cortical surface. The porosities from 0% to 16% are examined as in Fig. 6.5. In Figs. 6.9a and d, low FAS velocities are observed for the receivers which are placed before x = 12 mm due to the direct propagation of the FAS via the soft tissues.

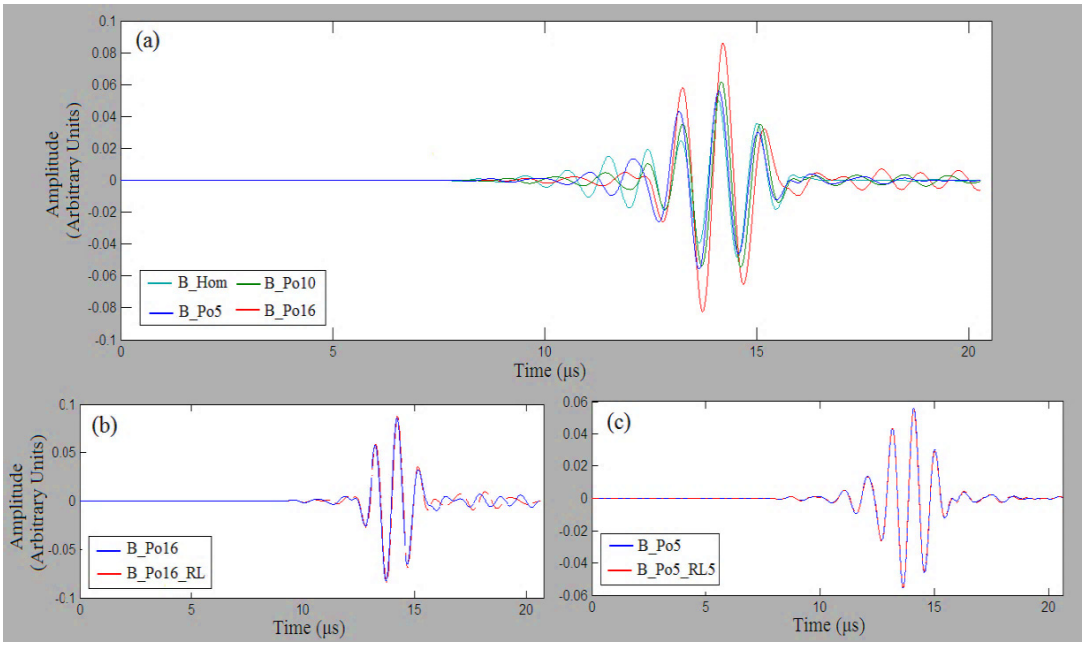

Figure 6.8: Waveforms derived from receiver R8 for the excitation frequency 1 MHz and simulation time 20 μs comparing the examined cases: (a) B_Hom, B_Po5, B_Po10 and B_Po16, (b) B_Po16 and B_Po16_RL, (c) B_Po5 and B_Po5_RL5.

More specifically, considering the case B_Hom as the reference case, the relative percentage differences in Fig. 8a for 0.5 MHz and B_Po5, B_Po10 and B_Po16 were calculated in the range 4.71–7.65%, 7.22–12.83% and 12.90–17.60%, respectively. For the excitation frequency 1 MHz (Fig. 6.9d), the relative percentage differences for B_Po5, B_Po10 and B_Po16 were from 4.24% to 6.89%,

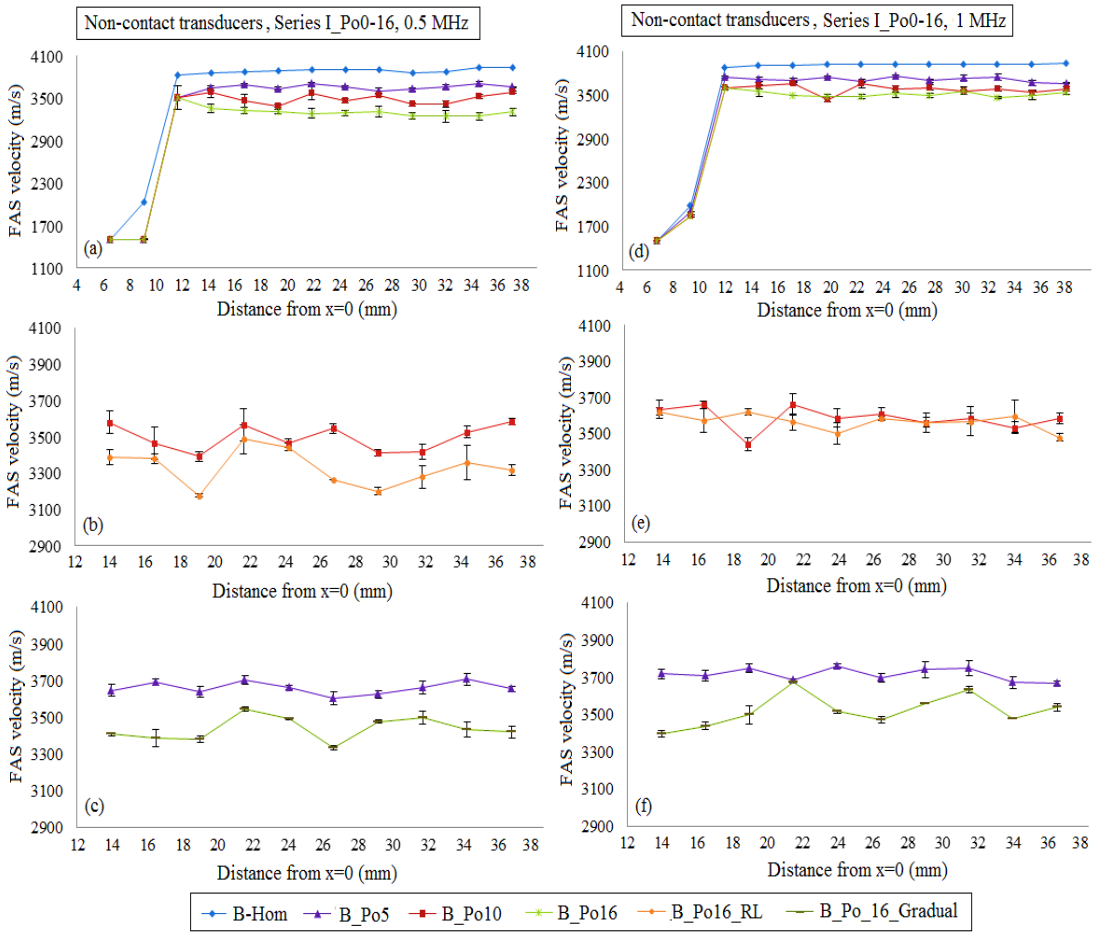

Figure 6.9: The potential of the mean local FAS velocity to detect changes in cortical porosity from 0% to 16%. The diagrams correspond to the first set of simulations when the transducers are placed at a distance of 2 mm from the cortical cortex. The results for the excitation frequencies: (a)–(c) 0.5 MHz, (d)–(f) 1 MHz are presented. The standard error bars demonstrate the FAS velocity variation for the three numerical models established for each porosity scenario.

6.37–12.19% and 8.78–11.82%, respectively. Then, Figs. 6.9b and e correspond to the case B_Po16_RL and are directly compared with the case B_Po10. Keeping B_Hom as the reference case the relative percentage differences for B_Po16_RL were from 10.51 to 18.33% for 0.5 MHz (Fig. 6.9b) and 7.17–11.62% for 1 MHz (Fig. 6.9e).

Thus, even if according to Fig. 6.8b, the two waveforms seem to coincide for propagation time less than 10 μs, however the calculation of the FAS in small propagation paths shows quantitative differences when large pores are considered. The results for the gradual distribution of the pores are shown in Figs. 6.9c and 9f. The relative percentage differences for B_Po16_Gradual were derived from 9.02% to 14.55% for the excitation frequency 0.5 MHz (Fig. 6.9c) and from 6.31% to 12.95% for 1 MHz (Fig. 6.9f), respectively. It should be mentioned that Figs. 6.9b, c, e, and 9f do not show the whole propagation path as the initial low values of Figs. 6.9a, b corresponding to the direct FAS propagation through the water were neglected. In addition, linear regression analysis was performed and the results are depicted in Tables 6.3 and 6.4. It was shown that the examined cases can be discriminated even for the diagrams of Figure 6.9e in which the mean local FAS velocities do not show a specific behavior with increasing the porosity.

Concerning one-way ANOVA, the p-value was lower than 0.05 ($p \approx 0$) ignoring the receiving positions near the source ($d < 12$ mm). The reason for not considering the first receivers in the calculations is that as it can be seen in Figs. 6.9a, d for $d < 12$ mm, the FAS wave propagates directly in the soft tissues and low velocities are derived in comparison to the bulk longitudinal velocity of bone. This assumption was also considered for the cases of Fig. 6.5 to keep the same conditions.

6.4.2. Second set of simulations (Series II_RL)

This section presents the results corresponding to the occurrence of: (a) a single RL at different depths, lengths and sizes under the assumption of cortical homogeneous bone (Figs. 6.10, 6.12), (b) a single or a cluster of RL taking into account cortical microstructure (Figs. 6.11, 6.13).

6.4.2.1. Implanted transducers

In Figs. 6.10 and 6.11, implanted transducers are used and the excitation frequencies 0.5 and 1 MHz are examined. Figs. 6.10a, b, and c depict the local FAS velocity variation profile for the excitation frequency 0.5 MHz and the presence of a single RL. For comparison purposes, all the diagrams include the calculated values for the intact bone (blue line) and the case of a single RL with center coordinates (x, y) = (20, 2) (red line). All the diagrams start from a distance of 15 mm in the x axis as for lower

cortical lengths all the curves coincide. In Fig. 6.10a, it can be observed that for 0.5 MHz the occurrence of one RL in the center of the plate can be captured by the receivers which are placed directly above the region of interest showing an increase of the FAS velocity of 35 m/s compared to the homogeneous bone diagram. In addition, keeping the same RL position and doubling the diameter of the pore (orange line), the receivers which are placed in the position x = 19–21 mm are the first to detect an increase of the FAS velocity of 58 m/s in comparison to the homogeneous bone value. Fig. 6.10b shows the impact of the depth of the RL occurrence on the FAS velocity. It can be seen that, if by placing the RL at a higher cortical surface (grey line), the receivers which first capture the presence of a pore are placed again in the propagation path between x = 19–21 mm showing a velocity decrease of 29 m/s comparing to the reference case of homogeneous bone. On the other hand, when the depth from the cortical surface increases (purple line), there is a delay in the identification of the RL by the receivers above the region of x = 25–21 mm showing an increase of the FAS velocity of 57 m/s. Finally, Fig. 6.10c shows that if by changing the RL position along the x axis, the receivers which are placed above the region of interest are the first to detect an increase of the FAS velocity of 23 m/s revealing the position of the RL formation.

Figs. 6.10d, e, and f present the local FAS velocity variation profile for the excitation frequency 1 MHz and the presence of a single RL. In Fig. 6.10d, it can be seen that the occurrence of a single RL in the center of the plate (red line) can be identified with a delay by the receivers which follow the region of interest (around x = 23 mm) showing an increase of the FAS velocity of 23 m/s. In addition, it was found that when the diameter of the RL is doubled (orange line), the same receivers are the first to detect an increase of the FAS velocity of 41 m/s. Then, Fig. 6.10e indicates that by increasing the depth from the cortical surface (purple line), the larger pore cannot be detected as this diagram coincides with the case of homogeneous bone (blue line). On the other hand, the occurrence of the RL near the upper cortical surface (grey line) leads to a decrease of the FAS velocity of 46 m/s derived from the receivers directly above the region of interest. Finally, Fig. 6.10f shows that by changing the position of the RL along the x axis, the receivers which are placed approximately at a distance of 3 mm after the pore are the first to capture an increase of the FAS velocity of 47 m/s.

Then, Fig. 6.11 deals with the potential of the local FAS velocity to detect the occurrence of a single or a cluster of three or five large pores in the center of the plate taking into account the nonhomogeneous nature of cortical bone. Fig. 6.11a presents the FAS velocity variation profile for the excitation frequency 0.5 MHz, while Fig. 6.11b the FAS values for 1 MHz considering the diagram of B_Po5 (red line) as the reference case. For the excitation frequency 0.5 MHz the relative percentage differences were calculated in the range: (a) 0.04 – 0.28% for B_Po5_RL1, (b) 0.04 – 1.36 % for B_Po5_RL3 and (c) 0.04 – 3.08 % for B_Po5_RL5. It can be seen that the first receivers which can identify the RL occurrence are placed above the region of interest (x = 20–22 mm). A 2-mm delay in the detection of the larger pores

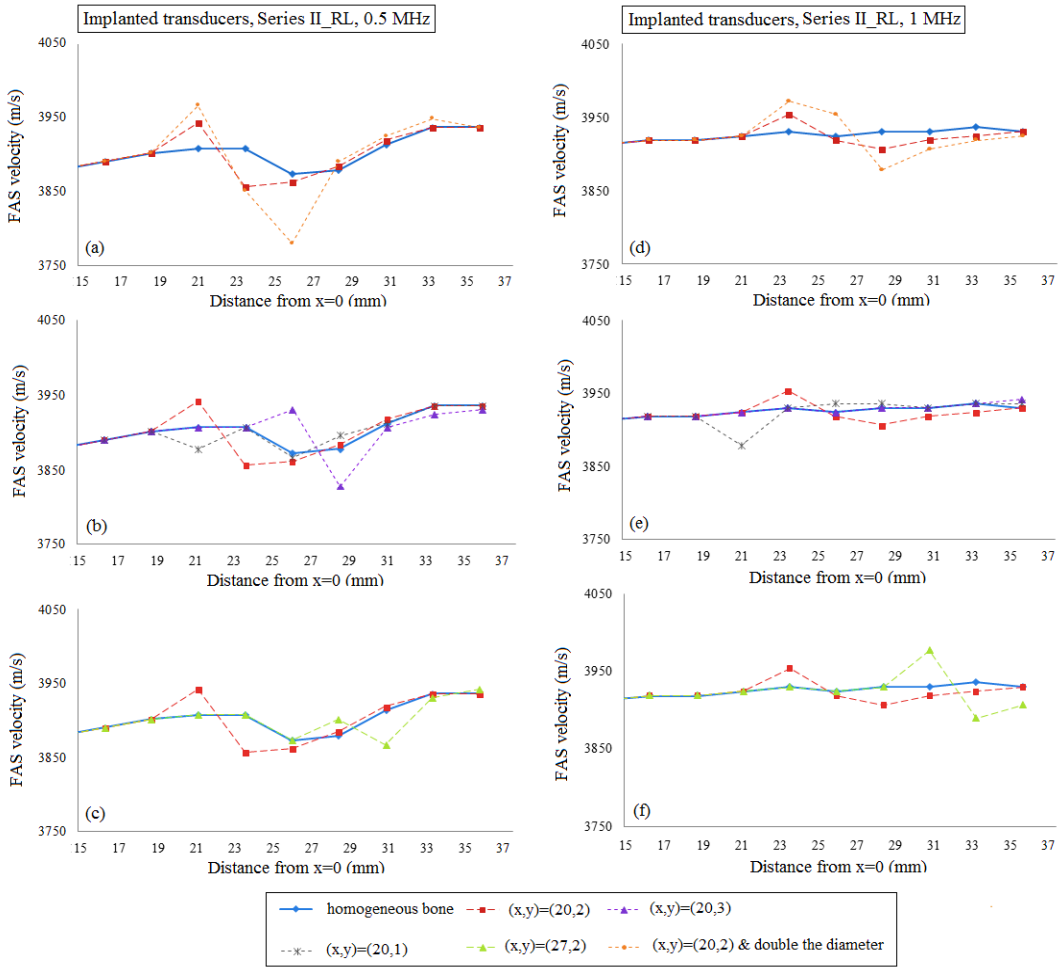

Figure 6.10: The potential of the local FAS velocity to detect the occurrence of a single RL considering cortical bone as a homogeneous medium (geometries illustrated in Figs. 6.3a–e). The diagrams correspond to the second set of simulations under the assumption of implanted transducers and the excitation frequencies: (a)–(c) 0.5 MHz, and (d)–(f) 1 MHz. The legend describes the center coordinates of the RL.

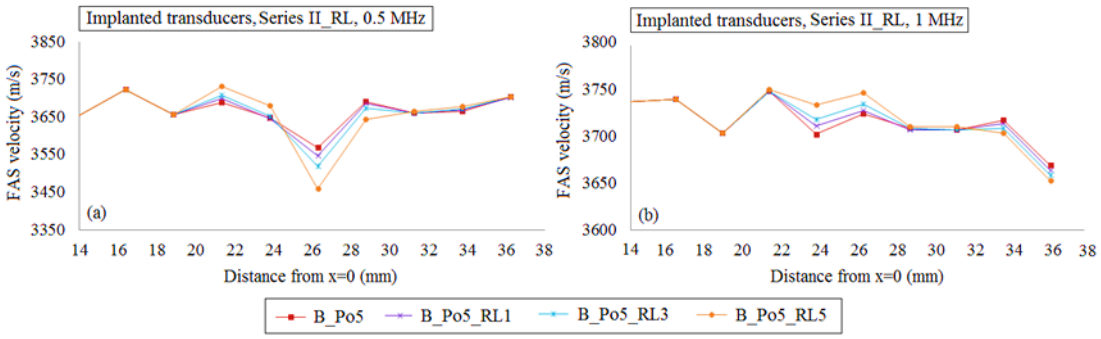

Figure 6.11: The potential of the local FAS velocity to detect the occurrence of a single or a cluster of RL considering cortical bone as a nonhomogeneous medium for the cases B_Po5, B_Po5_RL1, B_Po5_RL3 and B_Po5_RL5 (geometries illustrated in Figs. 6.4f–h). The diagrams correspond to the second set of simulations under the assumption of implanted transducers and the excitation frequencies: (a) 0.5 MHz, and (b) 1 MHz.

is observed in Fig. 6.11b for 1 MHz as they are first identified from the receivers in the region x = 22–24 mm. Lower relative percentage differences were calculated compared to 0.5 MHz from: (a) 0.05–0.24% for B_Po5_RL1, (b) 0.23–0.42% for B_Po5_RL3, and (c) 0.05–0.85% for B_Po5_RL5.

6.4.2.2. Transducers at a distance of two millimeters from the cortical cortex

Figs. 6.12a–c present the local FAS velocity variation profile for the excitation frequency 0.5 MHz and the presence of a single RL by placing the transducers at a distance of 2 mm from the cortical cortex. All the diagrams include the case of intact homogeneous bone (blue line) and the case of a single RL with center coordinates (x, y) = (20, 2) (red line). In Fig. 6.12a, it can be seen that, for 0.5 MHz, the occurrence of one RL in the center of the plate can be captured by the receivers which are placed directly after the region of interest (between x = 21–23 mm) showing a decrease of the FAS velocity of 17 m/s compared to the homogeneous bone diagram. Then, if we keep the same RL position and double the diameter of the RL (orange line) the same receivers are the first to detect an increase of the FAS velocity of 41 m/s in comparison to the homogeneous bone value. Fig. 6.12b shows the impact of the RL depth on the FAS values. It can be observed that by placing the RL at a higher cortical layer (grey line), the receivers which first capture the presence of a pore are placed directly above the region of interest showing a velocity decrease of 89 m/s compared to the reference case of homogeneous bone. However, if we increase the depth from the cortical cortex (purple line), the receivers which are placed at a

distance almost 5 mm from the RL are the first to identify its occurrence showing an increase of the FAS velocity of 51 m/s. Finally, Fig. 6.12c shows that if we change the RL position along the x-axis, the receivers which are placed above the region of interest are the first to capture an increase of the FAS velocity of 23 m/s revealing the position of the larger pore.

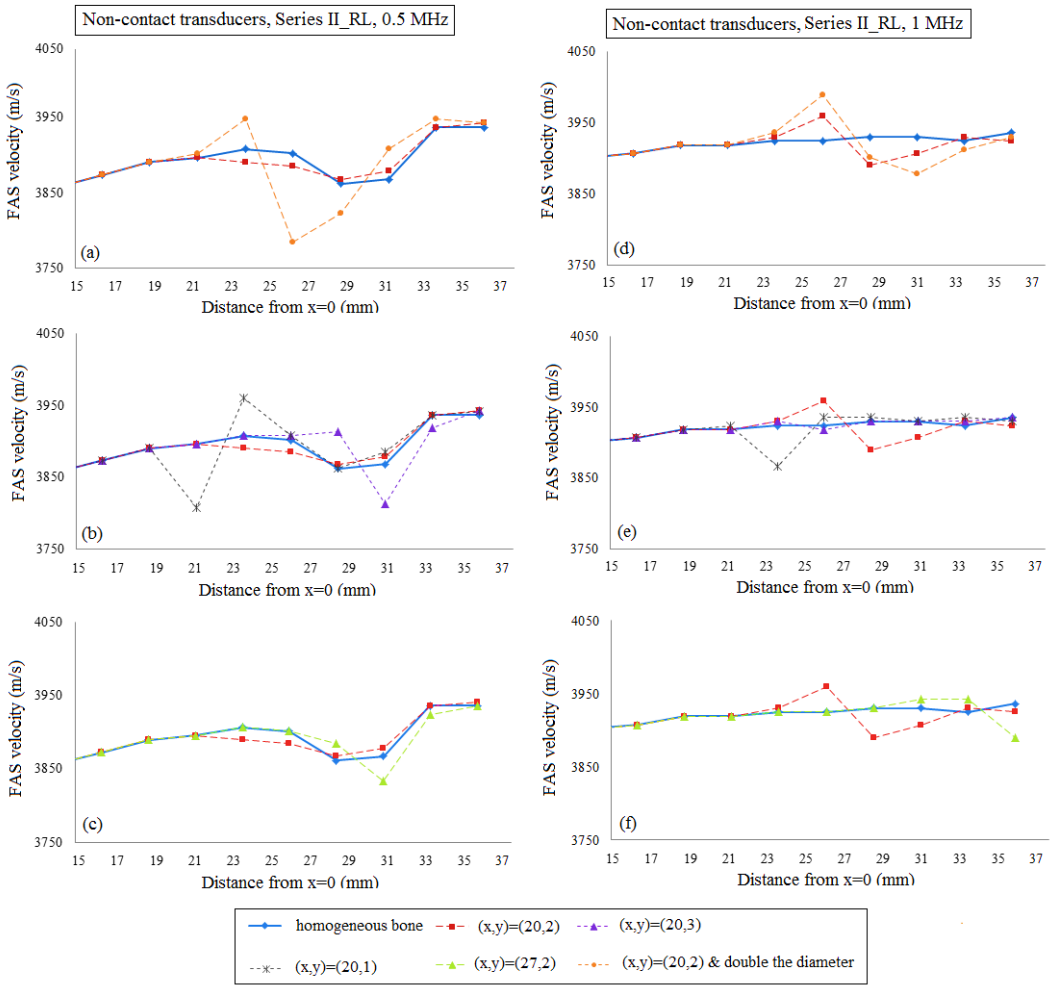

Figure 6.12: The potential of the local FAS velocity to detect the occurrence of a single RL considering cortical bone as a homogeneous medium (geometries illustrated in Figs. 6.4a–e). The diagrams correspond to the second set of simulations when the transducers are placed at a distance of 2 mm from the cortical cortex. The results for the excitation frequencies: (a)–(c) 0.5 MHz, and (d)–(f) 1 MHz are presented. The legend describes the center coordinates of the RL.

Additionally, Figs. 6.12d–f present the local FAS velocity variation profile for the excitation frequency 1 MHz and the presence of a single RL. Specifically, Fig. 6.12d shows that the occurrence of a single RL in the center of the plate (red line) can be

identified with a delay by the receivers which follow the region of interest (around x = 23–25 mm) showing an increase of the FAS velocity of 35 m/s. In addition, it can be observed that by doubling the diameter of the RL (orange line) the same receivers are the first to identify an increase of the FAS velocity of 65 m/s. Fig. 6.12e shows that when the depth from the cortical surface is increased (purple line), the larger pore cannot be detected as this diagram almost coincides with the case of homogeneous bone. On the contrary, the occurrence of the RL near the upper cortical surface (grey line) leads to a decrease of the FAS velocity of 57 m/s, and it can be identified with a small delay by the receivers placed above the propagation path between x = 21–23 mm. Finally, Fig. 6.12f shows that by changing the position of the RL along the x-axis, the receivers which are placed between x=29–31 mm are the first to detect an increase of the FAS velocity of 17 m/s.

Next, Fig. 6.13 deals with the potential of the local FAS velocity variation profile to identify the occurrence of a single or a cluster of three or five large pores in the center of the plate taking into account the cortical microstructure. Fig. 6.13a illustrates the local FAS velocities for the excitation frequency 0.5 MHz, while Fig. 6.13b shows the FAS values for 1 MHz considering B_Po5 (red line) as the reference case. For the excitation frequency 0.5 MHz, the relative percentage differences were calculated in the range: (a) 0.05–0.75% for B_Po5_RL1, (b) 0.05–1.41% for B_Po5_RL3 and (c) 0.18–2.71% for B_Po5_RL5. It can be observed that the first receivers which capture the RL are placed between x = 21–23 mm showing a short delay. A 4-mm delay in the detection of the larger pores can be seen in Fig. 6.11b for 1 MHz and lower relative percentage differences were calculated compared to 0.5 MHz from: (a) 0.04–0.32% for B_Po5_RL1, (b) 0.14–0.46% for B_Po5_RL3, (c) 0.05–0.79% for B_Po5_RL5, respectively.

6.5 Discussion

This chapter presented a 2D parametric and systematic computational study aiming to investigate the effect of cortical porosity on ultrasound wave propagation in healthy and osteoporotic long bones. In comparison to previous studies (Rohde *et al.,* 2014; Bourgnon *et al.,* 2014), more realistic porosity scenarios were established, as this is the first time that the distribution of the pores was randomized including normal pores, as well as pores with diameters larger than the Haversian canal size. Moreover,

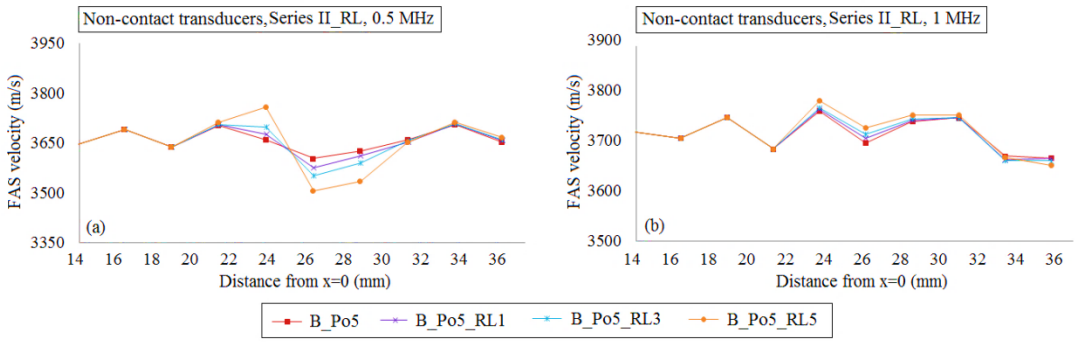

Figure 6.13: The potential of the local FAS velocity to detect the occurrence of a single or a cluster of RL considering cortical bone as a nonhomogeneous medium for the cases B_Po5, B_Po5_RL1, B_Po5_RL3 and B_Po5_RL5 (geometries illustrated in Figs. 6.4f–h). The diagrams correspond to the second set of simulations when the transducers are placed at a distance of 2 mm from the cortical cortex. The excitation frequencies: (a) 0.5 MHz, (b) 1 MHz are examined.

the analysis was not limited to a small segment of cortical bone with the presence of only one large BMU as in (Bourgnon *et al.,* 2014).

The gradual formation of osteoporosis was also considered by simulating more physiological distributions of pores with larger pores in the endosteal cortex and smaller ones in the periosteum. The excitation frequencies 0.5 and 1 MHz were examined to investigate which frequency is more sensitive to detect changes in cortical porosity and the occurrence of RLs. Numerical simulations of wave propagation were performed in the tangential direction and various microstructural models mimicking normal and pathological tissue states were investigated. In comparison to traditional FAS velocity measurements using one emitter and one receiver, calculations of "local" FAS values were conducted in small successive propagation paths along the cortical cortex aiming to better comprehend the interaction of ultrasound with cortical microstructure.

Initially, in Fig. 6.5 the FAS velocity variation profile was examined along cortical bone for microstructural models with porosities from 0–16%. It was made clear that as the porosity increases, the FAS velocities calculated in small propagation paths decrease for both the examined frequencies. However, the relative percentage differences calculated considering B_Hom as the reference case were higher for 0.5 MHz comparing to 1 MHz. Moreover, Fig. 6.8a shows a delay in the time of arrival with increasing the porosity followed by an amplitude increase. This may be

explained by the reflection mechanisms, which enhance the received signal for higher porosities. However, despite the significance of the calculation of the FAS velocities from the first signal extremum, the evaluation of the whole waveform would be a possible direction for future research based on guided wave analysis or on the waveform rectification followed by numerical integration via the trapezoidal method.

Additionally, the use of implanted transducers led to higher relative percentage differences compared to the use of non-contact transducers, while a delay in the detection of a single or a cluster of RL was observed for non-contact transducers. This can be attributed to the attenuation mechanisms induced by the presence of the soft tissues in the propagation path. The attenuation mechanisms include the evolution of absorption and scattering phenomena. Scattering is induced in bone due to the presence of the pores while soft tissues are major sources of acoustic wave absorption. Despite the accuracy of the FDTD method, which was demonstrated via a convergence study, a limitation of the present work is the simulation weakness of the software to account for attenuation effects resulting from the viscoelasticity (Rohde *et al.,* 2014). In addition, it should be mentioned that the use of implanted transducers is considered as an invasive procedure for osteoporosis and was examined only for comparison purposes with the non-contact transducers. In clinical practice, their insertion is easy for fracture healing assessment (Protopappas *et al.,* 2005), but, for the evaluation of osteoporosis, this configuration is not applied during *in vivo* measurements.

Concerning the case of pathology with porosity 16%, two additional scenarios were investigated to account for the presence of pores with different diameters, as well as for the gradual formation of osteoporosis. It was found that the FAS velocity variation profile shows a decrease along the cortical cortex for both B_Po16_RL and B_Po16_Gradual for 0.5 MHz. On the other hand, the excitation frequency 1 MHz was not convenient for B_Po16_RL (Figs. 6.5e and 6.9e) as no specific FAS velocity tendency was observed, while, for B_Po16_Gradual, it was sensitive to the gradual porosity increase. A direct comparison of the received signals from B_Po16 and B_Po16_RL was also included in Fig. 6.8b showing a difference in the received signals due to the occurrence of large pores.

Additionally, a statistical analysis was conducted based on the estimation of the standard errors, one-way ANOVA and linear regression analysis. It should be

mentioned that the receiving positions near the source (d < 12 mm) were ignored as for short distances between the transducers, low velocities are calculated, revealing that the FAS propagates directly via water (Figs. 6.9a and d). The calculated p-values were lower than 0.05 indicating that there are statistically significant differences between group means as the porosity increases from 0 to 16%. The low p-values can be explained by the high dispersion of the FAS velocity derived from serial measurements for porosity 16%. Linear regressions analysis revealed a specific FAS velocity trend even for the cases of Figs 6.5e and 6.9e. Nevertheless, low R^2 values were derived implying that this analysis could be used only for supplementary observations following traditional local and successive FAS velocity measurements. The establishment of three numerical models for each case is another parameter which requires further discussion. The use of three models is considered as a good compromise to reduce the computational cost and derive accurate conclusions taking into account the calculated standard error values. More specifically, for all the examined cases, the maximum FAS velocity variation among the three computational models was far less than 5%, thus it was decided not to proceed to additional runs to keep calculations and simulations simpler.

Then, the case of normal remodeling was examined including the presence of a single or a cluster of RL. Specifically, it was shown that for implanted transducers and 0.5 MHz, as well as for both the hypothetic case of homogeneous and the realistic of nonhomogeneous bone, the presence of one or more RLs can be identified by the receivers which are placed directly above the region of interest revealing the effectiveness of the FAS wave as an indicator. The same observation was made for all the sizes, numbers, depths and lengths of the RL. However, the use of 1 MHz or the transducers' placement into the water led to the detection of larger pores with a short delay when the RLs are placed in the center of the plate (approximately 4 mm) or near the upper cortical cortex (approximately 2 mm). It should be emphasized that the occurrence of a single RL near the lower surface of cortical bone could not be identified when the excitation frequency 1 MHz was applied irrespective of the transducers' configuration. In addition, it was observed that as the receivers are removed from the region of interest the calculated values gradually approximate the values of healthy bone. Nonetheless, the combination of low and high frequencies for the detection of larger pores could be useful, as low frequencies can detect the region

of interest along the x axis and higher frequencies can reveal the depth of the pores along the y-axis. For example, in Figs. 6.10b and e, when the RL is placed near the upper cortical layer (grey line), for both frequencies, the large pore can be detected in the same position implying that the pore is near the cortical upper surface. By placing the RL in the center of the plate (red line), the use of 0.5 MHz frequency leads to the detection of the exact x position of the RL, but 1 MHz shows a delay. This reveals that the pore is placed deeper. Finally, Fig. 6.10e shows that for 1 MHz the RL at y = 3 (purple line) cannot be detected, indicating in combination with 0.5 MHz findings that a large pore exist, but this pore is positioned near the lower surface of the cortical cortex. Thus, even from the limitations of 1 MHz, specific information may be derived concerning the depth of the RL interpreted in combination with 0.5 MHz findings when the occurrence of large basic multicellular units is a factor of major concern.

A possible explanation for the low sensitivity of 1 MHz is that, when the wavelengths are comparable to or smaller ($\lambda_{0.5MHz}$ = 7.88 mm, λ_{1MHz} = 3.94 mm) than the thickness of the cortical cortex (4 mm), the FAS wave propagates as a subsurface, lateral wave which travels at the bulk longitudinal velocity of the medium and cannot reflect changes occurring at deeper cortical layers. The calculation of the wavelengths depends on the frequency and the bone's bulk velocity which is 3939 m/s considering the material properties of Table 6.1. However, bone velocity may vary from 3500 m/s to 4100 m/s depending on the type and anatomic region of bone. According to the literature (Nicholson *et al.,* 2002; Moilanen *et al.,* 2007), the use of low excitation frequencies (0.2 MHz) has been chosen to yield information on the correlation of the FAS velocity with changes in cortical thickness due to osteoporosis, while it was reported in (Moilanen *et al.,* 2007) that the FAS velocities for high frequencies such as 1 MHz were weakly correlated with cortical thicknesses. Therefore, future research should address the question of which frequency range below 0.5 MHz is more convenient for the assessment of osteoporosis considering the occurrence of pores with different sizes.

Concerning the case of homogeneous bone, it was observed that, for 1 MHz, the FAS velocity along the propagation path increases slightly, approximating the bone's bulk velocity (Figs. 6.10d, e, and f), while this is not the case for 0.5 MHz in Figs. 6.10a, b, and c. The observed behavior at 0.5 MHz can be attributed to the fact that the

wavelength is almost twice the cortical thickness implying that more complex wave propagation phenomena evolve and the investigation of the propagation of guided waves could convey significant information. On the other hand, for 1 MHz, the FAS propagates as a lateral wave.

Finally, several assumptions were made which require further numerical research and improvements. First of all, although two dimensional geometries were developed, they incorporated various porosity scenarios. Moreover, changes in cortical thickness in cases of pathology in combination with changes in cortical porosity were not considered. Imaging modalities could be also exploited to establish more realistic computational models (Raum *et al.,* 2014; Raum *et al.,* 2006b). In addition, the use of point transducers should be mentioned as in experimental procedures the transducers have a finite size. It was reported in (Moilanen *et al.,* 2007) that the choice of using point elements instead of finite-sized ones did not affect significantly the recorded ultrasound velocities. However, further numerical research is needed to investigate the impact of the transducers' size in relation to the scatterers' size on the results. Furthermore, according to (Roschger *et al.,* 2014), the majority of patients with osteoporosis have changes in the mineralization pattern. In particular, a reduction of the average mineral content was described when compared with age-matched controls or when compared with reference values for healthy adults. QUS was used in (Cortet *et al.,* 2004) for bone characterization and the role of bone mineral density as a major determinant of acoustic properties was highlighted, as well as the significance of density-independent relationships with bone microarchitecture. However, according to (Sasso *et al.,* 2007), the main cause of sound attenuation coefficient in bone is porosity, while matrix stiffness has a minor effect. In addition, it was reported in (Granke *et al.,* 2011) that in aged women the changes in porosity prevail over those of of matrix elasticity to drive the variations of the bone mesoscopic elasticity.

Finally, according to (Grasel *et al.,* 2017), although simulation studies of QUS propagation through cortical bone indicate that anisotropy, calculated from the ratio of the velocities in axial and tangential directions, is correlated with porosity, this relationship is affected by error sources, specifically bone surface curvature and variability of probe positioning. With the aim of *in vivo* estimation of cortical porosity a new ultrasound device was presented in (Grasel *et al.,* 2017), which sequentially measures velocities in 3 different directions using the axial transmission method. The

results of this work indicate that the estimation of porosity using velocity measurements in different directions might be feasible, even in bones with curved surface. These results obtained on phantom material indicate that the approach tested may be suited for porosity measurements on human tibia bone.

Nevertheless, the results clearly indicated that the excitation frequency 0.5 MHz is more sensitive to detect changes in cortical porosity and the occurrence of RLs. In addition, it was shown that the calculation of the FAS velocity in small propagation paths could potentially provide significant quantitative information for the early diagnosis of osteoporosis and detection of pathologic regions with large pores with a high risk for fracture.

Chapter 7: Conclusions and Future Work

7.1 Monitoring of Fracture Healing

The current thesis presented numerical simulations of ultrasound propagation in healing long bones which incorporate the porosity of osseous and callus tissues. Compared to the literature, more realistic computational models were established based on scanning acoustic microscopy images. The material properties, the geometrical features of cortical bone and callus and more specifically cortical and callus porosity were derived from SAM data from a sheep animal study. Previous numerical studies neglected the evolution of porosity during fracture healing which, however, increases for the case of cortical bone and decreases for the callus at successive healing stages.

Going beyond the state of the art, the evolution of scattering phenomena was evaluated during fracture healing using theoretical and numerical methods. In the first stage of this study an iterative effective medium approximation was used to evaluate wave dispersion and attenuation for the callus tissue at different healing stages, as well as the frequency dependence of these parameters. This method was first validated and comparisons were performed with previous theoretical and experimental findings in cancellous bone mimicking phantoms. Keeping all the examined parameters constant and modifying the frequency, the phase velocities calculated theoretically using IEMA were in better agreement with the corresponding phase velocities derived experimentally compared to other theoretical studies. A very good agreement between experimental and theoretical results was also observed when the volume concentration was changing keeping the frequency constant.

Then, the material properties and porosity of the callus in successive healing stages were derived from SAM images and for the first time estimations of the group velocity and the attenuation coefficient were performed up to 1.2 MHz. The group velocity was found to decrease with increasing frequency. Also, higher group velocities were calculated at late healing stages and the corresponding values for week 3 were almost half the values of week 9. According to the literature several authors aiming at the ultrasonic assessment of cancellous bone have reported phase velocities that decrease with frequency, a phenomenon known as negative dispersion, while similar findings have not been presented for healing long bones. On the other hand, the attenuation coefficient was found to increase with increasing frequency. Also, a higher attenuation was calculated during the early healing stages having a higher porosity and pores' size.

This study is also innovative as the microstructure features of the osseous and callus tissues derived using SAM images when then incorporated to 2D computational models of healing long bones and simulations of ultrasonic wave propagation were presented. Previous numerical studies used only the axial transmission method to investigate wave propagation during fracture healing and the parameters of interest were the velocity of the FAS and the analysis of the propagation of guided waves. In the present study, the axial transmission method was used in the first stage of the research, while the backscattering method was also examined and new quantitative and qualitative parameters were proposed for the monitoring of fracture healing.

More specifically, the axial transmission method was initially applied and FAS velocity calculations as well as a guided wave analysis were conducted in computational models of 2D healing long bones which integrated callus porosity. The multimodal analysis of guided waves revealed that during the healing process the dominant modes are restored. Additionally, a parametric study was presented on the impact of callus porosity and pores' size on the FAS velocity for the same healing stage. It was shown that the FAS velocity decreases with increasing the callus porosity. Also, it was observed that changes in callus porosity concentration have a more significant influence on the propagation of the FAS velocity in comparison to changes in the size of the scatterers. Nevertheless, FAS velocity calculations revealed that the scatterers' size plays a key role on FAS velocity when larger porous areas are examined such as the whole surface of cortical bone.

Then, except for the application of traditional wave propagation methods, the backscattering method was used for the first time to assess the evolution of the propagating acoustic field in healing long bones. The porosities of cortical bone and callus were incorporated into 2D computational models using IEMA. The alteration of the scattering amplitude in the backward direction was examined as a new quantitative parameter for the monitoring of fracture healing. The results showed that the scattering amplitude at late stages of healing is lower compared to earlier stages of healing. Also, the scattering amplitude was found to slightly increase in week 9 for the frequencies 0.2, 0.4 and 1 MHz showing a restoration tendency. Also, the assessment of the acoustic pressure alterations in the backward direction could provide supplementary qualitative information on the interaction of the scattered energy with bone and callus. More specifically, for low frequencies in the range 0.2-0.4 MHz, material and structural alterations in the callus tissue change the distribution of the acoustic pressure map derived from multiple measurements in the backward direction reflecting the propagation of the scattered energy field.

However, several assumptions were made. First of all, 2D numerical models were developed based on 2D SAM images which do not account for the 3D geometrical features of bone and callus. According to the literature, only one 3D numerical study has been presented on the evaluation of fracture healing, while several 2D numerical models have been presented since the last decade. Moreover, the use of a plane wave in backscattering numerical simulations is another limitation, while in the future this work will be further extended to examine ultrasound stimulations which are applied in experimental procedures. Finally, IEMA introduces the assumption that the geometry of the callus' inclusions is circular, while a more realistic representation for the newly formed callus tissue could integrate cylindrical scatterers in the region of interest.

7.2 Prevention of an Osteoporotic Fracture

The evaluation of cancellous bone porosity using ultrasonic methods has attracted the interest of several researchers worldwide using theoretical and computational approaches. On the other hand, the numerical evaluation of cortical porosity using ultrasonic techniques has been studied to a lesser extent. The novelty of this thesis is reflected on the development of 2D numerical models which account for different porosity scenarios, pores' sizes and more specifically for the occurrence of pores with

sizes larger than the Haversian canals called large BMUs. The main objective was to detect regions of the cortical cortex which are subjected to a higher risk of fracture due to the formation and concentration of a cluster of BMUs. In this way, the early signs of an osteoporotic fracture could potentially be detected aiming at the effective prognosis of the disease at the first stages and the prevention of a future fracture. The role of the excitation frequency was also examined. It was shown for the first time that the "local" FAS velocity calculated in small propagation paths from successive receivers can capture the occurrence of a cluster of BMUs indicating a region which is more susceptible to a future osteoporotic fracture. It was also shown that the combination of low and high frequencies for the detection of large pores could be useful, as low frequencies can detect the region of interest along the cortical length and higher frequencies can reveal the depth of the pores along the cortical thickness.

The gradual formation of osteoporosis was also examined considering larger pores in the region of the endosteum and smaller pores in the periosteum. Compared to the case of healthy nonhomogeneous bone, it was found that the local FAS velocity decreases as the porosity increases and this behavior is constant along the examined propagation path.

Nevertheless, this work is subject to several limitations. First of all, 2D geometries were developed. Moreover, changes in cortical thickness in cases of pathology in combination with changes in cortical porosity were not considered. Also, point transducers were used, while in experimental procedures the transducers have a finite size. Also, the majority of patients with osteoporosis have changes in the mineralization pattern which was not considered in this thesis. Nonetheless, the main cause of sound attenuation coefficient in bone is porosity, while matrix stiffness has a minor effect.

7.3 Future Work

This thesis is considered as a springboard for the investigation of the complex wave scattering phenomena induced by the composite nature of osteoporotic and healing long bones. Although the computational models which were presented incorporate cortical and callus porosity features based on 2D SAM images, the establishment of 3D computational models is the next step of this work.

Concerning the monitoring of fracture healing using the backscattering method, this study will be extended in the future to consider higher frequencies up to 5 MHz based on (Ferreira *et al.*, 2010), as well as different propagation angles in the forward and backward direction.

In addition, the application of IEMA was based on the consideration of circular pores, while a more realistic scenario based on the geometry of the osteon and trabeculae in the microstructure level would be to account for cylindrical pores. Therefore, this study could be further extended to examine the impact of the shape of the pores. Finally, the use of a continuous incident wave when the backscattering method was applied is another constraint reflecting effectively the theoretical aspect of the wave scattering problem. Thus, this thesis should be further extended to examine ultrasound stimulations which are applied in experimental applications.

Another direction for future research could be the monitoring of the early stages of bone healing using ultrasonic methods and numerical means based on μCT data from the study of (Rohrbach *et al.,* 2013). More specifically, this pilot study investigated the feasibility of QUS in a transverse-transmission mode for the assessment of the early stages of callus formation in a rat osteotomy model and the FAS attenuation and velocity were the parameters of interest. The potential of ultrasound to detect material and geometrical alterations in the callus and osseous tissues during the first healing stages could early indicate signs of a non-successful healing process and prevent a non-union or pseudarthrosis. Therefore, in future work the axial and backscattering methods will be used to investigate numerically the features of ultrasonic propagation during the early stages of bone healing.

Finally, in this work the ultrasonic evaluation of cortical porosity was based on a parametric and systematic study investigating various porosity scenarios in 2D cortical plates using the axial transmission method. This study will be further extended to establish more realistic geometries based on SAM images from human tibia cross-sections presented in (Raum *et al.,* 2014). These data could be exploited to account for alterations not only in cortical porosity, but also in the whole cortical geometry and thickness. In addition, the backscattering method will be used for the assessment of the scattering effects in healthy and osteoporotic long bones and the detection of resorption lacunae. Even though the first results of this study (Gortsas *et*

al., 2015) are quite encouraging showing that the scattering amplitude calculated in the backward direction could detect changes in cortical porosity, various porosity scenarios should be considered based on (Potsika *et al.,* 2016a) to identify regions which are more susceptible to a fracture.

Bibliography

1. Abendschein W F and Hyatt G W (1972). Ultrasonics and physical properties of healing bone, J Trauma, 12(4), 297–301.
2. Aliabadi M H (2002). The Boundary Element Method, Volume 2: Applications in Solids and Structures, John Wiley, England.
3. Aggelis D G, Tsinopoulos S V, Polyzos D (2004). An iterative effective medium approximation (IEMA) for wave dispersion and attenuation predictions in particulate composites, suspensions and emulsions, J Acoust Soc Am, 116(5), 3443–3452
4. Aldrich J E (2007). Basic physics of ultrasound imaging, Crit Care Med 35, 2007.
5. Anderson C C, Marutyan K R, Holland M R, Wear K A, Millera J G (2008). Interference between wave modes may contribute to the apparent negative dispersion observed in cancellous bone, J Acoust Soc Am, 124(3), 1781–1789.
6. Bae W C, Chen P C, Chung C B, Masuda K, D'Lima D, Du J (2012). Quantitative Ultrashort Echo Time (UTE) MRI of Human Cortical Bone: Correlation with Porosity and Biomechanical Properties, J Bone Miner Res, 27(4), 848–857.
7. Bankoff A D P (2012). Biomechanical Characteristics of the Bone, Human Musculoskeletal Biomechanics.
8. Barbieri G, Barbieri C H, Mazzer B, Péla A (2011). Ultrasound Propagation Velocity and Broadband Attenuation Can Help Evaluate the Healing Process of an Experimental Fracture, J Orthop Res, 29(3), 444–451.
9. Barkaoui A, Chamekh A, Merzouki T, Hambli R, Mkaddem A (2014). Multiscale approach including microfibril scale to assess elastic constants of cortical bone based on neural network computation and homogenization method, Int J Numer Meth Biomed Engng, 30, 318–338.
10. Barkmann R, Dencks S, Laugier P, Padilla F, Brixen K, Ryg J, Seekamp A, Mahlke L, Bremer A, Heller M, Gluer C C (2010). Femur ultrasound (FemUS)-first clinical results on hip fracture discrimination and estimation of femoral BMD, Osteoporos Int, 21(6), 969–976.
11. Barkmann R, Laugier P, Moser U, Dencks S, Klausner M, Padilla F, Haiat G, Heller M, Gluer C C (2008). In vivo measurements of ultrasound transmission through the human proximal femur, Ultrasound Med Biol, 34(7), 1186–1190.
12. Baron C, Talmant M, Laugier P (2007). Effect of porosity on effective diagonal stiffness coefficients (c_{ii}) and elastic anisotropy of cortical bone at 1 MHz:A finite-difference time domain study, J AcoustSoc Am, 122(3),1810–1817.
13. Bart Z R, Wallace J M (2013). Microcomputed tomography applications in bone and mineral research, Adv Computed Tomography, 2(3), 121–127.
14. Bauer A, Marutyan K, Holland M, Miller J (2008). Negative dispersion in bone: The role of interference in measurements of the apparent phase velocity of two temporally overlapping signals, J AcoustSoc Am, 123(4), 2407–2414.
15. Ben-Amoz M (1976). A dynamic theory for composite materials, J.Appl. Math. Ph. 27(1), 83–99.
16. Bienz Mand SaadF (2015). Androgen-deprivation therapy and bone loss in prostate cancer patients: a clinical review, BoneKEy Reports 4, Article number: 716, International Bone & Mineral Society, 1–9.
17. Blake G M and Fogelman I (2007). The role of DXA bone density scans in the diagnosis and treatment of osteoporosis, Postgrad Med J, 83 (982), 509–517.

18. Bochud N, Vallet Q, Minonzio J G, Laugier P (2017). Predicting bone strength with ultrasonic guided waves, Scientific Reports 7, Article number: 43628.
19. Bossy E and Grimal Q (2010). Numerical methods for ultrasonic bone characterization. In Bone Quantitative Ultrasound, Springer: New York, NY, USA, 181–228.
20. Bossy E, Laugier P, Peyrin F, Padilla F (2007). Attenuation in trabecular bone: A comparison between numerical simulation and experimental results in human femur, J Acoust Soc Amer, 122(4), 2469–2475.
21. Bossy E,Talmant M, Laugier P (2002). Effect of bone cortical thickness on velocity measurementsusing ultrasonic axial transmission: A 2D simulation study, J Acoust Soc Am, 112(1), 297–307.
22. Bossy E, Talmant M, Laugier P (2004). Three-dimensional simulations of ultrasonic axial transmission velocity measurement on cortical bone models, J Acoust Soc Am, 115(5), 2314–2324.
23. Bossy E, Talmant M, Peyrin F, Akrout L, Cloetens P, Laugier P (2004b). An *in vitro* study of the ultrasonic axial transmission technique at the radius: 1-MHz velocity measurements are sensitive to both mineralization and intracortical porosity, J Bone Miner Res, 19(9), 1548–1556.
24. Bouxsein M L, Boyd S K, Christiansen B A, Guldberg R E, Jepsen K J, Muller R (2010). Guidelines for assessment of bone microstructure in rodents using micro-computed tomography. J Bone Miner Res, 25(7), 1468–1486.
25. Bourgnon A, Sitzer A, Chabraborty A, Rohde K, Varga P, Wendlandt R, Raum K (2014). Impact of microscale properties measured by 50-MHz acoustic microscopy on mesoscale elastic and ultimate mechanical cortical bone properties. Proc IEEE International Ultrasonics Symposium, Chicago, IL, USA, 636–638.
26. Brekhovskikh L M and Godin O (1999). The Lateral Wave, In Acoustics of Layered Media II, Springer Series on Wave Phenomena.
27. Brennan T C, Rizzoli R, Ammann P (2009). Selective modification of bone quality by PTH, pamidronate, or raloxifene, J Bone Miner Res, 24(5), 800–808.
28. Bruel A, Olsen J, Birkedal H, Risager M, Andreassen T T, Raffalt A C, Andersen J E, Thomsen J S (2011). Strontium is incorporated into the fracture callus but does not influence the mechanical strength of healing rat fractures. Calcif Tissue Int, 88(2), 142–152.
29. Camus E, Talmant M, Berger G, Laugier P (2000). Analysis of the axial transmission technique for the assessment of skeletal status, J Acoust Soc Am 108(6), 3058–3065.
30. Carden A, Morris M D (2000). Application of vibrational spectroscopy to the study of mineralized tissues (review), J Biomed Opt, 5(3), 259–268.
31. Carovac A, Smajlovic F, Junuzovic D (2011). Application of Ultrasound in Medicine, Acta Inform Med, 19(3), 168–171.
32. Casanova M, Schindeler A, Little D, Muller R, Schneider P (2014). BoneKEy Reports 3, Article number: 550 (2014) | doi:10.1038/bonekey.2014.45.
33. Casciaro S, Conversano F, Pisani P, Muratore M (2015). New perspectives in echographic diagnosis of osteoporosis on hip and spine, Clin Cases Min & Bone Metab, 12(2), 142–150.
34. Chakraborty A (2008). Prediction of negative dispersion by a nonlocal poroelastic theory, J Acoust Soc Am, 123(1), 56–67.
35. Chen H and Kubo K-Y (2014). Bone three-dimensional microstructural features of the common osteoporotic fracture sites, World J Orthop, 5(4): 486–495.

36. Chen H, Zhou X, Fujita H, Onozuka M, Kubo K-Y (2013). Age-Related Changes in Trabecular and Cortical Bone Microstructure, International Journal of Endocrinology, 13, 1–9.
37. Cheung W H, Chow S K, Sun M H, Qin L, Kwok-Sui L (2011). Low-Intensity Pulsed Ultrasound Accelerated Callus Formation, Angiogenesis and Callus Remodeling in Osteoporotic Fracture Healing, Ultr Med Biol, 37(2), 231–238.
38. Cheung A M, Adachi J D, Hanley D A, Kendler D L, Davison K S, Josse R, Brown J P, Ste-Marie L-G, Kremer R, Erlandson M C, Dian L, Burghardt A J, Boyd SK (2013). High-Resolution Peripheral Quantitative Computed Tomography for the Assessment of Bone Strength and Structure: A Review by the Canadian Bone Strength Working Group, CurrOsteoporos Rep 11(2), 136–146.
39. Christensen R M (1990). A critical evaluation for a class of micromechanics models, J Mech Phys Solids, 38, 379–404.
40. Claes L and Heigele C (1999). Magnitudes of local stress and strain along bony surfaces predict the course and type of fracture healing, J Biomech, 32(3), 255–266.
41. Cortet B, Boutry N, Dubois P, Legroux-Gérot I, Cotton A, Marchandise X (2004). Does quantitative ultrasound of bone reflect more bone mineral density than bone microarchitecture,Calcif Tissue Int, 74(1), 60–67.
42. Courant R, Friedrichs K, Lewy H (1928). Uber die partiellen Differenzengleiehungen der mathematisehen Physik, Mathematische Annalen, 100, 32–74.
43. Cowin S C (2001). Bone Mechanics, Handbook, 2nd Edition, CRC Press LLC, USA.
44. Dall'Ara E, Schmidt R, Zysset P (2012). Microindentation can discriminate between damaged and intact human bone tissue, Bone 50(4), 925–929.
45. Dassios G, Kiriaki K, Polyzos D (1987). On the Scattering Amplitudes for Elastic Waves,(ZAMP), J Appl Math and Phys 38(6), 856–873.
46. De Marco T, Peccarisi M, Conversano F, Greco A, Chiozzi S, De Pascalis F, Casciaro S (2016). A new approach for measuring the trabecular bone density through the echosound backscattering: An ex vivo validation on human femoral heads, Measurement, 87, 51–61.
47. Doan N, Reher P, Meghji S, Harris M (1999). *In vitro* effects of therapeutic ultrasound on cell proliferation, protein synthesis, and cytokine production by human fibroblasts, osteoblasts, and monocytes, J Oral Maxillofac Surg, 57(4), 409–419.
48. Dodd S P, Cunningham J L, Miles A W, Gheduzzi S, Humphrey V F (2008). Ultrasound transmission loss across transverse and oblique bone fractures: an *in vitro* study, Ultrasound in Med & Biol, 34(3), 454–462.
49. Dodd S P, Miles A W, Gheduzzi, Humphrey V F, Cunningham J L (2007). Modelling the effects of different fracture geometries and healing stages on ultrasound signal loss across a long bone fracture, Comp Meth Biomec Biomed Eng, 10(5), 371–375.
50. Doblare M, Garcia J M, Gomez M J (2004). Modelling bone tissue fracture and healing: a review, Engineering Fracture Mechanics, 71(13–14), 1809−1840.
51. Donnelly E (2011). Methods for Assessing Bone Quality,Clin Orthop Relat Res, 469(8), 2128–2138, 2011.
52. Einhorn T A and Gerstenfeld L C (2015). Fracture healing: mechanisms and interventions, Nature Reviews Rheumatology, 11(1), 45–54.

53. Eckardt I and Hein H J (2001). Quantitative measurements of the mechanical properties of human bone tissues by scanning acoustic microscopy, Ann Biomed Eng, 29(12), 1043–1047.
54. Eneh C T M, Afara I O, Malo M K H, Jurvelin J S, Toyras J (2017). Porosity predicted from ultrasound backscatter using multivariate analysis can improve accuracy of cortical bone thickness assessment, J Acoust Soc Am, 141 (1), 575–585.
55. Ferreira M L, Matusin D P, Machado C B, Silva P C, Mello N B, Amara A C, Franco R S, de Albuquerque Pereira W C, Schanaider A (2010). Characterization of pseudarthrosis with ultrasound backscattered signals in rats, Acta Cirúrgica Brasileira, 25(1), 13–17.
56. Floriani L P, Debervoise N T, Hyatt G W (1967). Mechanical properties of healing bone by use of ultrasound, Surg Forum, 18, 468–470.
57. Foiret J, Minonzio J G, Chappard C, Talmant M, Laugier P (2014). Combined Estimation of Thickness and Velocities Using Ultrasound Guided Waves: A Pioneering Study on In Vitro Cortical Bone Samples, IEEE Trans on Ultras, Ferroel, and Freq control, 61(9), 1478–1488.
58. Fotiadis D I, Protopappas V C, Massalas C V (2006). Elasticity, Wiley Encyclopedia of Biomedical Engineering.
59. Freeland A E, Jabaley M E, Hughes J L (1986). Delayed Union, Nonunion, and Pseudarthrosis, In: Stable Fixation of the Hand and Wrist Springer, New York, NY, 167-178.
60. Foldy L L (1945). The multiple scattering of waves, PhysRev, 67, 107–119.
61. Georgiadis H G, Vardoulakis I, Velgaki E G (2004). Dispersive Rayleigh-wave propagation in microstructured solids characterized by dipolar gradient elasticity, J Elasticity, 74(1), 17–45.
62. Geris L, Sloten J V, Oosterwyck H V (2009). In silico biology of bone modelling and remodelling: regeneration, Phil Trans R Soc A, 367, 2031–2053.
63. Gill P J, Kernohan G, Mawhinney I N, Mollan R A, McIlhagger R (1989). Investigation of the mechanical properties of bone using ultrasound, Proc Inst Mech Eng, 203, 61–63.
64. Geusens P, Chapurlat R, Schett G, Ghasem-Zadeh A, Seeman E, de Jong J, van den Bergh J (2014). High-resolution in vivo imaging of bone and joints: a window to microarchitecture, Nature Reviews Rheumatology, 10(5), 304–313.
65. Glinkowskia W and Gorecki A (2006). Clinical experiences with ultrasonometric measurement of fracture healing, Technology and Health, Care, 14(4,5), 321–333.
66. Gortsas T, Grivas K, Polyzos D, Potsika V, Protopappas V, Fotiadis D, Raum K. (2015).The effect of cortical bone porosity on ultrasonic backscattering parameters, Proc of the IEEE 6th ESUCB, Corfu, Greece, 10–12 June, 40.
67. Graff K F (1991). Wave Motion in Elastic Solids (New York: Dover).
68. Granke M, Grimal Q, Saïed A, Nauleau P, Peyrin F, Laugier P (2011). Change in porosity is the major determinant of the variation of cortical bone elasticity at the millimeter scale in aged women, Bone, 49(5), 1020–1026.
69. Gräsel M, Glüer C-C, Barkmann R (2017). Characterization of a new ultrasound device designed for measuring cortical porosity at the human tibia: A phantom study, Ultrasonics, 76, 183–191.
70. Grimal Q, Rohrbach D, Grondin J, Barkmann R, Gluer C C, Raum K, Laugier, P (2013a). Modeling of femoral neck cortical bone for the numerical simulation of ultrasound propagation, Ultrasound in Med & Biol, 40(5),1–12.

71. Grimal Q, Grondin J, Guérard S, Barkmann R, Engelke K, Glüer C-C, Laugier P (2013b). Quantitative ultrasound of cortical bone in the femoral neck predicts femur strength: Results of a pilot study, J Bone Mineral Research, 28(2), 302–312.
72. Grivas K N (2016). Numerical Modelling of the ultrasound effect on bone fracture healing, Doctoral thesis, University of Patras, Greece.
73. Grondin J, Grimal Q, Engelke K, Laugier P (2010). Potential of first arriving signal to assess cortical bone geometry at the hip with QUS: A model based study, Ultrasound in Med & Biol, 36(4), 656–666.
74. Haïat G, Lhémery A, Renaud F, Padilla F, Laugier P, Naili S (2008). Velocity dispersion in trabecular bone: Influence of multiple scattering and of absorption, J Acoust Soc Am, 124(6), 4047–4058.
75. Haïat G and Naili S (2011). Independent scattering model and velocity dispersion in trabecular bone: comparison with a multiple scattering model, Biomech Model Mechanobiol, 10(1), 95–108.
76. Hata T, Nagatani Y, Takano K, Matsukawa M (2016). Simulation study of axial ultrasonic wave propagation in heterogeneous bovine cortical bone, J Acoust Soc Am, 140(5), 3710–3717.
77. Hayward L N M, De Bakker CM-J, Lusic H, Gerstenfeld L C, Grinstaff M W, Morgan EF-I (2012). MRT letter: contrast-enhanced computed tomographic imaging of soft callus formation in fracture healing, Microsc Res Tech, 75(1), 7–14.
78. Hoffmeister B K, Smathers M R, Miller C J, McPherson J A, Thurston C R, Spinolo P L, Lee S-R (2016). Backscatter Difference Measurements of Cancellous Bone Using an Ultrasonic Imaging System, Ultrason Imaging, 38(4), 285–297.
79. Hoffmeister B K (2011). Frequency dependence of apparent ultrasonic backscatter from human cancellous bone, Phys Med Biol, 56(3), 667–683.
80. Hoffmeister B K, Wilson A R, Gilbert M J, Sellers M E (2012). A backscatter difference technique for ultrasonic bone assessment, J Acoust Soc Am, 132(6), 4069–4076.
81. Hube R, Mayr H, Hein W, Raum K (2006). Prediction of biomechanical stability after callus distraction by high resolution scanning acoustic microscopy, Ultrasound Med Biol, 32(12), 1913–1921.
82. http://www.bemsands.com
83. Iori G, Raum K, Potsika V, Gortsas T, Fotiadis D (2015). High-frequency cortical backscatter reveals cortical microstructure – a simulation study, Proc of the IEEE 6th ESUCB, Corfu, Greece, 10–12 June, 48.
84. Jilka RL, Biology of the basic multicellular unit and the pathophysiology of osteoporosis, Med Pediatr Oncol, 41(3), 182–5, 2003.
85. Jimenez-Palomar I, Shipov A, Shahar R, Barber A H (2015). Mechanical behavior of osteoporotic bone at sub-lamellar length scales, Front Mater, 2, 1–7.
86. Juillard A, Falgayrac G, Cortet B, Vieillard M-H, Azaroual N, Hornez J-C, Penel G (2010). Molecular interactions between zoledronic acid and bone: an in vitro Raman microspectroscopic study, Bone, 47(5), 895–904.
87. Karjalainen J P, Riekkinen O, Töyräs J, Hakulinen M, Kröger H, Rikkonen T, Salovaara K, Jurvelin J S (2012). Multi-site bone ultrasound measurements in elderly women with and without previous hip fractures, Osteoporos Int, 23(4), 1287–1295.

88. Katz J L (1980). Anisotropy of Young's modulus of bone, Nature, 283, 106–107.
89. Kaufman J J, Luo G, Siffert R S (2007). A portable real-time ultrasonic bone densitometer, Ultrasound in Med & Biol, 33(9), 1445–1452.
90. Kilappa V, Xu K, Moilanen P, Heikolla E, Ta D, Timonen J (2013). Assessment of the fundamental flexular guided wave in cortical bone by an axial-transmission array transducer, Ultrasound in Med & Biol, 39(7), 1223–1232.
91. Kilappa V (2014). Ultrasound Measurements in Bone Using an Array Transducer, Academic Dissertation for the Degree of Doctor of Philosophy, University of Jyvaskyla, Jyvaskyla, Finland.
92. Kim N, Lee J G, Song Y, Kim H J, Yeom J S, Cho G (2012). Evaluation of MRI resolution affecting trabecular bone parameters: determination of acceptable resolution, Magn Reson Med, 67(1), 218–225.
93. Kim J-Y, Ih J-G, Lee B-H (1995). Dispersion of elastic waves in random particulate composites, J Acoust Soc Am, 97(3), 1380–1388.
94. Krieg M-A, Barkmann R, Gonnelli S, Stewart A, Bauer D C, Del Rio Barquero L, Kaufman J, Lorenc R, Miller P D, Olszynski W P, Poiana C, Schott A-M, Lewiecki M, Hans D (2008). Quantitative Ultrasound in the Management of Osteoporosis: The 2007 ISCD Official Positions, J Clin Dens: Assess of Skel Health, 11(1), 163–187.
95. Lam K H, Lui T H (2013). Low-intensity pulsed ultrasound in the treatment for fracture. Hard Tissue, Trauma & Orthopaedics, 2(3):22.
96. Laugier P and Haïat G (2011). Introduction to the Physics of Ultrasound, Chapter 2 in Bone Quantitative Ultrasound, Springer: New York, NY, USA.
97. Laugier P, Padilla F, Talmant M (2002). Quantitative Ultrasound for Bone Properties, In Acoustical Imaging, Springer-Verlag, 26, 45–52.
98. Lautrup B (2011). Elastic Vibrations, In Physics of Continuous Matter, Second Edition: Exotic and Everyday Phenomena in the Macroscopic World, CRC Press.
99. Leong P and Morgan E (2008). Measurement of fracture callus material properties via nanoindentation, Acta Biomater, 4(5), 1569–1575.
100. Li Y, Liu D, Xu K, Ta D, Le L H, Wang W (2017). Transverse and Oblique Long Bone Fracture Evaluation by Low Order Ultrasonic Guided Waves: A Simulation Study, BioMed Research International.
101. Liu D, Xu K, Ta D (2015). Impact of the fracture on low-order guided waves in long bone, Chinese Journal of Acoustics.
102. Liu C, Zhang R, Li Y, Xu F, Ta D, Wang W (2015). An Ultrasonic Backscatter Instrument for Cancellous Bone Evaluation in Neonates, Engineering, 1(3), 336–343.
103. Machado C B, de Albuquerque Pereira W C, Talmant M, Padilla F, Laugier P (2010). Computational evaluation of the compositional factors in fracture healing affecting ultrasound axial transmission measurements, Ultrasound in Med & Biol, 36(8), 1314–1326.
104. Machado C B, Pereira W C D A, Granke M, Talmant M, Padilla F, Laugier P (2011). Experimental and simulation results on the effect of cortical bone mineralization in ultrasound axial transmission measurements: A model for fracture healing ultrasound monitoring, Bone, 48(5), 1202–1209.
105. Malizos K N, Papachristos A A, Protopappas V C, Fotiadis D I (2006). Transosseous application of low-intensity ultrasound for the enhancement and

monitoring of fracture healing process in a sheep osteotomy model, Bone, 38(4), 530–539.
106. Malo M K H, Rohrbach D, Isaksson H, Töyräs J, Jurvelin J S, Tamminena I S, Kröger H, Raum K (2013). Longitudinal elastic properties and porosity of cortical bone tissue vary with age in human proximal femur, Bone, 53(2), 451–458.
107. Malo M K H, Töyräs J, Karjalainena J P, Isakssonc H, Riekkinena O, Jurvelin, J S (2014). Ultrasound backscatter measurements of intact human proximal femurs—Relationships of ultrasound parameters with tissue structure and mineral density, Bone 64, 240–245.
108. Manjubala I, Liu Y, Epari DR, Roschger P, Schell H, Fratzl P, Duda G (2009). Spatial and temporal variations of mechanical properties and mineral content of the external callus during bone healing, Bone, 45(2), 185–192.
109. Mano I, Horii K, Takai S, Suzaki T, Nagaoka H, Otani T (2006). Development of novel ultrasonic bone densitometry using acoustic parameters of cancellous bone for fast and slow waves, Jpn J Appl Phys 45(5B), 4700–4702.
110. Manolagas S C (2000). Birth and death of bone cells: Basic regulatory mechanisms and implications for the pathogenesis and treatment of osteoporosis, Endocr rev, 21 (2), 115–137.
111. Manolis G D, Dineva P S, Rangelov T V, Wuttke F (2017). Elastodynamic Problem Formulation, Chapter 3 in Seismic Wave Propagation in Non-Homogeneous Elastic Media by Boundary Elements, Springer.
112. Marcus R, Feldman D, Nelson D A, Rosen C J, Fundamentals of Osteoporosis, Academic Press, Elsevier, California, USA, 2010.
113. Marieb E N and Hoehn K N (2014), Human Anatomy & Physiology, 10th Edition, Published by Pearson.
114. Marutyan K R, Holland M R, Miller J G (2006). Anomalous negative dispersion in bone can result from the interference of fast and slow waves, Acoust Soc Am, 120(5), EL 55–61.
115. Marsell R and Einhorn T A (2011). The biology of fracture healing, Injury 42(6), 551–555.
116. Maylia E and Nokes L D (1999). The use of ultrasonics in orthopaedics—A review, Technol Health Care, 7(1), 1–28.
117. Meganck J, Begun D, McElderry J, Swick A, Kozloff K, Goldstein S, Morris M, Marini J, Caird M (2013). Fracture healing with alendronate treatment in the Brtl/+ mouse model of osteogenesis imperfecta, Bone, 56(1), 204–212
118. Mehta M, Heyland M, Toben D, Duda G N (2013). Microstructure and homogeneity of distribution of mineralised struts determine callus strength, Eur Cell Mater, 25, 366–379.
119. Mendelsohn R, Paschalis EP, Sherman PJ, Boskey AL (2000). IR microscopic imaging of pathological states and fracture healing of bone, Appl Spectrosc, 54(8), 1183–1191.
120. Minonzio J-G, Talmant M Laugier P (2010). Guided wave phase velocity measurement using multi-emitter and multi-receiver arrays in the axial transmission configuration, J Acoust Soc Am, 127(5), 2913–2919.
121. Minonzio J-G, Foiret J, Talmant M, Laugier P (2011). Impact of attenuation on guided mode wavenumber measurement in axial transmission on bone mimicking plates, J Acoust Soc Am, 130(6), 3574–82.

122. Moilanen P, Nicholson P H, Kärkkäinen T, Wang Q, Timonen J, Cheng S (2003). Assessment of the tibia using ultrasonic guided waves in pubertal girls, Osteoporos Int, 14, 1020 –1027.
123. Moilanen P, Kilappa V, Nicholson P H F, Timonen J, Cheng S (2004). Thickness sensitivity of ultrasound velocity in long bone phantoms, Ultras in Med & Biol, 30(11), 1517–1521 (2004).
124. Moilanen P, Talmant M, Nicholson P H F, Cheng S, Timonen J, Laugier, P (2007). Ultrasonically determined thickness of long cortical bones: Three-dimensional simulations of in vitro experiments, J Acoust Soc Amer, 122(3), 2439–2445.
125. Molero M and Medina L (2012). Comparison of phase velocity in trabecular bone mimicking-phantoms by time domain numerical (EFIT) and analytical multiple scattering approaches, Ultrasonics, 52(7), 809–814.
126. Mora-Macías J, Pajares A, Miranda P, Domínguez J, Reina-Romo E (2017). Mechanical characterization via nanoindentation of the woven bone developed during bone transport, J Mech Behav Biomed Mater, 74, 236–244.
127. Morris M D (2010). Raman spectroscopy of bone and cartilage, In Emerging Raman Applications and Techniques in Biomedical and Pharmaceutical Fields, Springer: Berlin, 347–364.
128. Morse P and Ingard K (1986). Theoretical Acoustics (Princetown University Press, Princetown, NJ.
129. Muller M, Moilanen P, Bossy E, Nicholson P, Kilappa V, Timonen J, Talmant M, Cheng S, Laugier, P (2005). Comparison of three ultrasonic axial transmission methods for bone assessment, Ultrasound Med Biol, 31(5), 633–642.
130. Mundi R, Petis S, Kaloty R, Shetty V, and Bhandari M (2009). Low-intensity pulsed ultrasound: Fracture healing, Indian J Orthop, 43(2), 132–140.
131. Nakahira A, Konishi S, Nishimura F, Iwasaka M, Ueno S (2003). Effect of a high magnetic field on the bioactivity of apatite-based biomaterials, J Appl Phys, 93(10), 8513–8515.
132. Nazarchuk Z, Skalskyi V, Serhiyenko O (2017). Propagation of Elastic Waves in Solids, Chapter 2 in Acoustic Emission Methodology and Application, Springer International Publishing AG, 29–73.
133. Njeh C F, Hans D, Wu C, Kantorovich E, Sister M, Fuerst T, Genant H K (1999). An *in vitro* investigation of the dependence on sample thickness of the speed of sound along the specimen, Medical Engineering & Physics 21(9), 651–659.
134. Nicholson P H F, Moilanen P, Karkkainen T, Timonen J, Cheng S (2002). Guided ultrasonic waves in long bones: Modeling, experiment and *in vivo* application, Phys Meas, 23(4), 755–768.
135. Ojanena X, Töyräs J, Inkinen S I, Malo M K H, Isaksson H, Jurvelin J S (2016). Differences in acoustic impedance of fresh and embedded human trabecular bone samples-Scanning acoustic microscopy and numerical evaluation, J Acoust Soc Am, 140(3), 1931–1936.
136. Otani T, Mano I, Tsujimoto T, Yamamoto T, Teshima R, Naka H (2009). Estimation of *in vivo* cancellous bone elasticity, Jap J Appl Phys, 123(4),
137. Ouyang H, Sherman P J, Paschalis E P, Boskey A L, Mendelsohn R (2004). Fourier transform infrared microscopic imaging: effects of estrogen and estrogen deficiency on fracture healing in rat femurs, Appl Spectrosc, 58(1), 1–9.

138. Oyen M L (2010). Handbook of Nanoindentation: With Biological Applications. Pan Stanford Publishing: Singapore.
139. Padilla F, Jenson F, Laugier P (2006). Estimation of trabecular thickness using ultrasonic backcatter, Ultrason Imaging 28(1), 3–22.
140. Papacharalampopoulos A, Vavva M G, Protopappas V C, Fotiadis D I, Polyzos D (2011). A numerical study on the propagation of Rayleigh and guided waves in cortical bone according to Mindlin's Form II gradient elastic theory, J Acoust Soc Am, 130(2), 1060–1070.
141. Peiffer V, Gerisch A, Vandepitte D, Van O H, Geris L (2011). A hybrid bioregulatory model of angiogenesis during bone fracture healing, Biomech Model Mechanobiol, 10(3), 383–395.
142. Pezzuti J A, Morris M D, Bonadio J F, Goldstein S K (1998). Hyperspectral Raman imaging of bone growth and regrowth chemistry, In Three-Dimensional and Multidimensional Microscopy: Image Acquisition and Processing V. SPIE: Bellingham, 270–276.
143. Pilla A A, Mont M A, Nasser P R, Khan S A, Figueiredo M, Kaufman J J, Siffert RS (1990). Non-invasive low-intensity pulsed ultrasound accelerates bone healing in the rabbit, J Orthop Trauma, 4(3), 246–253.
144. Polyzos D, Tsinopoulos S V, and Beskos D E (1998). Static and Dynamic Boundary Element Analysis in Incompressible Linear Elasticity, European Journal of Mechanics A/Solids, 17, 515–536.
145. Potsika V T, Protopappas V C, Vavva M G, Raum K, Rohrbach D, Polyzos D, Fotiadis D I (2012). Two-dimensional simulations of wave propagation in healing long bones based on scanning acoustic microscopy images, International Ultrasonics Symposium, Dresden, Germany.
146. Potsika V T, Grivas K N, Protopappas V C, Vavva M G, Raum K, Rohrbach D, Polyzos D, Fotiadis D I (2014a). Application of an effective medium theory for modeling ultrasound wave propagation in healing long bones, Ultrasonics, 54(5), 1219–1230.
147. Potsika V T, Vavva M G, Protopappas V C, Polyzos D, Fotiadis D I (2014b). Computational Modeling of Ultrasound Wave Propagation in Bone, In Computational Medicine in Data Mining and Modeling, Springer, New York, NY, USA, 349–376.
148. Potsika V T, Spiridon I F, Protopappas V C, Vavva M G, Lymperopoulos P D, Massalas C V, Polyzos D K, Fotiadis D I (2014c). Computational study of the influence of callus porosity on ultrasound propagation in healing bones. Proc of 36th Annual International Conference of the IEEE Engineering in Medicine and Biology Society, Chicago, IL, USA, 3–6, 636–638.
149. Potsika V T, Gortsas T, Grivas K N, Spiridon I F, Protopappas V C, Vavva M G, Raum K, Polyzos D K, Fotiadis D I (2014d). Computational modeling of guided ultrasound wave propagation in healthy and osteoporotic bones, 6th Conference of the Hellenic Society of Biomechanics, Patras, Greece.
150. Potsika V T, Grivas K N, Gortsas T, Iori G, Protopappas V C, Raum K, Polyzos D, Fotiadis D I (2016a). Computational Study of the Effect of Cortical Porosity on Ultrasound Wave Propagation in Healthy and Osteoporotic Long Bones, Materials, 9(3), 1–21.
151. Potsika V T, Protopappas V C, Grivas K N, Gortsas T V, Raum K, Polyzos D K, Fotiadis D I (2017). Numerical evaluation of ultrasonic backscattering in healing long bones, The Journal of the Acoustical Society of America, 142 (2), 962–973.

152. Potsika V T, Protopappas V C, Grivas K N, Gortsas T V, Vavva M G, Polyzos D K, Fotiadis D I (2016b). Ultrasonic Evaluation of Intact, Healing and Osteoporotic Long Bones, Journal of the Serbian Society for Computational Mechanics, 10(1), 168–189.
153. Preininger B, Checa S, Molnar F L, Fratzl P, Duda G N, Raum K (2011). Spatial-temporal mapping of bone structural and elastic properties in a sheep model following osteotomy, Ultrasound in Med & Biol, 37(3), 474–483.
154. Prevrhal S, Fuerst T, Fan B, Njeh C, Hans D, Uffmann M, Srivastav S, Genant H K (2001). Quantitative ultrasound of the tibia depends on both cortical density and thickness, Osteoporosis International 12(1), 28–34.
155. Protopappas V C, Baga D A, Fotiadis D I, Likas A C, Papachristos A A, Malizos K N (2005). An Ultrasound Wearable System for the Monitoring and Acceleration of Fracture Healing in Long Bones, IEEE Trans Biomed Engin, 52(9), 1597–1608.
156. Protopappas V C, Fotiadis D I, Malizos K N (2006a). Guided ultrasound wave propagation in intact and healing long bones, Ultrasound in Med & Biol, 32(5), 693–708.
157. Protopappas V C (2006b). Development of Osteogenesis Diagnostic Environment, Doctoral thesis, University of Ioannina, Greece.
158. Protopappas V C, Kourtis I C, Kourtis L C, Malizos K N, Massalas C V, Fotiadis D I (2007). Three-dimensional finite element modeling of guided ultrasound wave propagation in intact and healing long bones, J Acoust Soc Am, 121(6), 3907–3921.
159. Protopappas V C, Vavva M G, Fotiadis D I, Malizos K N (2008). Ultrasonic Monitoring of Bone Fracture Healing, IEEE Trans Ultras, Ferroel & Freq Contr, 55(6), 1243–1255.
160. Raum K, Leguerney I, Chandelier F, Bossy E, Talmant M, Saied A, Peyrin F, Laugier P (2005). Bone microstructure and elastic tissue properties are reflected in QUS axial transmission measurements, Ultrasound Med Biol, 31(9), 1225–1235.
161. Raum K, Grimal Q, Varga P, Barkmann R, Glüer C C, Laugier P (2014). Ultrasound to Assess Bone Quality, Curr Osteoporos Rep, 12(2), 154–162.
162. Raum K, Leguerney I, Chandelier F, Talmant M, Saïed A, Peyrin F, Laugier P (2006B). Site-matched assessment of structural and tissue properties of cortical bone using scanning acoustic microscopy and synchrotron radiation μCT, Phys Med Biol, 51, 733–746.
163. Raum K, Cleveland R O, Peyrin F, Laugier P (2006b). Derivation of elastic stiffness from site-matched mineral density and acoustic impedance, Phys Med Biol, 51(3),747–758.
164. Raum K (2011). Microscopic Elastic Properties, Chapter 16 in Bone Quantitative Ultrasound, 409–440.
165. Rayleigh J W S and Lindsay R B (1878). Theory of Sound, Macmillan, London, UK.
166. Regauer M, Jürgens P, Budenhofer U, Hartstock M, Böcker W, Bürklein D , Mutschler W, Sader R, Schieker M (2006). Quantitative scanning acoustic microscopy compared to microradiography for assessment of new bone formation, Bone, 38(4), 564–570.
167. Reher P, Doan N, Bradnock B, Meghji S, Harris M (1999). Effect of ultrasound on the production of IL-8, basic FGF and VEGF. Cytokine, 11, 416–423.

168. Rho J-Y, Kuhn-Spearing L, Zioupos P (1998). Mechanical properties and the hierarchical structure of bone, Medical Engineering & Physics, 20, 92–102.
169. Rohde K, Rohrbach D, Gluer C C, Laugier P, Grimal Q, Raum K, Barkmann R (2014). Influence of Porosity, Pore Size, and Cortical Thickness on the Propagation of Ultrasonic Waves Guided Through the Femoral Neck Cortex: A Simulation Study, IEEE Trans Ultras Ferroel Freq Control, 61(2), 302–313.
170. Rohrbach D, Lakshmanan S, Peyrin F, Langer M, Gerisch A, Grimal Q, Laugier P, Raum K (2012). Spatial distribution of tissue level properties in human a femoral cortical bone, J Biomech, 45(13), 2264–2270.
171. Rohrbach D, Preininger B, Hesse B, Gerigk H, Perka C, Raum K (2013). The early phases of bone healing can be differentiated in a rat osteotomy model by focused transverse-transmission ultrasound, Ultrasound in Med & Biol, 39(9), 1642–1653.
172. Roschger P, Misof B, Paschalis E, Fratzl P, Klaushofer K (2014). Changes in the Degree of Mineralization with Osteoporosis and its Treatment, Curr Osteoporos Rep, 12(3), 338–350.
173. Rupin F, Saied A, Dalmas D, Peyrin F, Haupert S, Raum K, Barthel E, Boivin G, Laugier P (2009). Assessment of Microelastic Properties of Bone Using Scanning Acoustic Microscopy: A Face-to-Face Comparison with Nanoindentation, Japanese Journal of Applied Physics, 48, 1–6.
174. Sadat-Shojai M, Khorasani M-T, Dinpanah-Khoshdargi E, Jamshidi A (2013). Synthesis methods for nanosized hydroxyapatite with diverse structures, Acta Biomaterialia, 9(8), 7591–7621.
175. Saha S, Rao V V, Malakanok V, Albright J A (1982). Quantitative measurement of fracture healing by ultrasound, Proc 1st Southern Biomed. Eng Conf, 247–249.
176. Sakata S, Barkmann R, Lochmuller E-M, Heller M , Gluer C C (2004). Assessing Bone Status Beyond BMD: Evaluation of Bone Geometry and Porosity by Quantitative Ultrasound of Human Finger Phalanges, J Bone & Mineral Research, 19(6), 2004.
177. Sasso M, Haïat G, Yamato Y, Naili S, Matsukawa M (2007). Frequency Dependence of Ultrasonic Attenuation in Bovine Cortical Bone: An *In Vitro* Study, Ultrasound in Med & Biol, 33(12), 1933–1942.
178. Schrof S, Varga P, Hesse B, Schöne M, Schütz R, Masic A, Raum K (2016). Multimodal correlative investigation of the interplaying microarchitecture, chemical composition and mechanical properties of human cortical bone tissue reveals predominant role of fibrillar organization in determining microelastic tissue properties, Acta Biomaterialia, 3–14.
179. Sfeir C, Ho L, Doll B A,Azari K, Hollinger J O (2005). Fracture Repair, Chapter 1 in Bone Regeneration and Repair: Biology and Clinical Applications, Humana Press Inc, Totowa, New Jersey, 21–44.
180. Shang-Lian B, Jiang D, Song G (2013). Review of the ultrashort echo time magnetic resonance imaging of cortical bone, Acta Physica Sinica, 62(8), 1–7.
181. Shefelbine S J, Augat P, Claes L, Simon U (2005). Trabecular bone fracture healing simulation with finite element analysis and fuzzy logic, J of Biomechanics, 38(12), 2440–2450.
182. Shuler F D, Conjeski J, Kendall D, Salava J (2012). Understanding the Burden of Osteoporosis and Use of the World Health Organization FRAX, CME Review Article, 35(9), 798–805.

183. Talmant M, Kolta S, Roux C, Haguenauer D, Vedel I, Cassou B, Bossy E, Laugier P (2009). *In vivo* performance evaluation of bi-directional ultrasonic axial transmission for cortical bone assessment, Ultrasound in Med & Biol, 35(6), 912–919.
184. Thompson D D (1980). Age changes in bone mineralization, cortical thickness, and haversian canal area, Calcif Tissue Int, 31(1), 5–11.
185. Treeby B E, Jaros J, Rendell A P, Cox B T (2012). Modeling nonlinear ultrasound propagation in heterogeneous media with power law absorption using a k-space pseudospectral method, J Acoust Soc Amer, 131(6), 4324–4336.
186. Vavva M G, Protopappas V C, Gergidis L N, Charalampopoulos A, Fotiadis D I, Polyzos D (2008a). The effect of boundary conditions on guided wave propagation in two-dimensional models of healing bone, Ultrasonics, 48(6–7), 598–606.
187. Vavva M G, Protopappas V C, Fotiadis D I, Malizos K N (2008b). Ultrasound Velocity Measurements on Healing Bones Using the External Fixation Pins: A Two-Dimensional Simulation, J Serb Soc Comp Mech, 2(2), 1–15.
188. Vavva M G, Protopappas V C, Gergidis L N, Charalampopoulos A, Fotiadis D I, Polyzos D (2009). Velocity dispersion of guided waves propagating in a free gradient elastic plate: Application to cortical, J Acoust Soc Am, 125(5), 3414–3427.
189. Vavva M G, Gergidis L N, Protopappas V C, Charalampopoulos A, Polyzos D, Fotiadis D I (2014). A study on Rayleigh wave dispersion in bone according to Mindlin's Form II gradient elasticity, J Acoust Soc Am, 135(5), 3117–3126.
190. Vavva M G, Grivas K N, Polyzos D, Fotiadis D I, Carlier A, Geris L, Van O H (2015). A Mathematical model for bone healing predictions under the ultrasound effect, Proc 6th ESUCB, Corfu, Greece.
191. Verbis J T, Kattis S E, Tsinopoulos S V, Polyzos D (2001). Wave dispersion and attenuation in fiber composites, Comp Mechan, 27(3), 244–252.
192. Wang X, Xu S, Zhou S, Xu W, Leary M, Choong P, Qian M, Brant M, Xie Y M (2016). Topological design and additive manufacturing of porous metals for bone scaffolds and orthopaedic implants: A review, Biomaterials, 83, 127–141.
193. Waterman P C and Truell R (1961). Multiple scattering of waves, J Math Phys 2(4), 512–537.
194. Waters K R and Hoffmeister B K (2005). Kramers-Kronig analysis of attenuation and dispersion in trabecular bone, J Acoust Soc Am ,118(6), 3912–3920.
195. Watts N B (2011). The Fracture Risk Assessment Tool (FRAX): Applications in Clinical Practice, J of Women's Health, 20(4), 525–531.
196. Wear K A (1999). Frequency dependence of ultrasonic backscatter from human trabecular bone: theory and experiment, J Acoust Soc Am, 106(6), 3659–3664.
197. Wear K A (2005). The dependencies of phase velocity and dispersion on cancellous thickness and spacing in cancellous bone-mimicking phantoms, J Acoust Soc Am, 118(2), 1186–1192.
198. Wolff J (1982). Das Gaesetz der Transformation der Knochen, Hirchwild, Berlin.
199. Wrobel L C (2002). The Boundary Element Method, Volume 1: Applications in Thermo-Fluids and Acoustics, John Wiley, England.
200. Yang K-Y, Parvizi J, Wang S-J, Lewallen D G, Kinnick R R, Greenleaf J F, Bolander M E (1996). Exposure to Low-Intensity Ultrasound IncreasesAggrecan

Gene Expression in a Rat Femur Fracture Model, Journal of Orthopaedic Research, 14(5), 802–809.
201. Zimmermann E A, Busse B, Ritchie R O (2015). The fracture mechanics of human bone: influence of disease and treatment, BoneKEy Reports 4, Article number: 743, International Bone & Mineral Society.
202. Zhou Q, Lam K H, Zheng H, Qiu W, Shunga K K (2014). Piezoelectric single crystals for ultrasonic transducers in biomedical applications, Prog Mater Science, 66, 87–111.

Author's Publications

Journal Papers

1. Potsika V T, Grivas K N, Protopappas V C, Vavva M G, Raum K, Rohrbach D, Polyzos D, Fotiadis D I (2014a). Application of an effective medium theory for modeling ultrasound wave propagation in healing long bones, Ultrasonics, 54(5), 1219–1230.

2. Potsika V T, Protopappas V C, Vavva M G, Raum K, Rohrbach D, Polyzos D, Fotiadis D I (2013). Estimation of wave dispersion and attenuation for the assessment of healing bones, Journal of the Serbian Society for Computational Mechanics. 7(1), 28–35.

3. Potsika V T, Grivas K N, Gortsas T, Iori G, Protopappas V C, Raum K, Polyzos D, Fotiadis D I (2016). Computational Study of the Effect of Cortical Porosity on Ultrasound Wave Propagation in Healthy and Osteoporotic Long Bones, Materials, 9(3), 1–21.

4. Potsika V T, Protopappas V C, Grivas K N, Gortsas T V, Vavva M G, Polyzos D K, Fotiadis D I (2016). Ultrasonic Evaluation of Intact, Healing and Osteoporotic Long Bones, Journal of the Serbian Society for Computational Mechanics, 10(1), 168–189.

5. Potsika V T, Protopappas V C, Grivas K N, Gortsas T V, Raum K, Polyzos D K, Fotiadis D I (2017). Numerical evaluation of ultrasonic backscattering in healing long bones, The Journal of the Acoustical Society of America, 142 (2), 962–973.

Conference Papers

1. Potsika V, Tsipouras M, Kalatzis F, Pappas I, Danilatou V, Kafetzopoulos D, Tsiknakis M, Vorgia P, Fotiadis D (2011). Hercules: Medical Genetics and Biomechanical Informatics Infrastructure in support of early diagnosis, monitoring and treatment of children with neurological disorders in Greece, 29th International Epilepsy Congress, Rome, Italy.

2. Potsika V T, Protopappas V C, Vavva M G, Raum K, Rohrbach D, Polyzos D, Fotiadis D I (2012). Two-dimensional simulation of wave propagation in fractured long bones based on scanning acoustic microscopy images, International Ultrasonics Symposium, Dresden, Germany.

3. Potsika V T, Protopappas V C, Vavva M G, Raum K, Rohrbach D, Polyzos D, Fotiadis D I (2013). Estimation of wave dispersion and attenuation for the assessment of healing bones, Serbian Congress on Theoretical and Applied Mechanics, Vrnjacka Banja, Serbia.

4. Potsika V T, Protopappas V C, Vavva M G, Polyzos D, Fotiadis D I (2013). Phase velocity and attenuation predictions of waves in cancellous bone using an iterative effective medium approximation. 35th Annual International Conference of the IEEE Engineering in Medicine and Biology Society, Osaka, Japan.

5. Potsika V T, Protopappas V C, Vavva M G, Raum K, Rohrbach D, Polyzos D, Fotiadis D I (2013). Effect of fracture callus scattering on wave dispersion and

attenuation in healing bones, 19th Congress of the European Society of Biomechanics, Patras, Greece.

6. Potsika V T, Protopappas V C, Vavva M G, Polyzos D, Fotiadis D I (2013). Predictions of phase velocity and attenuation in healing long bones based on A multiple scattering theory, 10th HSTAM International Congress on Mechanics, Chania, Crete, Greece.

7. Potsika V T, Protopappas V C, Vavva M G, Raum K, Rohrbach D, Polyzos D, Fotiadis D I (2014). An iterative effective medium approximation for wave dispersion and attenuation estimations in the healing of long bones, 5th European Symposium on Ultrasonic Characterization of Bone, Granada, Spain.

8. Potsika V T, Protopappas V C, Vavva M G, Grivas K, Polyzos D, Fotiadis D I (2013). Computational modeling of ultrasound wave propagation in healing bones, AIChE Annual Meeting, San Francisco, California, United States.

9. Potsika V, Spiridon I, Protopappas V C, Vavva M, Lymperopoulos P, Massalas C, Polyzos D, Fotiadis D I (2014). Computational study of the influence of callus porosity on ultrasound propagation in healing bones, 36th Annual International Conference of the IEEE Engineering in Medicine and Biology Society, Chicago, Illinois, United States.

10. Georga E I, Protopappas V C, Bellos C, Potsika V, Fotiadis D I (2014). Prediction of Long-Term Glucose Control and Complications of Type 2 Diabetes Using Data Mining", 36th Annual International Conference of the IEEE Engineering in Medicine and Biology Society, Chicago, Illinois, United States.

11. Potsika V T, Gortsas T, Grivas K N, Spiridon I F, Protopappas V C, Vavva M G, Raum K, Polyzos D K, Fotiadis D I (2014). Computational modeling of guided ultrasound wave propagation in healthy and osteoporotic bones, 6th Conference of the Hellenic Society of Biomechanics, Patras, Greece.

12. Spiridon I, Pakos E, Potsika V, Protopappas V, Massalas C, Xenakis T, Agathopoulos S, Fotiadis D (2014). Effects of uncemented THA on biomechanical environment of femoral bones, 6th Conference of the Hellenic Society of Biomechanics, Patras, Greece.

13. Georga E I, Protopappas V C, Bellos C, Potsika V T, Arvaniti E, Fotiadis D I (2014). Long-term Prediction of Type 2 Diabetes Complications Using Machine Learning Techniques, 6th Conference of the Hellenic Society of Biomechanics, Patras, Greece.

14. Georga E I, Protopappas V C, Bellos C V, Potsika V T, Arvaniti E, Makriyiannis D, Fotiadis D I (2014). Development of a Smart Environment for Diabetes Data Analysis and New Knowledge Mining, MOBIHEALTH, Athens, Greece.

15. Potsika V T, Protopappas V C, Spiridon I F, Polyzos D, Fotiadis D I (2014). Modelling of Long Bone Microstructure and Ultrasonic Assessment of Healing Mechanisms, International Conference on Applied Informatics for Health and Life Sciences, Kusadasi, Turkey.

16. Potsika V, Protopappas V, Fotiadis D, Gortsas T, Grivas K, Polyzos D, Raum K (2015). In-silico evaluation of cortical porosity by tangential axial transmission, 6th European Symposium on Ultrasonic Characterization of Bone, Corfu, Greece.

17. Gortsas T, Grivas K, Polyzos D, Potsika V, Protopappas V, Fotiadis D, Raum K (2015). The effect of cortical bone porosity on ultrasonic backscattering parameters, 6th European Symposium on Ultrasonic Characterization of Bone, Corfu, Greece.

18. Potsika V T, Fotiadis D I, Gortsas T, Iori G, Raum K (2015). High-frequency cortical backscatter reveals cortical microstructure – a simulation study, 6th European Symposium on Ultrasonic Characterization of Bone, Corfu, Greece.

19. Hradilova J, Schone M, Raum K, Potsika V T, Fotiadis D I, Polyzos D (2015), Numerical Simulation of high-frequency Ultrasound Scattering on Articular Cartilage Cellular Structure, 6th European Symposium on Ultrasonic Characterization of Bone, Corfu, Greece.

20. Potsika V, Gortsas T, Protopappas V C, Polyzos D, Fotiadis D I (2015). Computational modeling of ultrasonic backscattering to evaluate fracture healing, 37th Annual International Conference of the IEEE Engineering in Medicine and Biology Society, Milano, Italy.

21. Potsika V, Grivas K, Gortsas T, Protopappas V C, Polyzos D, Raum K, Fotiadis D I (2015). Ultrasound propagation in cortical bone: axial transmission and backscattering simulations, 37th Annual International Conference of the IEEE Engineering in Medicine and Biology Society, Milano, Italy.

22. Potsika V T, Grivas K N, Gortsas T, Protopappas V C, Raum K, Polyzos D, Fotiadis D I (2016). Finite-Difference Time-Domain modeling of ultrasound wave propagation in intact and osteoporotic long bones, 11th HSTAM International Congress on Mechanics, Athens, Greece.

23. Potsika V T, Grivas K N, Gortsas T, Protopappas V C, Polyzos D K, Fotiadis D I (2016). Boundary element simulation of ultrasonic backscattering during the fracture healing process, 38th Annual International Conference of the IEEE Engineering in Medicine and Biology Society, Orlando, Florida, United States.

24. Potsika V T, Grivas K N, Gortsas T, Protopappas V C, Polyzos D K, Fotiadis D I (2016). Acoustic pressure measurements in the backward direction for the assessment of the fracture healing process, 7th Conference of the Hellenic Society of Biomechanics, Athens, Greece.

25. Potsika V T, Grivas K N, Gortsas T, Protopappas V C, Polyzos D, Fotiadis D I (2016). Evaluation of ultrasonic scattering during the bone healing process, 19th International Conference on Medical Image Computing and Computer Assisted Intervention, Athens, Greece.

26. Potsika V T, Protopappas V C, Grivas K N, Gortsas T, Polyzos D, Fotiadis D I (2016). Ultrasonic techniques for the assessment of intact, osteoporotic and healing long bones, 10th anniversary of the Serbian Society for Computational Mechanics, Kragujevac, Serbia.

27. Potsika V T, Grivas K N, Gortsas T, Protopappas V C, Polyzos D, Fotiadis D I (2017). Evaluation of ultrasonic scattering for different cortical bone porosities and excitation frequencies: a numerical study, 39th Annual International Conference of the IEEE Engineering in Medicine and Biology Society, Jeju Island, Korea.

28. Potsika V T, Grivas K N, Gortsas T V, Protopappas V C, Polyzos D K, Fotiadis D I (2017). Ultrasonic evaluation of cortical porosity, 7th National Conference of the Hellenic Society of Biomedical Technology (ELEVIT), Athens, Greece.

29. Potsika V T, Polyzos D, Fotiadis D I (2017). Computational Modeling of Long Bone Microstructure and Ultrasonic Evaluation of the Fracture Healing Process, 4th South-East European Conference on Computational Mechanics, Kragujevac, Serbia.

Books

1. Massalas C V, Potsika V T, Fotiadis D I, Introduction to Biomechanics (in Greek), to be published by University of Creta Publications.

Book Chapters

1. Potsika V T, Vavva M G, Protopappas V C, Polyzos D, Fotiadis D I (2013). Computational modeling of ultrasound wave propagation in bone, in Computational Medicine in Data Mining and Modeling, Springer Science+Business Media New York, 349–376.

2. Potsika V T, Grivas K N, Gortsas T, Protopappas V, Polyzos D, Fotiadis D I (2016). Numerical Simulation of Ultrasonic Backscattering During Fracture Healing Using Numerical Models Based on Scanning Acoustic Microscopy Images, in Simulation and Synthesis in Medical Imaging, Springer, 55–64.

Fellowships

Program IKYDA 2014: A program co-sponsored by the State Scholarships Foundation (IKY) and the German Academic Exchange Service (DAAD) promoting exchanges of young researchers and scientific cooperation between Greece and Germany.